



저작자표시-비영리-변경금지 2.0 대한민국

이용자는 아래의 조건을 따르는 경우에 한하여 자유롭게

- 이 저작물을 복제, 배포, 전송, 전시, 공연 및 방송할 수 있습니다.

다음과 같은 조건을 따라야 합니다:



저작자표시. 귀하는 원저작자를 표시하여야 합니다.



비영리. 귀하는 이 저작물을 영리 목적으로 이용할 수 없습니다.



변경금지. 귀하는 이 저작물을 개작, 변형 또는 가공할 수 없습니다.

- 귀하는, 이 저작물의 재이용이나 배포의 경우, 이 저작물에 적용된 이용허락조건을 명확하게 나타내어야 합니다.
- 저작권자로부터 별도의 허가를 받으면 이러한 조건들은 적용되지 않습니다.

저작권법에 따른 이용자의 권리는 위의 내용에 의하여 영향을 받지 않습니다.

이것은 [이용허락규약\(Legal Code\)](#)을 이해하기 쉽게 요약한 것입니다.

[Disclaimer](#)

공학박사 학위논문

고용량 층상구조 산화물 기반 리튬
이차전지 양극 소재에 관한 연구

**Study on high-capacity layered oxides
cathode materials for lithium
rechargeable batteries**

2021 년 8 월

서울대학교 대학원

재료공학부

김 병 훈

고용량 층상구조 산화물 기반

리튬 이차전지 양극소재에 관한 연구

Study on high-capacity layered oxides cathode materials
for lithium rechargeable batteries

지도 교수 강 기 석

이 논문을 공학박사 학위논문으로 제출함

2021 년 8 월

서울대학교 대학원

재료공학부

김 병 훈

김병훈의 박사 학위논문을 인준함

2021 년 6 월

위 원 장	<u>한 승 우</u>
부위원장	<u>강 기 석</u>
위 원	<u>김 미 영</u>
위 원	<u>정 연 준</u>
위 원	<u>한 상 수</u>

Abstract

Study on high-capacity layered oxides cathode materials for lithium rechargeable batteries

Kim, Byunghoon

Department of Material Science and Engineering

College of Engineering

The Graduate School

Seoul National University

With the advent of new market segment aiming at societal energy and environmental concerns such as electrified transportation and grid-scale energy storage applications, there has been the pressing demand for the improvements in the performance of energy storage systems. Among energy storage systems, rechargeable lithium-ion batteries have been the de facto standards for portable electronic devices and electrified transportation for decades owing to their high energy density, power capability and stable cyclability. However, the full-fledged placement of green energy technologies requires a significant breakthrough in the energy density of

current battery systems, which has prompted the search for alternative battery electrode materials. In this regard, lithium-rich layered oxide electrodes have garnered tremendous research attention as a next-generation cathode system with exceptionally high energy density. But, the supply of high capacity from lithium-rich layered oxides has been known to compromise energy retention properties, thus it is of great importance to enhance the cycling performance of those electrodes. In this thesis, I present a theoretical investigation on the voltage depression problem of lithium-rich layered oxide electrodes, and propose a design strategy to improve electrochemical reversibility of electrodes during cycling.

In Chapter 2, I designed a unified a theoretical picture of the relations between redox chemistry and structural disorders in lithium-rich layered oxide electrodes. Oxygen redox provides high energy density for lithium- and sodium-rich layered oxides electrodes, but simultaneously leads to electrochemical irreversibility and voltage depression. Despite the observation of the associations between the irreversible oxygen redox and structural disorders, their intrinsic relations have yet been fully understood because there has been little consideration of bonding rearrangements involved with structural disordering. In this respect, I comprehensively address the multifaceted connections between structural disorder, bonding arrangement, and oxygen redox chemistry. My work encompasses a wide range of lithium-rich electrodes in charge-transfer systems and Mott-Hubbard systems, and covers both cation and anion disorders. It is unraveled that cation disorders stabilize oxygen

redox by driving strong oxygen-oxygen and/or metal-oxygen hybridization, and the nature of bonding reorganization depends on the occupancy of oxygen non-bonding states and metal-oxygen covalency. I further answer how the formation of short covalent bonds affects electrochemical and structural reversibility. And importantly, the free movement of oxygen dimer is spotted, suggesting poor structural resilience of oxygen dimers. On the other hand, anion disorder is found to compensate for the electron deficiency of oxygen network without significantly regulating bonding arrangements. My findings rationalize long-reported phenomenological correlations between structural disorders and oxygen redox, and offer a scientific basis for optimizing the reversibility of oxygen redox considering structural disorders.

In Chapter 3, I present a design strategy to improve the structural reversibility of lithium-rich layered oxide electrodes during charging and discharging. There has been a consensus that the voltage decay is mainly originated from structural transformations involving irreversible cation migration. While many previous studies have succeeded in inhibiting cation migration itself to some extent, the thermodynamically spontaneous nature of cation migration requires a paradigm shift toward managing the reversibility of inevitable cation migration. I demonstrate for cobalt-free lithium-rich nickel manganese oxides that by tweaking the oxygen lattice of compounds from typical O3 to O2 staking, the reversibility of cation migration can be remarkably improved, thereby dramatically suppressing the voltage decay. Preeminent intra-cycle reversibility of cation migration is visualized via scanning

transmission electron microscope, and such reversibility is proved to aid in the preservation of pristine structure over extended cycles. First-principle calculations verify that a large electrostatic repulsion between face-sharing cations restricts the movements of transition metals in the lithium layer, thereby streamlining the returning migration path of transition metals. Furthermore, I prove that the enhanced reversibility help mitigate the asymmetry of anion redox, which arises from the intra-cycle asymmetry of transition metal locations, ameliorating voltage hysteresis concurrently.

Keywords : Energy storage, Batteries, First-principles calculation, Cathodes, Li-rich layered oxides, Oxygen redox

Student Number : 2016-20773

Table of Contents

Abstract	i
List of Figures	vii
List of Tables	xix
Chapter 1. Introduction	1
1.1 Motivation and outline	1
1.2 References	6
Chapter 2. Trilateral correlation of structural disorder, bond covalency, and oxygen redox chemistry in lithium-rich layered oxide electrodes	9
2.1 Introduction	9
2.2 Computational details	13
2.3 Result and Discussion	15
2.3.1 Cation disordering in charge-transfer systems	15
2.3.2 Cation disordering in Mott-Hubbard systems	36
2.3.3 Reversibility and asymmetry of the oxygen redox	63
2.3.4 Anionic disorder and oxygen redox chemistry	94
2.3.5 Theoretical voltage profiles considering structural disorder	108
2.3.6 Electronic structure of electrodes	111
2.3.7 Effects of metal-oxygen decoordination on the electronic structure	114
2.3.8 Types of oxygen dimer	116
2.3.9 Cation migration in $\text{Na}_{0.6}[\text{Li}_{0.2}\text{Mn}_{0.8}]\text{O}_2$ and $\text{Na}_{2/3}[\text{Mg}_{1/3}\text{Mn}_{2/3}]\text{O}_2$	119

2.3.10 Effects of metal substitution on bond rearrangements	122
2.4 Concluding remarks	143
2.5 References	144
Chapter 3. Voltage decay and redox asymmetry mitigation by reversible cation migration in lithium-rich layered oxide electrodes	156
3.1 Introduction	156
3.2 Experimental and computational details	162
3.3 Results and discussion	167
3.3.1 Electrochemistry of O2-LLNMOs	167
3.3.2 Reversible cation migration in O2-LLNMOs	174
3.3.3 High-potential O redox behavior preserved in O2-LLNMOs	190
3.3.4 Synthesis of O2-LLNMOs	198
3.3.5 Structural characterization of O2-LLNMOs	204
3.3.6 Theoretical investigation of cation migration pathways	205
3.3.7 Partial manganese reduction during discharge	217
3.4 Concluding remarks	218
3.5 References	220
Chapter 4. Summary	231
Abstract in Korean	233

List of Figures

Figure 2-1. Bonding rearrangements involved with cation disordering in charge-transfer systems. **a**, Bonding rearrangements involved with charging and $Mn_{Li, octa}$ formation in $Li_{2-x}MnO_3$. **b**, Relaxed structure of $Na_0[Mg_{1/3}Mn_{2/3}]O_2$ with $Mn_{Li, octa}$. **c**, Bond rearrangements involved with in-plane cation migration in $Na_0[Li_0Mn_{0.8}]O_2$ with the ribbon superstructure. **d**, **e**, Changes in the electronic structure of oxygen atoms involved with O-O dimerization (**d**) and Mn-O π hybridization (**e**). **f**, Schematic representation of the electronic reshuffling of oxygen redox states due to cation disordering.

Figure 2-2. The in-plane Li-M arrangements and electronic structures of pristine electrodes belonging to charge-transfer systems. **a**, Li_2MnO_3 , **b**, $Na_{0.6}[Li_{0.2}Mn_{0.8}]O_2$, and **c**, $Na_{2/3}[Mg_{1/3}Mn_{2/3}]O_2$.

Figure 2-3. Schematic representations of possible cation disorders. $M_{Li}-V_M$ antisite cation-vacancy defects pair can be formed by **a**, out-of-plane cation migration to the tetrahedral site in the Li layer (denoted as $M_{Li, tetra}$), **b**, out-of-plane cation migration to the octahedral site in the Li layer (denoted as $M_{Li, octa}$), and **c**, In-plane cation migration to the empty Li site (denoted as $M_{Li, TM layer}$).

Figure 2-4. a, DOS of Li_2MnO_3 and $Li_{0.5}MnO_3$ without any structural disorder. (Inset) Isosurface of charge density for the electronic states near the Fermi level. **b**, The formation energies of $Mn_{Li, tetra}$, $Mn_{Li, octa}$, and $Mn_{Li, TM layer}$ disorders in $Li_{0.5}MnO_3$. In

addition, for each combination of cation disorder and dimer type, properties of the most stable structure are presented in **c-n**.

Figure 2-5. a, DOS of $\text{P3-Na}_{2/3}[\text{Mg}_{1/3}\text{Mn}_{2/3}]\text{O}_2$ and $\text{O3-Na}_0[\text{Mg}_{1/3}\text{Mn}_{2/3}]\text{O}_2$ without any structural disorder. **b**, Bonding rearrangements involved with charging and $\text{Mn}_{\text{Na, octa}}$ formation, where dangling oxygen ions formed with Mn migration are colored green. **c-e**, Bonding arrangements and electronic structures of $\text{O3-Na}_0[\text{Mg}_{1/3}\text{Mn}_{2/3}]\text{O}_2$ with $\text{Mn}_{\text{Na, tetra}}$ (**c**), $\text{Mn}_{\text{Na, octa}}$ (**d**), and $\text{Mn}_{\text{Mg, TM layer}}$ (**e**) disorder.

Figure 2-6. a, DOS of $\text{P3-Na}_{0.6}[\text{Li}_{0.2}\text{Mn}_{0.8}]\text{O}_2$ and $\text{P3-Na}_0[\text{Li}_0\text{Mn}_{0.8}]\text{O}_2$ without any structural disorder. **b**, Schematic representation of possible in-plane Mn migration pathways in $\text{P3-Na}_0[\text{Li}_0\text{Mn}_{0.8}]\text{O}_2$. For each case, the relaxed structures and corresponding electronic structures are presented in **c-f**.

Figure 2-7. a, b, Bonding rearrangements involved with $\text{M}_{\text{Li, octa}}$ formation in $\text{Li}_{0.5}\text{RuO}_3$ (**a**) and $\text{Li}_{0.5}\text{IrO}_3$ (**b**). **c, d**, Changes in the electronic structure of dangling oxygen involved with $\text{M}_{\text{Li, octa}}$ formation in $\text{Li}_{0.5}\text{RuO}_3$ (**c**) and $\text{Li}_{0.5}\text{IrO}_3$ (**d**). **e, f**, Bonding rearrangements involved with $\text{M}_{\text{Li, octa}}$ formation in $\text{Li}_{0.5}\text{Ru}_{0.5}\text{Sn}_{0.5}\text{O}_3$ (**e**) and $\text{Li}_{0.5}\text{Ir}_{0.5}\text{Sn}_{0.5}\text{O}_3$ (**f**).

Figure 2-8. The in-plane Li-M arrangements and electronic structures of pristine electrodes belonging to Mott-Hubbard systems. **a**, Li_2IrO_3 , **b**, Li_2RuO_3 , and **c**, $\text{Li}_2\text{Ru}_{0.5}\text{Mn}_{0.5}\text{O}_3$.

Figure 2-9. a, DOS of Li_2RuO_3 , Li_1RuO_3 , and $\text{Li}_{0.5}\text{RuO}_3$ without any structural

disorder. **b**, Bonding rearrangements involved with charging and $\text{Ru}_{\text{Li, octa}}$ formation in $\text{Li}_{2-x}\text{RuO}_3$. Dangling oxygen ions formed with cation migration are colored green. **c-e**, Bonding arrangements and corresponding electronic structures calculated for $\text{Li}_{0.5}\text{RuO}_3$ with $\text{Ru}_{\text{Li, tetra}}$ (**c**), $\text{Ru}_{\text{Li, octa}}$ (**d**), and $\text{Ru}_{\text{Li, TM layer}}$ (**e**).

Figure 2-10. a, DOS of Li_2IrO_3 , Li_1IrO_3 , and $\text{Li}_{0.5}\text{IrO}_3$ without any structural disorder. **b**, Bonding rearrangements involved with charging and $\text{Ir}_{\text{Li, octa}}$ formation in $\text{Li}_{2-x}\text{IrO}_3$. Dangling oxygen ions formed with cation migration are colored green. **c-e**, Bonding arrangements and corresponding electronic structures calculated for $\text{Li}_{0.5}\text{IrO}_3$ with $\text{Ir}_{\text{Li, tetra}}$ (**c**), $\text{Ir}_{\text{Li, octa}}$ (**d**), and $\text{Ir}_{\text{Li, TM layer}}$ (**e**).

Figure 2-11. Disorder formation energies ($\Delta G_{\text{structural change}}$) in $\text{Li}_{0.5}\text{RuO}_3$ and $\text{Li}_{0.5}\text{IrO}_3$. The minimum O-O distance in supercells are represented together.

Figure 2-12. a, DOS of $\text{Li}_2\text{Ru}_{0.5}\text{Mn}_{0.5}\text{O}_3$, $\text{Li}_{1.5}\text{Ru}_{0.5}\text{Mn}_{0.5}\text{O}_3$, $\text{Li}_1\text{Ru}_{0.5}\text{Mn}_{0.5}\text{O}_3$, and $\text{Li}_{0.5}\text{Ru}_{0.5}\text{Mn}_{0.5}\text{O}_3$ without any structural disorder. **b, f**, Bonding rearrangements involved with charging and $\text{Ru}_{\text{Li, octa}}$ (**b**) and $\text{Mn}_{\text{Li, octa}}$ (**f**) formation in $\text{Li}_{2-x}\text{Ru}_{0.5}\text{Mn}_{0.5}\text{O}_3$. **c-e, g-i**, Bonding arrangements and corresponding electronic structures calculated for $\text{Li}_{0.5}\text{Ru}_{0.5}\text{Mn}_{0.5}\text{O}_3$ with $\text{Ru}_{\text{Li, tetra}}$ (**c**), $\text{Ru}_{\text{Li, octa}}$ (**d**), $\text{Ru}_{\text{Li, TM layer}}$ (**e**), $\text{Mn}_{\text{Li, tetra}}$ (**g**), $\text{Mn}_{\text{Li, octa}}$ (**h**), and $\text{Mn}_{\text{Li, TM layer}}$ (**i**).

Figure 2-13. The in-plane Li-M arrangements and electronic structures of **a**, $\text{Li}_2\text{Ru}_{0.5}\text{Sn}_{0.5}\text{O}_3$, **b**, $\text{Li}_2\text{Ir}_{0.5}\text{Sn}_{0.5}\text{O}_3$, and **c**, $\text{Li}_2\text{Ni}_{0.5}\text{Te}_{0.5}\text{O}_3$.

Figure 2-14. COOPs calculated for M-O bands in a range of 1.5 ~ 2.4 Å. **a**, COOPs

of M-O bonds present in $\text{Li}_2\text{Ru}_{0.5}\text{Sn}_{0.5}\text{O}_3$, $\text{Li}_2\text{Ir}_{0.5}\text{Sn}_{0.5}\text{O}_3$, and $\text{Li}_2\text{Ni}_{0.5}\text{Te}_{0.5}\text{O}_3$. **b**, COOPs of M-O bonds present in Li_2MnO_3 , Li_2VO_3 , Li_2RuO_3 , Li_2IrO_3 , and Li_2SnO_3 .

Figure 2-15. Effects of bonding rearrangements and oxygen vacancy on electrochemical and structural reversibility. **a**, Schematic illustration of redox asymmetry that arises from cation disordering and consequent strong TM-O π hybridization. **b-c**, (left) Changes in O-O and Mn-O distances involved with $\text{Mn}_{\text{Li, octa}}$ formation and concomitant oxygen dimerization in $\text{Li}_{0.5}\text{MnO}_3$, where the dimer type is the floating dimer(**b**), and edge dimer (**c**). (right) Snapshots of *ab initio* MD calculations at 300 K. **d**, V_{O} formation energy according to h^{O} of charged electrodes. **e**, (left) Formation energy of cation disorders calculated for $\text{Li}_{0.5}\text{RuO}_3$ with or without V_{O} . (right) V_{O} formation energy calculated for $\text{Li}_{0.5}\text{RuO}_3$ with or without cationic disorders.

Figure 2-16. (left) TM migration pathways that include out-of-plane TM migration from the TM layer (A_{octa}) to the lithium tetrahedral site (B_{tetra}), and intra-layer TM migration within the Li layer ($B_{\text{tetra}} \rightarrow C_{\text{octa}} \rightarrow D_{\text{tetra}} \rightarrow E_{\text{octa}}$). (right) Energy landscape of TM migration calculated for the left trajectory in $\text{Li}_{0.5}\text{RuO}_3$.

Figure 2-17. a-c, Bonding rearrangements involved with $\text{Mn}_{\text{Li, octa}}$ formation and concomitant oxygen dimerization in $\text{Li}_{0.5}\text{MnO}_3$, where the dimer type is floating dimer and dangling dimer (**a**), bridge dimer (**b**), and edge dimer (**c**). **d**, O-O and Mn-O distances of O-O pairs. **e**, O-O ICOOP and Mn-O ICOOP of O-O pairs, where ICOOP is the integration of COOP up to the Fermi level.

Figure 2-18. Snapshots of *ab initio* MD calculations at 300 K, in which the initial structure describes the state where a floating dimer is produced with $\text{Mn}_{\text{Li,octa}}$ formation in $\text{Li}_{0.5}\text{MnO}_3$ (figure 2.17a).

Figure 2-19. Snapshots of *ab initio* MD calculations at 300 K, in which the initial structure describes the state where a dangling dimer is produced with $\text{Mn}_{\text{Li,octa}}$ formation in $\text{Li}_{0.5}\text{MnO}_3$ (figure 2.17a).

Figure 2-20. Snapshots of *ab initio* MD calculations at 300 K, in which the initial structure describes the state where a bridge dimer is produced with $\text{Mn}_{\text{Li,octa}}$ formation in $\text{Li}_{0.5}\text{MnO}_3$ (figure 2.17b).

Figure 2-21. Snapshots of *ab initio* MD calculations at 300 K, in which the initial structure describes the state where an edge dimer is produced with $\text{Mn}_{\text{Li,octa}}$ formation in $\text{Li}_{0.5}\text{MnO}_3$ (figure 2.17c).

Figure 2-22. Snapshots of *ab initio* MD calculations at 300 K, in which the initial structure is $\text{Li}_{0.5}\text{MnO}_3$ without any structural disorder.

Figure 2-23. Snapshots of *ab initio* MD calculations at 300 K, in which the initial structure describes the state where manganese ion is migrated along path A in $\text{Na}_0[\text{Li}_0\text{Mn}_{0.8}]\text{O}_2$ (figure 2.1c).

Figure 2-24. Snapshots of *ab initio* MD calculations at 300 K, in which the initial structure describes the state where an edge dimer is produced with $\text{Mn}_{\text{Li,octa}}$ formation in $\text{Na}_0[\text{Mg}_{1/3}\text{Mn}_{2/3}]\text{O}_2$ (figure 2.1b).

Figure 2-25. Snapshots of *ab initio* MD calculations at 300 K, in which the initial structure is $\text{Li}_{0.5}\text{IrO}_3$ without any structural disorder (**a**), and $\text{Li}_{0.5}\text{IrO}_3$ with $\text{Ir}_{\text{Li, octa}}$ disorder (**b**).

Figure 2-26. The relation between bader charge of extracted oxygen and $G_{\text{f}}(\text{V}_\text{O})$ in $\text{Li}_{2-x}\text{MnO}_3$.

Figure 2-27. a, c, Local structure changes involved with V_O formation in Li_2MnO_3 (**a**) and $\text{Li}_{0.5}\text{MnO}_3$ (**d**). **b, e,** DOS of Li_2MnO_3 (**b**) and $\text{Li}_{0.5}\text{MnO}_3$ (**e**) without any structural disorder. **c, f,** Changes in electronic structure involved with V_O formation in Li_2MnO_3 (**c**) and $\text{Li}_{0.5}\text{MnO}_3$ (**f**).

Figure 2-28. a, c, Local structure changes involved with V_O formation in Li_2RuO_3 (**a**) and $\text{Li}_{0.5}\text{RuO}_3$ (**d**). **b, e,** DOS of Li_2RuO_3 (**b**) and $\text{Li}_{0.5}\text{RuO}_3$ (**e**) without any structural disorder. **c, f,** Changes in electronic structure involved with V_O formation in Li_2RuO_3 (**c**) and $\text{Li}_{0.5}\text{RuO}_3$ (**f**).

Figure 2-29. a, c, Local structure changes involved with V_O formation in Li_2IrO_3 (**a**) and $\text{Li}_{0.5}\text{IrO}_3$ (**d**). **b, e,** DOS of Li_2IrO_3 (**b**) and $\text{Li}_{0.5}\text{IrO}_3$ (**e**) without any structural disorder. **c, f,** Changes in electronic structure involved with V_O formation in Li_2IrO_3 (**c**) and $\text{Li}_{0.5}\text{IrO}_3$ (**f**).

Figure 2-30. Voltage profiles considering structural disorders. **a,** (center) Calculated disorder formation energies, where $G_{\text{f}}(\text{M}_{\text{Li}})$ corresponds to the lowest value among $G_{\text{f}}(\text{M}_{\text{Li, tetra}})$, $G_{\text{f}}(\text{M}_{\text{Li, octa}})$, and $G_{\text{f}}(\text{M}_{\text{Li, TM layer}})$. In I-IV, schematic illustrations of

expected voltage profiles considering structural disorders are presented. **b**, Influence of structural constraints on voltage profiles.

Figure 2-31. a, The molecular orbital energy diagram of $\text{Li}_4\text{M}_2\text{-O}$ octahedron, which constitutes lithium-rich layered oxides Li_2MO_3 . **b-c**, Predictions for the electronic reshuffling of TM-O bond involved with cation disordering in charge-transfer systems (**b**) and Mott-Hubbard systems (**c**). **d**, (left) Schematic illustration of O-O dimerization process during the charging and subsequent cation disordering. (right) The transition of the oxygen electronic structure from oxide ion O^{2-} , to peroxide $(\text{O}_2)^{2-}$, superoxide $(\text{O}_2)^{1-}$, and gaseous oxygen O_2 .

Figure 2-32. a, Bonding rearrangements involved with charging and $\text{Ru}_{\text{Li, octa}}$ formation in $\text{Li}_{2-x}\text{Ru}_{0.5}\text{Sn}_{0.5}\text{O}_3$. Dangling oxygen ions formed with cation migration are colored green. **b-d**, Bonding arrangements and corresponding electronic structures calculated for $\text{Li}_{0.5}\text{Ru}_{0.5}\text{Sn}_{0.5}\text{O}_3$ with $\text{Ru}_{\text{Li, tetra}}$ (**b**), $\text{Ru}_{\text{Li, octa}}$ (**c**), and $\text{Ru}_{\text{Li, TM layer}}$ (**d**).

Figure 2-33. a, Bonding rearrangements involved with charging and $\text{Ir}_{\text{Li, octa}}$ formation in $\text{Li}_{2-x}\text{Ir}_{0.5}\text{Sn}_{0.5}\text{O}_3$. Dangling oxygen ions formed with cation migration are colored green. **b-d**, Bonding arrangements and corresponding electronic structures calculated for $\text{Li}_{0.5}\text{Ir}_{0.5}\text{Sn}_{0.5}\text{O}_3$ with $\text{Ir}_{\text{Li, tetra}}$ (**b**), $\text{Ir}_{\text{Li, octa}}$ (**c**), and $\text{Ir}_{\text{Li, TM layer}}$ (**d**).

Figure 2-34. a, Bonding rearrangements involved with charging and $\text{Sn}_{\text{Li, octa}}$

formation in $\text{Li}_{2-x}\text{Ru}_{0.5}\text{Sn}_{0.5}\text{O}_3$. Dangling oxygen ions formed with cation migration are colored green. **b-d**, Bonding arrangements and corresponding electronic structures calculated for $\text{Li}_{0.5}\text{Ru}_{0.5}\text{Sn}_{0.5}\text{O}_3$ with $\text{Sn}_{\text{Li, tetra}}$ (**b**), $\text{Sn}_{\text{Li, octa}}$ (**c**), and $\text{Sn}_{\text{Li, TM layer}}$ (**d**).

Figure 2-35. a, Bonding rearrangements involved with charging and $\text{Sn}_{\text{Li, octa}}$ formation in $\text{Li}_{2-x}\text{Ir}_{0.5}\text{Sn}_{0.5}\text{O}_3$. Dangling oxygen ions formed with cation migration are colored green. **b-d**, Bonding arrangements and corresponding electronic structures calculated for $\text{Li}_{0.5}\text{Ir}_{0.5}\text{Sn}_{0.5}\text{O}_3$ with $\text{Sn}_{\text{Li, tetra}}$ (**b**), $\text{Sn}_{\text{Li, octa}}$ (**c**), and $\text{Sn}_{\text{Li, TM layer}}$ (**d**).

Figure 2-36. We exchanged one Ru and one Sn in the most stable Ru/Sn ordering of $\text{Li}_2\text{Ru}_{0.5}\text{Sn}_{0.5}\text{O}_3$ (figure 2.13a), so that a Sn ion is surrounded by three Sn ions. **a-c**, Bonding rearrangements and electronic reshuffling involved with $\text{Sn}_{\text{Li, tetra}}$ (**a**), $\text{Sn}_{\text{Li, octa}}$ (**b**), and $\text{Sn}_{\text{Li, TM layer}}$ (**c**) disordering.

Figure 2-37. We exchanged one Ir and one Sn in the most stable Ir/Sn ordering of $\text{Li}_2\text{Ir}_{0.5}\text{Sn}_{0.5}\text{O}_3$ (figure 2.13b), so that a Sn ion is surrounded by three Sn ions. **a-c**, Bonding rearrangements and electronic reshuffling involved with $\text{Sn}_{\text{Li, tetra}}$ (**a**), $\text{Sn}_{\text{Li, octa}}$ (**b**), and $\text{Sn}_{\text{Li, TM layer}}$ (**c**) disordering.

Figure 2-38. a, DOS of $\text{Li}_2\text{Ni}_{0.5}\text{Te}_{0.5}\text{O}_3$ and $\text{Li}_1\text{Ni}_{0.5}\text{Te}_{0.5}\text{O}_3$ without any structural disorder. Their in-plane Ni/Te ordering is represented in figure 2.13c. **b**, Bonding rearrangements involved with charging and $\text{Ni}_{\text{Li, octa}}$ formation in $\text{Li}_{2-x}\text{Ni}_{0.5}\text{Te}_{0.5}\text{O}_3$.

Dangling oxygen ions formed with cation migration are colored green. **c-e**, Bonding arrangements and corresponding electronic structures calculated for $\text{Li}_1\text{Ni}_{0.5}\text{Te}_{0.5}\text{O}_3$ with $\text{Ni}_{\text{Li, tetra}}$ (**c**), $\text{Ni}_{\text{Li, octa}}$ (**d**), and $\text{Ni}_{\text{Li, TM layer}}$ (**e**).

Figure 2-39. **a**, Bonding rearrangements involved with charging and $\text{Te}_{\text{Li, octa}}$ formation in $\text{Li}_{2-x}\text{Ni}_{0.5}\text{Te}_{0.5}\text{O}_3$. **b-d**, Bonding arrangements and corresponding electronic structures calculated for $\text{Li}_1\text{Ni}_{0.5}\text{Te}_{0.5}\text{O}_3$ with $\text{Te}_{\text{Li, tetra}}$ (**b**), $\text{Te}_{\text{Li, octa}}$ (**c**), and $\text{Te}_{\text{Li, TM layer}}$ (**d**).

Figure 3-1. Comparison of crystal structures and cation migration paths. Schematic illustrations of crystal structures of **a**, O3-type and **b**, O2-type lithium layered oxides.

Figure 3-2. Suppression of voltage decay in O2-LLNMOs. **a**, First and second charge–discharge curves of O2-LLNMOs cycled in the voltage range of 2.0–4.8 V at a current density of 5 mA g^{-1} . **b**, Normalized discharge curves of O2-LLNMOs for 40 cycles. The data were collected every 10 cycles. **c**, Comparison of voltage decay in $dQ \text{ dV}^{-1}$ curves of O2- and O3-LLNMOs. **d**, Comparison of discharge capacity and energy density retention in O2- and O3-LLNMOs.

Figure 3-3. First cycle electrochemical profile of O3-LLNMOs measured at a current density of 5 mA g^{-1} between 4.8 and 2.0 V.

Figure 3-4. STXM spectra of the O K-edge and Ni, Mn L_3 -edges for different five points in the electrochemical curve of O2-LLNMOs. The signal profiles at the bottom of each plot indicate the differences between absorbance of 4.8 V charged

and pristine samples.

Figure 3-5. Normalized discharge capacity curves of O3-LLNMOs for 40 cycles. The data are collected for every 10 cycles.

Figure 3-6. Highly reversible cation migration in O2-LLNMOs. HAADF-STEM images along the $[1\bar{1}0]$ zone axis for **a**, 4.8-V charged and **b**, 2.0-V discharged O2-LLNMOs. The graphs below are the HAADF signal profiles of the regions enclosed by the dotted lines in the STEM images. SAED patterns of **c**, 4.8-V charged and **d**, 2.0-V discharged O2-LLNMOs along the $[1\bar{1}0]$ direction. **e**, TM migration paths from initial to intermediate and final Li sites. **f**, Relative site energies of intermediate and final sites calculated along the migration path of TM ions.

Figure 3-7. The $[1\bar{1}0]$ HAADF-STEM image of pristine O2-LLNMOs with 15M \times magnification.

Figure 3-8. Simulated SAED patterns along the $[1\bar{1}0]$ zone axis for **a**, ordered (Or) and **b**, **c**, disordered (Dis) O2-LLNMOs.

Figure 3-9. Mitigation of structural evolution in O2-LLNMOs for 40 cycles. **a**, *Ex situ* XRD patterns of pristine and 10-, 20-, and 40-cycled O2-LLNMOs. **b**, Comparison of Raman spectra for pristine and 40-cycled samples. **c**, SAED pattern of O2-LLNMOs along the $[3\bar{3}1]$ zone axis after 40 cycles (top, Or: ordered).

Figure 3-10. The $[1\bar{1}0]$ HAADF-STEM image of 4.8 V charged O2-LLNMOs with 15M \times magnification.

Figure 3-11. The $[1\bar{1}0]$ HAADF-STEM image of O2-LLNMOs after one cycle (2.0 V discharged) with 15M \times magnification.

Figure 3-12. SAED patterns of pristine O2-LLNMOs along the $[3\bar{3}1]$ zone axis (Or: ordered).

Figure 3-13. Simulated SAED patterns along the $[3\bar{3}1]$ zone axis for **a**, ordered (Or) and **b, c**, disordered (Dis) O2-LLNMOs.

Figure 3-14. Anomalous anionic redox behavior in O2-LLNMOs. **a**, STXM differential absorbance spectra of O K-edge and Ni, Mn L_3 -edges for the first charge and discharge cycle. **b**, O K-edge mRIXS of O2-LLNMOs for the first cycle obtained at each point of **a**. **c**, $dQ\ dV^{-1}$ curve of O2-LLNMOs measured at a current density of 5 mA g^{-1} . **d**, Electrochemical curves of O2-LLNMOs for current densities ranging from 5 to 200 mA g^{-1} . **e**, Variation of discharge capacity as a function of current density estimated for the two classified voltage ranges, 2.0–3.4 V and 3.4–4.8 V.

Figure 3-15. Ni and Mn K-edge XANES spectra measured for five points in the electrochemical curve of O2-LLNMOs.

Figure 3-16. **a**, Electrochemical curves of O3-LLNMOs for current densities ranging from 5 to 200 mA g^{-1} . **b**, Variation of discharge capacity of O3-LLNMOs as a function of current density estimated for the two classified voltage ranges, 2.0–3.4 V and 3.4–4.8 V.

Figure 3-17. HRPD pattern of $P2-Na_{5/6}(Li_{0.2}Ni_{0.2}Mn_{0.6})O_2$ material refined with
xvii

$P6_3/mmc$ and $R\bar{3}m$ space groups.

Figure 3-18. **a**, HRPD data for $P2\text{-Na}_{5/6}(\text{Li}_{0.2}\text{Ni}_{0.2}\text{Mn}_{0.6})\text{O}_2$ and $\text{O2-Li}_x(\text{Li}_{0.2}\text{Ni}_{0.2}\text{Mn}_{0.6})\text{O}_2$ with reference peaks. SEM and HR-TEM images for P2- (**b**, **d**) and O2-phases (**c**, **e**), respectively.

Figure 3-19. TM migration pathways in lithium-rich layered oxides with O2- and O3- staking. **a**, The in-plane cation arrangements in the most stable structures of LLNMOs, which are same for both O2- and O3-LLNMOs. **b-d**, Migration of Mn ion **b**, in O3-LLNMOs, and along **c**, the path A and **d**, the path B in O2-LLNMOs. **e-g**, Migration of Ni ion **e**, in O3-LLNMOs, and along **f**, the path A and **g**, the path B in O2-LLNMOs. **h** and **i** present the TM migration behavior in O2-LLNMOs where the Li sites in the TM layer are vacant ($\text{Li}_{0.5}[\text{Li}_0\text{Mn}_{0.58}\text{Ni}_{0.25}]\text{O}_2$ composition), for the **h**, Mn and **i**, Ni, respectively.

List of Tables

Table 2-1. Bader charge changes after $\text{Mn}_{\text{Li, tetra}}$ formation in $\text{Li}_{0.5}\text{MnO}_3$. Positive value means the loss of electron.

Table 2-2. Bader charge changes after $\text{Mn}_{\text{Li, octa}}$ formation in $\text{Li}_{0.5}\text{MnO}_3$. Positive value means the loss of electron.

Table 2-3. Bader charge changes after $\text{Mn}_{\text{Li, TM layer}}$ formation in $\text{Li}_{0.5}\text{MnO}_3$. Positive value means the loss of electron.

Table 2-4. Bond length changes and bond order changes of dangling oxygen ions accompanying $\text{M}_{\text{Li, tetra}}$ formation in $\text{Li}_{0.5}\text{RuO}_3$ and $\text{Li}_{0.5}\text{IrO}_3$.

Table 2-5. Bond length changes and bond order changes of dangling oxygen ions accompanying $\text{M}_{\text{Li, octa}}$ formation in $\text{Li}_{0.5}\text{RuO}_3$ and $\text{Li}_{0.5}\text{IrO}_3$.

Table 2-6. Bond length changes and bond order changes of dangling oxygen ions accompanying $\text{M}_{\text{Li, TM layer}}$ formation in $\text{Li}_{0.5}\text{RuO}_3$ and $\text{Li}_{0.5}\text{IrO}_3$.

Table 2-7. Bader charge changes involved with cation disordering in $\text{Li}_{0.5}\text{RuO}_3$ and $\text{Li}_{0.5}\text{IrO}_3$.

Table 2-8. Disorder formation energies calculated for $\text{Li}_{2-x}\text{RuO}_3$ and $\text{Li}_{2-x}\text{IrO}_3$ ($0 \leq x \leq 2$).

Table 2-9. Bond length changes and bond order changes of dangling oxygen ions accompanying cation disordering in $\text{Li}_{0.5}\text{Ru}_{0.5}\text{Mn}_{0.5}\text{O}_3$.

Table 2-10. Bader charge changes involved with cation disordering in $\text{Li}_{0.5}\text{Ru}_{0.5}\text{Mn}_{0.5}\text{O}_3$.

Table 2-11. V_O formation energy of electrodes belonging to charge-transfer systems. Cation disorder is not considered here.

Table 2-12. V_O formation energy of electrodes belonging to Mott-Hubbard systems. Cation disorder is not considered here.

Table 2-13. Bader charge changes involved with V_O formation in charge-transfer systems. The ratio of each change to the total charge difference is presented.

Table 2-14. Bader charge changes involved with V_O formation in Mott-Hubbard systems.

Table 2-15. Bond length changes and bond order changes of dangling oxygen ions accompanying Ru migration in $\text{Li}_{0.5}\text{Ru}_{0.5}\text{Sn}_{0.5}\text{O}_3$ and Ir migration in $\text{Li}_{0.5}\text{Ir}_{0.5}\text{Sn}_{0.5}\text{O}_3$.

Table 2-16. Bader charge changes involved with Ru migration in $\text{Li}_{0.5}\text{Ru}_{0.5}\text{Sn}_{0.5}\text{O}_3$ and Ir migration in $\text{Li}_{0.5}\text{Ir}_{0.5}\text{Sn}_{0.5}\text{O}_3$.

Table 2-17. Bond length changes and bond order changes of dangling oxygen ions accompanying Sn migration in $\text{Li}_{0.5}\text{Ru}_{0.5}\text{Sn}_{0.5}\text{O}_3$ and $\text{Li}_{0.5}\text{Ir}_{0.5}\text{Sn}_{0.5}\text{O}_3$.

Table 2-18. Bader charge changes involved with Sn migration in $\text{Li}_{0.5}\text{Ru}_{0.5}\text{Sn}_{0.5}\text{O}_3$ and $\text{Li}_{0.5}\text{Ir}_{0.5}\text{Sn}_{0.5}\text{O}_3$.

Table 2-19. Bond length changes and bond order changes of dangling oxygen ions

accompanying cation migration in $\text{Li}_1\text{Ni}_{0.5}\text{Te}_{0.5}\text{O}_3$.

Table 2-20. Bader charge changes involved with cationic disordering in $\text{Li}_1\text{Ni}_{0.5}\text{Te}_{0.5}\text{O}_3$.

Table 3-1. Lattice parameters of pristine and 10-, 20-, and 40-cycled O2-LLNMOs obtained from *ex-situ* XRD results.

Table 3-2. Rietveld refinements of $\text{P2-Na}_{5/6}(\text{Li}_{0.2}\text{Ni}_{0.2}\text{Mn}_{0.6})\text{O}_2$ materials. ($R_p = 12.5\%$)

Table 3-3. ICP - AES results for $\text{P2-Na}_{5/6}(\text{Li}_{0.2}\text{Ni}_{0.2}\text{Mn}_{0.6})\text{O}_2$ and $\text{O2-Li}_x(\text{Li}_{0.2}\text{Ni}_{0.2}\text{Mn}_{0.6})\text{O}_2$ materials.

Table 3-4. Relative Site energies calculated along the migration path of TM ions in O3-LLNMOs.

Table 3-5. Relative Site energies calculated along the migration path A in O2-LLNMOs.

Table 3-6. Relative Site energies calculated along the migration path B in O2-LLNMOs.

Chapter 1. Introduction

1.1 Motivation and outline

Against the backdrop of imminent global climate change, vehicle electrification is now at the heart of the decarbonization pathway¹. The growing success of electric vehicles (EVs) has been achieved with the rapid development of electrochemical storage technology represented by rechargeable lithium-ion batteries^{1,2}. Nonetheless, the International Energy Agency' scenario predicts that the market share of EVs, which is approximately 2.6% in 2019, should be increased to 86% by 2060 to limit the global temperature rise below 1.75 °C³. Such expansion of EV market necessitates a significant breakthrough in current battery technologies in terms of energy storage capacity, power capability, safety, and cost⁴. In particular, as 'range anxiety' is a primary concern of consumers⁵, increasing the specific energy density (Wh kg⁻¹) of lithium-ion batteries has been a major goal of many researchers over the past decade.

In this respect, the use of lithium-rich layered oxides as a cathode in lithium-ion batteries offers an unparalleled opportunity to improve the energy density of current batteries. Lithium-rich layered oxides ($\text{Li}[\text{Li}_x\text{M}_{1-x}]\text{O}_2$, where M is transition metal, $0 < x < 1$) refer to a class of materials in which some cation sites in the transition metal layers are occupied by lithium ions to contain more lithium than conventional lithium-stoichiometric layered oxides (LiMO_2). These electrodes provide extraordinarily high reversible capacity (over 250 mAh g⁻¹) and relatively high

operating voltage⁶. However, despite the great promise of lithium-rich layered oxides, their practical implementation has been limited due to the inevitable voltage decay, which indicates a gradual decrease in average discharge voltage during cycling, and the voltage hysteresis problems, which means the path independence between charge and discharge⁷. Moreover, the voltage decay and voltage hysteresis problems are aggravated in layered lithium-rich 3d metal oxides which are of practical importance^{7,8}. Therefore, for the real-world application of lithium-rich layered oxides electrodes, it is necessary to resolve their voltage depression problems.

Prior to the engineering of electrodes, the scientific origin of voltage decay and hysteresis phenomena needs to be understood first. It is widely accepted that extra capacities of lithium-rich layered oxides arise from the anionic oxygen redox activity⁹. However, oxygen redox during charging has known to entail structural transformations of electrode materials. Structural disorders observed during oxygen redox include cation disorders represented by transition metal-vacancy anti-site defect pairs (equivalently, cation migration), and anion disorders such as oxygen dimer and oxygen vacancy^{10,11}. Unfortunately, the formation of these structural disorders was found to be only partially reversible, and such irreversibility leads to a structural asymmetry between charge and discharge and consequent voltage hysteresis¹². In addition, it has been proved that the extent of voltage decay is proportional to the amount of irreversibly migrated cations¹³.

Despite the significant effects of structural disorders on the oxygen redox chemistry, the close interplay between them has been only limitedly reported¹⁴. Due to the

complexity from the dynamic changes in the structure, *e.g.*, cation migrations/disorders and bond alternations, and the corresponding redox activity change, the comprehensive understanding of this class of materials has been elusive to date, making it difficult to achieve the highly reversible oxygen redox. Unraveling the multifaceted connections between the oxygen redox chemistry and the structural disorders is a prerequisite for the rational optimization of oxygen-redox-active electrodes. In **Chapter 2**, I propose a consistent theoretical framework that bridges structural disorders, concomitant bonding rearrangements, and oxygen redox chemistry for both charge-transfer and Mott-Hubbard electrode systems of lithium-rich layered oxides. The trilateral relations are presented for a wide range of oxygen-redox-active electrodes concerning the commonly observed disorders including various modes of transition metal migrations, oxygen dimers and vacancies. I show that the cation disorders stabilize the oxygen redox by promoting strong oxygen-involving hybridizations. It is also revealed that the extent of bond rearrangements is proportional to the utilization of non-bonding oxygen states, and certain conditions of metal-oxygen covalency particularly drive the formation of oxygen dimers. More importantly, I demonstrate how bond rearrangements affect the electrochemical and structural reversibility, conveying the caveat that the oxygen dimerization severely penalizes the structural reversibility by leading the oxygen astray in the structure. It is observed for the first time that oxygen dimers that are found to freely move in the lattice structure serve as a key catalyst of the poor structural resilience.

Based on the understanding of the relationship between structural disorder and

oxygen chemistry, I propose a strategy to improve the structural reversibility of electrode materials in **Chapter 3**. As the voltage decay has known to be primarily originated from irreversible cation migration in the structure, various effective approaches have been used to mitigate the cation migration itself, including surface coating, cation doping, additives to electrolyte, and composition tuning¹⁵⁻¹⁹. However, the ultimate prevention of cation migration during long-term cycling has not yet been achieved due to its high thermodynamic spontaneity. Considering the underlying origin of the voltage decay and the inevitability of cation migration (particularly at a certain charged state), I believed that improving the intra-cycle reversibility of cation migration would play a key role in addressing the voltage decay issue. I thus devised a structural tool to regulate the reversibility of cation migration rather than to suppress the migration in lithium-rich layered oxides, which had the unexpected benefit of also suppressing the voltage decay and hysteresis. I demonstrate that the reversibility of the TM migration can be remarkably improved by changing the oxygen lattice structure of cobalt-free lithium-rich nickel manganese oxides from the typical O3 to O2 layered stacking, thereby dramatically suppressing the voltage decay and hysteresis. I show that the primary factor limiting the reversible migration of transition metal ions in the typical O3 layered structure is the intralayer movements of transition metal ions within the Li layer and that the O2 layered structure restricts these movements. The preeminent intra-cycle reversibility of the TM migration for O2-type layered compounds is confirmed using scanning transmission electron microscopy and complementary X-ray diffraction, Raman

spectroscopy, and high-resolution transmission electron microscopy. This high level of intra-cycle reversibility leads to preservation of the pristine layered structure over extended cycles as well as successful voltage retention. I further confirm that the improved reversibility of cation migration helps remove the asymmetry of the anion redox (*i.e.*, the voltage hysteresis), which has been suspected to stem from the presence of transition metal ions in the Li layer during discharge²⁰.

1.2 References

1. Cano, Z. P. *et al.* Batteries and fuel cells for emerging electric vehicle markets. *Nature Energy* **3**, 279-289 (2018).
2. Li, W., Erickson, E. M. & Manthiram, A. High-nickel layered oxide cathodes for lithium-based automotive batteries. *Nature Energy* **5**, 26-34 (2020).
3. IEA (2020), Global EV Outlook 2020, IEA, Paris
<https://www.iea.org/reports/global-ev-outlook-2020>
4. Kwade, A. *et al.* Current status and challenges for automotive battery production technologies. *Nature Energy* **3**, 290-300 (2018).
5. Li, W., Long, R., Chen, H. & Geng, J. A review of factors influencing consumer intentions to adopt battery electric vehicles. *Renewable and Sustainable Energy Reviews* **78**, 318-328 (2017).
6. Hong, J., Gwon, H., Jung, S.-K., Ku, K. & Kang, K. Review—Lithium-Excess Layered Cathodes for Lithium Rechargeable Batteries. *Journal of The Electrochemical Society* **162**, A2447-A2467 (2015).
7. Assat, G. & Tarascon, J.-M. Fundamental understanding and practical challenges of anionic redox activity in Li-ion batteries. *Nature Energy* **3**, 373-386 (2018).
8. Zheng, J. *et al.* Li- and Mn-Rich Cathode Materials: Challenges to Commercialization. *Advanced Energy Materials* **7**, 1601284 (2017).
9. Seo, D.-H. *et al.* The structural and chemical origin of the oxygen redox activity in layered and cation-disordered Li-excess cathode materials.

- Nature Chemistry* **8**, 692-697 (2016).
10. Gent, W. E., Abate, I. I., Yang, W., Nazar, L. F. & Chueh, W. C. Design Rules for High-Valent Redox in Intercalation Electrodes. *Joule* **4**, 1369-1397 (2020).
 11. Eum, D. *et al.* Voltage decay and redox asymmetry mitigation by reversible cation migration in lithium-rich layered oxide electrodes. *Nature Materials* **19**, 419-427 (2020).
 12. Ku, K. *et al.* A new lithium diffusion model in layered oxides based on asymmetric but reversible transition metal migration. *Energy & Environmental Science* **13**, 1269-1278 (2020).
 13. Sathiya, M. *et al.* Origin of voltage decay in high-capacity layered oxide electrodes. *Nature Materials* **14**, 230-238 (2015).
 14. Assat, G. *et al.* Fundamental interplay between anionic/cationic redox governing the kinetics and thermodynamics of lithium-rich cathodes. *Nature Communications* **8**, 2219 (2017).
 15. Gu, M. *et al.* Formation of the Spinel Phase in the Layered Composite Cathode Used in Li-Ion Batteries. *ACS Nano* **7**, 760-767 (2013).
 16. Li, Q. *et al.* K⁺-Doped Li_{1.2}Mn_{0.54}Co_{0.13}Ni_{0.13}O₂: A Novel Cathode Material with an Enhanced Cycling Stability for Lithium-Ion Batteries. *ACS Applied Materials & Interfaces* **6**, 10330-10341 (2014).
 17. Nayak, P. K., Grinblat, J., Levi, M. & Aurbach, D. Understanding the Effect of Lithium Bis(oxalato) Borate (LiBOB) on the Structural and

- Electrochemical Aging of Li and Mn Rich High Capacity $\text{Li}_{1.2}\text{Ni}_{0.16}\text{Mn}_{0.56}\text{Co}_{0.08}\text{O}_2$ Cathodes. *Journal of The Electrochemical Society* **162**, A596-A602 (2015).
18. Ku, K. *et al.* Suppression of Voltage Decay through Manganese Deactivation and Nickel Redox Buffering in High-Energy Layered Lithium-Rich Electrodes. *Advanced Energy Materials* **8**, 1800606 (2018).
19. Shi, J.-L. *et al.* Mitigating Voltage Decay of Li-Rich Cathode Material via Increasing Ni Content for Lithium-Ion Batteries. *ACS Applied Materials & Interfaces* **8**, 20138-20146 (2016).
20. Gent, W. E. *et al.* Coupling between oxygen redox and cation migration explains unusual electrochemistry in lithium-rich layered oxides. *Nature Communications* **8**, 2091 (2017).

Chapter 2. Trilateral correlation of Structural disorder, Bond covalency, and Oxygen redox chemistry in lithium-rich layered oxide electrodes

The content of this chapter is now submitted to a scientific journal.

2.1 Introduction

The full switch-over to the sustainable and affordable energy utilizations necessitates a substantial breakthrough in the energy density of current battery systems¹. Lithium-rich layered oxides are strong contenders for the next-generation lithium-ion battery chemistry as they enlist the additional oxygen redox activity aside from the conventional transition metal redox to offer a significantly higher capacity². However, the extra capacities from the oxygen redox come at a price as the electrodes typically suffer from the large voltage hysteresis, sluggish kinetics and gradual voltage fades with cycling³⁻⁵. Extensive studies have suggested that those issues are exclusively observed in the oxygen redox region and are generally accompanied by structural instabilities that are engendered during the oxygen redox⁴⁻⁷. It has been discussed that the oxygen redox entails series of structural rearrangement steps that are energetically spontaneous, during which its reversibility is gradually compromised in the prolonged cycles^{6,8,9}. Moreover, recent findings have revealed that substantial cation (*i.e.*, transition metal, TM) migrations do occur in lithium-rich layered materials not only through out-of-plane but also through in-plane directions

of the layered structure, giving rise to the substantial rearrangement of the oxygen local environment with structural disorders, thus significantly altering the oxygen redox activity^{10,11}.

Common structural disorders observed during the oxygen redox include (i) cation disorders such as $\text{TM}_{\text{Li}}\text{-V}_{\text{M}}$ anti-site defect pairs¹², and (ii) anion disorders represented by the oxygen vacancy (V_{O})¹³. Chueh group reported that the occurrence of out-of-plane TM migrations coincides with the oxygen redox in lithium-rich layered oxides, suggesting the coupling between the oxygen redox activity and the cation disorder¹⁴. It was proposed that the cation migration serves as a critical trigger for the oxygen redox by promoting the ligand to metal charge transfer in the oxygen redox mechanism^{14,15}. It has been similarly demonstrated that the oxygen redox potential can be markedly affected by the electrostatic destabilization resulting from the loss of metal coordination via cation migration during the redox reaction^{9,16}. The evolution of oxygen defects were often observed, as evidenced by the V_{O} formation energy that decreases sharply with the onset of oxygen redox from both experimental¹⁷ and theoretical^{18,19} investigations, exacerbating the voltage hysteresis with redox asymmetry^{20,21}. Previous studies also signified the presence of the continuous feedback between the oxygen redox mechanism and the local bond rearrangements. It was supposed that the depletion of highly localized non-bonding O 2p (O 2p NB) states renders oxygen unstable, violating the “octet rule”²², and hence the oxidized oxygen tends to form supplementary covalent bonds for self-stabilization^{8,23-25}. Of particular significance is that the de-coordination of some

metal-oxygen bonds results in the under-coordinated oxygen that becomes more prone to forming short covalent bonding^{2,8}. It infers that the structural disordering that involves the de-coordination of metal-oxygen bonds can catalyze further bond rearrangements or disorders to stabilize the oxygen redox chemistry.

The complexities in these dynamic structure-electrochemistry relationships suggest the close interplay behind the local bonding restructurings associated with dynamic disorders and the subsequent oxygen redox activity. While there still remains a large of uncharted terrain concerning this triptych, a comprehensive grasp of the intrinsic relation is a prerequisite for the better understanding and the optimization of oxygen-redox-active electrodes. In this work, we propose a consistent theoretical framework that bridges structural disorders, concomitant bonding rearrangements, and oxygen redox chemistry for both charge-transfer and Mott-Hubbard electrode systems of lithium-rich layered oxides²⁶. The trilateral relations are presented for a wide range of oxygen-redox-active electrodes concerning the commonly observed disorders including out-of-plane and in-plane TM migrations, oxygen dimers and vacancies. We show that the cation disordering stabilizes the oxygen redox by allowing strong oxygen-oxygen and/or metal-oxygen hybridization, in consistent with the previous observations^{10,14,27}. More importantly, it is revealed that the extent of bond rearrangements is proportional to the utilization of O 2*p* NB states, and certain conditions of metal-oxygen covalency particularly promote the formation of oxygen dimers. Furthermore, we demonstrate how bond restructurings affect the electrochemical and structural reversibility, conveying the caveat that the oxygen

dimerization severely penalizes the structural reversibility by leading the oxygen astray in the structure. The anion disordering, on the other hand, is found to effectively stabilize the oxygen network by compensating for electron deficiencies, suggesting the possible beneficial effects. Our findings successfully address the unanswered linkage between the oxygen redox and dynamic structural disorders, and provide a generalized guidance for the material engineering of lithium- and sodium-rich layered electrodes.

2.2 Computational details

All *ab initio* calculations are performed based on spin-polarized density functional theory (DFT) calculations, as implemented in the Vienna *ab initio* simulation package (VASP)^{28,29}. The exchange-correlation energy was described using the Perdew–Burke–Ernzerhof (PBE) generalized gradient approximation³⁰. Hubbard parameters (GGA+U) were applied to correct the self-interaction error related with strongly correlated *d* electrons, and effective Hubbard-U parameters was adopted from the previous literatures^{2,14}. We also conducted comparative calculations using the Heyd–Scuseria–Ernzerhof (HSE06) hybrid functional with the standard mixing parameter of 0.25 for representative cases³¹, and confirmed the consistency of the results. Projector-augmented wave (PAW) pseudopotentials were used³², and valence electrons were depicted with the plane-wave basis set. An energy cutoff 520 eV and an appropriate number of k-points were used in all calculations. All structures were fully relaxed until the forces acting on each atom were smaller than 0.02 eV Å⁻¹. The COOPs were calculated using the Lobster program^{33,34}.

Pristine electrode compounds with Li₂MO₃ stoichiometry were modelled using supercells containing 24 formula units of the LiMO₂ primitive cell (space group: C2/m), and Li_{1/3}M_{2/3} honeycomb arrangement was applied to the TM layers. These supercells consist of two TM layers and two Li layers. Na_{0.6}(Li_{0.2}Mn_{0.8})O₂ electrode with the P3 staking was modelled using Na₃₆(Li₁₂Mn₄₈)O₁₂₀ supercell which is composed of three TM layers and three Na layers. Pristine Na_{2/3}(Mg_{1/3}Mn_{2/3})O₂

electrode with the P3 staking was described with $\text{Na}_{12}(\text{Mg}_6\text{Mn}_{12})\text{O}_{36}$ supercell, and the charged phase, $\text{Na}_0(\text{Mg}_{1/3}\text{Mn}_{2/3})\text{O}_2$ with the O3 staking, was depicted with a larger supercell of $\text{Na}_0(\text{Mg}_8\text{Mn}_{16})\text{O}_{48}$. The in-plane cation arrangements of structural models are represented in figures 2.2, 2.8, and 2.13. All structural models were designed so that the minimum distance between structural disorders is approximately 10 Å, excluding the influence of defect-defect interactions.

Unless otherwise stated, we generated 300 Li/Na/Mg-vacancy orderings for each phase, using the enumeration technique³⁵, and performed DFT calculations on the generated structures. In this process, all octahedral and tetrahedral sites in the alkali metal layers and all vacant sites in the TM layers were considered. After the formation of structural disorder, Li-vacancy orderings were re-sampled in the same way. While computing $G_f(V_O)$, the overestimation of the O_2 binding energy was corrected using the method by Wang *et al*³⁶, and the entropy term is obtained from JANAF thermochemical table³⁷. *Ab initio* MD calculations were conducted using the canonical (NVT) ensemble with a Nose–Hoover thermostat^{38,39}. Each structure was simulated at 300 K with a time step of 1.0 fs for 100 ps.

2.3 Result and discussion

2.3.1 Cation disordering in charge-transfer systems

Prior to discussing the effects of structural disordering, we first refer to the charging process of layered transition metal oxides in the absence of structural disorder. In charge-transfer electrode systems, O $2p$ NB states typically lie at the Fermi level (Chapter 2.3.6), and thus is immediately depopulated upon charging, as evidenced for archetypal electrodes such as Li_2MnO_3 ⁴⁰, $\text{Na}_{0.6}[\text{Li}_{0.2}\text{Mn}_{0.8}]\text{O}_2$ ⁴¹, and $\text{Na}_{2/3}[\text{Mg}_{1/3}\text{Mn}_{2/3}]\text{O}_2$ ⁴² (figure 2.2). Our investigations on these three representative materials depicted that O-O and Mn-O bond lengths simply reduce in the structure during the charge process when no structural disorder was allowed. For example, during charging of Li_2MnO_3 to $\text{Li}_{0.5}\text{MnO}_3$, the minimum lengths of O-O bonds and Mn-O bonds slightly decrease from 2.57 Å to 2.43 Å, and 1.93 Å to 1.88 Å, respectively (i \rightarrow ii in figure 2.1a). We note that these 2.43 Å O-O pairs correspond to the typical bond lengths of peroxo-like species (2.1 ~ 2.5 Å), and are distinct from short oxygen dimers such as peroxo (O_2)²⁻, superoxo (O_2)¹⁻, and molecular O_2 species, which are in a range of 1.2 ~ 1.5 Å^{14,43,44}. It is generally understood that the O-O covalent bond is difficult to be formed when the distance between two oxygen atoms exceeds 2 Å²⁷. No significant distortion of Mn-O bonds in the octahedra was detected, which is ascribed to the highly directional covalent bond between the oxygen and the transition metal with partially filled d shells, preventing the rotation of bonds^{2,45}.

The presence of cation disordering, however, could lift the restrictions on bond

rearrangements by diversifying the coordination environment of oxygen. As illustrated in figure 2.1a (ii \rightarrow iii), a cation migration generates single-coordinated (or, dangling) oxygen ions (denoted as green) which have high degrees of freedom for bonding rearrangements. Figure 2.3 portrays all the representative point-type cation disorders: out-of-plane TM migrations to the tetrahedral site ($M_{Li, \text{tetra}}$) or to the octahedral site ($M_{Li, \text{octa}}$) in the lithium layer, and in-plane TM migration ($M_{Li, \text{TM layer}}$) to the vacant Li site in transition metal layer. Figure 2.1a exemplifies the case of $Mn_{Li, \text{octa}}$, which produces four dangling oxygen ions. It shows that in the presence of the cation disorder in $Li_{0.5}MnO_3$ (iii \rightarrow iv, figure 2.1a), some dangling oxygen ions form short covalent bonding with adjacent oxygen, as can be seen from 1.28 Å O-O dimer (iv in the figure: highlighted with green and red atoms in the blue box). This bond length matches with the typical value of superoxo (O_2)¹⁻ species⁴⁶. It was further confirmed that various cation disorder types in the layered structure could generate these oxygen dimers depending on the coordination environments, as extensively illustrated in Chapter 2.3.8.

Moreover, we note that the O-O dimerization was universally observed for the charged phases of $Na_{2/3}[Mg_{1/3}Mn_{2/3}]O_2$ and $Na_{0.6}[Li_{0.2}Mn_{0.8}]O_2$ involved with cation disordering. Figure 2.1b displays that the desodiation of $Na_{2/3}[Mg_{1/3}Mn_{2/3}]O_2$ with a cation disorder includes the formation of the short oxygen dimer (1.30 Å) as denoted with green atoms within the honeycomb ordering of Mg and Mn similar to that of the Li_2MnO_3 case (figure 2.5). Analogous oxygen dimer formation was witnessed in the case of $Na_{0.6}[Li_{0.2}Mn_{0.8}]O_2$ in figure 2.1c (path A TM migration) and figure 2.6,

which appears with the bond lengths of ~ 1.36 Å (blue box in the figure). It was noteworthy, nevertheless, that the oxygen dimerization could be slightly inhibited in $\text{Na}_{0.6}[\text{Li}_{0.2}\text{Mn}_{0.8}]\text{O}_2$ due to its ribbon-type ordering in the transition metal layer, which partly agrees with the previous observations¹⁰. As comparatively presented in figure 2.1c, the cation migration along the path B in the ribbon-type ordering does not allow the formation of the single-coordinated oxygen, thus the bond rearrangements of oxygen ions are still structurally restricted, preventing the oxygen dimerization (see Chapter 2.3.9 for more details regarding on cation disorder and oxygen dimers on $\text{Na}_{2/3}[\text{Mg}_{1/3}\text{Mn}_{2/3}]\text{O}_2$ and $\text{Na}_{0.6}[\text{Li}_{0.2}\text{Mn}_{0.8}]\text{O}_2$).

Regarding the other dangling oxygen ions that do not form a dimer in figure 2.1a, it was observed that they tend to form short covalent bonds with coordinated manganese ions as indicated with black dotted lines (iii and iv in the figure). In this case, the lengths of three Mn-O dangling bonds (~ 1.89 Å) reduce to 1.65 Å, 1.69 Å, and 1.85 Å respectively. The bond length of 1.65 Å is close to the reported length of $\text{Mn}^{4+}=\text{O}$ bond (1.66 Å) in metal-oxo complexes⁴⁷, implying the formation of strong Mn-O π bonds arising from the dangling oxygen ions. These concerted O-O and Mn-O bond restructurings were consistently observed for all the possible combinations of cation disorders and dimer types in $\text{Li}_{0.5}\text{MnO}_3$, $\text{Na}_0[\text{Mg}_{1/3}\text{Mn}_{2/3}]\text{O}_2$ and $\text{Na}_0[\text{Li}_{0.2}\text{Mn}_{0.8}]\text{O}_2$ (figures. 2.4c-n, 2.5c-e and 2.6c-e, respectively).

The substantial change in the oxygen bonding neighbor leads to the electronic reshuffling in the material. Figure 2.1d compares the electronic structures of oxygen atoms, *i.e.*, projected density of state (pDOS), before (green) and after (red) the Mn_{Li} ,

formation that involved the O-O dimerization (1.28 Å, figure 2.1a). The pDOS exhibits that O 2p band splits into sharp and discrete bands after the cation disorder, which is ascribed to the shortening of the O-O distance from 2.83 Å to 1.28 Å. The oxygen bands can be assigned as σ^* , π^* , π , and σ states, respectively, in order of energy, as illustrated by the charge density plots on the right. This assignment could be supported by the crystal orbital overlap population (COOP) between oxygen atoms plotted at the bottom of the figure, which informs bonding/antibonding characteristics of bonds in a crystal⁴⁸. The positive and negative value of COOP indicates bonding and antibonding nature, respectively, and the zero value means the absence of overlap, *i.e.*, non-bonding character. Whereas the COOP value is negligible between two oxygens in the disorder-free system, the formation of O-O dimer (1.28 Å) results in positive and negative COOP values that correspond well with σ^*/π^* and π/σ states, respectively, indicating the strong hybridization.

We further examined the change in the electronic structure of oxygen that constitutes the bonding with neighboring Mn in figure 2.1a, particularly focusing on the short Mn-O covalent bonds (1.65 Å). Figure 2.1e reveals that a new state emerges above the Fermi level after the cation disorder, which is attributed to the development of Mn 3d-O 2p π^* state. Since the formation of Mn_{Li, octa} reduces the number of manganese ions capable of orbital hybridization with oxygen, it results in the quantitative imbalance between intact O 2p orbitals and Mn 3d t_{2g} orbitals, making three discrete states, Mn 3d-O 2p π^* , O 2p NB, Mn 3d-O 2p π states (see Chapter 2.3.7 for details). The shortening of Mn-O bond subsequently strengthens

the Mn-O π hybridization, which would increase the energy gap between π and π^* of Mn 3d-O 2p, thus Mn-O π^* states evolve in a higher energy range than O 2p NB states. The antibonding character is supported by the negative COOP values of the new π^* states, which additionally confirms that the short Mn-O length of 1.65 Å has non-negligible effect on the Mn-O π -interaction.

The electronic reshuffling around the oxygen consequently engenders the overall charge redistribution in DOS, as schematically summarized in figure 2.1f. The simple depopulation of O 2p NB state is expected for the ideal charge-transfer system without disorder upon charging (left in figure 2.1f). On the other hand, after the cation disorder, there should appear two new states due to the dangling oxygen, which is stabilized either by the oxygen dimer formation or the strong Mn-O hybridization (right in figure 2.1f). The oxygen in the dimer produces the O-O σ^* and π^* states, whereas the oxygen with the strong hybridization with the Mn ion yields the Mn-O π^* states, both of which arise above the Fermi level. We also observed that some of the charge released from dangling oxygen ions due to the emergence of the new σ^* and π^* states is transferred to the oxygen network according to our analyses in Tables 2.1-2.3, indicating the charge redistribution. It implies that the covalent bond formation of dangling oxygen partially compensates for the oxidation of other oxygen in the electrode, contributing to the stabilization of the overall material system. These stabilizing effects may further make the cation disordering a thermodynamically spontaneous process, as is commonly identified for electrodes in charge-transfer systems (figures 2.4-2.6).

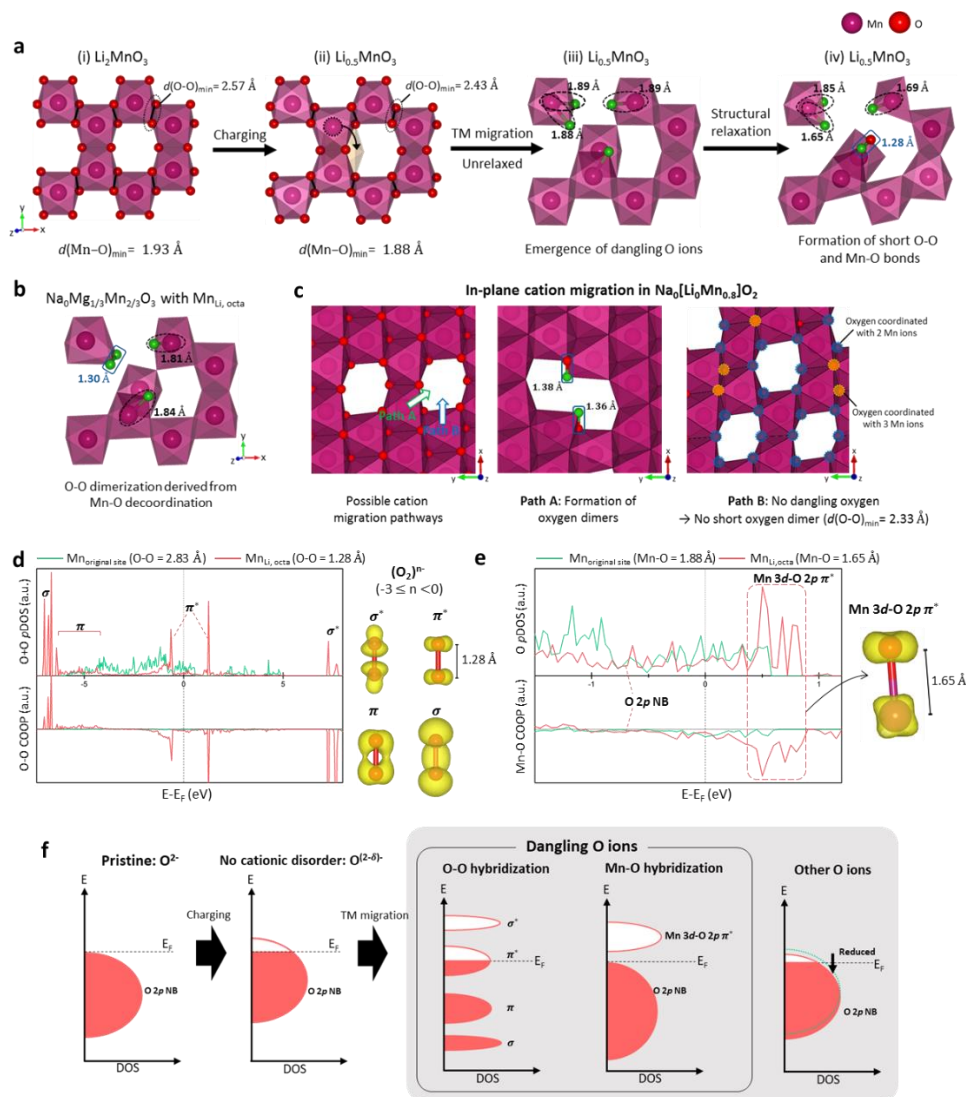


Figure 2.1. Bonding rearrangements involved with cation disordering in charge-transfer systems. **a**, Bonding rearrangements involved with charging and $\text{Mn}_{\text{Li, octa}}$ formation in $\text{Li}_{2-x}\text{MnO}_3$. **b**, Relaxed structure of $\text{Na}_0[\text{Mg}_{1/3}\text{Mn}_{2/3}]\text{O}_2$ with $\text{Mn}_{\text{Li, octa}}$. **c**, Bond rearrangements involved with in-plane cation migration in $\text{Na}_0[\text{Li}_0\text{Mn}_{0.8}]\text{O}_2$ with the ribbon superstructure. In **a-c**, dangling oxygen ions formed

with cation migration are colored green, and Li and Mg ions are omitted for clarity. **d, e**, Changes in the electronic structure of oxygen atoms involved with O-O dimerization (**d**) and Mn-O π hybridization (**e**), which are illustrated in **a**. The charge density plots that visualize oxygen states are also presented. **f**, Schematic representation of the electronic reshuffling of oxygen redox states due to cation disordering.

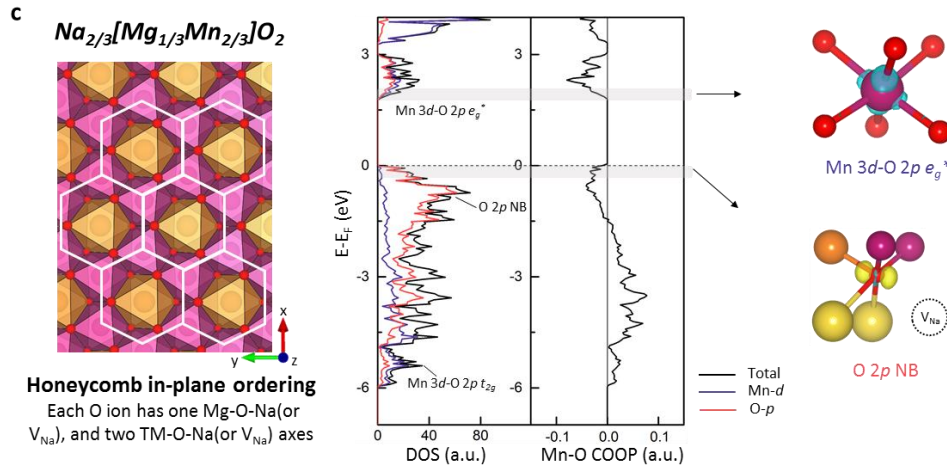
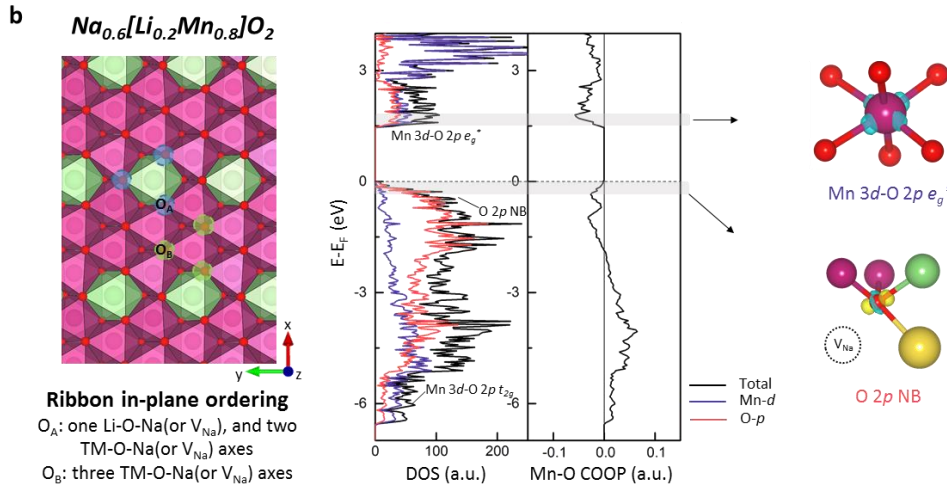
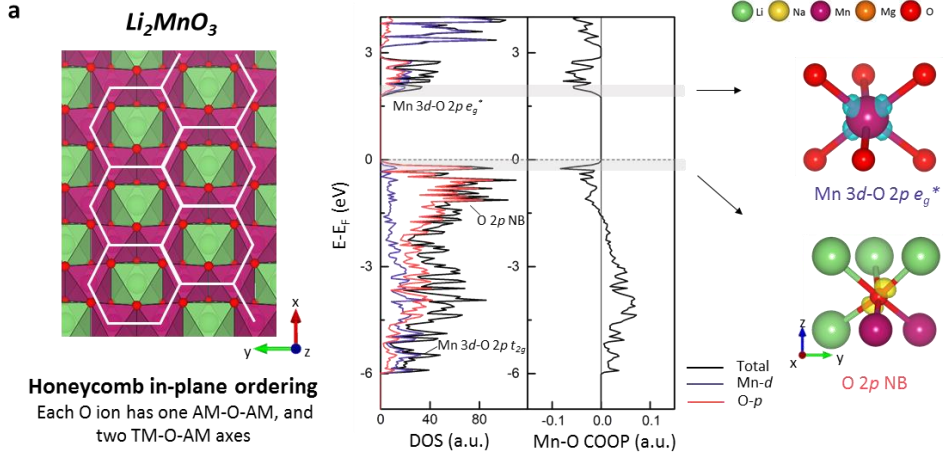


Figure 2.2. The in-plane Li-M arrangements and electronic structures of pristine electrodes belonging to charge-transfer systems. **a**, Li_2MnO_3 , **b**, $\text{Na}_{0.6}[\text{Li}_{0.2}\text{Mn}_{0.8}]\text{O}_2$, and **c**, $\text{Na}_{2/3}[\text{Mg}_{1/3}\text{Mn}_{2/3}]\text{O}_2$. $\text{Li}_{1/3}\text{Mn}_{2/3}$ honeycomb arrangement, $\text{Li}_{1/5}\text{Mn}_{4/5}$ ribbon arrangement, and $\text{Mg}_{1/3}\text{Mn}_{2/3}$ honeycomb arrangement was applied for Li_2MnO_3 ⁴⁹, $\text{Na}_{0.6}[\text{Li}_{0.2}\text{Mn}_{0.8}]\text{O}_2$ ¹⁰, $\text{Na}_{2/3}[\text{Mg}_{1/3}\text{Mn}_{2/3}]\text{O}_2$ ⁴², respectively, according to the previous reports. We generated 100 Na-vacancy orderings for $\text{Na}_{0.6}[\text{Li}_{0.2}\text{Mn}_{0.8}]\text{O}_2$ and $\text{Na}_{2/3}[\text{Mg}_{1/3}\text{Mn}_{2/3}]\text{O}_2$, respectively, using the enumeration technique³⁵, and the most stable configurations were designated through DFT calculations. On the right are the positive and negative Fukui functions that visualize the charge density of electronic states just above and below the Fermi level, respectively. Yellow and blue in the Fukui functions corresponds to negative and positive changes, respectively. Here, the charge density lying along the Li-O-Li axis (**a**), V_{Na} -O-Li axis (**b**), and V_{Na} -O-Mg axis (**c**) corresponds to O 2p NB states². Therefore, electronic structures and the negative Fukui functions show in common that O 2p NB states lie at the Fermi level in charge-transfer systems.

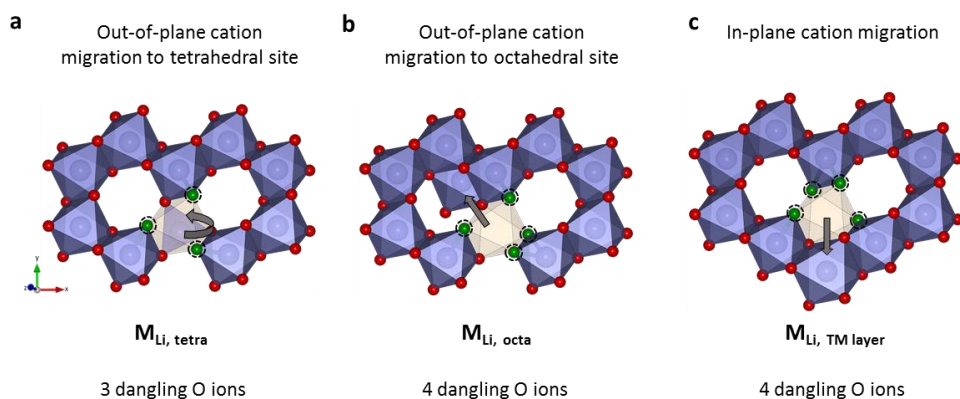
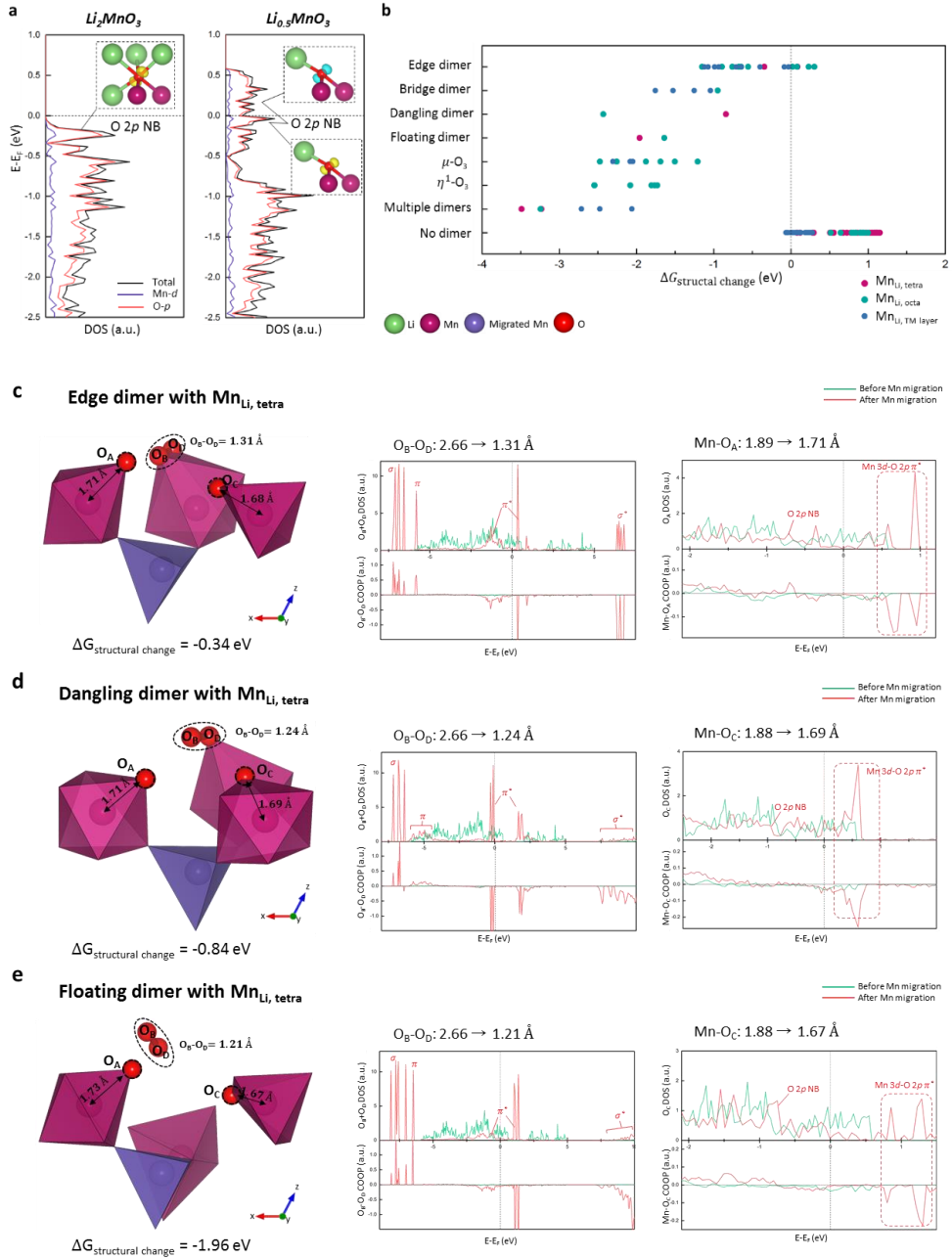
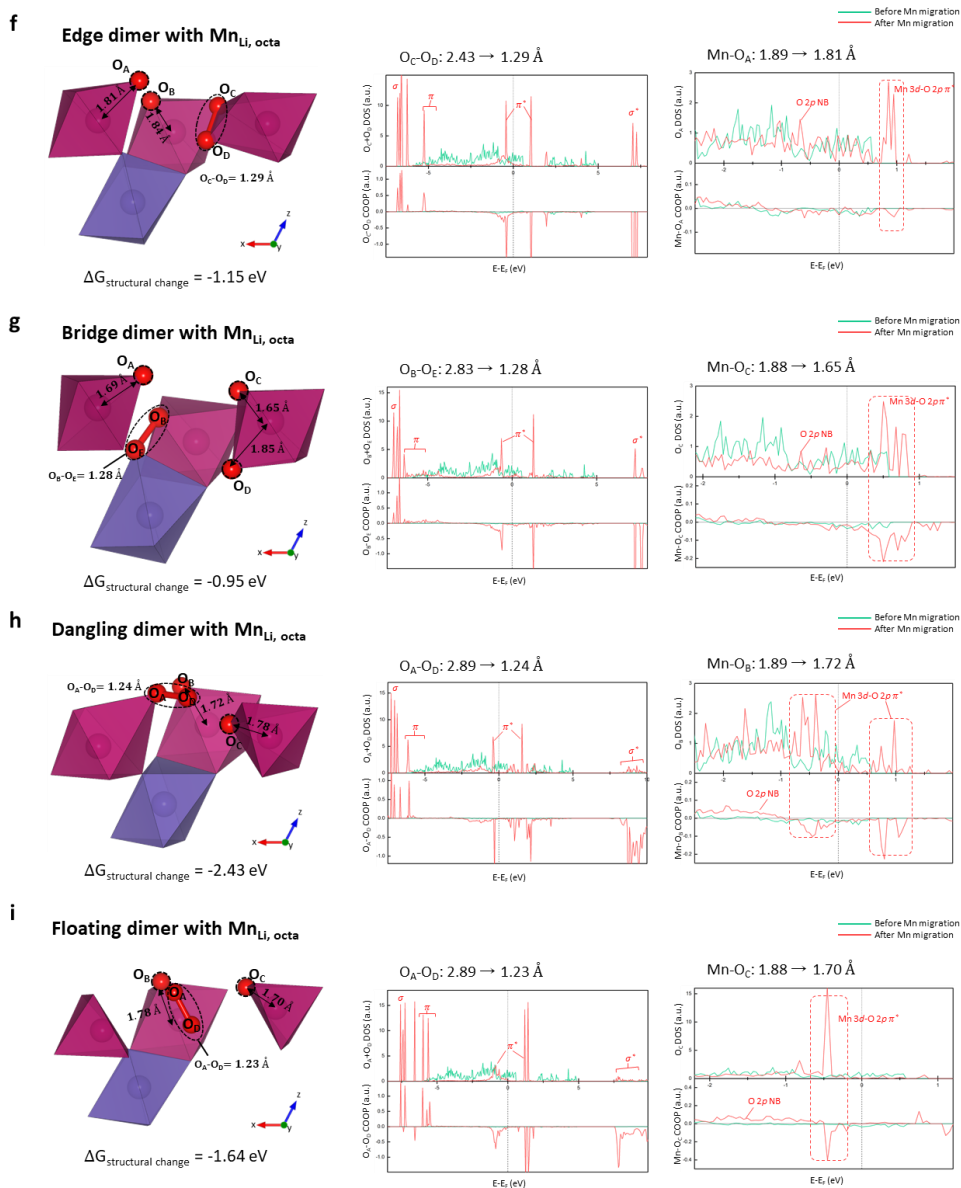
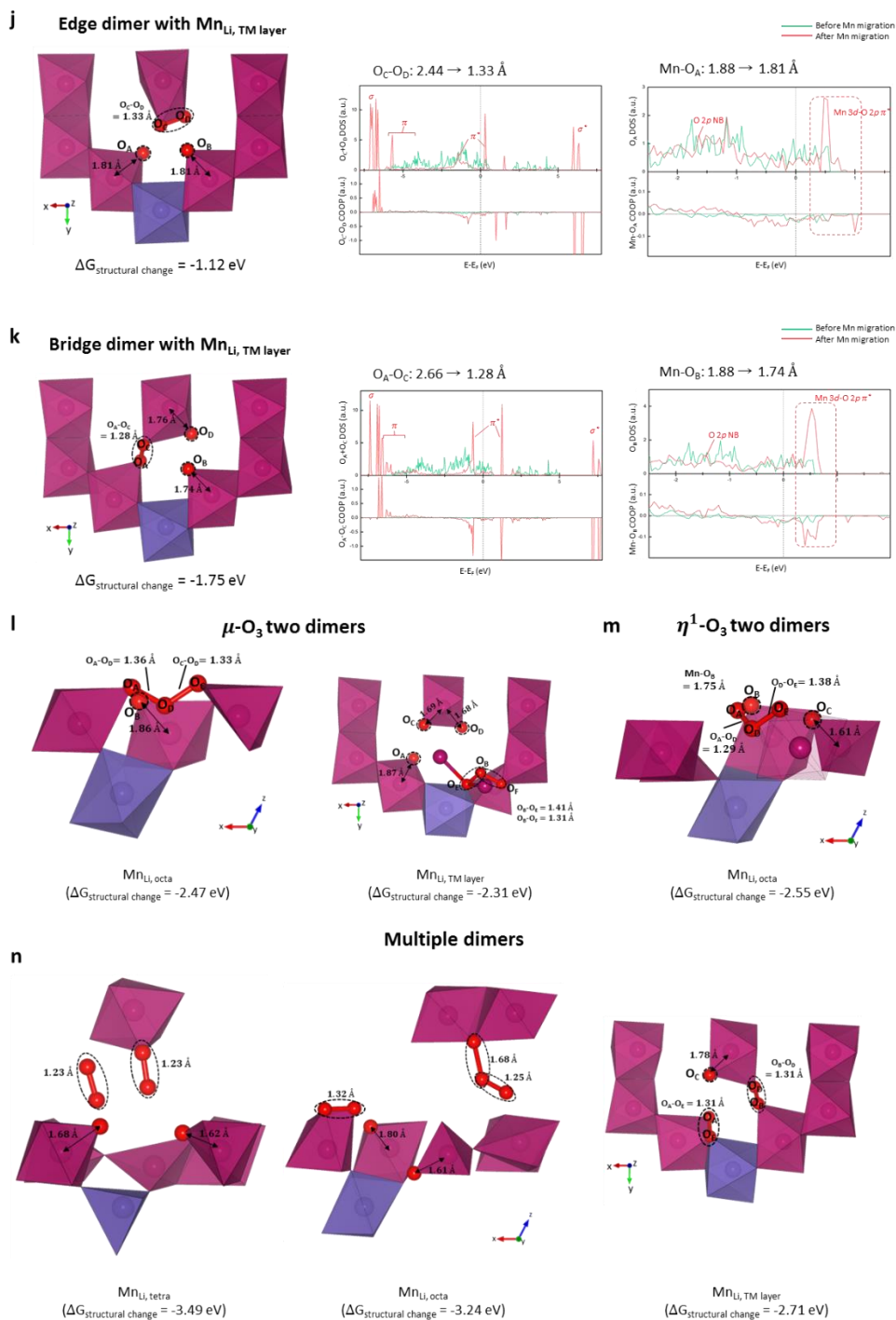


Figure 2.3. Schematic representations of possible cation disorders. M_{Li} - V_M antisite cation-vacancy defects pair can be formed by **a**, out-of-plane cation migration to the tetrahedral site in the Li layer (denoted as $M_{Li, tetra}$), **b**, out-of-plane cation migration to the octahedral site in the Li layer (denoted as $M_{Li, octa}$), and **c**, In-plane cation migration to the empty Li site (denoted as $M_{Li, TM layer}$). Cation migration generates single-coordinated oxygen ions, and such dangling oxygen ions are colored green.







Isosurface of charge density for the electronic states near the Fermi level. Yellow and blue corresponds to negative and positive changes, respectively. Here, the charge density lying along the Li-O-Li axis and V_{Li} -O- V_{Li} axis correspond to O 2p NB states². **b**, The formation energies of $Mn_{Li, tetra}$, $Mn_{Li, octa}$, and $Mn_{Li, TM layer}$ disorders in $Li_{0.5}MnO_3$. $\Delta G_{structural change}$ indicates the energy difference between a structure without structural disorder and a structure with a cation disorder. For the 50 most stable Li-vacancy configurations of each case, their values are plotted according to the type of oxygen dimer formed. Herein, O-O pairs whose bond length is below 1.7 Å are classified as oxygen dimers, according to the previous literature⁵⁰. In addition, for each combination of cation disorder and dimer type, properties of the most stable structure are presented in **c-n**: **c**, Edge dimer formed with $Mn_{Li, tetra}$, **d**, Dangling dimer formed with $Mn_{Li, tetra}$, **e**, Floating dimer formed with $Mn_{Li, tetra}$, **f**, Edge dimer formed with $Mn_{Li, octa}$, **g**, Bridge dimer formed with $Mn_{Li, octa}$, **h**, Dangling dimer formed with $Mn_{Li, octa}$, **i**, Floating dimer formed with $Mn_{Li, octa}$, **j**, Edge dimer formed with $Mn_{Li, TM layer}$, **k**, Bridge dimer formed with $Mn_{Li, TM layer}$, **l**, μ -O₃ dimers formed with cation disordering, **m**, η^1 -O₃ dimers formed with cation disordering, **n**, The formation of multiple oxygen dimers generated with cation disordering. In **c-n**, $Mn_{Li, tetra}$, $Mn_{Li, octa}$, and $Mn_{Li, TM layer}$ are colored blue, and Li ions are omitted for clarity.

Table 2.1. Bader charge changes after $\text{Mn}_{\text{Li, tetra}}$ formation in $\text{Li}_{0.5}\text{MnO}_3$. Positive value means the loss of electron.

Dimer type		Edge	Dangling	Floating
O ions forming short covalent bond	O-O bond	+1.24	+1.66	+2.01
	Mn-O bond	+0.20	+0.10	+0.43
Sum(The other O ions in the cell)		-1.09	-1.60	-2.20
<i>cf.</i> O ion newly coordinated with migrated Mn		-0.05	-0.07	-0.05
Sum(All Mn ions in the cell)		-0.35	-0.16	-0.24

Table 2.2. Bader charge changes after $\text{Mn}_{\text{Li, octa}}$ formation in $\text{Li}_{0.5}\text{MnO}_3$. Positive value means the loss of electron.

Dimer type		Edge	Bridge	Dangling	Floating	$\mu\text{-O}_3$	$\eta^1\text{-O}_3$
O ions forming short covalent bond	O-O bond	+1.15	+1.38	+1.57	+1.51	+1.75	+2.05
	Mn-O bond	+0.52	+0.40	+0.25	+0.25	+0.41	+0.09
Sum(The other O ions in the cell)		-1.25	-1.28	-1.69	-1.56	-1.83	-1.89
<i>cf.</i> Sum(Four O ions newly coordinated with migrated Mn)		-0.50	-0.62	-0.51	-0.60	-0.44	-0.55
Sum(All Mn ions in the cell)		-0.42	-0.49	-0.14	-0.20	-0.33	-0.25

Table 2.3. Bader charge changes after $\text{Mn}_{\text{Li, TM layer}}$ formation in $\text{Li}_{0.5}\text{MnO}_3$. Positive value means the loss of electron.

Dimer type		Edge	Bridge	$\mu\text{-O}_3$
O ions forming short covalent bond	O-O bond	+1.37	+1.36	+1.94
	Mn-O bond	+0.06	+0.21	+0.24
Sum(The other O ions in the cell)		-1.08	-1.28	-1.87
<i>cf.</i> Sum(Four O ions newly coordinated with migrated Mn)		-0.72	-0.74	-0.58
Sum(All Mn ions in the cell)		-0.35	-0.29	-0.30

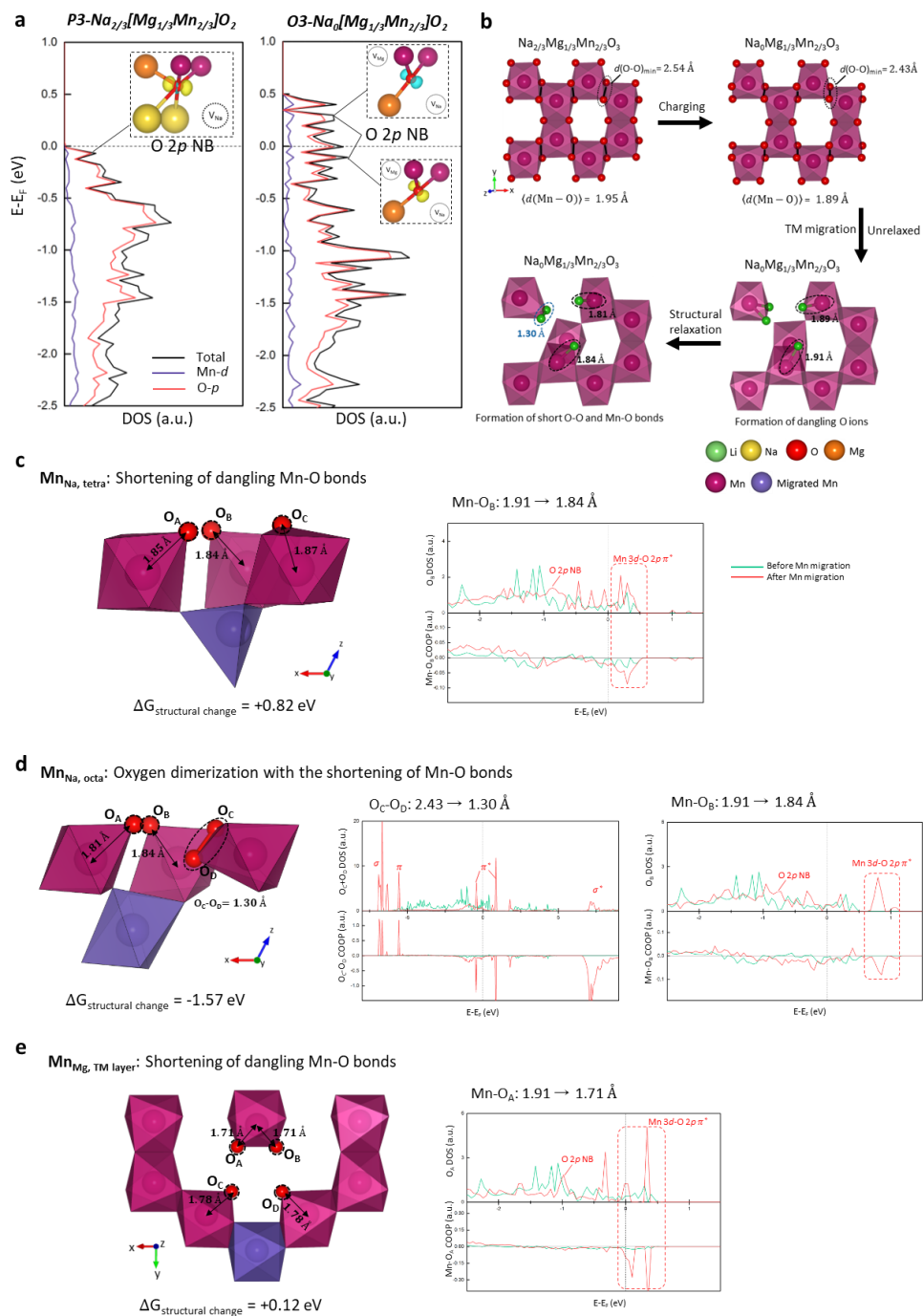


Figure 2.5. a, DOS of $P3\text{-Na}_{2/3}[\text{Mg}_{1/3}\text{Mn}_{2/3}]\text{O}_2$ and $O3\text{-Na}_0[\text{Mg}_{1/3}\text{Mn}_{2/3}]\text{O}_2$ without

any structural disorder. (Inset) Isosurface of charge density for the electronic states near the Fermi level. Yellow and blue corresponds to negative and positive charges, respectively. Here, the charge density lying along the Mg-O- V_{Na} axis and V_{Mg} -O- V_{Na} axis correspond to O $2p$ NB states². **b**, Bonding rearrangements involved with charging and $Mn_{Na, octa}$ formation, where dangling oxygen ions formed with Mn migration are colored green. **c-e**, Bonding arrangements and electronic structures of $O3-Na_0[Mg_{1/3}Mn_{2/3}]O_2$ with $Mn_{Na, tetra}$ (**c**), $Mn_{Na, octa}$ (**d**), and $Mn_{Mg, TM layer}$ (**e**) disorder. In **c-e**, $Mn_{Na, tetra}$, $Mn_{Na, octa}$, and $Mn_{Mg, TM layer}$ are colored blue, and Mg ions are omitted for clarity in **b-e**.

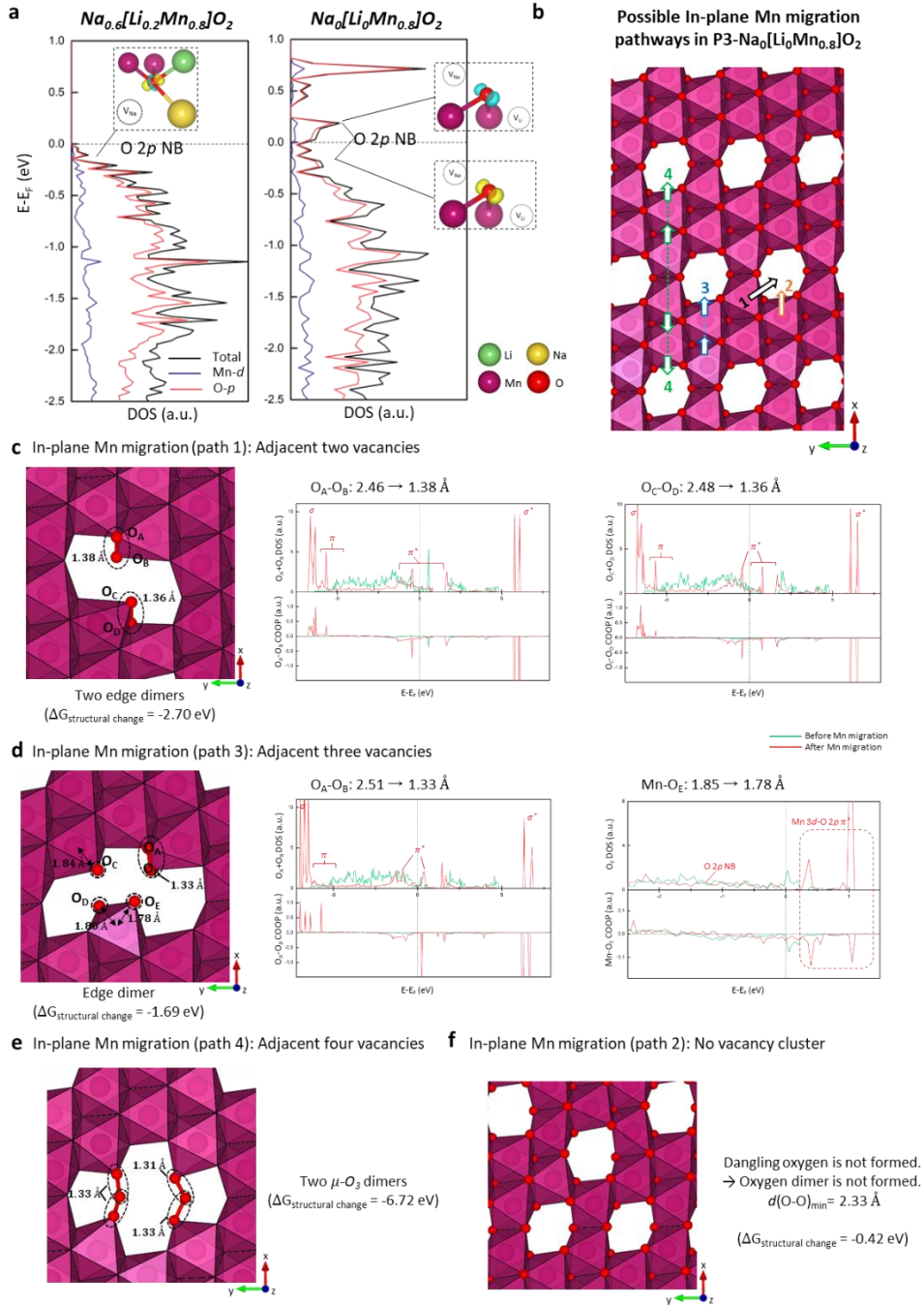


Figure 2.6. **a**, DOS of $\text{P3-Na}_{0.6}[\text{Li}_{0.2}\text{Mn}_{0.8}]\text{O}_2$ and $\text{P3-Na}_0[\text{Li}_0\text{Mn}_{0.8}]\text{O}_2$ without any structural disorder. (Inset) Isosurface of charge density for the electronic states near

the Fermi level. Yellow and blue corresponds to negative and positive changes, respectively. Here, the charge density lying along the Li-O- V_{Na} axis and V_{Li} -O- V_{Na} axis correspond to O $2p$ NB states². **b**, Schematic representation of possible in-plane Mn migration pathways in P3- $Na_0[Li_0Mn_{0.8}]O_2$. For each case, the relaxed structures and corresponding electronic structures are presented in **c-f**. **c**, path 1. **d**, path 3. **e**, path 4. **f**, path 2. To describe path 4 without the influence of defect-defect interactions, we employed a $Na_0[Li_0Mn_{96}]O_{240}$ supercell twice larger than the other cases.

2.3.2 Cation disordering in Mott-Hubbard systems

In Mott-Hubbard electrode systems, occupied M nd -O $2p$ t_{2g}^* states typically lie above the O $2p$ NB states (figure 2.8); thus, the initial oxidation of the electrode takes place by the cationic redox. And, depending on the relative position of the Fermi level, O $2p$ NB states may either participate in the redox in the high-voltage region, or remain fully filled until the end of the charge. The representative example of the former case is the charging process of Li_2RuO_3 electrode, which presents both cationic and anionic redox according to the previous studies^{51,52}. Our calculations in figure 2.9a also confirm that the initial charging to Li_1RuO_3 occurs by $\text{Ru}^{4+/5+}$ redox based on Ru $4d$ -O $2p$ t_{2g}^* states, whereas the subsequent delithiation continues by the depopulation of O $2p$ NB states. Upon the significant oxygen oxidation during the delithiation ($\sim\text{Li}_{0.5}\text{RuO}_3$), it was found that the cation disordering significantly stabilizes the oxygen by enabling the formation of strong covalent bonding. Figure 2.7a presents the $\text{Ru}_{\text{Li, octa}}$ disorder can be spontaneously formed with the negative ΔG (~ -0.33 eV) in $\text{Li}_{0.5}\text{RuO}_3$. It accompanies four dangling oxygens in the neighbor, which end up with the strong hybridization in Ru-O bonds as evidenced by the shortened bond length to $1.64 \sim 1.73$ Å. It manifests the formation of terminal oxo ligands considering that the previously reported lengths of $\text{Ru}^{5+}=\text{O}$ bond are in the range of $1.63 \sim 1.72$ Å^{53,54}. The formation of short Ru-O bonds (< 1.7 Å) was consistently and universally observed for other types of disorders such as $\text{Ru}_{\text{Li, tetra}}$ and $\text{Ru}_{\text{Li, TM layer}}$ (More details are provided in figure 2.9).

On the other hand, some of the Mott-Hubbard electrode systems such as layered

Li_2IrO_3 do not employ the oxygen redox, thus the O $2p$ NB states remain fully filled until the end of the charge. As described in figure 2.10a, the delithiation of Li_2IrO_3 is charge compensated by $\text{Ir}^{4+/5.5+}$ redox at Ir $5d$ -O $2p$ t_{2g}^* state, which is in agreement with the previous report¹⁴. Interesting contrast could be witnessed from the tendency of the cation disordering in this material. It was observed that the bond rearrangements accompanying $\text{Ir}_{\text{Li, octa}}$ in $\text{Li}_{0.5}\text{IrO}_3$ is energetically unfavorable ($\Delta G \sim +1.80$ eV) in figure 2.7b. With the hypothetical Ir migration, four dangling oxygens are produced and are supposed to strengthen Ir-O bonds similar to the case of $\text{Li}_{0.5}\text{RuO}_3$. However, the subsequent bond contractions ($1.79 \sim 1.83$ Å) were significantly weaker than the typical length of Ir=O bonds (1.725 Å)⁵³. Noteworthy is that $\text{M}_{\text{Li, octa}}$ formation in $\text{Li}_{0.5}\text{RuO}_3$ decreases the total length of dangling Ru-O bonds by 1.08 Å, whereas that in $\text{Li}_{0.5}\text{IrO}_3$ reduces Ir-O bond lengths only by 0.65 Å. Further analysis in Tables 2.4-2.7 and figures 2.9-2.10 also revealed that the amount of charge transfer involved with bond contractions are substantially small in $\text{Li}_{0.5}\text{IrO}_3$ for all the cation disorders considered in comparisons to $\text{Li}_{0.5}\text{RuO}_3$.

Figure 2.7c and d comparatively display the electronic structural change in oxygen atoms pertaining to 1.64 Å Ru-O bond in $\text{Li}_{0.5}\text{RuO}_3$, and 1.79 Å Ir-O bond in $\text{Li}_{0.5}\text{IrO}_3$. In both cases, the strong M nd -O $2p$ π^* band arises after the cation migration ($\text{Ru}_{\text{Li, octa}}$ or $\text{Ir}_{\text{Li, octa}}$), which is due to the loss of metal coordination and the quantitative imbalance between O $2p$ orbitals and M nd orbitals, as previously explained in Chapter 2.3.7. However, the center of M nd -O $2p$ π^* band appears at a much higher energy state for Ru-O bond (2.28 eV) than Ir-O bond (0.77 eV) in reference to the O

2p NB, as indicated by blue arrows. It demonstrates that the induced Ru-O π hybridization is far stronger than Ir-O π hybridization. We suppose that the substantial oxygen oxidation in $\text{Li}_{0.5}\text{RuO}_3$ causes the structural stabilization by inducing strong covalent bonds through cation disordering unlike $\text{Li}_{0.5}\text{IrO}_3$ that does not display apparent oxygen redox at O 2p NB band, which will be further discussed later (Table 2.8).

It should be noted that the short oxygen dimer ($< 1.7 \text{ \AA}$) was not detected in Mott-Hubbard $\text{Li}_{0.5}\text{RuO}_3$ and $\text{Li}_{0.5}\text{IrO}_3$ systems even after cation migrations, which is in contrast to the charge-transfer electrode systems. The absence of oxygen dimer could be additionally verified by our extensive analysis of disorders in figure 2.11, and has also been evidenced by previous experiments^{51,55} and calculations^{26,54}. We attribute this discrepancy to the less anionic redox participation in Mott-Hubbard systems in comparisons to charge-transfer systems. The Mott-Hubbard electrode systems generally utilize a smaller amount of hole per oxygen (h^{O}) than those of charge-transfer systems for a given charged state. For example, the combined cationic and anionic redox in $\text{Li}_{0.5}\text{RuO}_3$ makes the h^{O} of the disorder-free $\text{Li}_{0.5}\text{RuO}_3$ ($\sim 1/6$) significantly smaller than that of $\text{Li}_{0.5}\text{MnO}_3$ ($\sim 1/2$). Accordingly, the former holds a weaker motive to stabilize the oxygen while taking the enthalpic penalty associated with the structural deformation involving oxygen dimers. We also suppose that the radial distributions of M 4d orbitals are typically more diffusive than those of M 3d orbitals, and thus the overlap integrals between O 2p and Ru 4d orbitals are greater than those between O 2p and Mn 3d orbitals²⁶. On that account, the rotation of highly

covalent Ru-O bond is expected to be more resilient than that of Mn-O bond, which is required for the oxygen rearrangements, therefore impeding the formation of the oxygen dimer.

The correlation between the degree of h^O and the propensity of dimer formation could be simply experimented for the $\text{Li}_{0.5}\text{RuO}_3$ by systematically altering the h^O value via the substitution of cations. When some of Ru^{4+} was replaced by the Mn^{4+} , *i.e.*, $\text{Li}_{0.5}\text{Ru}_{0.5}\text{Mn}_{0.5}\text{O}_3$, the expected h^O increases to approximately $\sim 1/3$, which is twice that of $\text{Li}_{0.5}\text{RuO}_3$. In this case, the Ru migration ($\text{Ru}_{\text{Li,octa}}$) was found to generate a significant oxygen bond rearrangement, and, in particular, the oxygen dimer with 1.24 Å distance was evidently observed at the disorder, as illustrated in figure 2.12b. It confirms that the Ru migration can also induce the oxygen dimerization at high h^O states (see figure 2.12 for more details). It implies to a greater extent that the substitutions of TMs with redox-inactive metals having fully filled d shells (d^{10} ; Sn^{4+} , Sb^{5+} , and Te^{6+}) or completely empty d shells (d^0 ; Ti^{4+}) may promote the oxygen dimerization in the electrode materials. In principle, these substitutions would exacerbate the reliance on oxygen redox owing to the decrease of the accessible cationic redox capacity. Assuming the oxidation limits of +5 for Ru and +5.5 for Ir^8 , the half substitution of Sn would increase h^O of $\text{Li}_{0.5}\text{RuO}_3$ and $\text{Li}_{0.5}\text{IrO}_3$ from 1/6 and 0 to 1/3 and 1/4, respectively. Furthermore, the covalency between TMs with d^0 or d^{10} and oxygen is relatively weak compared with that of typical TM-O bonds (figure 2.14), thus, is less resilient for rotation than other highly directional TM-O bonds. Figure 2.7e and f validate this theory by showing that short oxygen dimers could be

readily formed in $\text{Li}_{0.5}\text{Ru}_{0.5}\text{Sn}_{0.5}\text{O}_3$ and $\text{Li}_{0.5}\text{Ir}_{0.5}\text{Sn}_{0.5}\text{O}_3$ through the rotation of Sn-O dangling bonds. Notable in the results is that if dangling bonds include Sn-O bonds, the dimerization can be induced regardless of whether the migrating cation is TM or Sn (see Chapter 2.3.10). However, if the opposite is the case, short dimers are not generated and the oxidized oxygen is stabilized only through TM-O hybridization. It infers that along with h^{O} exceeding the threshold, the presence of non-directional dangling bonds is an essential prerequisite for the oxygen dimerization in Mott-Hubbard systems. This finding accounts for the previous experimental observations of oxygen dimers in $\text{Li}_{2-x}\text{Ir}_{0.5}\text{Sn}_{0.5}\text{O}_3$ (Sn^{4+} , d^{10}), $\text{Li}_{4-x}\text{NiWO}_6$ (W^{6+} , d^0), and Li_8SnO_6 electrodes^{14,56,57}.

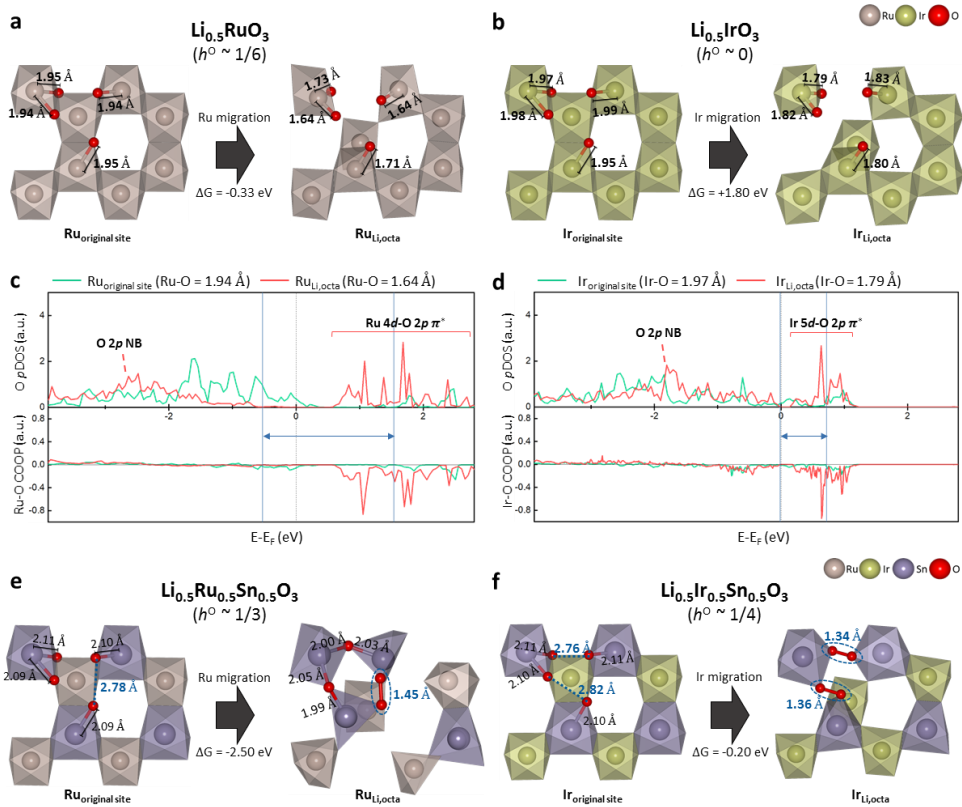


Figure 2.7. Bonding rearrangements involved with cation disordering in Mott-Hubbard systems. **a, b**, Bonding rearrangements involved with $\text{M}_{\text{Li, octa}}$ formation in $\text{Li}_{0.5}\text{RuO}_3$ (**a**) and $\text{Li}_{0.5}\text{IrO}_3$ (**b**). **c, d**, Changes in the electronic structure of dangling oxygen involved with $\text{M}_{\text{Li, octa}}$ formation in $\text{Li}_{0.5}\text{RuO}_3$ (**c**) and $\text{Li}_{0.5}\text{IrO}_3$ (**d**), which are described in **a** and **b**, respectively. Blue vertical lines indicate the top of O 2p NB band (red) and the center of M nd-O 2p π^* band, and the energy gaps between them are indicated by double arrows. The band center was evaluated following the method of previous reports^{58,59}. **e, f**, Bonding rearrangements involved with $\text{M}_{\text{Li, octa}}$ formation in $\text{Li}_{0.5}\text{Ru}_{0.5}\text{Sn}_{0.5}\text{O}_3$ (**e**) and $\text{Li}_{0.5}\text{Ir}_{0.5}\text{Sn}_{0.5}\text{O}_3$ (**f**). In each step of **a, b, e** and **f**, Li-vacancy configurations were optimized to be most stable.

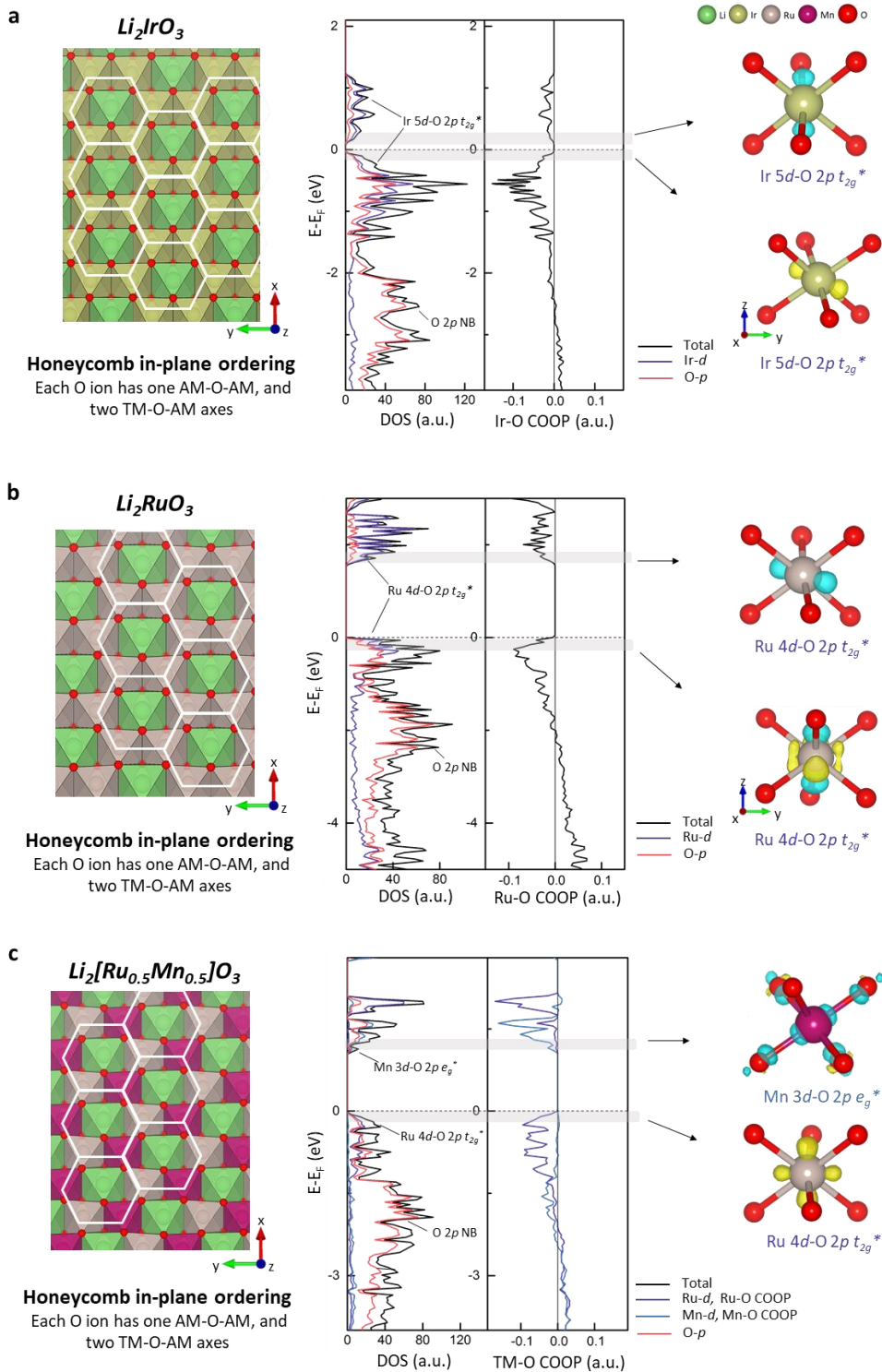
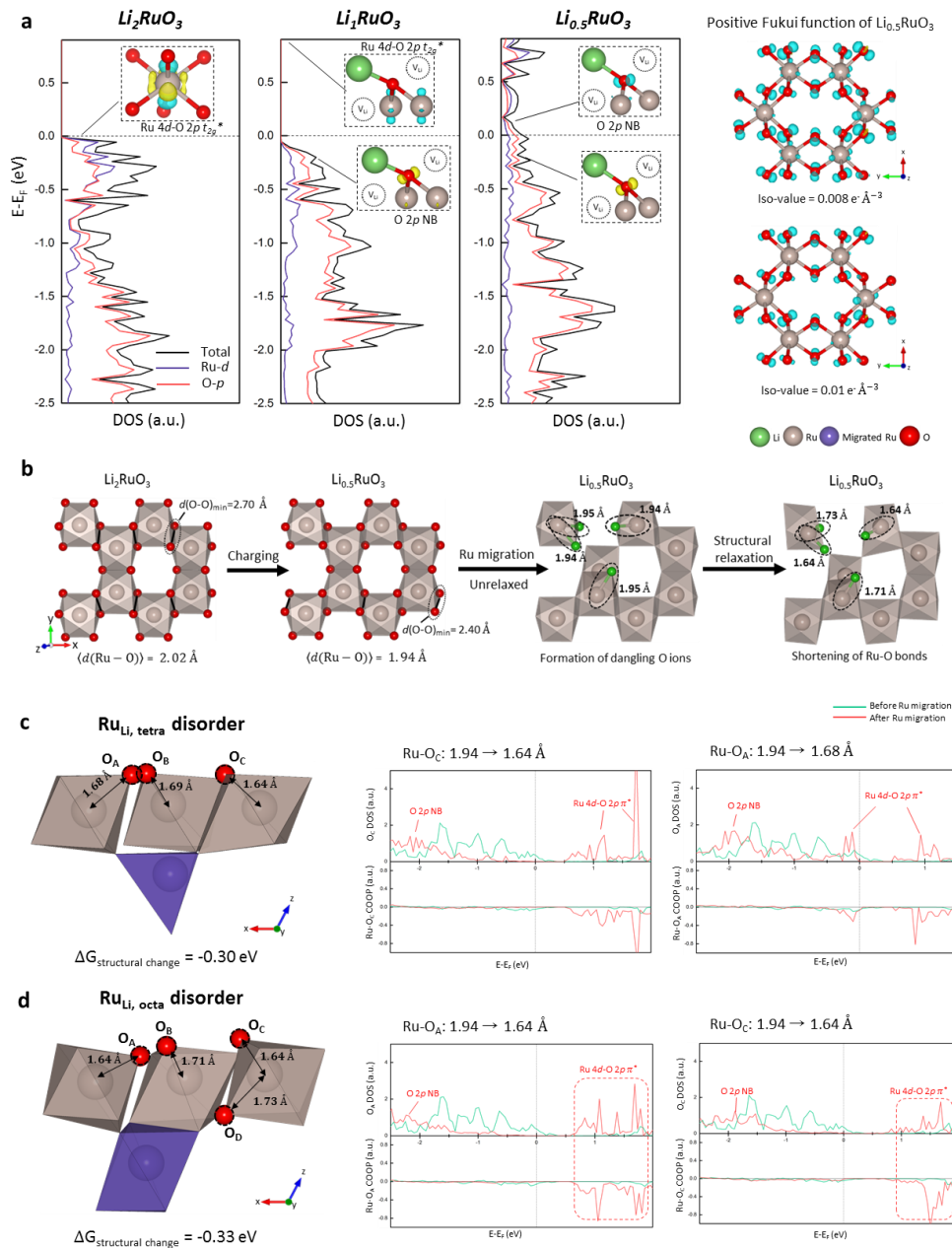


Figure 2.8. The in-plane Li-M arrangements and electronic structures of pristine electrodes belonging to Mott-Hubbard systems. **a**, Li_2IrO_3 , **b**, Li_2RuO_3 , and **c**, $\text{Li}_2\text{Ru}_{0.5}\text{Mn}_{0.5}\text{O}_3$. $\text{Li}_{1/3}\text{M}_{2/3}$ honeycomb arrangement is applied for these electrodes according to the previous reports^{14,60,61}. For $\text{Li}_2\text{Ru}_{0.5}\text{Mn}_{0.5}\text{O}_3$, various Ru/Mn arrangements were considered. In the most stable configuration, each metal component is arranged to form a regular triangular pattern. Then, each Ru(Mn) ion is surrounded by three Mn(Ru) ions and three Li ions. On the right are the positive and negative Fukui functions that visualize the charge density of electronic states just above and below the Fermi level, respectively. Yellow and blue in the Fukui functions corresponds to negative and positive changes, respectively. Electronic structures and the negative Fukui functions show in common that M nd -O $2p$ t_{2g}^* states are at the Fermi level in Mott-Hubbard systems.



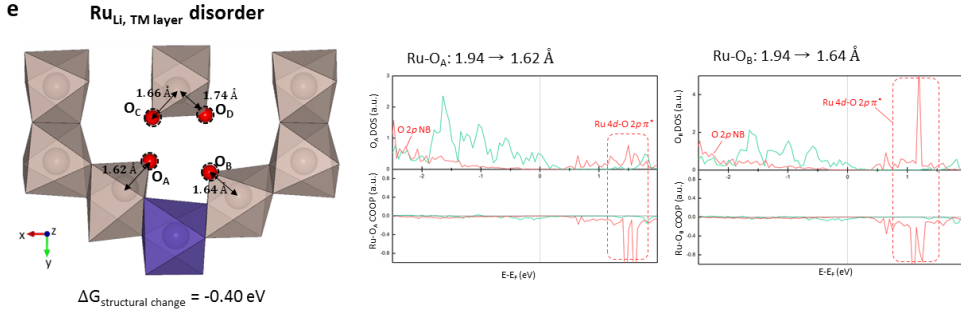


Figure 2.9. **a**, DOS of Li_2RuO_3 , Li_1RuO_3 , and $\text{Li}_{0.5}\text{RuO}_3$ without any structural disorder. (Inset) The positive and negative Fukui functions that visualize the charge density of electronic states just above and below the Fermi level, respectively. Yellow and blue corresponds to negative and positive changes, respectively. The negative Fukui function of Li_1RuO_3 and the positive Fukui function of $\text{Li}_{0.5}\text{RuO}_3$ indicate in common that the charging from Li_1RuO_3 to $\text{Li}_{0.5}\text{RuO}_3$ is mainly compensated by the depletion of O $2p$ NB states whose density lies along $V_{\text{Li}}\text{-O}-V_{\text{Li}}$ axis. On the right is the upper view of the positive Fukui function of $\text{Li}_{0.5}\text{RuO}_3$. It further supports that in $\text{Li}_1\text{RuO}_3 \rightarrow \text{Li}_{0.5}\text{RuO}_3$ process, the contribution of O $2p$ NB states (equivalently the charge density centered on O) is dominant, whereas the contribution of Ru $4d\text{-O } 2p \pi^*$ states (equivalently the charge density centered on Ru) is very minor. **b**, Bonding rearrangements involved with charging and $\text{Ru}_{\text{Li, octa}}$ formation in $\text{Li}_{2-x}\text{RuO}_3$. Dangling oxygen ions formed with cation migration are colored green. **c-e**, Bonding arrangements and corresponding electronic structures calculated for $\text{Li}_{0.5}\text{RuO}_3$ with $\text{Ru}_{\text{Li, tetra}}$ (**c**), $\text{Ru}_{\text{Li, octa}}$ (**d**), and $\text{Ru}_{\text{Li, TM layer}}$ (**e**). For each case, the Li-vacancy ordering was optimized to be most stable. In **c-e**, $\text{Ru}_{\text{Li, tetra}}$, $\text{Ru}_{\text{Li, octa}}$, and $\text{Ru}_{\text{Li, TM layer}}$ are colored blue, and Li ions are omitted for clarity in **b-e**.

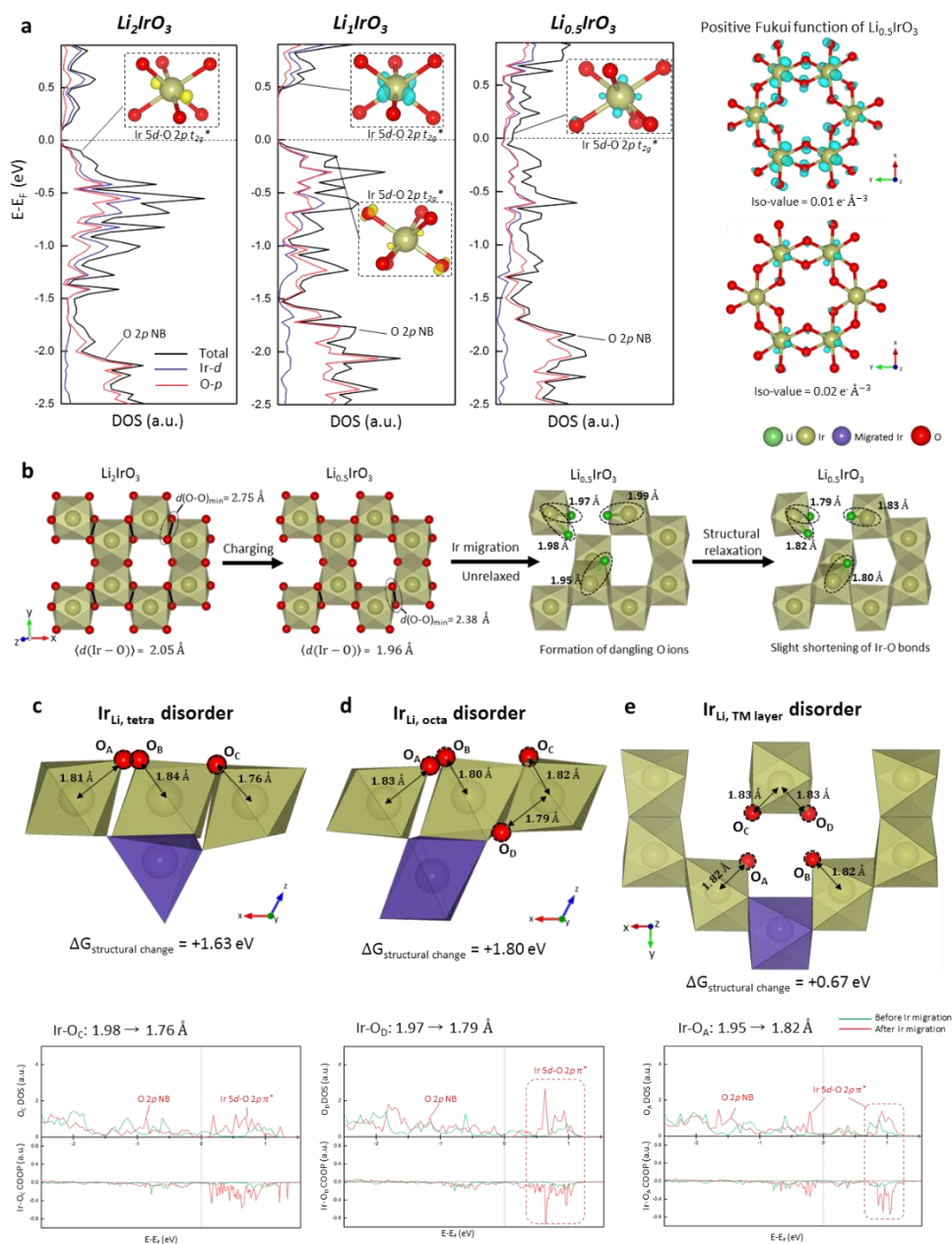


Figure 2.10. a, DOS of Li_2IrO_3 , Li_1IrO_3 , and $\text{Li}_{0.5}\text{IrO}_3$ without any structural disorder.

(Inset) The positive and negative Fukui functions that visualize the charge density of electronic states just above and below the Fermi level, respectively. Yellow and blue

corresponds to negative and positive changes, respectively. DOS and the Fukui functions indicate in common that the entire charging process is mainly charge compensated by the depopulation of Ir $5d$ -O $2p$ t_{2g}^* states. As can be seen from the upper view of the Fukui function on the right, in $\text{Li}_1\text{IrO}_3 \rightarrow \text{Li}_{0.5}\text{IrO}_3$ process, the contribution of O $2p$ NB states (equivalently the charge density centered on O) is very minor compared with that of Ir $5d$ -O $2p$ t_{2g}^* states (equivalently the charge density centered on Ir). **b**, Bonding rearrangements involved with charging and $\text{Ir}_{\text{Li, octa}}$ formation in $\text{Li}_{2-x}\text{IrO}_3$. Dangling oxygen ions formed with cation migration are colored green. **c-e**, Bonding arrangements and corresponding electronic structures calculated for $\text{Li}_{0.5}\text{IrO}_3$ with $\text{Ir}_{\text{Li, tetra}}$ (**c**), $\text{Ir}_{\text{Li, octa}}$ (**d**), and $\text{Ir}_{\text{Li, TM layer}}$ (**e**). For each case, the Li-vacancy ordering was optimized to be most stable. In **c-e**, $\text{Ir}_{\text{Li, tetra}}$, $\text{Ir}_{\text{Li, octa}}$, and $\text{Ir}_{\text{Li, TM layer}}$ are colored blue, and Li ions are omitted for clarity in **a-e**.

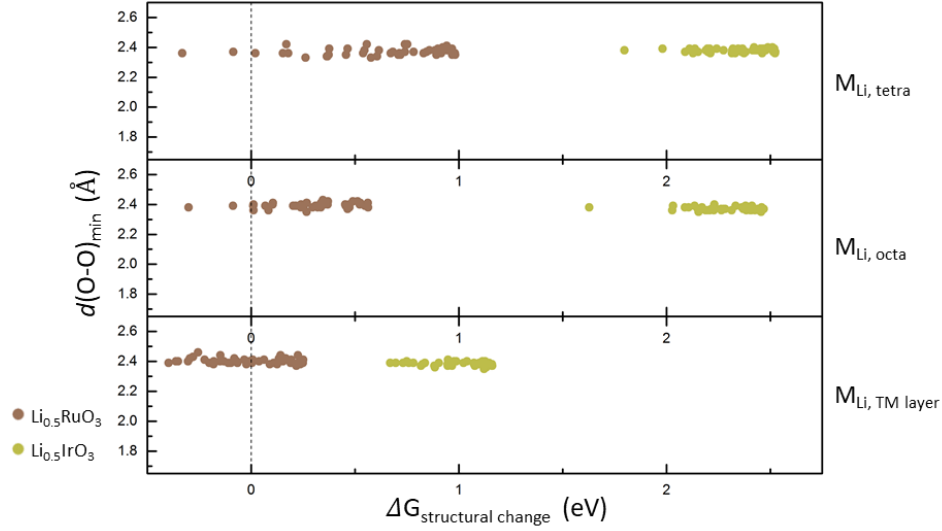


Figure 2.11. Disorder formation energies ($\Delta G_{\text{structural change}}$) in $\text{Li}_{0.5}\text{RuO}_3$ and $\text{Li}_{0.5}\text{IrO}_3$. The minimum O-O distance in supercells are represented together. For each case, we performed DFT calculations for 300 generated Li-vacancy configurations, and the values of 50 most stable structures are provided here. While $\text{Ru}_{\text{Li, tetra}}$, $\text{Ru}_{\text{Li, octa}}$, and $\text{Ru}_{\text{Li, TM layer}}$ formation in $\text{Li}_{0.5}\text{RuO}_3$ can be thermodynamically spontaneous, all types of cation disordering are estimated to be nonspontaneous in $\text{Li}_{0.5}\text{IrO}_3$. Importantly, in both $\text{Li}_{0.5}\text{RuO}_3$ and $\text{Li}_{0.5}\text{IrO}_3$, no short oxygen dimer ($< 1.7 \text{ \AA}$) was formed after cation disordering, regardless of the Li configuration.

Table 2.4. Bond length changes and bond order changes of dangling oxygen ions accompanying $M_{\text{Li, tetra}}$ formation in $\text{Li}_{0.5}\text{RuO}_3$ and $\text{Li}_{0.5}\text{IrO}_3$. ICOOP(eF) is the integration of COOP up to the Fermi level, which has been known to be proportional to the bond order^{14,26}.

Materials	Dangling bond	Bond length (Å)		ICOOP(eF) (a.u.)		Δ Bond length (Å)	Δ ICOOP (eF) (a.u.)	Δ ICOOP (eF) (%)
		$M_{\text{original site}}$	$M_{\text{Li, tetra}}$	$M_{\text{original site}}$	$M_{\text{Li, tetra}}$			
$\text{Li}_{0.5}\text{IrO}_3$	Ir-O _A	1.99	1.81	0.18	0.30	-0.18	+0.12	+66.4
	Ir-O _B	1.95	1.84	0.20	0.28	-0.11	+0.07	+36.8
	Ir-O _C	1.98	1.76	0.19	0.37	-0.21	+0.18	+96.0
	Sum					-0.5	0.37	+199.3
$\text{Li}_{0.5}\text{RuO}_3$	Ru-O _A	1.94	1.68	0.19	0.43	-0.26	+0.24	+123.2
	Ru-O _B	1.95	1.69	0.19	0.37	-0.26	+0.19	+100.1
	Ru-O _C	1.94	1.64	0.19	0.47	-0.30	+0.28	+147.4
	Sum					-0.82	+0.71	+370.6

Table 2.5. Bond length changes and bond order changes of dangling oxygen ions accompanying $M_{Li, octa}$ formation in $Li_{0.5}RuO_3$ and $Li_{0.5}IrO_3$. ICOOP(eF) is the integration of COOP up to the Fermi level, which has been known to be proportional to the bond order^{14,26}.

Materials	Dangling bond	Bond length (Å)		ICOOP(eF) (a.u.)		Δ Bond length (Å)	Δ ICOOP (eF) (a.u.)	Δ ICOOP (eF) (%)
		$M_{original}$ site	$M_{Li, octa}$	$M_{original}$ site	$M_{Li, octa}$			
$Li_{0.5}IrO_3$	Ir-O _A	1.99	1.83	0.18	0.30	-0.15	+0.12	+65.8
	Ir-O _B	1.95	1.80	0.20	0.33	-0.15	+0.12	+61.6
	Ir-O _C	1.98	1.82	0.19	0.3	-0.16	+0.11	+59.8
	Ir-O _D	1.97	1.79	0.19	0.35	-0.18	+0.17	+88.2
	Sum					-0.65	+0.52	+275.4
$Li_{0.5}RuO_3$	Ru-O _A	1.94	1.64	0.19	0.48	-0.31	+0.29	+150.1
	Ru-O _B	1.95	1.71	0.19	0.37	-0.24	+0.18	+97.1
	Ru-O _C	1.94	1.64	0.19	0.45	-0.30	+0.26	+134.9
	Ru-O _D	1.95	1.73	0.19	0.35	-0.23	+0.17	+89.8
	Sum					-1.08	+0.90	+472.0

Table 2.6. Bond length changes and bond order changes of dangling oxygen ions accompanying $M_{\text{Li, TM layer}}$ formation in $\text{Li}_{0.5}\text{RuO}_3$ and $\text{Li}_{0.5}\text{IrO}_3$. ICOOP(eF) is the integration of COOP up to the Fermi level, which has been known to be proportional to the bond order^{14,26}.

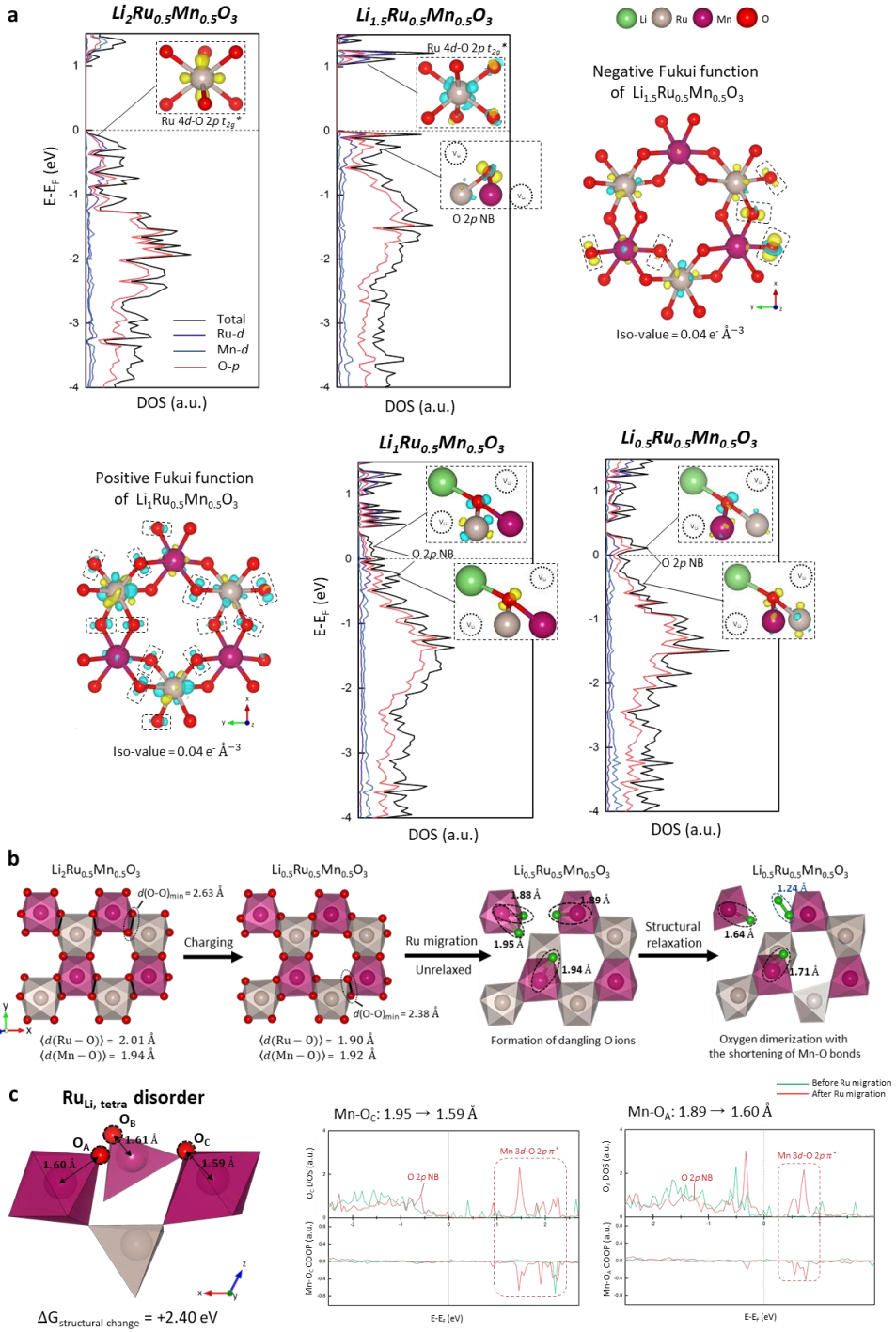
Materials	Dangling bond	Bond length (Å)		ICOOP(eF) (a.u.)		Δ Bond length (Å)	Δ ICOOP (eF) (a.u.)	Δ ICOOP (eF) (%)
		$M_{\text{original site}}$	$M_{\text{Li, TM layer}}$	$M_{\text{original site}}$	$M_{\text{Li, TM layer}}$			
$\text{Li}_{0.5}\text{IrO}_3$	Ir-O _A	1.95	1.82	0.20	0.32	-0.14	+0.12	+59.0
	Ir-O _B	1.98	1.82	0.19	0.31	-0.16	+0.12	+64.0
	Ir-O _C	1.95	1.83	0.20	0.31	-0.12	+0.10	+51.5
	Ir-O _D	2.00	1.83	0.17	0.30	-0.17	+0.13	+73.2
	Sum					-0.58	+0.47	+247.5
$\text{Li}_{0.5}\text{RuO}_3$	Ru-O _A	1.94	1.62	0.19	0.47	-0.32	+0.27	+142.7
	Ru-O _B	1.94	1.64	0.19	0.49	-0.31	+0.30	+155.1
	Ru-O _C	1.95	1.66	0.19	0.40	-0.30	+0.21	+114.6
	Ru-O _D	1.95	1.74	0.19	0.32	-0.2	+0.13	+65.3
	Sum					-1.12	+0.91	+477.7

Table 2.7. Bader charge changes involved with cation disordering in $\text{Li}_{0.5}\text{RuO}_3$ and $\text{Li}_{0.5}\text{IrO}_3$. Positive value means the loss of electron.

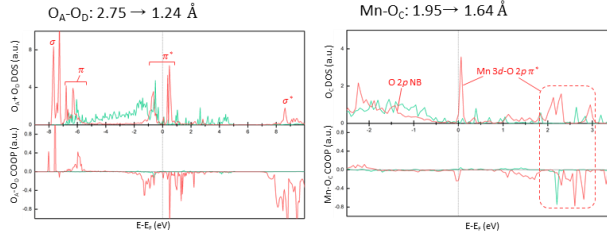
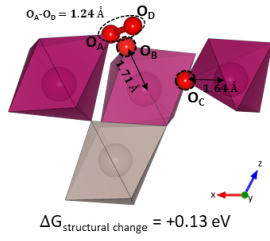
Disorder type			Li _{0.5} RuO ₃			Li _{0.5} IrO ₃		
			Ru _{Li, tetra}	Ru _{Li, octa}	Ru _{Li, TM layer}	Ir _{Li, tetra}	Ir _{Li, octa}	Ir _{Li, TM layer}
Dangling TM-O bonds	M-O _A	M	+0.18	+0.30	+0.18	+0.18	+0.15	+0.09
		O _A	+0.25	+0.17	+0.17	-0.07	-0.07	-0.08
	M-O _B	M	+0.17	+0.34	+0.20	+0.09	+0.16	+0.03
		O _B	+0.15	+0.17	+0.18	-0.08	-0.05	-0.05
	M-O _C	M	+0.29	+0.47	+0.43	+0.24	+0.38	+0.24
		O _C	+0.19	+0.20	+0.18	+0.07	-0.05	-0.04
	M-O _D	M	.	+0.13	+0.02	.	+0.08	-0.04
		O _D						
	Sum(ΔBader _M)		+0.64	+1.11	+0.81	+0.52	+0.69	+0.36
	Sum(ΔBader _O)		+0.59	+0.68	+0.54	-0.08	-0.08	-0.21
The other M ions in the cell			-0.26	-0.47	-0.46	-0.16	-0.33	-0.02
The other O ions in the cell			-0.98	-1.32	-0.89	-0.27	-0.27	-0.13

Table 2.8. Disorder formation energies calculated for $\text{Li}_{2-x}\text{RuO}_3$ and $\text{Li}_{2-x}\text{IrO}_3$ ($0 \leq x \leq 2$). For each case, the values corresponding to the most stable Li configuration are presented here. When x is 0, $M_{\text{Li, octa}}$ and $M_{\text{Li, TM layer}}$ disorders are described by exchanging one M ion and one Li ion in supercells. At this time, the values pertaining to $M_{\text{Li, tetra}}$ are not provided here due to the difficulty in structural relaxation, which is probably because $M_{\text{Li, tetra}}$ shares a face with three Li ions rendering the structure very unstable.

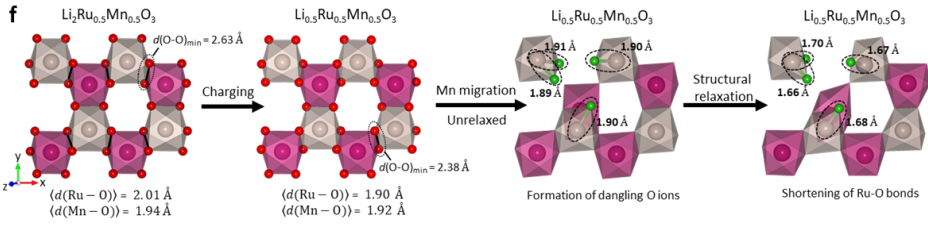
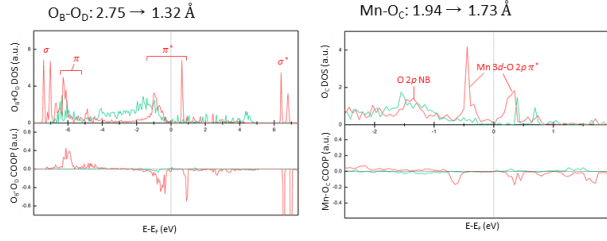
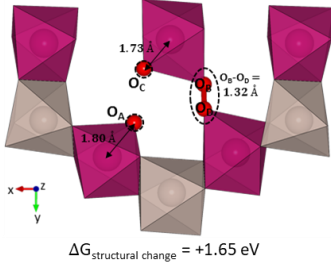
x in $\text{Li}_{2-x}\text{RuO}_3$		x = 0	x = 0.5	x = 1	x = 1.5	x = 2
G_f (cationic disorder)	$\text{Ru}_{\text{Li, tetra}}$.	+1.50 eV	+3.23 eV	-0.30 eV	-5.15 eV
	$\text{Ru}_{\text{Li, octa}}$	+1.58 eV	+1.21 eV	+3.01 eV	-0.33 eV	-2.61 eV
	$\text{Ru}_{\text{Li, TM layer}}$	+1.00 eV	+0.09 eV	+2.16 eV	-0.40 eV	-2.68 eV
x in $\text{Li}_{2-x}\text{IrO}_3$		x = 0	x = 0.5	x = 1	x = 1.5	x = 2
G_f (cationic disorder)	$\text{Ir}_{\text{Li, tetra}}$.	+1.69 eV	+2.91 eV	+1.63 eV	+0.43 eV
	$\text{Ir}_{\text{Li, octa}}$	+1.46 eV	+1.49 eV	+3.05 eV	+1.80 eV	+1.20 eV
	$\text{Ir}_{\text{Li, TM layer}}$	+0.43 eV	+0.03 eV	+1.36 eV	+0.67 eV	-0.08 eV



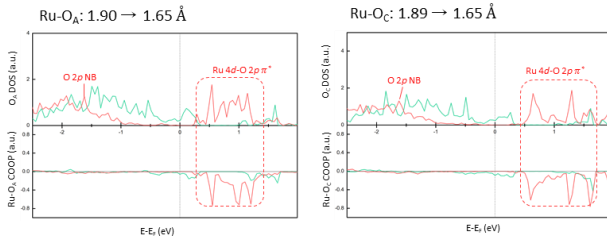
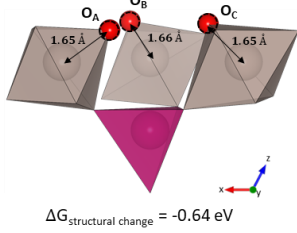
d Ru_{Li, octa} disorder



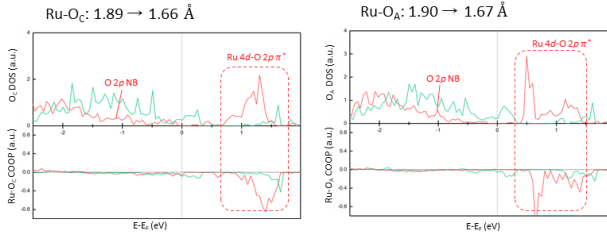
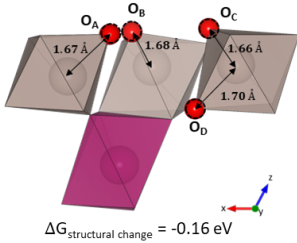
e Ru_{Li, TM layer} disorder



g Mn_{Li, tetra} disorder



h Mn_{Li, octa} disorder



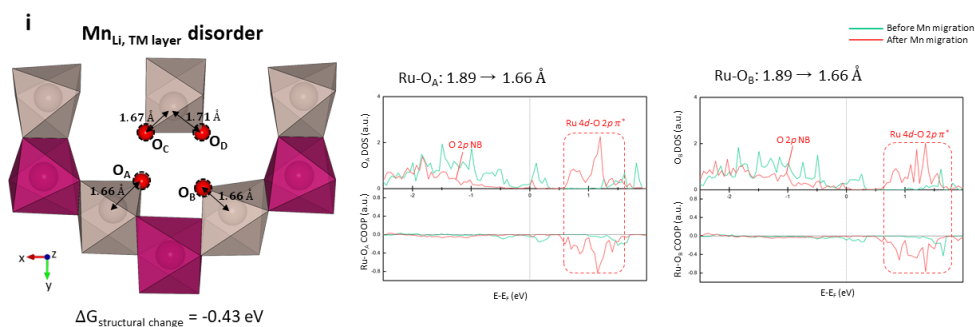


Figure 2.12. a, DOS of $\text{Li}_2\text{Ru}_{0.5}\text{Mn}_{0.5}\text{O}_3$, $\text{Li}_{1.5}\text{Ru}_{0.5}\text{Mn}_{0.5}\text{O}_3$, $\text{Li}_1\text{Ru}_{0.5}\text{Mn}_{0.5}\text{O}_3$, and $\text{Li}_{0.5}\text{Ru}_{0.5}\text{Mn}_{0.5}\text{O}_3$ without any structural disorder. The positive and negative Fukui functions that visualize the charge density of electronic states just above and below the Fermi level, respectively, are presented together. In Fukui functions, yellow and blue corresponds to negative and positive changes, respectively. Along with DOS, the negative Fukui function of $\text{Li}_{1.5}\text{Ru}_{0.5}\text{Mn}_{0.5}\text{O}_3$ and the positive Fukui function of $\text{Li}_1\text{Ru}_{0.5}\text{Mn}_{0.5}\text{O}_3$ indicate in common that the charging from $\text{Li}_{1.5}\text{Ru}_{0.5}\text{Mn}_{0.5}\text{O}_3$ to $\text{Li}_1\text{Ru}_{0.5}\text{Mn}_{0.5}\text{O}_3$ is mainly compensated by the depopulation of O 2p NB states whose charge density lies along the $V_{\text{Li}}\text{-O-}V_{\text{Li}}$ axis (dashed regions). In these Fukui functions, yellow and blue densities centered on Ru ions are may be due to the charge transfer between d orbitals of Ru ions. Taken together, it can be concluded that in the absence of structure disorder, the initial $\text{Li}_2\text{Ru}_{0.5}\text{Mn}_{0.5}\text{O}_3 \rightarrow \text{Li}_{1.5}\text{Ru}_{0.5}\text{Mn}_{0.5}\text{O}_3$ process is charge compensated by the depletion of Ru 4d-O 2p t_{2g}^* states, *i.e.* $\text{Ru}^{4+/5+}$ redox. And thereafter, the charging process up to $\text{Li}_{0.5}\text{Ru}_{0.5}\text{Mn}_{0.5}\text{O}_3$ is mainly compensated by the depopulation of O 2p NB states. **b, f,** Bonding rearrangements involved with charging and $\text{Ru}_{\text{Li, octa}}$ (**b**) and $\text{Mn}_{\text{Li, octa}}$ (**f**) formation in $\text{Li}_{2-x}\text{Ru}_{0.5}\text{Mn}_{0.5}\text{O}_3$. Dangling oxygen ions formed with cation migration are colored green. **c-e, g-i,** Bonding

arrangements and corresponding electronic structures calculated for $\text{Li}_{0.5}\text{Ru}_{0.5}\text{Mn}_{0.5}\text{O}_3$ with $\text{Ru}_{\text{Li, tetra}}$ (**c**), $\text{Ru}_{\text{Li, octa}}$ (**d**), $\text{Ru}_{\text{Li, TM layer}}$ (**e**), $\text{Mn}_{\text{Li, tetra}}$ (**g**), $\text{Mn}_{\text{Li, octa}}$ (**h**), and $\text{Mn}_{\text{Li, TM layer}}$ (**i**). For each case, the Li-vacancy ordering was optimized to be most stable. In **b-i**, Li ions are omitted for clarity.

Table 2.9. Bond length changes and bond order changes of dangling oxygen ions accompanying cation disordering in $\text{Li}_{0.5}\text{Ru}_{0.5}\text{Mn}_{0.5}\text{O}_3$. ICOOP(eF) is the integration of COOP up to the Fermi level, which has been known to be proportional to the bond order^{14,26}.

Disorder type	Dangling bond	Bond length (Å)		ICOOP (eF) (a.u.)		Δ Bond length (Å)	Δ ICOOP (eF) (a.u.)	Δ ICOOP (eF) (%)
		M _{original site}	M _{migrated site}	M _{original site}	M _{migrated site}			
Mn_{Li}, tetra	Ru-O _A	1.90	1.65	0.23	0.47	-0.25	+0.24	+103.4
	Ru-O _B	1.90	1.66	0.23	0.42	-0.24	+0.19	+79.0
	Ru-O _C	1.89	1.65	0.23	0.45	-0.24	+0.22	+92.6
	Sum					-0.73	+0.65	+275.0
Mn_{Li}, octa	Ru-O _A	1.90	1.67	0.23	0.43	-0.23	+0.19	+82.9
	Ru-O _B	1.90	1.68	0.23	0.39	-0.22	+0.16	+66.9
	Ru-O _C	1.89	1.66	0.23	0.44	-0.24	+0.21	+88.7
	Ru-O _D	1.91	1.70	0.23	0.39	-0.21	+0.17	+74.6
	Sum					-0.90	+0.73	+313.0
Mn_{Li}, TM layer	Ru-O _A	1.89	1.66	0.23	0.44	-0.24	+0.20	+86.4
	Ru-O _B	1.89	1.66	0.23	0.46	-0.23	+0.23	+96.8
	Ru-O _C	1.90	1.67	0.23	0.39	-0.23	+0.16	+66.2
	Ru-O _D	1.90	1.71	0.23	0.38	-0.20	+0.14	+62.7
	Sum					-0.90	+0.73	+312.1
Ru_{Li}, tetra	Mn-O _A	1.89	1.60	0.19	0.46	-0.29	+0.26	+135.6
	Mn-O _B	1.94	1.61	0.15	0.42	-0.33	+0.27	+182.5
	Mn-O _C	1.95	1.59	0.15	0.47	-0.36	+0.32	+216.3
	Sum					-0.62	+0.53	+318.1
Ru_{Li}, octa	Mn-O _B	1.94	1.71	0.15	0.38	-0.23	+0.23	+151.5
	Mn-O _C	1.95	1.64	0.15	0.38	-0.31	+0.23	+154.5
	O_A-O_D	2.75	1.32	-0.01	0.22	-1.43	+0.23	.
Ru_{Li}, TM layer	Mn-O _A	1.94	1.8	0.16	0.32	-0.14	+0.16	+99.5
	Mn-O _C	1.94	1.73	0.15	0.31	-0.21	+0.16	+104.3
	O_B-O_D	2.75	1.32	-0.01	0.22	-1.43	+0.23	.

Table 2.10. Bader charge changes involved with cation disordering in $\text{Li}_{0.5}\text{Ru}_{0.5}\text{Mn}_{0.5}\text{O}_3$. Positive value means the loss of electron.

Disorder type			Mn _{Li, tetra}	Mn _{Li, octa}	Mn _{Li, TM layer}	Ru _{Li, tetra}	Ru _{Li, octa}	Ru _{Li, TM layer}
Dangling M-O bonds	M-O _A	M	+0.26	+0.52	+0.30	+0.05	.	+0.02
		O _A	+0.21	+0.21	+0.14	+0.37	.	+0.26
	M-O _B	M	+0.26	+0.44	+0.29	+0.06	-0.01	.
		O _B	+0.13	+0.11	+0.18	+0.18	+0.15	.
	M-O _C	M	+0.33	+0.46	+0.55	+0.05	+0.09	-0.03
		O _C	+0.21	+0.21	+0.16	+0.31	+0.38	+0.20
	M-O _D	M	.	+0.11	+0.06	.	.	.
		O _D
	Sum(Δ Bader _M)		+0.85	+1.43	+1.15	+0.16	+0.08	-0.01
	Sum(Δ Bader _O)		+0.55	+0.64	+0.54	+0.86	+0.53	+0.46
O-O dimerization			O _A -O _D : +1.95	O _B -O _D : +1.29
The other Ru ions in the cell			-0.15	-0.37	-0.30	+0.17	-0.68	-0.56
The other Mn ions in the cell			-0.01	-0.17	-0.09	-0.06	-0.06	-0.07
The other O ions in the cell			-1.24	-1.52	-1.30	-1.13	-1.82	-1.11

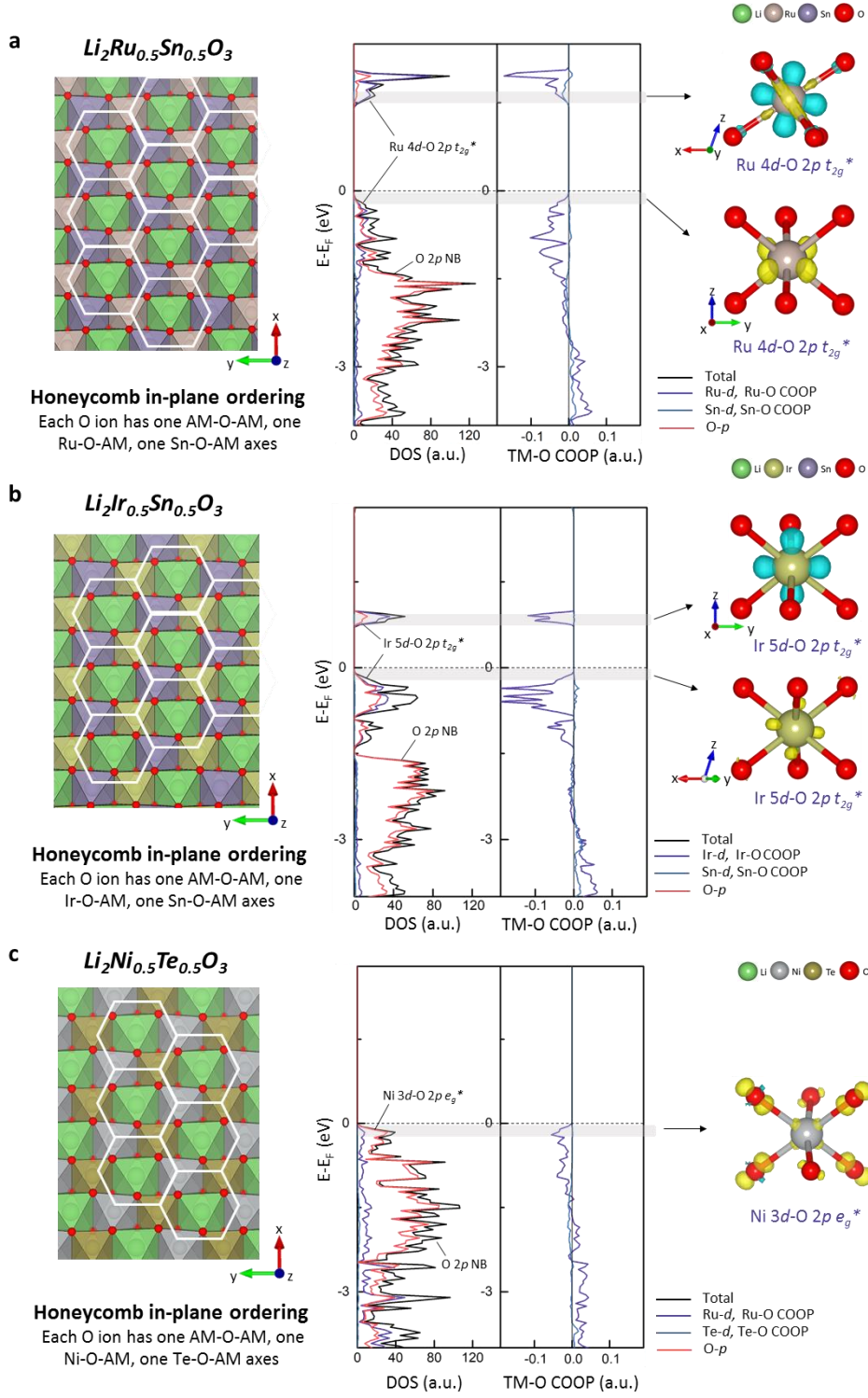


Figure 2.13. The in-plane Li-M arrangements and electronic structures of **a**, $\text{Li}_2\text{Ru}_{0.5}\text{Sn}_{0.5}\text{O}_3$, **b**, $\text{Li}_2\text{Ir}_{0.5}\text{Sn}_{0.5}\text{O}_3$, and **c**, $\text{Li}_2\text{Ni}_{0.5}\text{Te}_{0.5}\text{O}_3$. Those electrodes belong to Mott-Hubbard systems. $\text{Li}_{1/3}\text{M}_{2/3}$ honeycomb arrangement was applied for these electrodes according to the previous reports^{14,60,62}. For each material, various Ru/Sn, Ir/Sn, and Ni/Te in-plane arrangements were considered, respectively, and the most stable arrangements were selected. In common to the three materials, in the most stable arrangements, each metal component is arranged to form a regular triangular pattern. In these arrangements, each metal ion is surrounded by three Li ions and three foreign metal ions. On the right are the Fukui functions that visualize the charge density of electronic states near the Fermi level. Yellow and blue in the Fukui functions corresponds to negative and positive changes, respectively. We note that in COOP graphs, the signals of Sn-O and Te-O components are imperceptible near the Fermi level, indicating negligible Sn-O and Te-O hybridization.

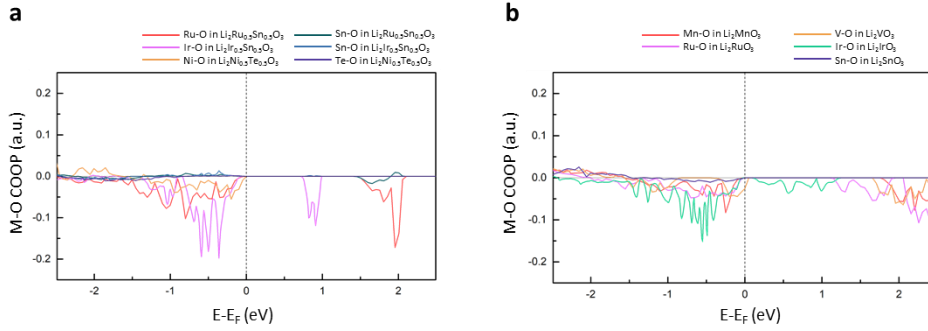


Figure 2.14. COOPs calculated for M-O bands in a range of 1.5 ~ 2.4 Å. **a**, COOPs of M-O bonds present in $\text{Li}_2\text{Ru}_{0.5}\text{Sn}_{0.5}\text{O}_3$, $\text{Li}_2\text{Ir}_{0.5}\text{Sn}_{0.5}\text{O}_3$, and $\text{Li}_2\text{Ni}_{0.5}\text{Te}_{0.5}\text{O}_3$. **b**, COOPs of M-O bonds present in Li_2MnO_3 , Li_2VO_3 , Li_2RuO_3 , Li_2IrO_3 , and Li_2SnO_3 . The number of M-O bonds calculated in each of **a** and **b** is the same for each material. In **a-b**, COOPs of Sn-O and Te-O bonds are negligible in contrast to significant COOPs of other TM-O bonds. It indicates that the orbital hybridizations between Sn/Te and O are very weak.

2.3.3 Reversibility and asymmetry of the oxygen redox

Inspired by the distinct oxygen stabilization mechanisms involving the cation disorder, we attempted to investigate its consequences on the reversibility of the oxygen redox. Figure 2.15a schematically illustrates the potential alternation of DOS when involving the dynamic cation disorder in the charge and the following discharge. The charging of the pristine electrode via the oxygen redox would depopulate the degenerated O 2p NB states (left figure), which would exhibit a typical flat voltage profile^{6,8,10,17}. However, the subsequent structural disordering that occurs at high h^0 eliminates this degeneracy and reorganizes the electronic structure. As depicted in figure 2.15a (right panel), the disorder induces the strong TM-O π hybridization, thus the empty M nd-O 2p π^* states appear above the Fermi level. Accordingly, the following discharge would fill up the empty M nd-O 2p π^* state rather than the original O 2p NB state, resulting in the redox asymmetry between charging and discharging, *i.e.*, voltage hysteresis. Such redox asymmetry is also expected for the case with the O-O dimerization, where O-O π^* states are generated above the Fermi level (figure 2.1d). It is believed that the redox asymmetry will be aggravated with the stronger TM-O and O-O hybridizations, since it determines the splitting of the states. While the shift of oxygen states was projected in previous studies simply with respect to the electrostatics¹⁶, our findings offer a more comprehensive picture revealing the systematic interplay involving the cation disorder, oxygen stabilization mechanism and the subsequent electronic structural change.

We presumed that the redox asymmetry and the resultant voltage hysteresis would be naturally mitigated if the original disorder-free structure is reversibly restored immediately upon the discharge⁹. However, the cation disordering in lithium-rich layered oxides is typically hysteretic¹², and our previous studies on O3-type $\text{Li}(\text{Li}_{0.2}\text{Ni}_{0.2}\text{Mn}_{0.6})\text{O}_2$ electrode^{9,63} have also shown that the restoration of the TM disorder is easily jeopardized by the intra-layer TM migrations within the lithium layer. Likewise, figure 2.16 presents that the intra-layer Ru migration in the lithium layer is energetically feasible, making the recovery to the disorder-free structure difficult. The energy landscape of cation migration in $\text{Li}_{0.5}\text{RuO}_3$ exhibits that the multi-step Ru migrations are energetically down-hill process and inevitably retard the return of Ru ions, impeding the recovery of the original disorder-free structure.

More importantly, the structural reversibility was found to be seriously undermined by the formation of the oxygen dimers. Our *ab initio* molecular dynamics (MD) calculations probing the oxygen dimer revealed that they can ‘freely’ migrate in the lattice and reproduce more oxygen dimers via catalytic reactions degrading the structure, as illustrated in figure 2.15b and c. The oxygen dimerization essentially accompanies the significant distortion in the bonding with the neighboring Mn, causing either the loss of Mn coordination with the dimer (figure 2.15b, left) or bond-weakening between the two (figure 2.15c, left) in $\text{Li}_{0.5}\text{MnO}_3$ (see figure 2.17 for more details). In this case, a floating dimer could drift continuously, to our surprise, within a range of several MO_6 octahedra sizes at 300 K as demonstrated in figure 2.15b and figure 2.18. More striking is that the diffusing dimer could rip off the lattice oxygen

by forming additional O-O bond ($t = 2.35$ ps), thereby catalytically promoting the formation of several more dimers ($t = 100$ ps) in figure 2.15b. It implies that even with the formation of a single oxygen dimer, its catalytic reproduction can rapidly degrade the structural integrity. Even in the case of the dimer that maintains a weak coordination with Mn ion (figure 2.15c), the oxygen dimer could be readily decoordinated with Mn through the thermal vibrations at 300 K, after which it displayed a similar behavior to the floating dimers. We could further confirm that these phenomena are consistently observed for various environments of oxygen dimers in the electrode materials that contain the oxygen dimers (Detailed descriptions of oxygen dimer migrations are provided in figures 2.18-2.25). It suggests that although the oxygen dimerization effectively stabilizes the oxygen redox, it simultaneously provides the potential risk of penalizing the structural reversibility in the long run. This finding elucidates the recent experimental observations of the molecular O₂ trapped inside the bulk structure of electrodes^{10,11}, and rationalizes the phenomenon that the voltage decay becomes more predominant when the oxygen-redox electrode remains charged for a long time⁵.

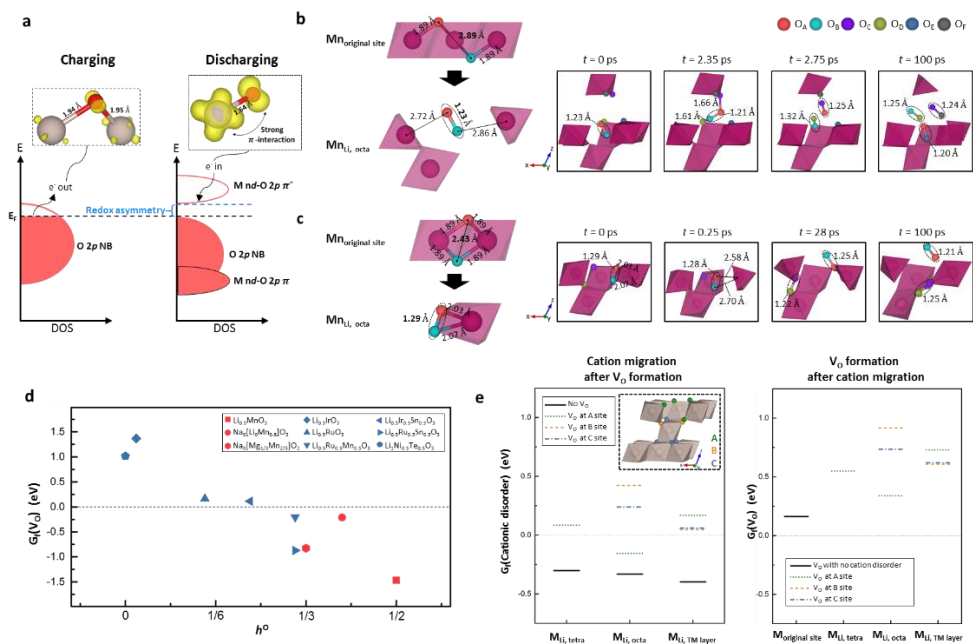


Figure 2.15. Effects of bonding rearrangements and oxygen vacancy on electrochemical and structural reversibility. **a**, Schematic illustration of redox asymmetry that arises from cation disordering and consequent strong TM-O π hybridization. **b-c**, (left) Changes in O-O and Mn-O distances involved with Mn_{Li} , octa formation and concomitant oxygen dimerization in $Li_{1.5}MnO_3$, where the dimer type is the floating dimer(**b**), and edge dimer (**c**). (right) Snapshots of *ab initio* MD calculations at 300 K. In **b** and **c**, short oxygen dimers are highlighted by dashed ovals, and Li ions are omitted for clarity. **d**, V_O formation energy according to h^O of charged electrodes. Red and blue symbols correspond to charge-transfer systems and Mott-Hubbard systems, respectively. **e**, (left) Formation energy of cation disorders calculated for $Li_{1.5}RuO_3$ with or without V_O . (right) V_O formation energy calculated for $Li_{1.5}RuO_3$ with or without cationic disorders. After cation migration, A sites lose

Ru coordination, B sites retain it, and C sites obtain it. When $M_{Li, tetra}$ and V_O in B or C sites exist together, the migrated metal ion returned to its original site during structural relaxation, indicating the instability of these combinations. Thus, the values of those combinations are not displayed.

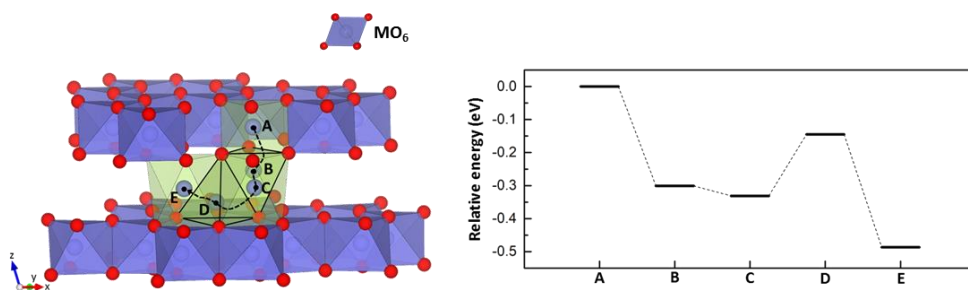


Figure 2.16. (left) TM migration pathways that include out-of-plane TM migration from the TM layer (A_{octa}) to the lithium tetrahedral site (B_{tetra}), and intra-layer TM migration within the Li layer ($B_{\text{tetra}} \rightarrow C_{\text{octa}} \rightarrow D_{\text{tetra}} \rightarrow E_{\text{octa}}$). (right) Energy landscape of TM migration calculated for the left trajectory in $\text{Li}_{0.5}\text{RuO}_3$. All possible next sites in each migration step were considered, and the most stable trajectory is presented here.

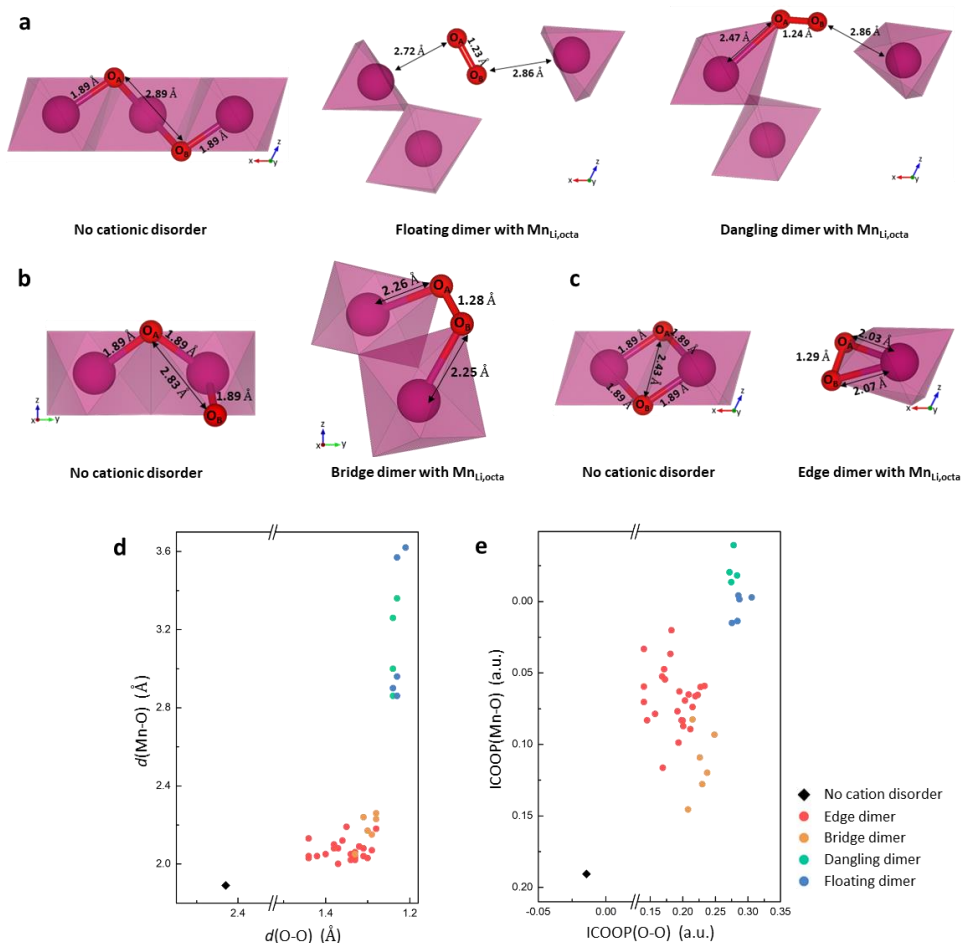
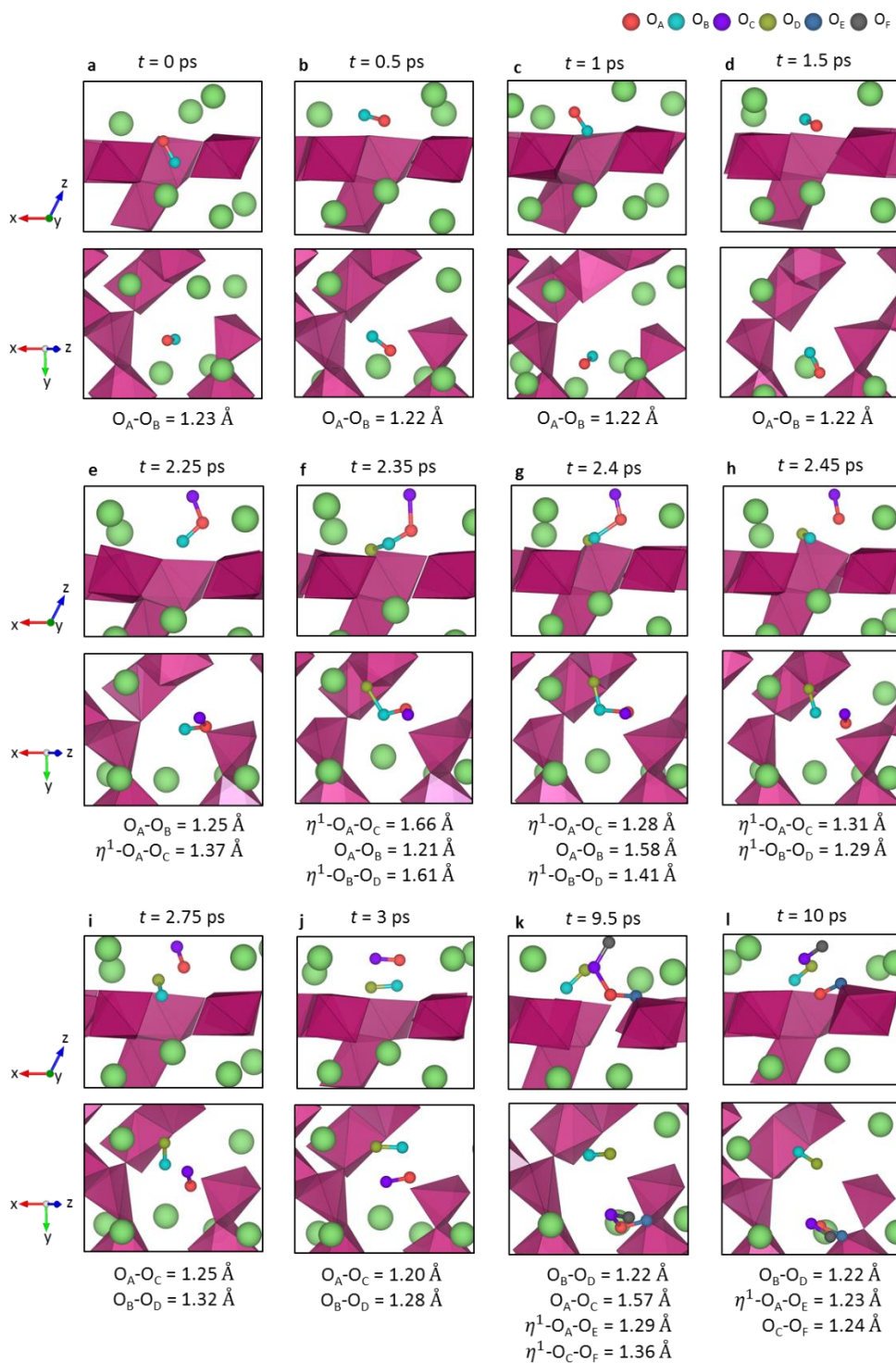


Figure 2.17. a-c, Bonding rearrangements involved with $\text{Mn}_{\text{Li, octa}}$ formation and concomitant oxygen dimerization in $\text{Li}_{0.5}\text{MnO}_3$, where the dimer type is floating dimer and dangling dimer (**a**), bridge dimer (**b**), and edge dimer (**c**). For each dimer type, representative structures with the most stable Li configurations are shown in **a-c**. Dimer classification is elaborated in Chapter 2.3.8. In **d** and **e**, we represented the values corresponding to points in figure 2.4b. **d**, O-O and Mn-O distances of O-O pairs. **e**, O-O ICOOP and Mn-O ICOOP of O-O pairs, where ICOOP is the integration of COOP up to the Fermi level. In **d** and **e**, the y value was measured for

one of the two oxygens with the longer minimum distance to Mn. **a-d** indicate that in terms of bond length, oxygen dimerization always entails some degree of Mn-O de-coordination. The extent of de-coordination is more pronounced in the cases of dangling dimer and floating dimer, where one or two oxygen atoms are fully de-coordinated and O-O distances are shorter than those of edge dimer and bridge dimer. In terms of orbital hybridization also, the enhancement of O-O hybridization inevitably compromises Mn-O hybridization, as shown in **e**.



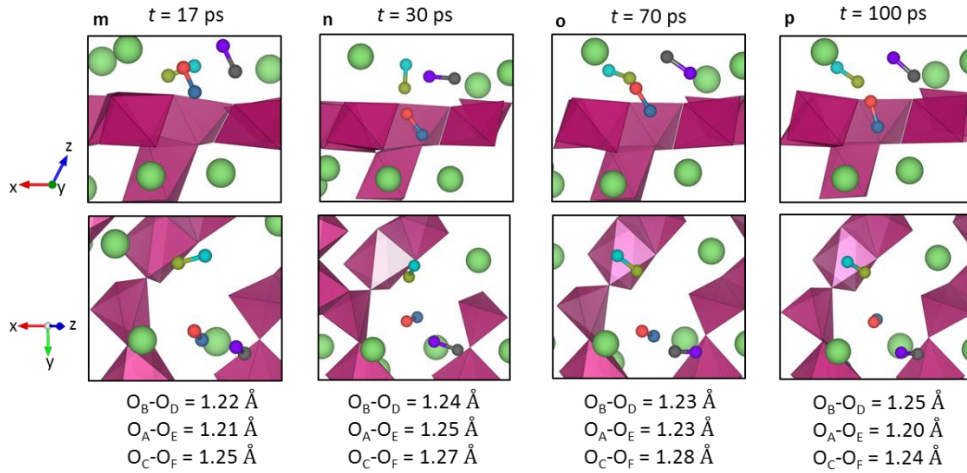


Figure 2.18. Snapshots of *ab initio* MD calculations at 300 K, in which the initial structure describes the state where a floating dimer is produced with $Mn_{Li,octa}$ formation in $Li_{0.5}MnO_3$ (figure 2.17a). Top and bottom panels correspond to views from the side and above, respectively. Large green spheres are Li ions. At the bottom of **a-p**, we presented the length and hapticity of short O-O pairs. η^1 describes an oxygen pair in which one oxygen atom is coordinated with Mn. If denoted by η^2 and μ , both oxygen atoms in O-O pair are coordinated with Mn. η^2 describes a situation where two oxygen atoms are coordinated to the same manganese ion (edge dimer), whereas μ describes a situation where they are coordinated to different manganese ions (bridge dimer). Without specific notation, neither oxygen in O-O pair is coordinated with manganese. Below, we elaborated each step:

a \rightarrow **b** \rightarrow **c** \rightarrow **d**: Translation and rotation of floating dimer.

d \rightarrow **e**: One oxygen of the existing dimer is bonded to other lattice oxygen to form an oxygen trimer.

e → f: Dangling oxygen of the oxygen trimer is bonded to other lattice oxygen to form an oxygen tetramer. This tetramer connects MnO₆ octahedra.

f → g: O-O distances at two ends of the tetramer are shortened, and the length of intermediate O-O bond increases.

g → h: As an extension of the previous step, the tetramer is separated into two dangling dimers. $d(\text{O}_\text{A}-\text{O}_\text{B})$ is 1.81 Å in **h**.

h → i: Two dangling dimers lose their coordination with Mn and become floating dimers.

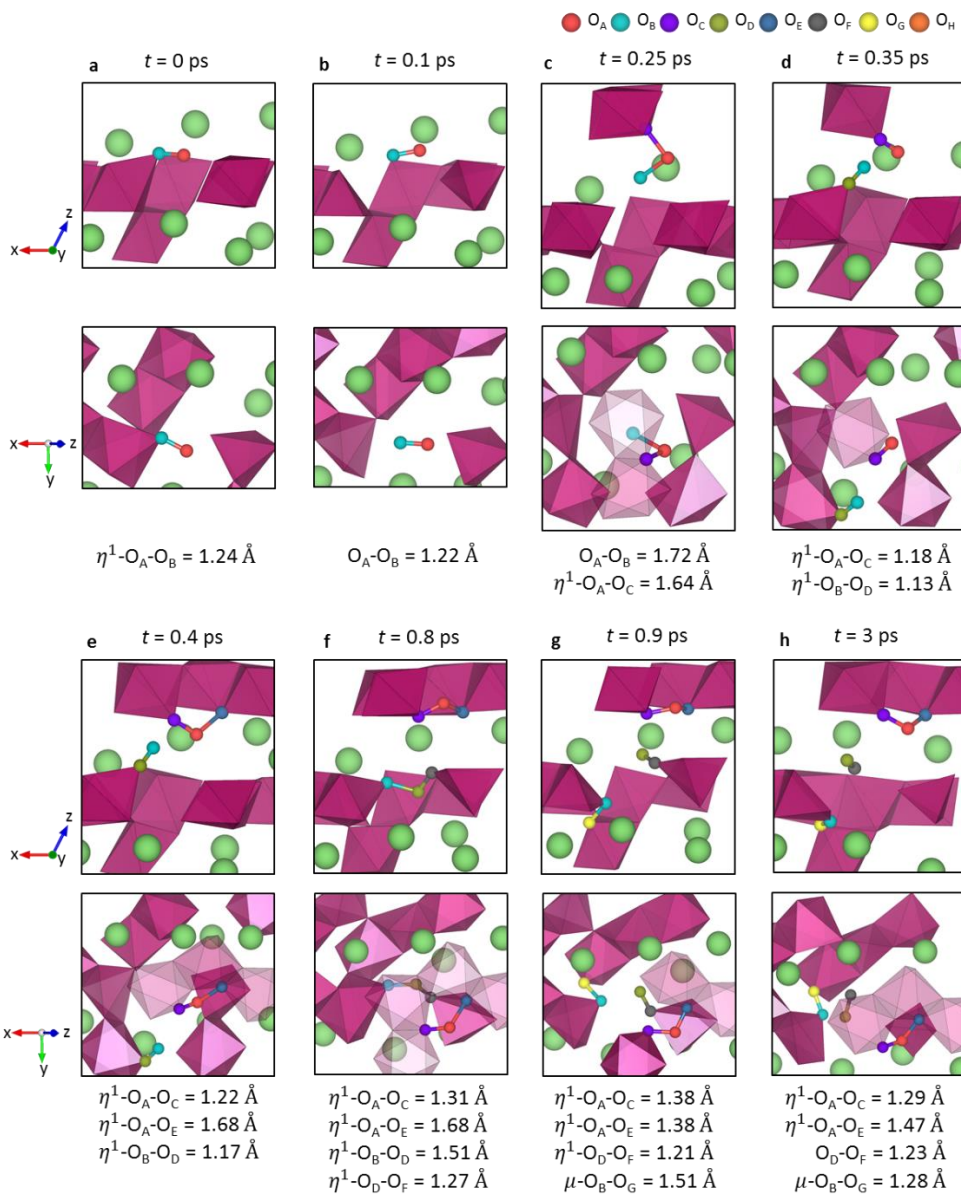
i → j: Translation and rotation of two floating dimers.

j → k: Similar to (**d → f**) process, O_A and O_C each combines with other lattice oxygen atoms to form a new tetramer. This tetramer connects two MnO₆ octahedra.

k → l: Similar to (**f → h**) process, the tetramer is separated into two dangling dimers. As a result, there are two floating dimers and one dangling dimer in **l**.

l → m: All generated dimers become floating dimers.

m → n → o → p: Continuous translation and rotation of floating dimers.



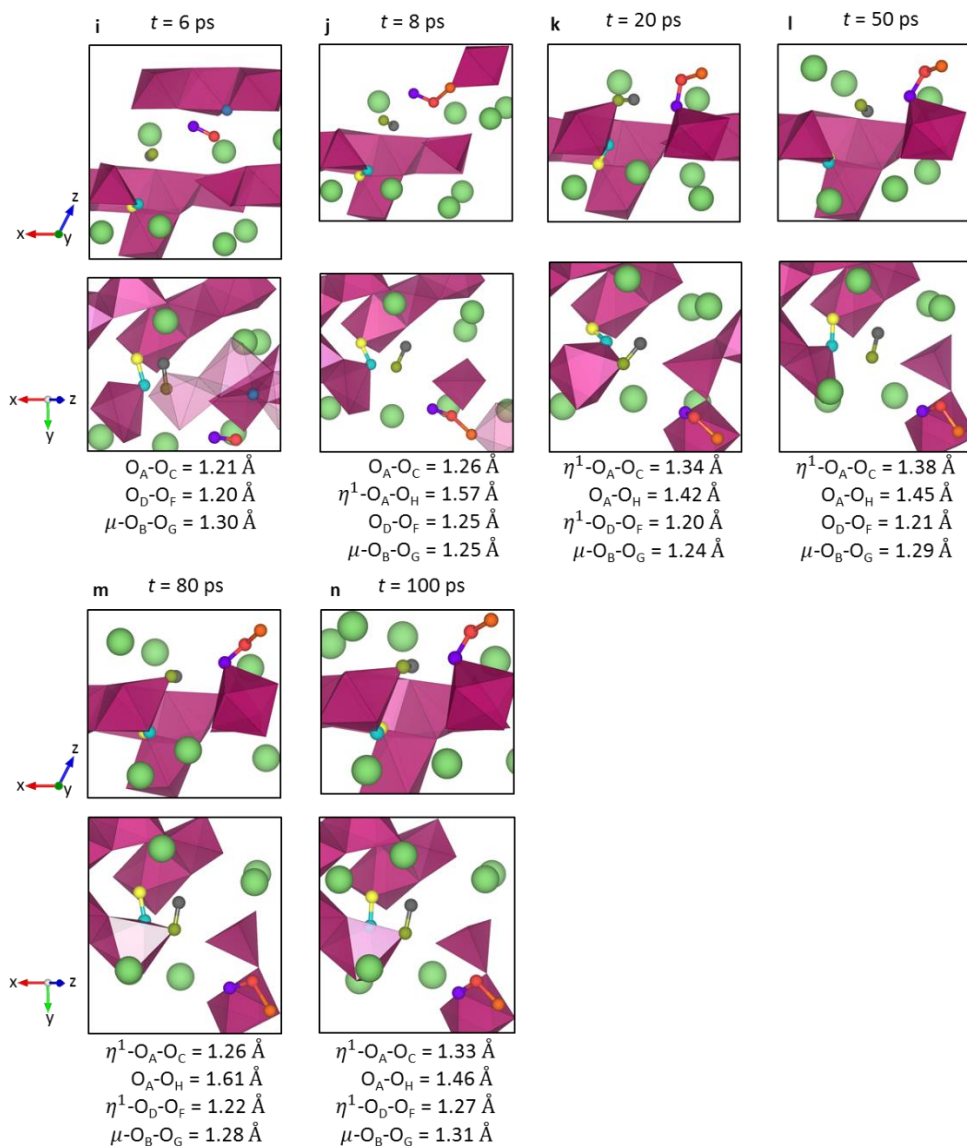


Figure 2.19. Snapshots of *ab initio* MD calculations at 300 K, in which the initial structure describes the state where a dangling dimer is produced with $Mn_{Li,octa}$ formation in $Li_{0.5}MnO_3$ (figure 2.17a). Top and bottom panels correspond to views from the side and above, respectively. Large green spheres are Li ions. At the bottom of **a-n**, we presented the length and hapticity of short O-O pairs. For the meaning of

hapticities, refer to the caption in figure 2.18. Below, we elaborated each step:

a \rightarrow **b**: Dangling dimer is de-coordinated and becomes a floating dimer.

b \rightarrow **c**: One oxygen of the existing dimer is bonded to other lattice oxygen to form an oxygen trimer.

c \rightarrow **d**: The terminal O-O bond of the trimer is cleaved, leaving a dangling dimer. The separated O_B moves to form a new dangling dimer.

d \rightarrow **e**: Through the rotation of $\eta^1-O_A-O_C$, O_A-O_E bond is newly formed.

e \rightarrow **f**: Similar to the previous step, O_D-O_F bond is newly formed through the rotation of $\eta^1-O_B-O_D$.

f \rightarrow **g**: O_B is separated from $\mu-O_B-O_D-O_F$, leaving a dangling O_D-O_F , and moves to form a new bridge dimer, O_B-O_G .

g \rightarrow **h**: O_D-O_F dimer becomes the floating type.

h \rightarrow **i**: O_A-O_E bond is cleaved and O_A-O_C dimer is separated as a floating dimer. O_E stays at its original lattice site.

i \rightarrow **j**: Similar to (**b** \rightarrow **c**) process, one oxygen of O_A-O_C dimer is bonded to other lattice oxygen to form an oxygen trimer, $\eta^1-O_H-O_A-O_C$.

j \rightarrow **k**: Due to the rotation and translation of $O_H-O_A-O_C$ trimer, $Mn-O_H$ bond is cleaved and $Mn-O_C$ bond is newly formed.

k \rightarrow **l** \rightarrow **m** \rightarrow **n**: Continuous vibration of the generated dimers.

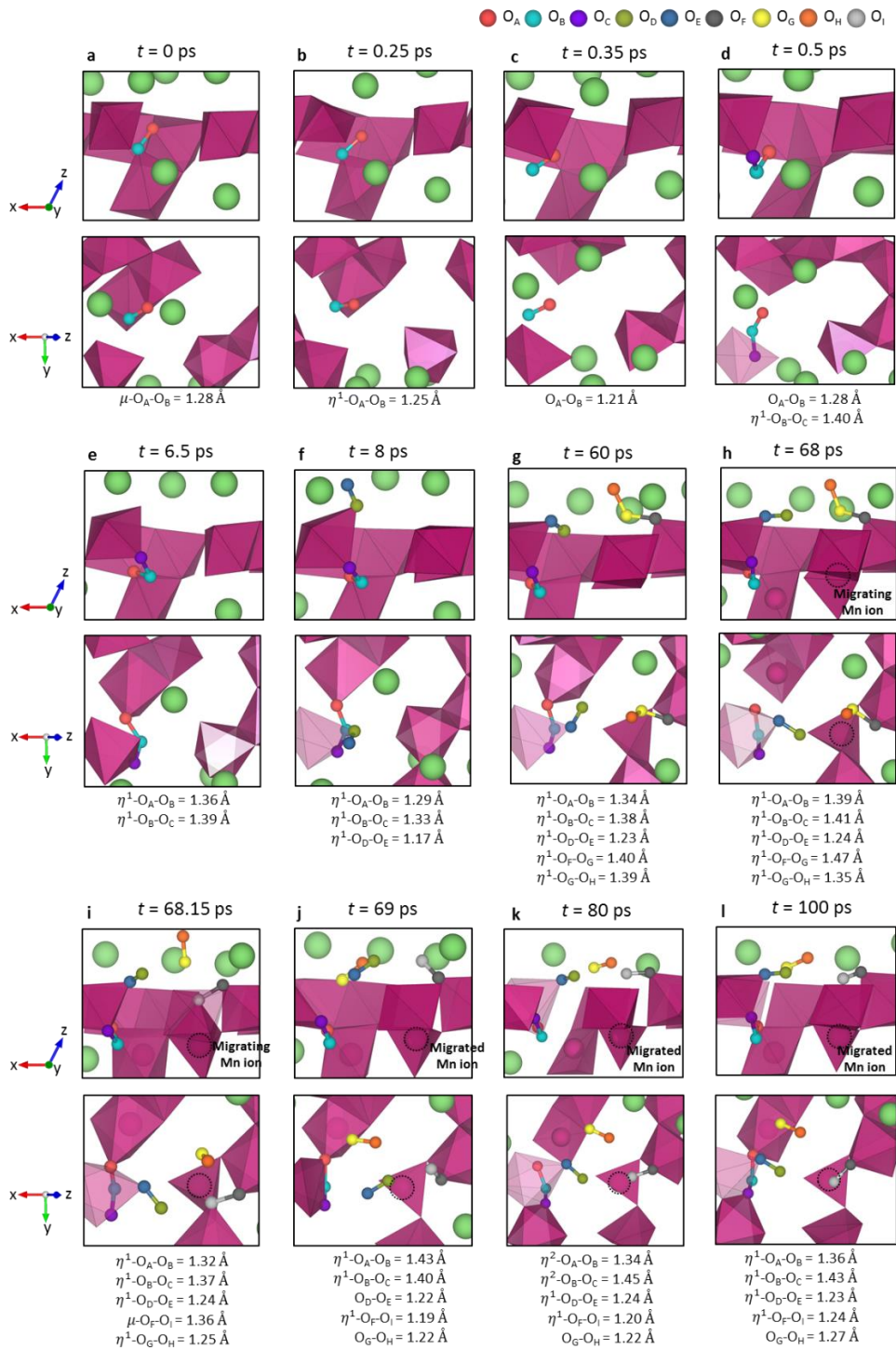


Figure 2.20. Snapshots of *ab initio* MD calculations at 300 K, in which the initial structure describes the state where a bridge dimer is produced with $\text{Mn}_{\text{Li,octa}}$ formation in $\text{Li}_{0.5}\text{MnO}_3$ (figure 2.17b). Top and bottom panels correspond to views from the side and above, respectively. Large green spheres are Li ions. At the bottom of **a-l**, we presented the length and hapticity of short O-O pairs. For the meaning of hapticities, refer to the caption in figure 2.18. Below, we elaborated each step:

a → b: Bridge dimer is partially de-coordinated and becomes a dangling dimer.

b → c: Dangling dimer is de-coordinated and becomes a floating dimer.

c → d: One oxygen of the existing dimer is bonded to other lattice oxygen to form an oxygen trimer.

d → e: The terminal oxygen of the existing dangling trimer is bonded to Mn to form a bridge trimer.

e → f: Another dangling oxygen (O_D) attracts oxygen from the upper TM slab (not shown) to form a dangling dimer, $\text{O}_\text{D}-\text{O}_\text{E}$.

f → g: Another dangling oxygen (O_F) in the supercell forms an oxygen trimer with O_G in the same TM slab and O_H that was in the upper TM slab. In this process, manganese ion, which lose its bond with O_G , slightly moves downward (-z direction).

g → h: Manganese ion, which slightly migrated in the previous step (denoted with dashed circle), moves closer to the Li layer. It can be seen as an intermediate process in which manganese ion migrates to the lithium tetrahedral site.

h → i: Manganese ion, which migrated in the previous steps, migrates a little further.

In the meantime, O_F is separated from $\mu-O_F-O_G-O_H$, leaving a dangling O_G-O_H , and moves to form a new bridge dimer, O_F-O_I .

i → j: Manganese ion that has been moving settles at the lithium tetrahedral site.

Meanwhile, the coordination of dimers changes continuously.

j → k → l: Continuous translation and rotation of the generated dimers.

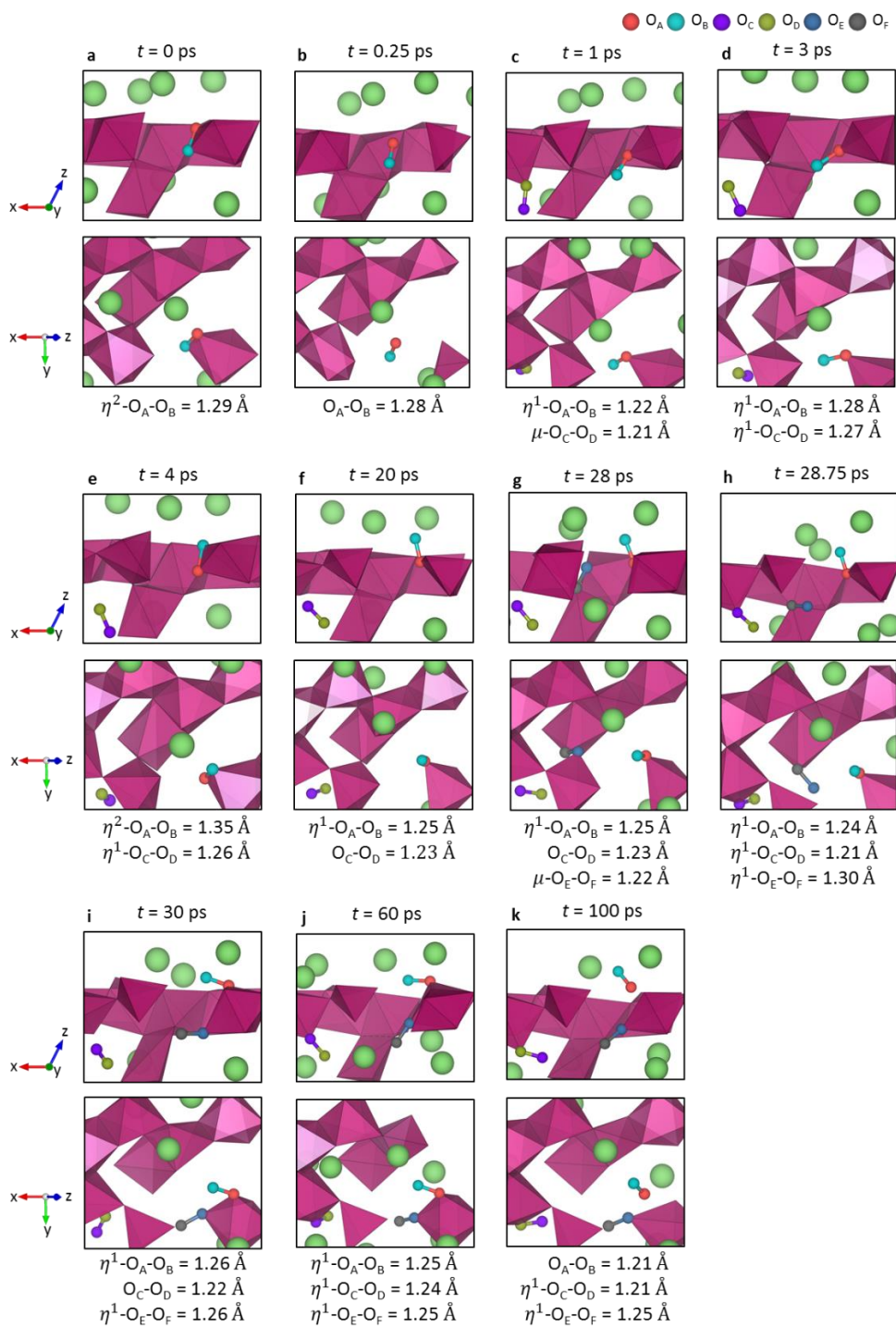


Figure 2.21. Snapshots of *ab initio* MD calculations at 300 K, in which the initial

structure describes the state where an edge dimer is produced with $\text{Mn}_{\text{Li,octa}}$ formation in $\text{Li}_{0.5}\text{MnO}_3$ (figure 2.17c). Top and bottom panels correspond to views from the side and above, respectively. Large green spheres are Li ions. At the bottom of **a-k**, we presented the length and hapticity of short O-O pairs. For the meaning of hapticities, refer to the caption in figure 2.18. Below, we elaborated each step:

a → b: Edge dimer is fully de-coordinated and becomes a floating dimer.

b → c: The existing floating dimer moves slightly to become a dangling dimer. In the meantime, a new bridge dimer ($\text{O}_\text{C}-\text{O}_\text{D}$) is spontaneously generated through the drastic distortion of MnO_6 octahedra.

c → d: $\text{O}_\text{A}-\text{O}_\text{B}$ dimer rotates around O_A . $\text{O}_\text{C}-\text{O}_\text{D}$ dimer is partially de-coordinated and becomes a dangling dimer.

d → e: $\text{O}_\text{A}-\text{O}_\text{B}$ dimer rotates further to restore the original MnO_6 octahedra. However, compared to **a**, the positions of O_A and O_B are exchanged.

e → f: $\text{O}_\text{A}-\text{O}_\text{B}$ dimer moves upward (+z direction) and becomes a dangling dimer. And $\text{O}_\text{C}-\text{O}_\text{D}$ dimer is fully de-coordinated.

f → g: Another dangling oxygen (O_E) in the supercell forms a bridge dimer with O_F that is coordinated with $\text{Mn}_{\text{Li, octa}}$.

g → h: $\text{O}_\text{E}-\text{O}_\text{F}$ dimer rotates to become a dangling dimer.

h → i: $\text{O}_\text{E}-\text{O}_\text{F}$ dimer migrates, and then is coordinated to the same manganese ion as $\text{O}_\text{A}-\text{O}_\text{B}$ dimer. This process will make it difficult for O_E and O_F to return to their

original positions.

$\mathbf{i} \rightarrow \mathbf{j} \rightarrow \mathbf{k}$: Continuous translation and rotation of the generated dimers.

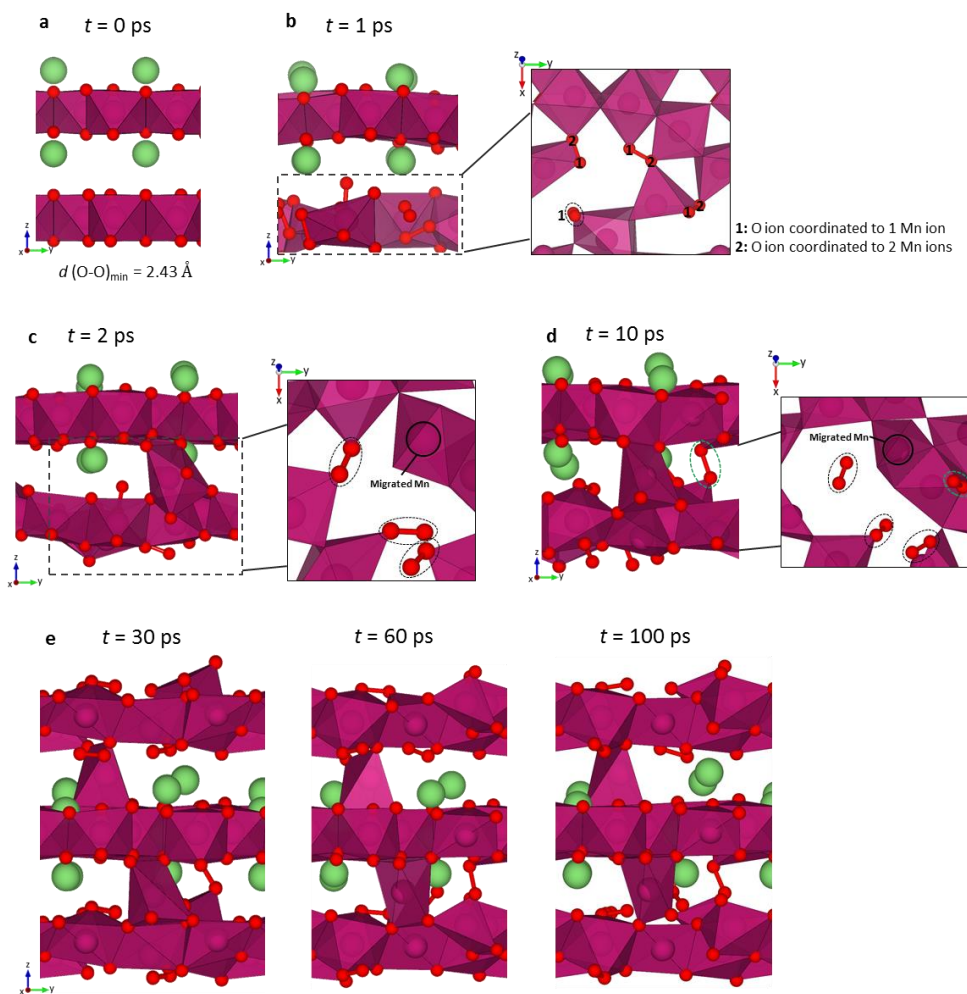


Figure 2.22. Snapshots of *ab initio* MD calculations at 300 K, in which the initial structure is $\text{Li}_{0.5}\text{MnO}_3$ without any structural disorder. Even when the cation disorder was not imposed in the initial state, Mn migration and oxygen dimerization occurred spontaneously during the simulations. Large green spheres are Li ions. Below, we elaborated each step:

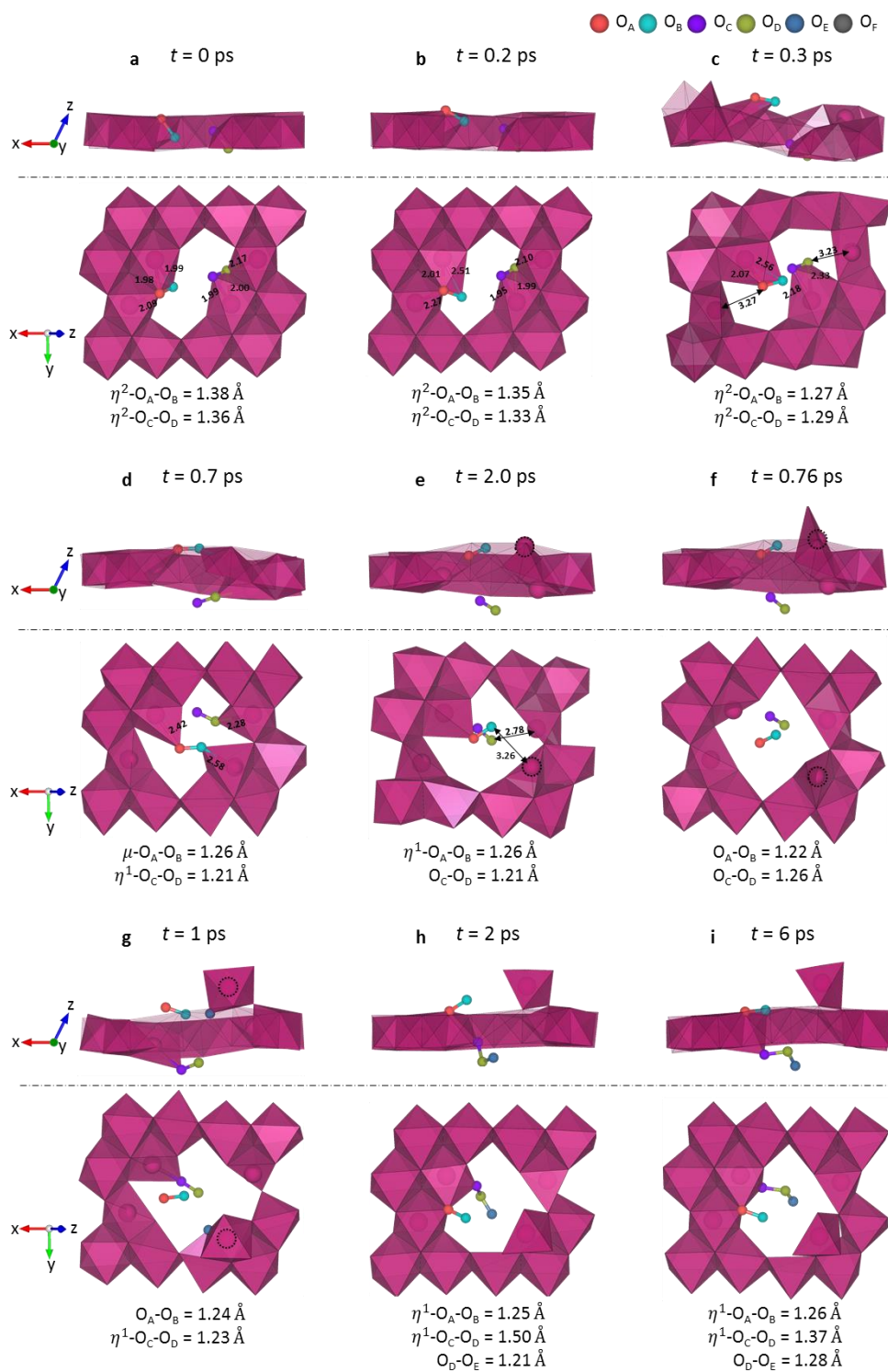
a \rightarrow b: In the absence of apparent cation migration, a significant number of Mn-O bonds are cleaved through the drastic distortion of MnO_6 octahedra. In this process,

dangling oxygen ions are generated, and they form short oxygen dimers. In **b**, we marked the Mn coordination number of oxygen atoms forming oxygen dimer.

b \rightarrow **c**: Manganese ion naturally migrates to the Li layer during *ab initio* MD simulations. From this, additional oxygen dimers are derived (dashed oval). This result indicates that Mn migration is very spontaneous in $\text{Li}_{0.5}\text{MnO}_3$.

c \rightarrow **d**: Oxygen atoms in different TM slabs come close to each other to form a dimer (green dashed oval). Manganese ions coordinating with these oxygen atoms move closer to the Li layer.

d \rightarrow **e**: Spontaneous out-of-plane Mn migration is also observed in the other Li layer. As a result, there are a large number of oxygen dimers in the supercell.



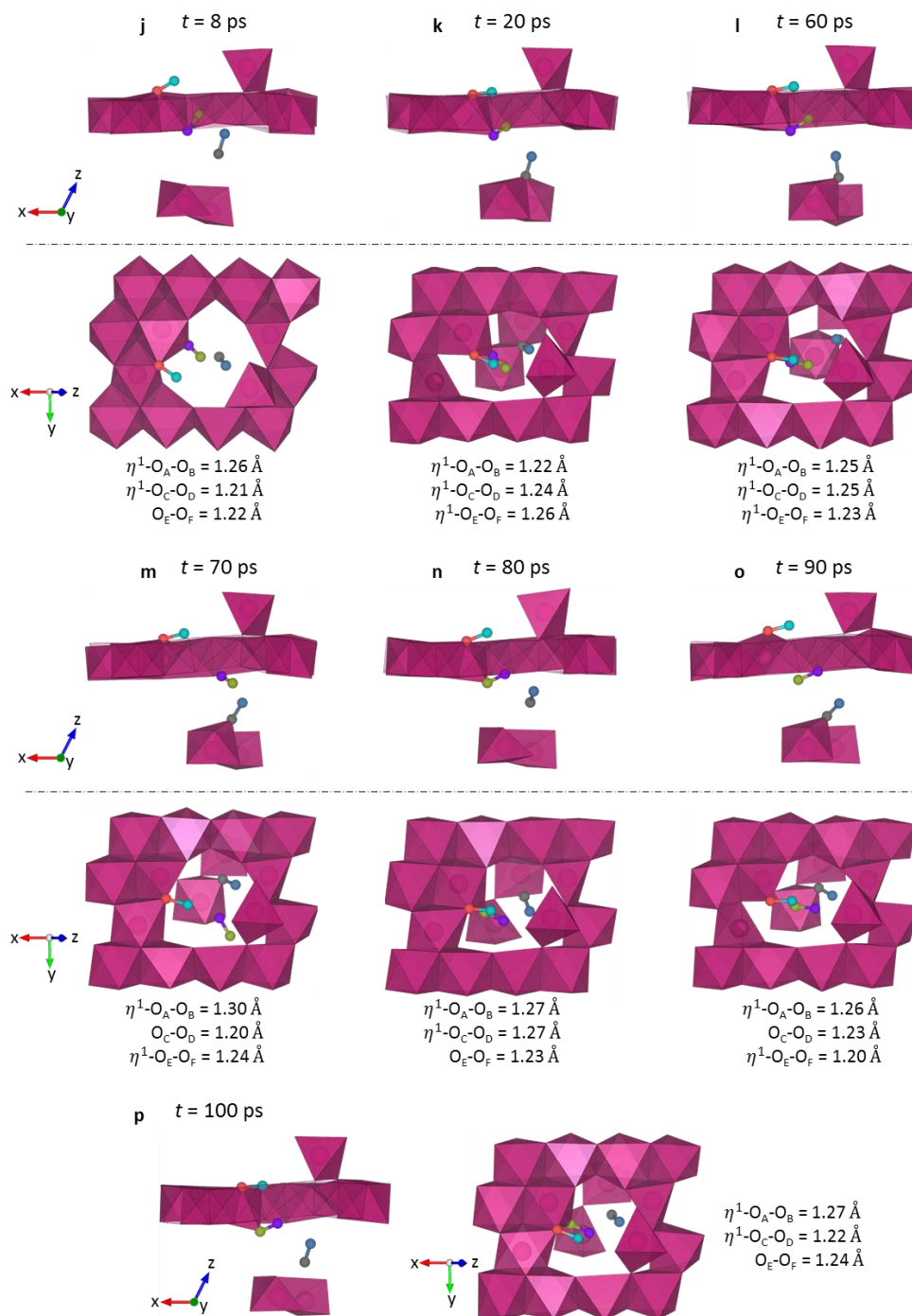


Figure 2.23. Snapshots of *ab initio* MD calculations at 300 K, in which the initial

structure describes the state where manganese ion is migrated along path A in $\text{Na}_0[\text{Li}_0\text{Mn}_{0.8}]\text{O}_2$ (figure 2.1c). Two edge dimers exist in this initial structure. Top and bottom panels correspond to views from the side and above, respectively. At the bottom of **a-p**, we presented the length and hapticity of short O-O pairs. For the meaning of hapticities, refer to the caption in figure 2.18. Below, we elaborated each step:

a → b: Due to the thermal vibrations of two edge dimers, Mn-O distances become slightly longer.

b → c: As an extension of the previous step, both dimers lose one Mn coordination each.

c → d: $\text{O}_\text{A}-\text{O}_\text{B}$ becomes a bridge dimer, and $\text{O}_\text{C}-\text{O}_\text{D}$ becomes a dangling dimer.

d → e: $\text{O}_\text{A}-\text{O}_\text{B}$ becomes a dangling dimer. $\text{O}_\text{C}-\text{O}_\text{D}$ is fully de-coordinated and moves to the Na layer. Manganese ion which lost two oxygen coordination in this process are slightly shifted upward (+z direction, dashed circle).

e → f: Manganese ion which moved in the previous step migrates further, forming a weak covalent bond with manganese ion in the upper TM slab. In the meantime, $\text{O}_\text{A}-\text{O}_\text{B}$ becomes a floating dimer.

f → g: Manganese ion which migrated in previous steps settles at the octahedral site. Although the initial structure was P3-type stacking, the local oxygen arrangement around this octahedral site is close to the “O” type. Thus, it can be said that some stacking faults are generated to allow Mn migration. In the meantime, $\text{O}_\text{C}-\text{O}_\text{D}$

becomes a dangling dimer.

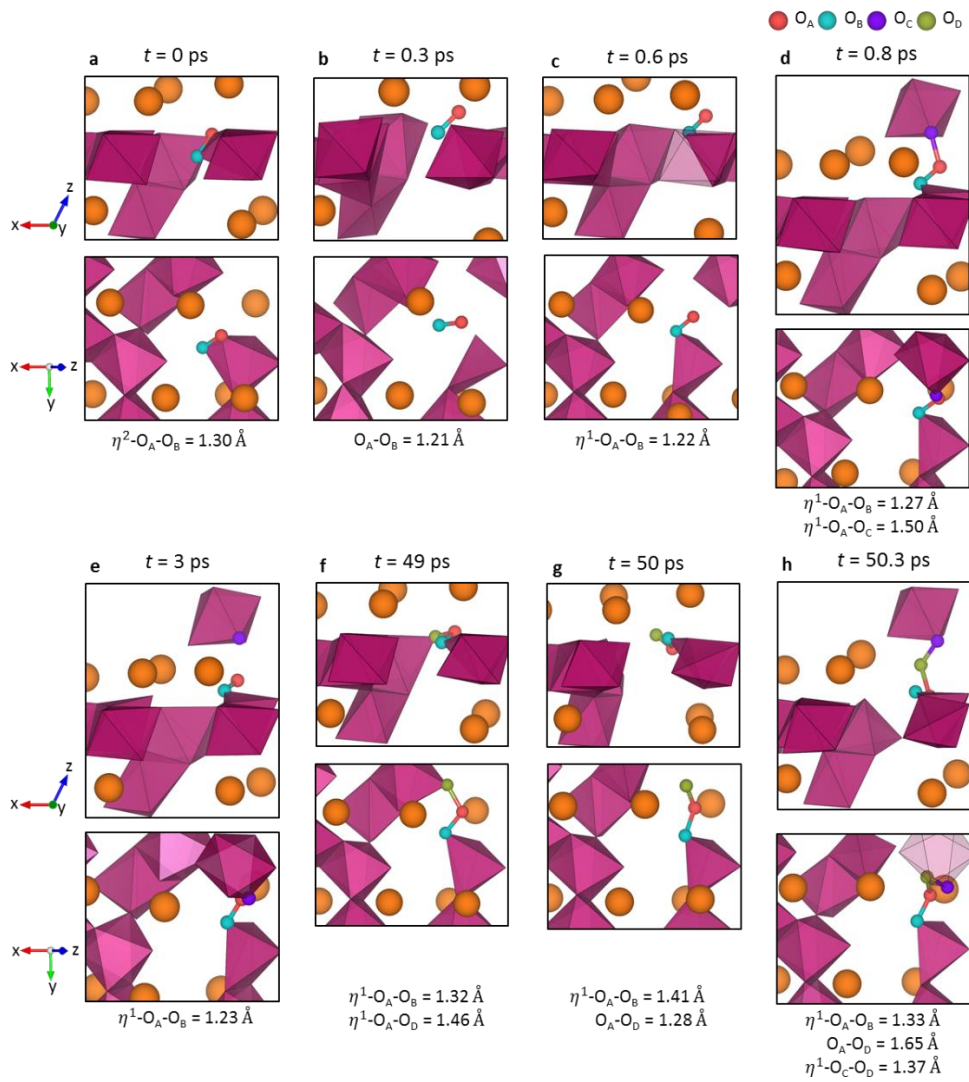
g → h: Dangling O_C-O_D attracts O_E to form a dangling trimer.

h → i: The dangling trimer rotates.

i → j: The terminal O-O bond of the trimer is cleaved, leaving a dangling dimer. The separated O_E forms a new floating dimer with O_F that was in the lower TM slab.

j → k: Floating O_E-O_F migrates to form a Mn-O bond with the lower TM slab. Since O_E and O_F have passed both TM and Na layers, it will be very difficult for them to return to their original positions.

k → l → m → n → o → p: As the generated dimers move continuously, their Mn coordination states also change continuously. This process will make it difficult for oxygen atoms to return to their original positions.



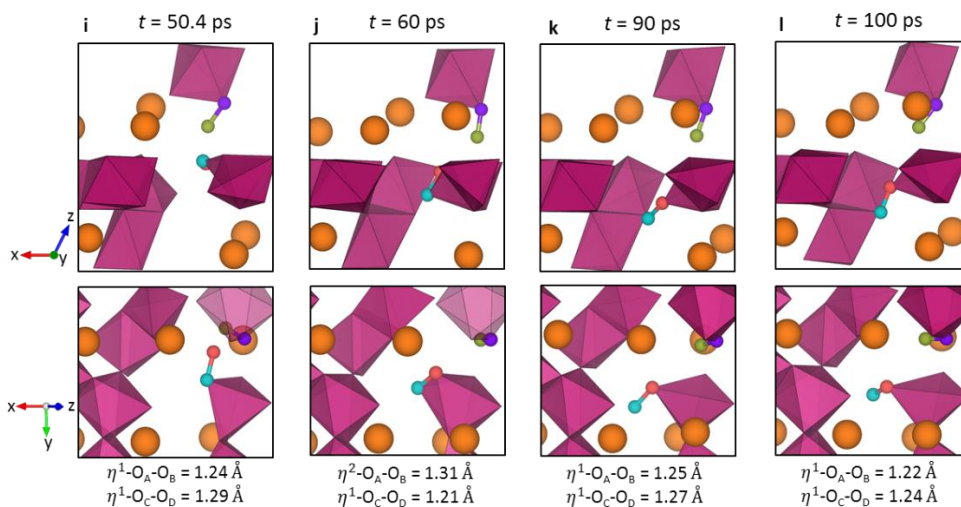


Figure 2.24. Snapshots of *ab initio* MD calculations at 300 K, in which the initial structure describes the state where an edge dimer is produced with $\text{Mn}_{\text{Li,octa}}$ formation in $\text{Na}_0[\text{Mg}_{1/3}\text{Mn}_{2/3}]\text{O}_2$ (figure 2.1b). Top and bottom panels correspond to views from the side and above, respectively. Large orange spheres are Mg ions. At the bottom of **a-l**, we presented the length and hapticity of short O-O pairs. For the meaning of hapticities, refer to the caption in figure 2.18. Below, we elaborated each step:

a \rightarrow **b**: Edge dimer is fully de-coordinated and becomes a floating dimer.

b \rightarrow **c**: One oxygen of the floating dimer is coordinated with Mn.

c \rightarrow **d**: The terminal oxygen of the existing dangling dimer forms a covalent bond with O_C in the upper TM slab.

d \rightarrow **e**: $\text{O}_\text{A}-\text{O}_\text{C}$ bond is cleaved again, leaving a dangling dimer. O_C stays at its original site.

e \rightarrow **f**: $\text{O}_\text{A}-\text{O}_\text{B}$ dangling dimer rotates to form $\text{O}_\text{A}-\text{O}_\text{D}$ bond, producing a bridge trimer.

f → g: Mn-O_D bond is cleaved, and the trimer becomes the dangling type.

g → h: The terminal oxygen of the dangling trimer forms a covalent bond with O_C in the upper TM slab, producing an oxygen tetramer.

h → i: The tetramer is divided into two dangling dimers. Those oxygen atoms will be very difficult to return to their original positions.

i → j → k → l: Continuous translation and rotation of the generated dimers.

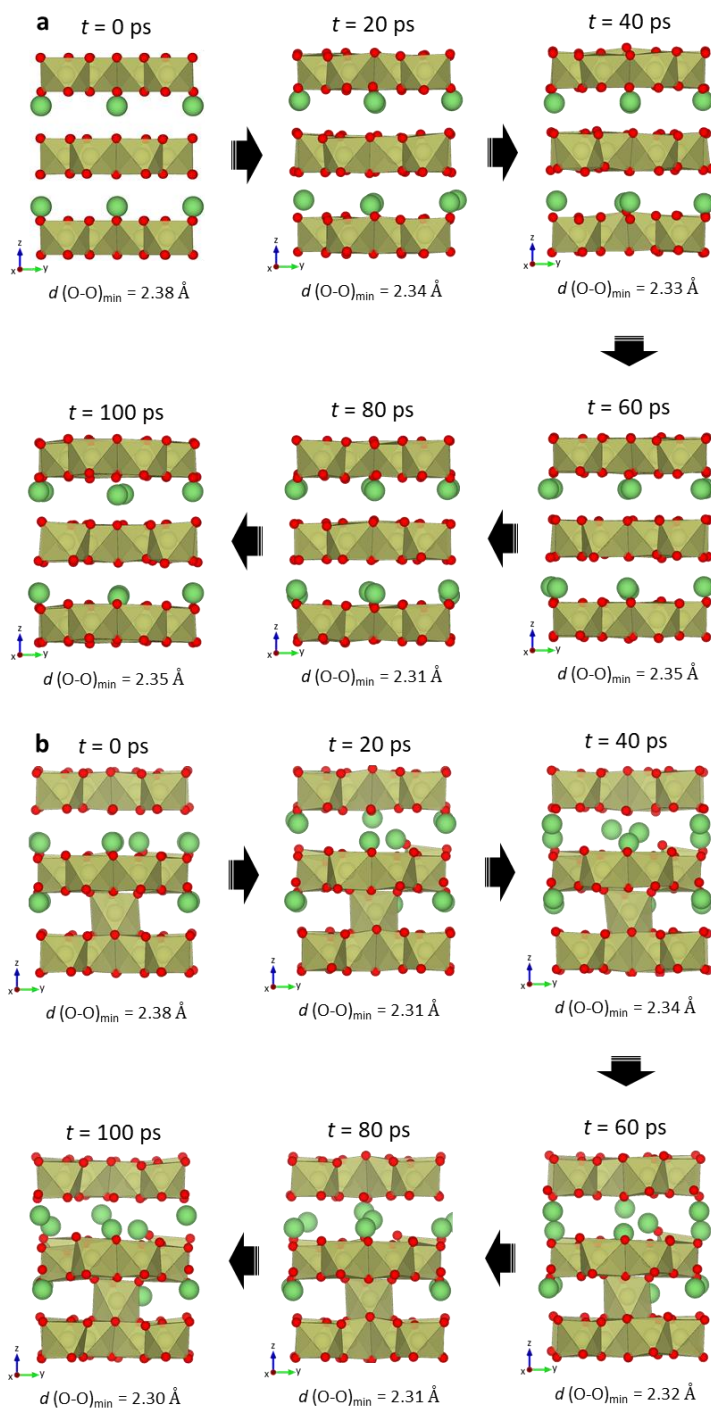


Figure 2.25. Snapshots of *ab initio* MD calculations at 300 K, in which the initial

structure is $\text{Li}_{0.5}\text{IrO}_3$ without any structural disorder (**a**), and $\text{Li}_{0.5}\text{IrO}_3$ with $\text{Ir}_{\text{Li, octa}}$ disorder (**b**). In both cases, the overall structure is well maintained during the simulation time. The lengths of the Ir-O and O-O bonds do not change significantly, and the minimum O-O distance in the supercell is well maintained in the range of $2.30 \sim 2.40 \text{ \AA}$. This means that even in the presence of cation disorder, the structure can be well maintained if short oxygen dimer is absent. Large green spheres are Li ions.

2.3.4 Anionic disorder and oxygen redox chemistry

We further investigated the effect of the anionic disorders in the lithium-rich layered oxides on the redox chemistry. As a representative anionic disorder, the presence of the lattice oxygen vacancy (V_O) was first validated. Figure 2.15d presents V_O formation energies ($G_f(V_O)$) of various oxygen-redox electrodes according to h^O at charged states. It is interesting that $G_f(V_O)$ linearly decreases as h^O of electrodes increases, indicating the feasibility of the anionic disorder in the charged electrodes (see Tables 2.11 and 2.12 for energetics of various state of charge). Such inverse relationship implies the efficacy of disordering particularly at charged states of oxygen redox, as systematically demonstrated for $Li_{2-x}MnO_3$ in figure 2.26. In figures 2.27-2.29, we plotted the effect of V_O formation with respect to the local coordinations and electronic structure for $Li_{2-x}MO_3$ ($M=Mn, Ru, \text{ and } Ir$). It reveals that the overall metal coordination does not undergo significant distortions or produce short covalent bonding such as TM-O and O-O bonds with $< 1.7 \text{ \AA}$, which is contrasts to the case of the cation disorders. Instead, V_O formation simply accompanies the reduction in the octahedral symmetry of the adjacent TM ions. Correspondingly, it results in the localized defect states as indicated by grey shaded areas in the figures^{64,65}, while the overall oxygen electronic structure did not alter significantly. Nonetheless, it was noted that the formation of the neutral vacancy contributed to the stabilization of oxygen redox by providing the extra charge held at the site. The charge analyses in Tables 2.13 and 2.14 present that after the onset of oxygen redox in each electrode, the substantial portion of charge left by V_O was

shifted to the oxygen network, effectively lowering the overall h^O in the oxygen redox.

Considering the distinct effects of cation and anion disorders, we examined the mutual interactions of the two disorder types and their cumulative effects on the oxygen redox. The left panel of figure 2.15e plots how the presence of V_O affects the formation of cation disorders in $Li_{0.5}RuO_3$. It clearly discloses that the formation of cation disorders is inhibited to some extent by the presence of V_O in the neighboring environment. While the formation energies of $Ru_{Li, \text{tetra}}$, $Ru_{Li, \text{octa}}$, and $Ru_{Li, \text{TM layer}}$ in the absence of V_O are -0.30 eV, -0.33 eV, and -0.40 eV, respectively, they increase to 0.09 eV, -0.16 eV, and 0.05 eV, respectively. The right panel of the figure depicts that the existence of cation disorder also impedes the anionic disorder, V_O . The presence of $Ru_{Li, \text{tetra}}$, $Ru_{Li, \text{octa}}$, and $Ru_{Li, \text{TM layer}}$ disorders increases the formation energy of V_O from 0.16 eV to 0.55 eV, 0.34 eV, and 0.61 eV, respectively, indicating that cation and anion disorders mutually restrict their formation. It is attributable to the relation that each disorder partly stabilizes the oxidized oxygen, thus lessens the driving force for additional structural disordering.

Given the significant electronic reorganization and structural irreversibility associated with cation disordering, we infer that the oxygen vacancy engineering could be a viable strategy to improve the reversibility of the oxygen redox if a small amount of V_O is strategically doped and effectively prevents the cation disordering and the subsequent formation of dimers. It reconciles some counterintuitive experimental observations that the oxygen-deficient lithium-rich layered oxide

electrodes exhibited better energy retention than the oxygen-stoichiometric counterparts^{13,66}. V_O formation accompanies a slight decrease in the redox capacity, and thus it would be important to consider the trade-off, which warrants further study.

Table 2.11. V_O formation energy of electrodes belonging to charge-transfer systems.

Cation disorder is not considered here.

	Li_2MnO_3	$\text{Li}_{1.5}\text{MnO}_3$	Li_1MnO_3	$\text{Li}_{0.5}\text{MnO}_3$	MnO_3
$G_f(V_O)$ (eV)	+2.95	+0.40	+0.51	-1.47	-2.15
	$\text{Na}_{0.6}[\text{Li}_{0.2}\text{Mn}_{0.8}]\text{O}_2$	$\text{Na}_0[\text{Li}_0\text{Mn}_{0.8}]\text{O}_2$	$\text{Na}_{2/3}[\text{Mg}_{1/3}\text{Mn}_{2/3}]\text{O}_2$		$\text{Na}_0[\text{Mg}_{1/3}\text{Mn}_{2/3}]\text{O}_2$
$G_f(V_O)$ (eV)	+2.40	-0.21	+3.03		-0.83

Table 2.12. V_O formation energy of electrodes belonging to Mott-Hubbard systems.
Cation disorder is not considered here.

$G_f(V_O)$ (eV)	x in $Li_{2-x}MO_3$			
	x = 0	x = 0.5	x = 1.0	x = 1.5
$Li_{2-x}IrO_3$	+3.00	+2.79	+3.01	+1.37
$Li_{2-x}RuO_3$	+3.82	+2.88	+3.26	+0.16
$Li_{2-x}Ru_{0.5}Mn_{0.5}O_3$	+4.20	+3.21	+2.90	-0.20
$Li_{2-x}Ir_{0.5}Sn_{0.5}O_3$	+3.75	.	+2.17	+0.11
$Li_{2-x}Ru_{0.5}Sn_{0.5}O_3$	+3.87	.	+0.35	-0.87
$Li_{2-x}Ni_{0.5}Te_{0.5}O_3$	+3.71	.	+1.01	.

Table 2.13. Bader charge changes involved with V_O formation in charge-transfer systems. The ratio of each change to the total charge difference is presented.

	Li_2MnO_3	$Li_{0.5}MnO_3$	$Na_{0.6}[Li_{0.2}Mn_{0.8}]O_2$	$Na_0[Li_{0.8}Mn_{0.8}]O_2$	$Na_{2/3}[Mg_{1/3}Mn_{2/3}]O_2$	$Na_0[Mg_{1/3}Mn_{2/3}]O_2$
Sum(M)	59.0%	3.4%	29.3%	-7.4%	42.9%	12.6%
Two M ions neighboring V_O	45.2%	-4.4%	39.2%	0.6%	39.5%	-0.5%
Sum(O)	41.0%	96.6%	70.7%	107.4%	57.1%	87.4%
O ion neighboring V_O	5.7%	21.1%	7.3%	8.3%	6.8%	14.9%

Table 2.14. Bader charge changes involved with V_O formation in Mott-Hubbard systems. The ratio of each change to the total charge difference is presented.

	$Li_2Ni_{0.5}Te_{0.5}O_3$	$Li_1Ni_{0.5}Te_{0.5}O_3$	Li_2IrO_3	$Li_{0.5}IrO_3$	Li_2RuO_3	$Li_{0.5}RuO_3$
Sum(M)	Ni: 5.7% Te: 88.3%	Ni: 20.7% Te: 0.0%	88.2%	41.8%	87.5%	27.0%
Two M ions neighboring V_O	Ni: 4.9% Te: 88.3%	Ni: 9.6% Te: 0.0%	81.9%	19.9%	77.6%	2.6%
Sum(O)	6.0%	79.3%	11.8%	58.2%	12.5%	73.0%
O ion neighboring V_O	0.9%	17.1%	-1.4%	10.6%	-1.7%	12.0%
	$Li_2Ir_{0.5}Sn_{0.5}O_3$	$Li_{0.5}Ir_{0.5}Sn_{0.5}O_3$	$Li_2Ru_{0.5}Mn_{0.5}O_3$	$Li_{0.5}Ru_{0.5}Mn_{0.5}O_3$	$Li_2Ru_{0.5}Sn_{0.5}O_3$	$Li_{0.5}Ru_{0.5}Sn_{0.5}O_3$
Sum(M)	91.4%	14.7%	Ru: 33.9% Mn: 14.0%	Ru: -1.3% Mn: 19.6%	Ru: 30.5% Sn: 51.3%	Ru: -32.5% Sn: 0.0%
Two M ions neighboring V_O	Ir: 89.2% Sn: 0.0%	Ir: -1.6% Sn: 0.0%	Ru: 33.3% Mn: 20.3%	Ru: -11.8% Mn: 8.7%	Ru: 32.9% Sn: 51.3%	Ru: 5.5% Sn: 0.0%
Sum(O)	8.6%	85.3%	52.1%	81.7%	18.2%	132.5%
O ion neighboring V_O	-5.4%	0.9%	4.9%	11.8%	-0.3%	21.4%

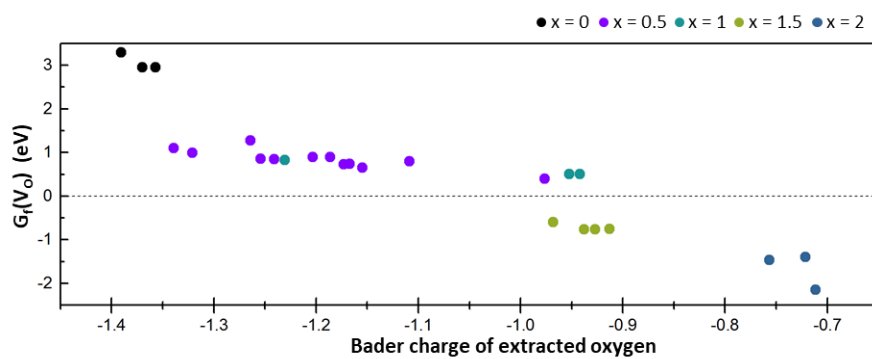


Figure 2.26. The relation between bader charge of extracted oxygen and $G_f(V_o)$ in $Li_{2-x}MnO_3$. Bader charge values, plotted on the x-axis, represent the electron gain of each oxygen compared to the neutral oxygen atom.

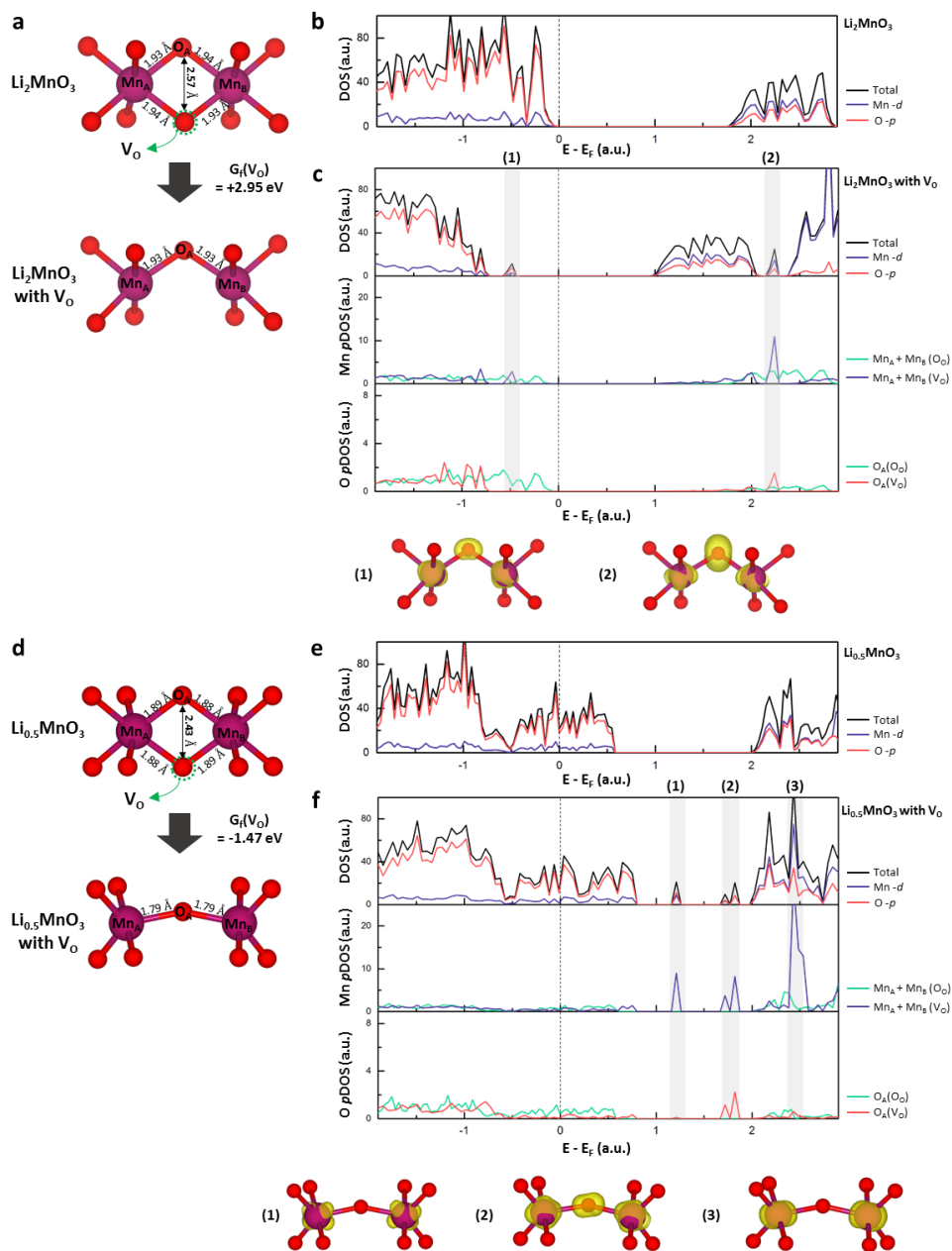


Figure 2.27. **a, c**, Local structure changes involved with V_O formation in Li_2MnO_3 (**a**) and $\text{Li}_{0.5}\text{MnO}_3$ (**d**). **b, e**, DOS of Li_2MnO_3 (**b**) and $\text{Li}_{0.5}\text{MnO}_3$ (**e**) without any structural disorder. **c, f**, Changes in electronic structure involved with V_O formation

in Li_2MnO_3 (**c**) and $\text{Li}_{0.5}\text{MnO}_3$ (**f**). The uppermost panel is total DOS of the structure with V_O , and the center and bottom panels show Mn p DOS and O p DOS before (O_O) and after (V_O) oxygen vacancy formation. Grey shaded areas indicate the defect states resulting from V_O formation. The charge density plots of these defect states are presented at the bottom.

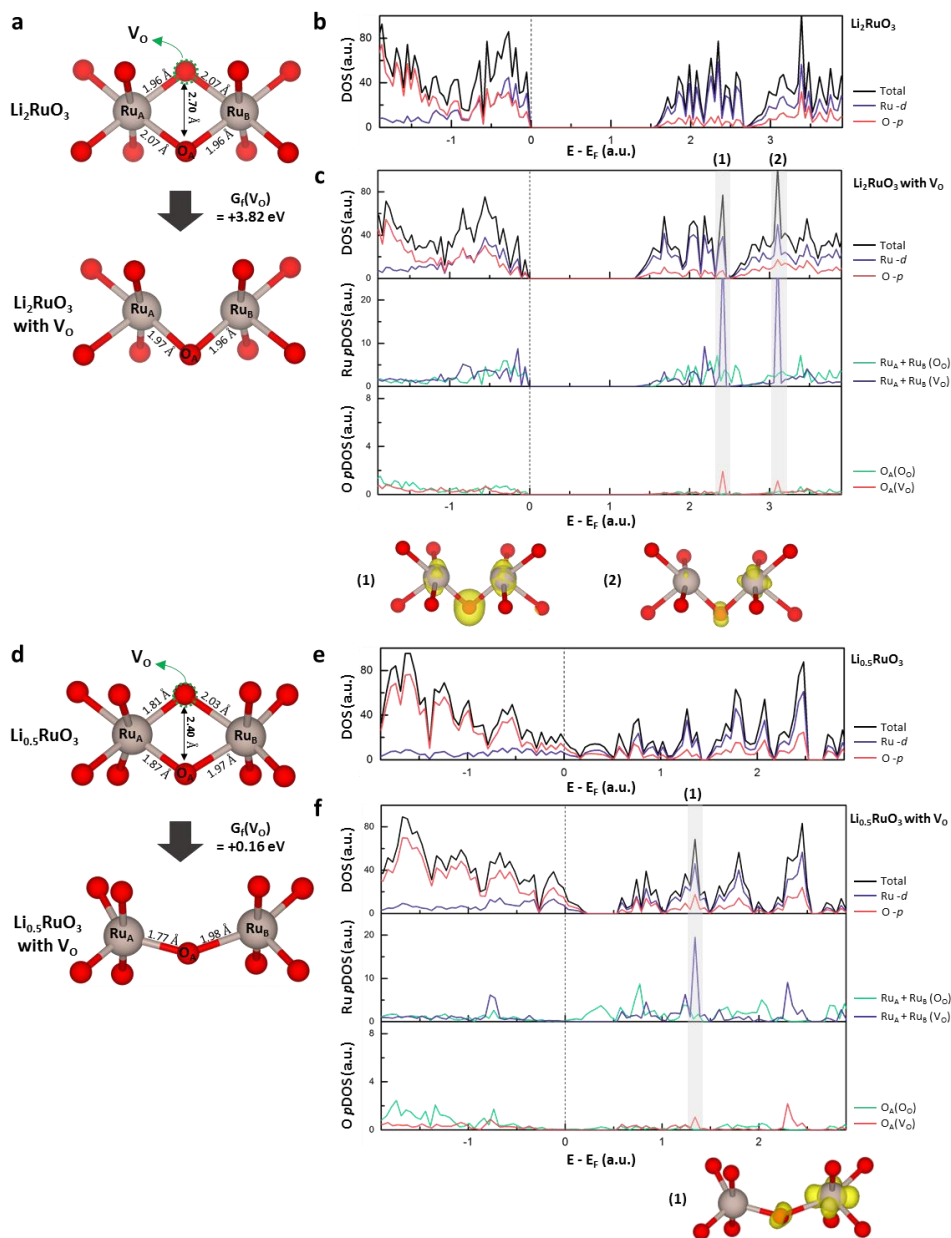


Figure 2.28. **a, c**, Local structure changes involved with V_O formation in Li_2RuO_3 (**a**) and $\text{Li}_{0.5}\text{RuO}_3$ (**d**). **b, e**, DOS of Li_2RuO_3 (**b**) and $\text{Li}_{0.5}\text{RuO}_3$ (**e**) without any structural disorder. **c, f**, Changes in electronic structure involved with V_O formation in Li_2RuO_3 (**c**) and $\text{Li}_{0.5}\text{RuO}_3$ (**f**). The uppermost panel is total DOS of the structure

with V_O , and the center and bottom panels show Ru p DOS and O p DOS before (O_O) and after (V_O) oxygen vacancy formation. Grey shaded areas indicate the defect states resulting from V_O formation. The charge density plots of these defect states are presented at the bottom.

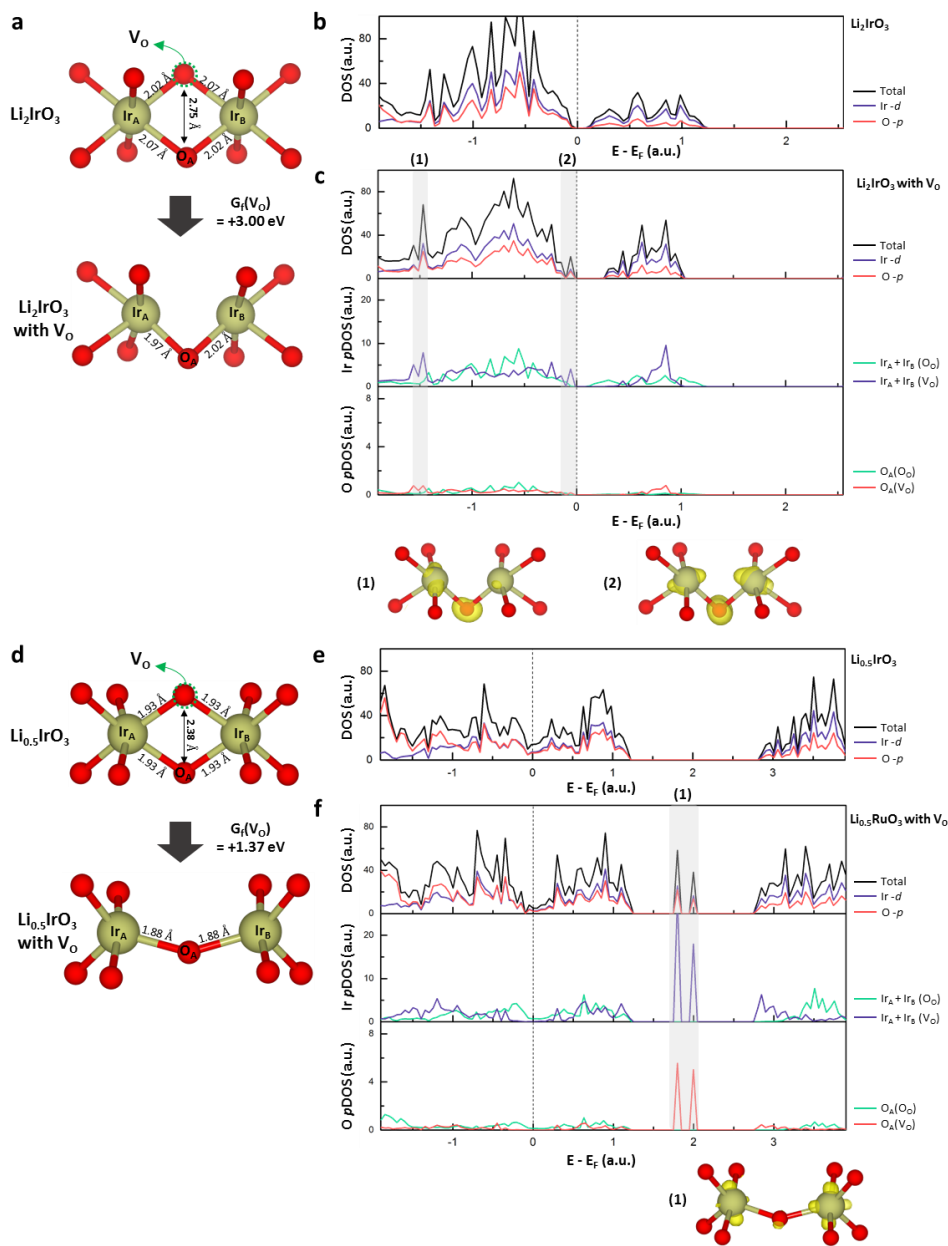


Figure 2.29. a, c, Local structure changes involved with V_O formation in Li_2IrO_3 (a) and $\text{Li}_{0.5}\text{IrO}_3$ (d). b, e, DOS of Li_2IrO_3 (b) and $\text{Li}_{0.5}\text{IrO}_3$ (e) without any structural disorder. c, f, Changes in electronic structure involved with V_O formation in Li_2IrO_3 (c) and $\text{Li}_{0.5}\text{IrO}_3$ (f). The uppermost panel is total DOS of the structure with V_O , and

the center and bottom panels show Ir p DOS and O p DOS before (O_o) and after (V_o) oxygen vacancy formation. Grey shaded areas indicate the defect states resulting from V_o formation. The charge density plots of these defect states are presented at the bottom.

2.3.5 Theoretical voltage profiles considering structural disorder

In figure 2.30a, we propose the types of voltage profiles for charge-transfer and Mott-Hubbard lithium-rich layered electrodes, when taking into account of various structural disorders and their effects on the redox mechanism. In the simple cationic redox materials with no structural disorder (*e.g.*, Li_2IrO_3 and $\text{Li}_2\text{Ni}_{0.5}\text{Te}_{0.5}\text{O}_3$), the charge and discharge profiles are similar with a small voltage hysteresis (I in figure 2.30a)^{14,55,62}, while there is no gain in the energy density from the oxygen redox. On the other hand, when the oxygen redox occurs to some extent during the charge process (II in figure 2.30a), as in the case of Mott-Hubbard Li_2RuO_3 , the degeneracy of the oxygen lattice is lifted due to cation migrations at the end of the charge (point C2 in II), and the discharge profile becomes significantly altered. Since the cation disordering is only partially reversible, the structure of the discharged state (D2 in II) is distinct from the pristine structure, from which a voltage hysteresis arises. When the oxygen redox is further utilized with higher h^{O} in Mott-Hubbard electrodes, such as $\text{Li}_{0.5}\text{Ru}_{0.5}\text{Mn}_{0.5}\text{O}_3$ and $\text{Li}_{0.5}\text{Ru}_{0.5}\text{Sn}_{0.5}\text{O}_3$, the V_{O} formation and oxygen dimerization are sequentially promoted and combined with cation disordering (III in figure 2.30a). Therefore, the structural irreversibility is further accelerated and the voltage hysteresis is supposed to be intensified. In charge-transfer electrode systems (IV), the cation and anion disordering are highly spontaneous with depopulated O $2p$ NB states, such as $\text{Li}_{0.5}\text{MnO}_3$, and the formation of the short oxygen dimers is easily accelerated. In this case, the structural integrity becomes extremely vulnerable, and the energy density rapidly fades with cycling.

It is worthy of mentioning that some of the charge-transfer electrodes can manage to mitigate the formation of structural disorders during the initial cycles, suppressing the voltage depression. According to the literature, it was partially achieved in electrodes with P-type stacking such as $\text{Na}_{0.6}[\text{Li}_{0.2}\text{Mn}_{0.8}]\text{O}_2$ and $\text{Na}_2\text{Mn}_3\text{O}_7$ by imposing structural constraints on out-of-plane cation migrations (figure 2.30b)^{41,67}. Since large prismatic sites are typically unoccupiable by TM ion, the out-of-plane cation migrations were projected to be prohibited. Moreover, the unique ribbon-type or mesh-type TM orderings in TM layer were supposed to delay the in-plane TM migrations^{10,67}, as demonstrated in figure 2.1c (path B), successfully suppressing the voltage fades during the first few cycles of these electrodes (point C5)^{50,67,68}. Nonetheless, the in-plane cation migrations were eventually observed in these electrodes after prolonged cycling, (C5' in the figure)^{10,68}. Our calculations also verified that those cation disorders should be ultimately formed due to thermodynamic energy gain, and trigger the oxygen dimerization (figure 2.6), canceling out the structural merits offered by the P-type stacking. It suggests that it would be necessary to explore alternative oxygen stabilization mechanisms that can persist over long cycles for achieving the reversible oxygen utilization.

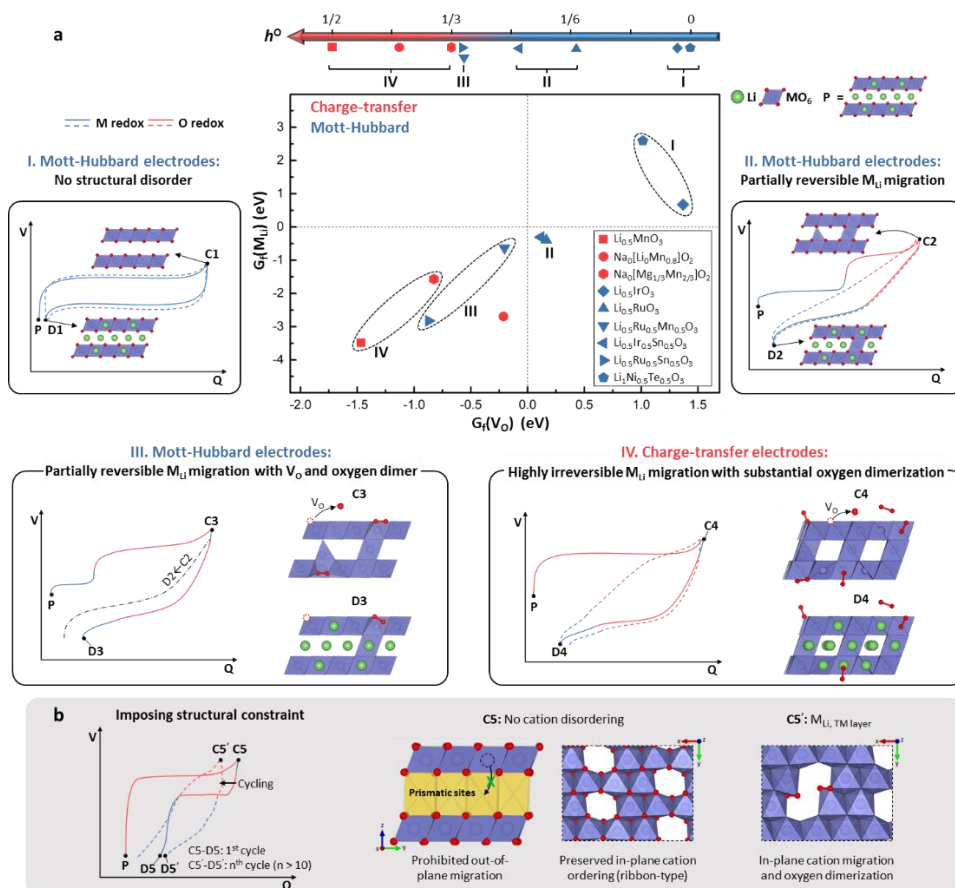
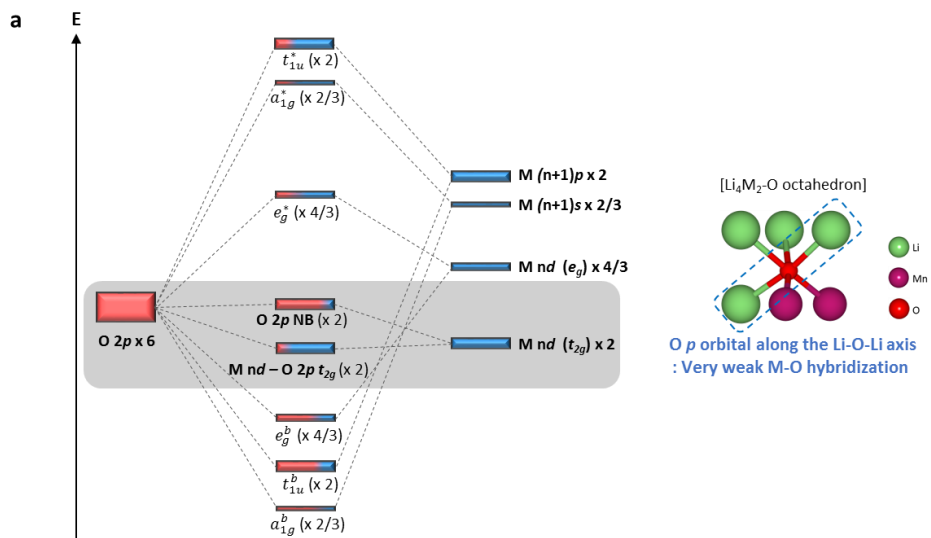


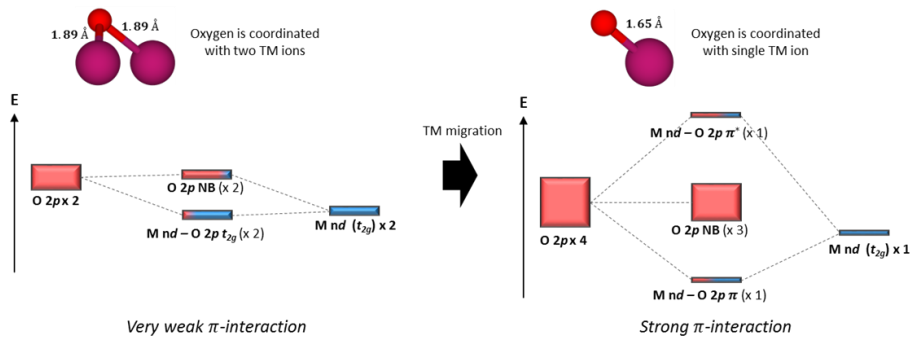
Figure 2.30. Voltage profiles considering structural disorders. **a**, (center) Calculated disorder formation energies, where $G_f(M_{Li})$ corresponds to the lowest value among $G_f(M_{Li, tetra})$, $G_f(M_{Li, octa})$, and $G_f(M_{Li, TM \text{ layer}})$. If a compound has two metal components, the migration of both metals is considered. Red and blue symbols correspond to charge-transfer systems and Mott-Hubbard systems, respectively. In I-IV, schematic illustrations of expected voltage profiles considering structural disorders are presented. **b**, Influence of structural constraints on voltage profiles. In **a** and **b**, P, C, and D correspond to the pristine, fully charged, and fully discharged state, respectively.

2.3.6 Electronic structure of electrodes

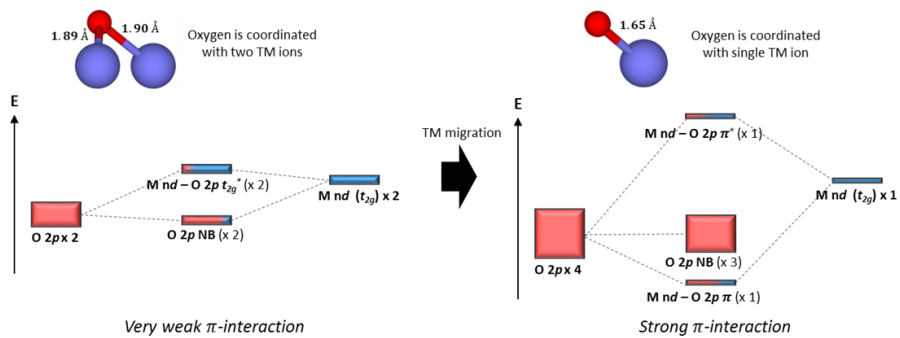
Figure 2.31a presents the molecular orbital energy diagram of $\text{Li}_4\text{M}_2\text{-O}$ octahedron, the basic unit of lithium-rich layered oxides. There is no significant $\text{Li(s,p)}/\text{O(s,p)}$ orbital mixing along the Li-O-Li axis, and as a result, non-bonding oxygen ($\text{O } 2p$ NB) states exist in proportion to the number of the Li-O-Li axis². The details of the molecular orbital energy diagram are well described in previous literatures^{69,70}. Of importance in the diagram is the energy of $\text{O } 2p$ NB and $\text{M nd-O } 2p t_{2g}$ states that can participate in redox process (grey shaded region). According to the relative energy of $\text{O } 2p$ NB and $\text{M nd-O } 2p t_{2g}$ states, electrode materials can be divided into charge-transfer systems and Mott-Hubbard systems^{26,71}. In charge-transfer systems, $\text{O } 2p$ NB states are located at the Fermi level, and thus will be immediately depleted upon charging (figure 2.31b). Electrodes such as Li_2MnO_3 , $\text{Na}_{0.6}[\text{Li}_{0.2}\text{Mn}_{0.8}]\text{O}_2$, and $\text{Na}_{2/3}[\text{Mg}_{1/3}\text{Mn}_{2/3}]\text{O}_2$ correspond to this systems, as evidenced in figure 2.2. On the other hand, for Mott-Hubbard systems, $\text{M nd-O } 2p t_{2g}^*$ states lie at the Fermi level (figure 2.31c and 2.8). $\text{O } 2p$ NB states lying below $\text{M nd-O } 2p t_{2g}^*$ states can be depleted in the high-voltage region of the charge⁵², or it can remain fully filled if $\text{M nd-O } 2p t_{2g}^*$ states compensate for the entire charging process¹⁴. The former case corresponds to the conventional charging process of Li_2RuO_3 (figure 2.9a) and $\text{Li}_2\text{Ru}_{0.5}\text{Mn}_{0.5}\text{O}_3$ (figure 2.12a), and the latter includes that of Li_2IrO_3 (figure 2.10a) and $\text{Li}_2\text{Ni}_{0.5}\text{Te}_{0.5}\text{O}_3$ (figure 2.38a).



b ❖ Electron energy: $\text{O } 2p > \text{M } t_{2g}$ (charge-transfer insulators, eg. Li_2MnO_3)



c ❖ Electron energy: $\text{O } 2p < \text{M } t_{2g}$ (Mott-hubbard insulators, eg. Li_2RuO_3)



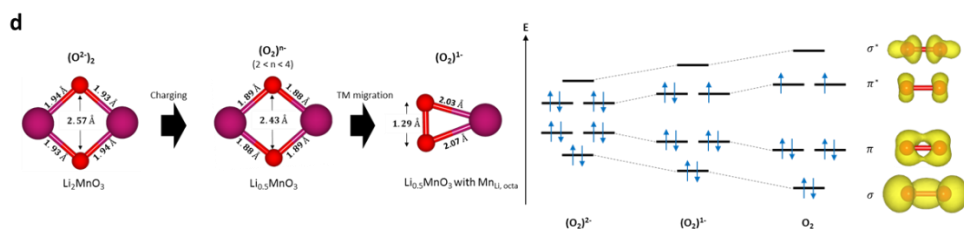


Figure 2.31. a, The molecular orbital energy diagram of $\text{Li}_4\text{M}_2\text{-O}$ octahedron, which constitutes lithium-rich layered oxides Li_2MO_3 . The number of each molecular orbital is normalized per oxygen. Blue and red color in the bars indicates the contribution of metal and oxygen, respectively. Note that each hybridized orbital is labeled according to the labeling of corresponding orbital in conventional layered oxides, LiMO_2 (t_{1u} , a_{1g} , e_g , and t_{2g}). Strictly, the point symmetry of $\text{Li}_4\text{M}_2\text{-O}$ octahedron (C_{2v}) requires a different orbital labeling⁶⁹. **b-c,** Predictions for the electronic reshuffling of TM-O bond involved with cation disordering in charge-transfer systems (**b**) and Mott-Hubbard systems (**c**). **d,** (left) Schematic illustration of O-O dimerization process during the charging and subsequent cation disordering. (right) The transition of the oxygen electronic structure from oxide ion O^{2-} , to peroxide $(\text{O}_2)^{2-}$, superoxide $(\text{O}_2)^{1-}$, and gaseous oxygen O_2 .

2.3.7 Effects of metal-oxygen decoordination on the electronic structure

As explained in the manuscript, cation disordering can lead to strong TM-O hybridization and/or O-O hybridization (figures 2.1 and 2.7). Assuming an electrode with Li-M honeycomb ordering in the TM layer, each oxygen is equally coordinated with two TM ions, as shown in the left of figure 2.31b-c. In this case, considering O $2p$ -M $(n+1)s/(n+1)p/nd\ e_g$ hybridization first, the remaining number of O $2p$ orbitals is equal to that of M $nd\ t_{2g}$ orbitals^{69,72}. O $2p$ orbitals and M $nd\ t_{2g}$ orbitals cannot form σ -type hybridization, but form π -type hybridization^{69,72}. This π -hybridization is typically negligibly weak when TM-O bond is longer than 1.8 Å⁸, so hybridized O $2p$ states and M nd -O $2p\ t_{2g}$ states retain a ‘non-bonding’ characteristic. This is why oxygen state that participated only in very weak π -hybridization is often called ‘unhybridized’, or ‘non-bonding’, or ‘orphaned’ O $2p$ state. Such oxygen state is denoted as O $2p$ NB state in our manuscript.

Meanwhile, if oxygen loses one metal coordination due to cation disordering, the number of metal orbitals that can hybridize with oxygen is halved. It means that the number of O $2p$ orbitals remaining without participating in O $2p$ -M $(n+1)s/(n+1)p/nd\ e_g$ hybridization is doubled, as described in the right of figure 2.31b-c. Whereas the number of M $nd\ t_{2g}$ orbitals is naturally halved. Due to the quantitative imbalance between the remaining O $2p$ orbitals and M $nd\ t_{2g}$ orbitals, some of O $2p$ orbitals will be hardly hybridized with M $nd\ t_{2g}$ orbitals and remain as

nearly complete non-bonding states (O $2p$ NB). Simultaneously, M nd t_{2g} orbitals and the same amount of O $2p$ orbitals will be hybridized to form M nd -O $2p$ π and π^* states. That is, metal-oxygen orbital hybridization of dangling oxygen is likely to generate O $2p$ NB, and M nd -O $2p$ π/π^* states (figure 2.31b-c). The dominance of M and O character in M nd -O $2p$ π/π^* states would be determined by the relative energy of intact O $2p$ and M nd t_{2g} orbitals. We note that the splitting to those three states is independent of the length of the TM-O bond and is derived from the quantitative imbalance between M and O orbitals. If TM-O π -hybridization is weak, the energy gaps between O $2p$ NB and M nd -O $2p$ π/π^* states will be small, and in practice, their energy ranges will partially overlap. However, we find that the metal-oxygen de-coordination can induce the shortening of dangling TM-O bonding, indicative of the improvement of TM-O π -hybridization. In that case, the extent of π/π^* splitting would be significant, and O $2p$ NB and M nd -O $2p$ π/π^* states will become distinguishable in DOS. The observations of the electronic structure of dangling TM-O bonds (figures 2.7c-d, 2.4-2.6, 2.9-2.10, and 2.12) validate our theory for the electronic reshuffling involved with cation disordering.

2.3.8 Types of oxygen dimer

We generated 300 Li-vacancy orderings for $\text{Li}_{0.5}\text{MnO}_3$ with single $\text{M}_{\text{Li, tetra}}$, $\text{M}_{\text{Li, octa}}$, and $\text{M}_{\text{Li, TM layer}}$ disorder, respectively, using the enumeration technique³⁵, and performed DFT calculations for the generated structures. For the 50 most stable configurations of each case, the disorder formation energies are presented in figure 2.4b. Depending on Li-vacancy configurations, various types of oxygen dimer are spontaneously formed during structural relaxation. We classified the dimer type according to the Mn coordination of dimers, and named them in the light of relevant literatures^{27,73}. In this process, the Li coordination was not considered. Dimer types are defined as follows:

- (1) Edge dimer: Two oxygen ions are coordinated with the same metal ion. Thus, the edge dimer belongs entirely to single MO_6 octahedron. (figure 2.4c, f, and j)
- (2) Bridge dimer: The bridge dimer connects two MO_6 octahedra. (figure 2.4g, and k)
- (3) Dangling dimer: One oxygen ion is coordinated with at least one metal ion, whereas the other O ion is not coordinated with metal ion at all. (figure 2.4d, and h)
- (4) Floating dimer: Neither oxygen atoms of the dimer are coordinated with metal at all. (figure 2.4e, and i)
- (5) $\mu\text{-O}_3$ dimers: There are the cases in which two dimers are generated and

connected to form an oxygen trimer. Among them, the case where oxygen ions at opposite ends are bonded to different metal ions is named μ -O₃ dimers.

Accordingly, μ -O₃ dimers connect two MnO_x polyhedra. (figure 2.4l)

(6) η^1 -O₃ dimers: If one end oxygen of μ -O₃ dimers is not coordinated with manganese ion, it is named η^1 -O₃ dimers. (figure 2.4m)

(7) Multiple dimers: This is the case where two or more dimers described above are simultaneously formed. (figure 2.4n)

Figure 2.4b shows that a series of structural transformations which involves the cation migration and concomitant oxygen dimerization are thermodynamically spontaneous on the whole in Li_{0.5}MnO₃. This is consistent with previous theoretical studies^{27,74,75}, and supports experimental observations of Mn migration in charged Li₂MnO₃^{76,77}. On the other hand, there are also cases where oxygen dimer is not generated even after cation migration ('No dimer' in figure 2.4b). It is notable that the energies of structures without oxygen dimer are considerably higher than those of structures with dimer on the whole. It indicates the stabilizing effects imparted by the formation of oxygen-oxygen covalent bonding. Figure 2.4c-k represents the changes in the electronic structure of oxygen involved with O-O dimerization and Mn-O π hybridization due to cation disordering. Electronic structures are provided for all observed combinations of cation disorder ($M_{Li, \text{tetra}}$, $M_{Li, \text{octa}}$, and $M_{Li, \text{TM layer}}$) and dimer type. Note that even when the length of dangling Mn-O bond is not significantly reduced (eg. $d(\text{Mn-O}) = 1.81 \text{ \AA}$ in figure 2.4f and j), the oxygen states

is divided into Mn 3d-O 2p π/π^* and O 2p NB states after Mn migration due to the Mn-O de-coordination itself, as explained in Chapter 2.3.7. But in those cases, COOP intensity of Mn 3d-O 2p π^* states is insignificant compared with that of short Mn-O bonds ($d(\text{Mn-O}) < 1.7 \text{ \AA}$).

2.3.9 Cation migration in $\text{Na}_{0.6}[\text{Li}_{0.2}\text{Mn}_{0.8}]\text{O}_2$ and $\text{Na}_{2/3}[\text{Mg}_{1/3}\text{Mn}_{2/3}]\text{O}_2$

$\text{Na}_{0.6}[\text{Li}_{0.2}\text{Mn}_{0.8}]\text{O}_2$ electrodes have known to have P3-type structure (AABBCC oxygen stacking, R3m space group)^{41,78,79} or P2-type structure (AABB oxygen stacking, P6₃/mmc space group)^{10,80,81}. We performed DFT calculations on the former structure. For the pristine $\text{Na}_{0.6}[\text{Li}_{0.2}\text{Mn}_{0.8}]\text{O}_2$, we designated the most stable Na-vacancy configuration in the sodium layers. And $\text{Li}_{1/5}\text{Mn}_{4/5}$ ribbon arrangement is applied for the TM layers in accordance with the previous reports (figure 2.2b). In depicting the charged phase, the P3 stacking is maintained according to the experimental results that the global oxygen sequence is preserved⁷⁸, and Li ions are also extracted from the supercell because most of Li ions are permanently extracted into the electrolyte after long cycles in which the cation migration can occur⁴¹. It is noteworthy that appreciable amounts of stacking faults exist in the charged sample⁷⁸, and the effects of stacking faults on cation disordering warrant further study. Figure 2.6a compares the electronic structures of the pristine phase and the charged phase without any structural disorder. It indicates that in the absence of structural disorder, the charge process is compensated only by the depopulation of O 2p NB states.

Due to the considerable size mismatch between manganese ion and large prismatic sites, out-of-plane Mn migration to the Na layer is expected to be energetically penalized, and neutron diffraction analyses confirmed the absence of out-of-plane Mn migration⁷⁸. Therefore, only in-plane cation migration was considered for the charged phase of $\text{Na}_{0.6}[\text{Li}_{0.2}\text{Mn}_{0.8}]\text{O}_2$. We addressed various possible in-plane Mn

migration pathways as shown in figure 2.6b. Basically, there are cases in which one manganese ion migrates, as in path 1 (figure 2.6c) and path 2 (figure 2.6f). In the case of path 1, two vacant sites are adjacent and two dangling oxygen ions are generated. As a result, two short dimers (1.36 Å and 1.38 Å) are formed after structural relaxation (figure 2.6c). On the other hand, vacancy cluster and dangling oxygen are not generated when Mn migrates through path 2. In this case, a short oxygen dimer is not formed (figure 2.6f). We also considered the cases in which several manganese ions move collectively to form a large vacancy cluster. If two manganese ions move sequentially along the path 3, three vacant sites are gathered, generating 4 dangling oxygen ions (figure 2.6d). More extremely, if four manganese ions migrate sequentially as in path 4, four vacant sites are gathered, producing four dangling oxygen ions and two fully de-coordinated oxygen ions (figure 2.6e). These collective movements certainly lead to the oxygen dimerization, although they are expected to be more difficult to occur compared to single Mn hopping. The oxygen dimerization originated from the vacancy clustering was also verified in DFT calculations for $\text{Na}_{0.75}[\text{Li}_{0.25}\text{Mn}_{0.75}]\text{O}_2$ by House et al¹⁰.

$\text{Na}_{2/3}[\text{Mg}_{1/3}\text{Mn}_{2/3}]\text{O}_2$ electrodes have also reported to have P3-type structure⁴² or P2-type structure^{24,79,82}. $\text{Na}_{0.67}[\text{Mg}_{0.28}\text{Mn}_{0.72}]\text{O}_2$ electrodes of similar composition have also been studied a lot⁸³⁻⁸⁶. We performed the calculations on P3- $\text{Na}_{2/3}[\text{Mg}_{1/3}\text{Mn}_{2/3}]\text{O}_2$ electrode. For the pristine state, $\text{Mg}_{1/3}\text{Mn}_{2/3}$ honeycomb arrangement was applied for the TM layers following the previous reports⁴², and Na-vacancy configuration was optimized to be most stable (figure 2.2c). To describe the

charged phase, we fully desodiated the supercell while leaving all Mg ions according to the previous report that Mg^{2+} with low mobility is scarcely extracted from the electrode even at very high voltage (5 V vs. Na^+/Na)⁸⁵. In addition, the O3 stacking was applied for the charged phase based on the report that the lattice oxygen stacking sequence is irreversibly converted from P3 to O3 stacking after charging⁴². We selected the most stable Mg-vacancy configuration in the charged phase considering all octahedral and tetrahedral sites in the alkali metal layers and vacant sites in the TM layers. In consequence, the configuration where all Mg ions are in the tetrahedral sites of the alkali metal layers is calculated to be most stable. The electronic structures of the pristine and charged phase without any structural disorder are compared in figure 2.5a. And figure 2.5b shows that the meaningful bonding contraction is possible only after oxygen ions are de-coordinated. We calculated the effects of $\text{Mn}_{\text{Na, tetra}}$, $\text{Mn}_{\text{Na, octa}}$, and $\text{Mn}_{\text{Mg, TM layer}}$ disorders in $\text{O3-Na}_0[\text{Mg}_{1/3}\text{Mn}_{2/3}]\text{O}_2$ phase. In each case, Mg-vacancy configuration is re-optimized, and the properties of the most stable structures are provided in figure 2.5b-e.

2.3.10 Effects of metal substitution on bond rearrangements

We investigated the effects of cation disordering in $\text{Li}_2\text{Ru}_{0.5}\text{Sn}_{0.5}\text{O}_3$ and $\text{Li}_2\text{Ir}_{0.5}\text{Sn}_{0.5}\text{O}_3$ whose in-plane cation orderings are displayed in figure 2.13. In the designated most stable Ru/Sn and Ir/Sn orderings, Ru and Ir migration produce three or four dangling Sn-O bonds. During structural relaxation of $\text{Li}_{0.5}\text{Ru}_{0.5}\text{Sn}_{0.5}\text{O}_3$ with Ru_{Li} disorder and $\text{Li}_{0.5}\text{Ir}_{0.5}\text{Sn}_{0.5}\text{O}_3$ with Ir_{Li} disorder, short oxygen dimers were naturally generated (figures 2.32 and 2.33). And those cation migration and concomitant oxygen dimerization were predicted to be thermodynamically spontaneous except for $\text{Ir}_{\text{Li, TM layer}}$ disorder.

On the other hand, it has been known that metal ions with fully filled or completely emptied d shells (d^0 , d^{10}) are prone to migrate in lithium layered oxides due to their zero crystal field splitting^{87,88}. We also calculated Sn migration in $\text{Li}_{0.5}\text{Ru}_{0.5}\text{Sn}_{0.5}\text{O}_3$ (figure 2.34) and $\text{Li}_{0.5}\text{Ir}_{0.5}\text{Sn}_{0.5}\text{O}_3$ (figure 2.35). In the designated most stable Ru/Sn and Ir/Sn orderings, Sn migration generates only Ru-O or Ir-O dangling bonds. During the relaxation of structures with Sn disorder, a short oxygen dimer ($< 1.7 \text{ \AA}$) was not formed, and dangling oxygens are stabilized only by TM-O π hybridization. The comparison of this result with abovementioned Ru/Ir migration situations suggests that the presence of non-directional dangling bonds is one of the prerequisites of oxygen dimerization. In order to create a situation in which dangling Sn-O bonds are generated with Sn migration, we also considered metastable Ru/Sn ordering in $\text{Li}_{0.5}\text{Ru}_{0.5}\text{Sn}_{0.5}\text{O}_3$ (figure 2.36) and metastable Ir/Sn ordering in $\text{Li}_{0.5}\text{Ir}_{0.5}\text{Sn}_{0.5}\text{O}_3$ (figure 2.37). These orderings are within the 25 meV per atom of the

global minimum. For those cases, it was found that short oxygen dimers can be formed with Sn migration through the rotation of Sn-O bonds. This result indicates that the type of dangling bonds, not the type of migrating metal ion, is important in determining the nature of bonding rearrangements.

Interestingly, $\text{Li}_2\text{Ni}_{0.5}\text{Te}_{0.5}\text{O}_3$ electrode has known to exhibit very small voltage hysteresis unlike Sn-substituted Li_2RuO_3 and Li_2IrO_3 systems^{62,89}. The major difference of $\text{Li}_2\text{Ni}_{0.5}\text{Te}_{0.5}\text{O}_3$ electrode with other lithium-rich electrodes is that their charging process does not employ oxygen redox. The conventional charging process of $\text{Li}_2\text{Ni}_{0.5}\text{Te}_{0.5}\text{O}_3$ electrode, 2-4.6 V (vs. Li/Li^+), utilizes only half of Li^{62} . Thus, the Li^+ removal is entirely charge compensated by $\text{Ni}^{2+/4+}$ redox and O 2p NB states are not depopulated (figure 2.38a). Therefore, bonding rearrangements are insignificant in $\text{Li}_1\text{Ni}_{0.5}\text{Te}_{0.5}\text{O}$ even if dangling Te-O bonds appear with cation migration because oxygen states do not need to be stabilized (figure 2.38b-e).

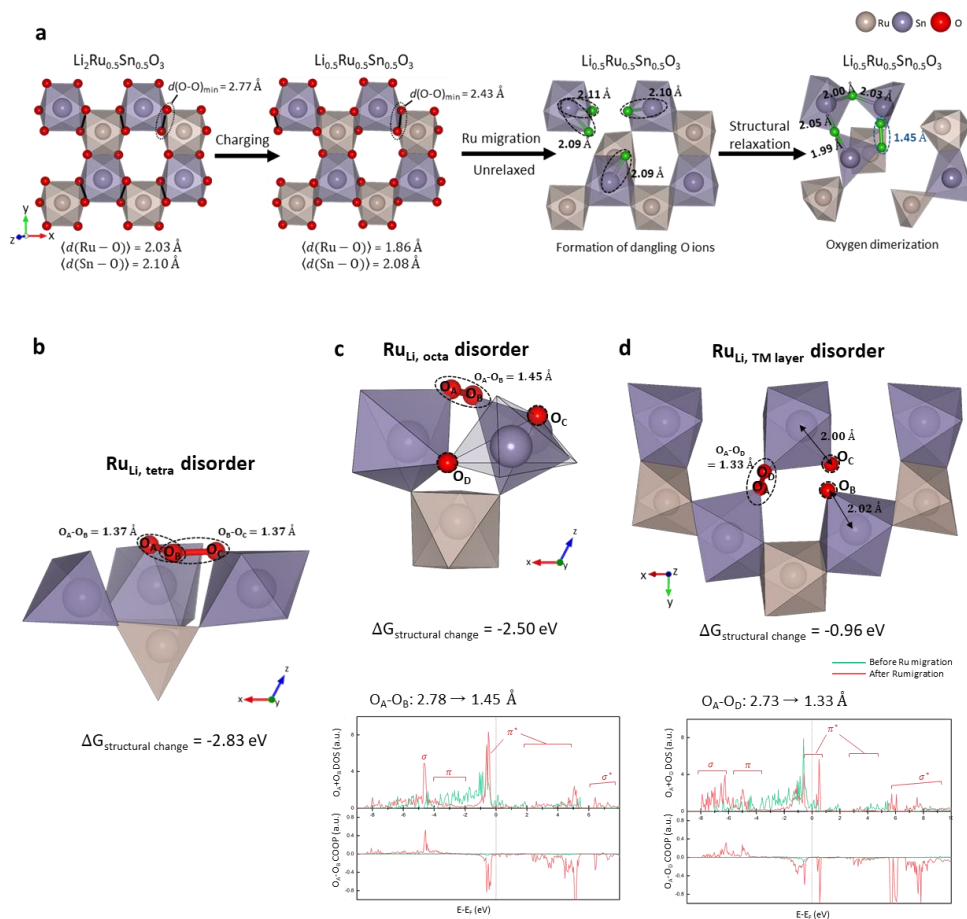


Figure 2.32. **a**, Bonding rearrangements involved with charging and $\text{Ru}_{\text{Li, octa}}$ formation in $\text{Li}_{2-x}\text{Ru}_{0.5}\text{Sn}_{0.5}\text{O}_3$. Dangling oxygen ions formed with cation migration are colored green. **b-d**, Bonding arrangements and corresponding electronic structures calculated for $\text{Li}_{0.5}\text{Ru}_{0.5}\text{Sn}_{0.5}\text{O}_3$ with $\text{Ru}_{\text{Li, tetra}}$ (**b**), $\text{Ru}_{\text{Li, octa}}$ (**c**), and $\text{Ru}_{\text{Li, TM layer}}$ (**d**). For each case, the Li-vacancy ordering was optimized to be most stable. In **a-d**, Li ions are omitted for clarity.

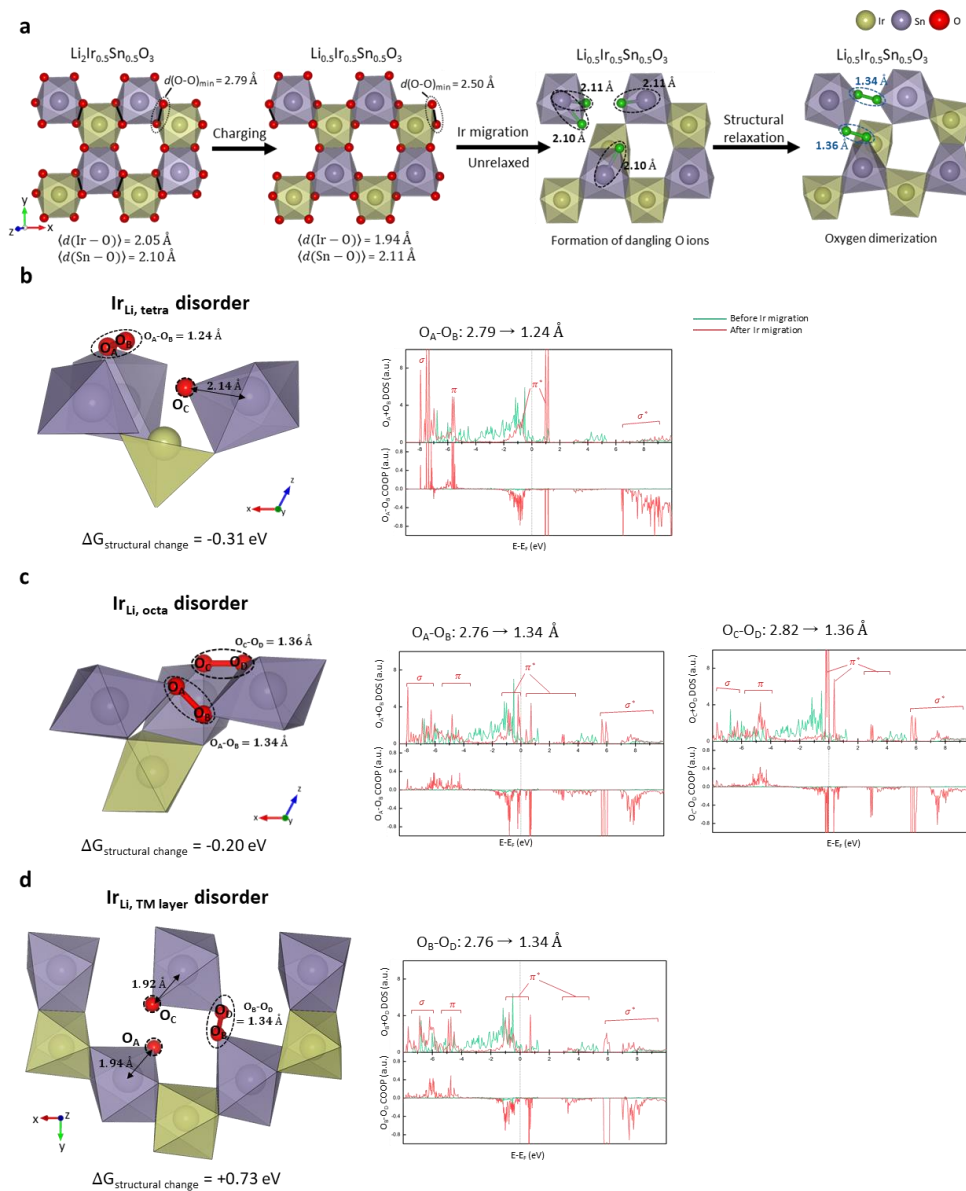


Figure 2.33. a, Bonding rearrangements involved with charging and Ir_{Li, octa} formation in Li_{2-x}Ir_{0.5}Sn_{0.5}O₃. Dangling oxygen ions formed with cation migration are colored green. **b-d**, Bonding arrangements and corresponding electronic structures calculated for Li_{0.5}Ir_{0.5}Sn_{0.5}O₃ with Ir_{Li, tetra} (**b**), Ir_{Li, octa} (**c**), and Ir_{Li, TM layer}

(**d**). For each case, the Li-vacancy ordering was optimized to be most stable. In **a-d**, Li ions are omitted for clarity.

Table 2.15. Bond length changes and bond order changes of dangling oxygen ions accompanying Ru migration in $\text{Li}_{0.5}\text{Ru}_{0.5}\text{Sn}_{0.5}\text{O}_3$ and Ir migration in $\text{Li}_{0.5}\text{Ir}_{0.5}\text{Sn}_{0.5}\text{O}_3$. ICOOP(eF) is the integration of COOP up to the Fermi level, which has been known to be proportional to the bond order^{14,26}.

Materials	Disorder type	Covalent bond	Bond length (Å)		ICOOP (eF) (a.u.)		Δ Bond length (Å)	Δ ICOOP (eF) (a.u.)
			M _{original site}	M _{migrated site}	M _{original site}	M _{migrated site}		
Li _{0.5} Ru _{0.5} Sn _{0.5} O ₃	Ru _{Li, tetra}	O _A -O _B	2.78	1.37	-0.01	0.17	-1.41	0.18
		O _B -O _C	2.78	1.37	-0.01	0.17	-1.41	0.17
	Ru _{Li, octa}	O _A -O _B	2.78	1.45	-0.01	0.13	-1.33	+0.13
		Sn-O _C	2.09	2.05	0.12	0.14	-0.04	+0.03
		Sn-O _D	2.11	2.00	0.11	0.17	-0.11	+0.06
	Ru _{Li, TM layer}	O _A -O _D	2.73	1.33	-0.01	0.20	-1.40	+0.21
		Sn-O _B	2.09	2.02	0.12	0.16	-0.07	+0.05
		Sn-O _C	2.09	2.00	0.11	0.19	-0.08	+0.07
	Li _{0.5} Ir _{0.5} Sn _{0.5} O ₃	Ir _{Li, tetra}	O _A -O _B	2.79	1.24	-0.01	0.26	-1.56
Sn-O _C			2.1	2.14	0.11	0.12	0.03	0.01
Ir _{Li, octa}		O _A -O _B	2.76	1.34	-0.01	0.19	-1.42	+0.20
		O _C -O _D	2.82	1.36	-0.01	0.17	-1.45	+0.18
Ir _{Li, TM layer}		O _B -O _D	2.76	1.34	-0.01	0.19	-1.42	+0.20
		Sn-O _A	2.10	1.94	0.11	0.21	-0.16	+0.10
		Sn-O _C	2.10	1.92	0.11	0.22	-0.18	+0.11

Table 2.16. Bader charge changes involved with Ru migration in $\text{Li}_{0.5}\text{Ru}_{0.5}\text{Sn}_{0.5}\text{O}_3$ and Ir migration in $\text{Li}_{0.5}\text{Ir}_{0.5}\text{Sn}_{0.5}\text{O}_3$. Positive value means the loss of electron.

Disorder type			Li _{0.5} Ru _{0.5} Sn _{0.5} O ₃			Li _{0.5} Ir _{0.5} Sn _{0.5} O ₃		
			Ru _{Li, tetra}	Ru _{Li, octa}	Ru _{Li, TM layer}	Ir _{Li, tetra}	Ir _{Li, octa}	Ir _{Li, TM layer}
Oxygen dimerizat ion	O-O		.	O _A -O _B : +0.77	O _A -O _D : +1.44	O _A -O _B : +2.55	O _A -O _B : +1.39 O _C -O _D : +1.20	O _B -O _D : +1.39
	μ-O ₃		O _A -O _B - O _C : +2.75
Dangling Sn-O bonds	Sn-O _A	Sn	0.00
		O _A			.			-0.34
	Sn-O _B	Sn			0.00			.
		O _B			-0.06			.
	Sn-O _C	Sn		0.00	0.00	0.00		0.00
		O _C		-0.30	-0.11	+0.12		-0.37
	Sn-O _D	Sn		-0.65	.	.		.
		O _D	
The other O ions in the cell			-2.62	-0.29	-1.30	-1.85	-1.52	-0.22
All Ru/Ir ions in the cell			-0.04	+0.58	+0.04	-0.56	-1.07	-0.47
All Sn ions in the cell			-0.10	-0.11	0.00	-0.25	0.00	0.00

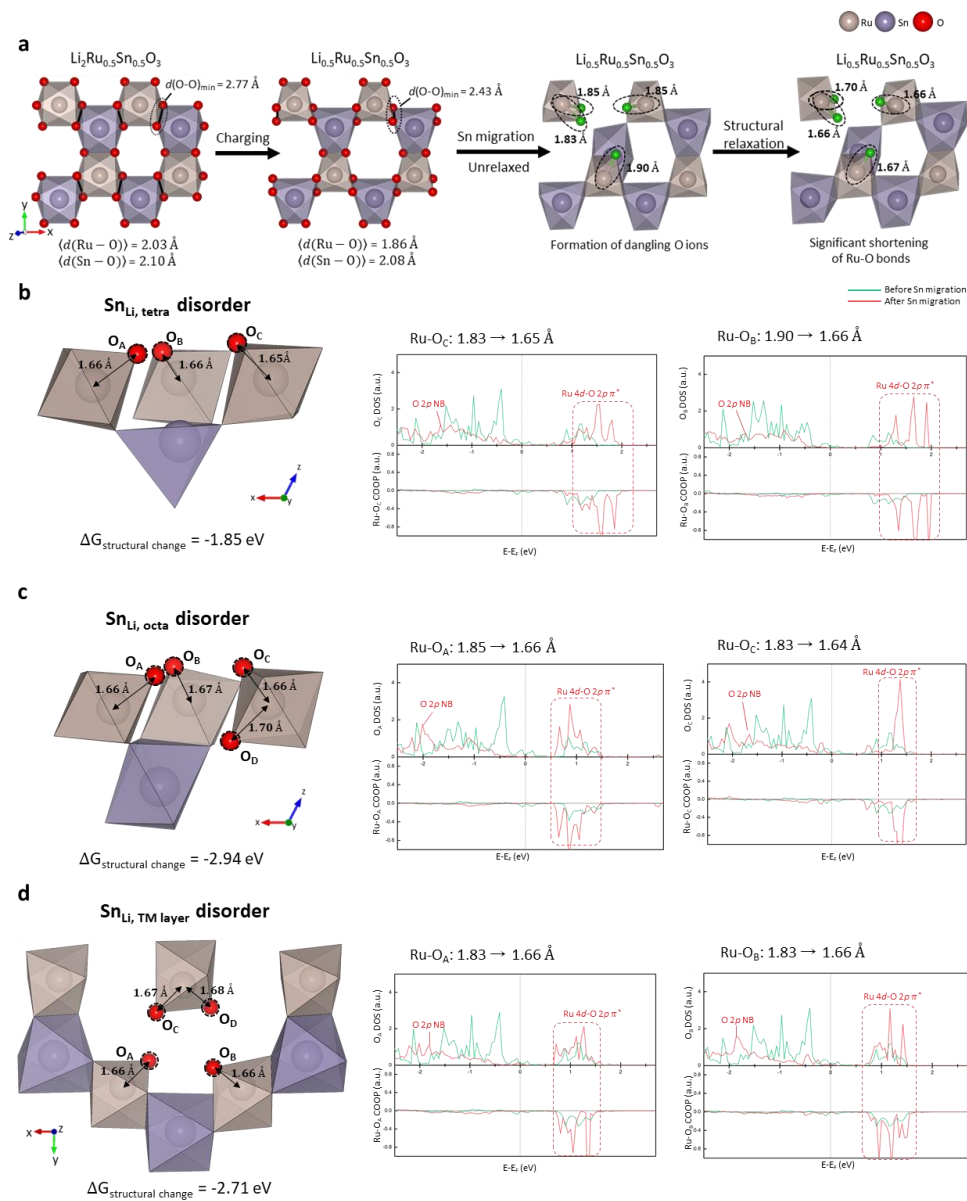


Figure 2.34. a, Bonding rearrangements involved with charging and $\text{Sn}_{\text{Li, octa}}$ formation in $\text{Li}_{2-x}\text{Ru}_{0.5}\text{Sn}_{0.5}\text{O}_3$. Dangling oxygen ions formed with cation migration are colored green. **b-d**, Bonding arrangements and corresponding electronic structures calculated for $\text{Li}_{0.5}\text{Ru}_{0.5}\text{Sn}_{0.5}\text{O}_3$ with $\text{Sn}_{\text{Li, tetra}}$ (**b**), $\text{Sn}_{\text{Li, octa}}$ (**c**), and $\text{Sn}_{\text{Li, TM}}$

_{layer} (**d**). For each case, the Li-vacancy ordering was optimized to be most stable. In **a-d**, Li ions are omitted for clarity.

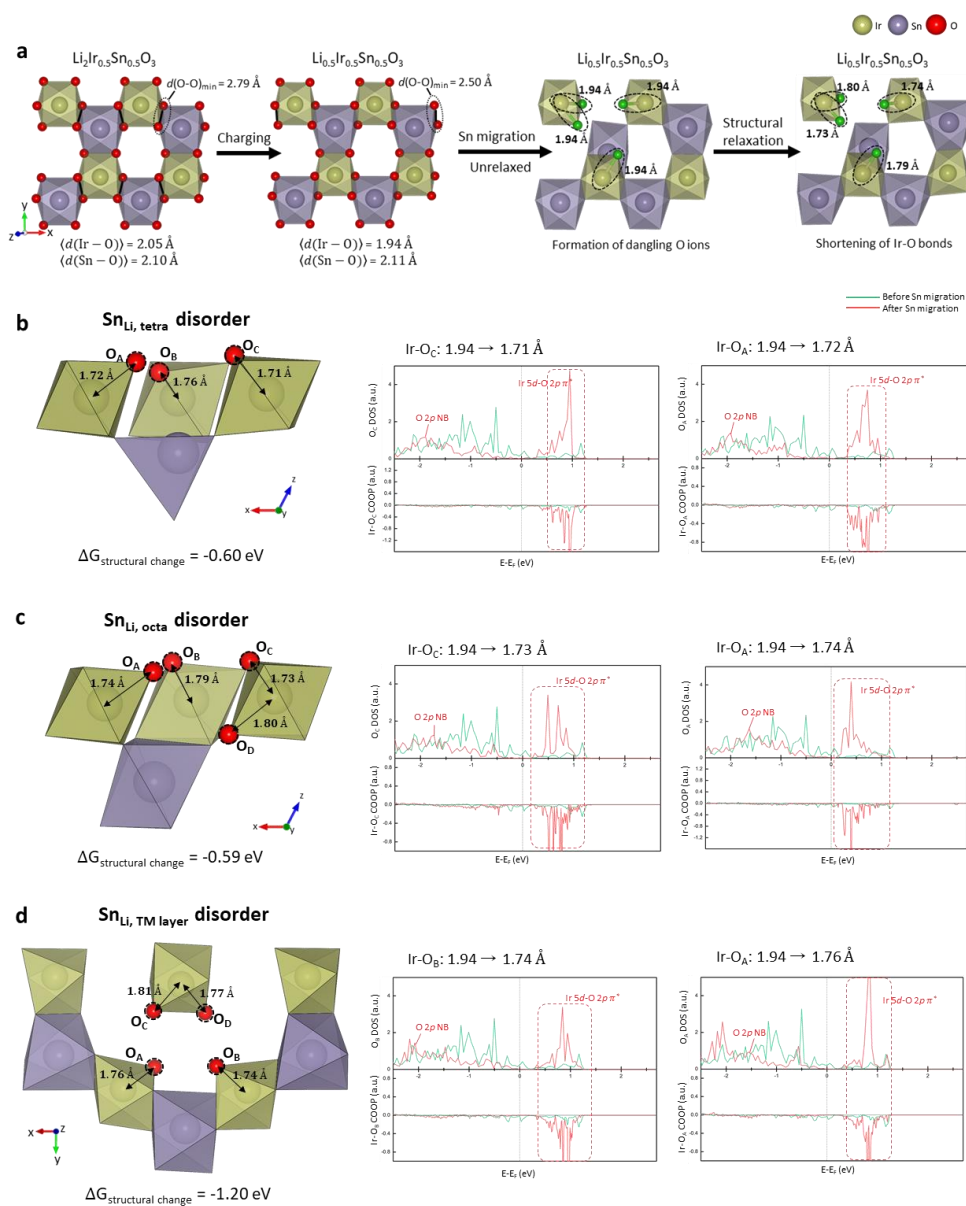


Figure 2.35. a, Bonding rearrangements involved with charging and $\text{Sn}_{\text{Li, octa}}$ formation in $\text{Li}_{2-x}\text{Ir}_{0.5}\text{Sn}_{0.5}\text{O}_3$. Dangling oxygen ions formed with cation migration are colored green. **b-d**, Bonding arrangements and corresponding electronic structures calculated for $\text{Li}_{0.5}\text{Ir}_{0.5}\text{Sn}_{0.5}\text{O}_3$ with $\text{Sn}_{\text{Li, tetra}}$ (**b**), $\text{Sn}_{\text{Li, octa}}$ (**c**), and $\text{Sn}_{\text{Li, TM layer}}$

(d). For each case, the Li-vacancy ordering was optimized to be most stable. In **a-d**, Li ions are omitted for clarity.

Table 2.17. Bond length changes and bond order changes of dangling oxygen ions accompanying Sn migration in $\text{Li}_{0.5}\text{Ru}_{0.5}\text{Sn}_{0.5}\text{O}_3$ and $\text{Li}_{0.5}\text{Ir}_{0.5}\text{Sn}_{0.5}\text{O}_3$. ICOOP(eF) is the integration of COOP up to the Fermi level, which has been known to be proportional to the bond order^{14,26}.

Materials	Disorder type	Dangling bond	Bond length (Å)		ICOOP (eF) (a.u.)		Δ Bond length (Å)	ΔICOOP P (eF) (a.u.)	ΔICOOP (eF) (%)
			Sn _{original} site	Sn _{migrated} site	Sn _{original} site	Sn _{migrated} site			
$\text{Li}_{0.5}\text{Ru}_{0.5}\text{Sn}_{0.5}\text{O}_3$	Sn_{Li}_{tetra}	Ru-O _A	1.85	1.66	0.28	0.45	-0.19	+0.17	+61.6
		Ru-O _B	1.9	1.66	0.19	0.4	-0.24	+0.20	+103.9
		Ru-O _C	1.83	1.65	0.29	0.43	-0.18	+0.14	+50.1
		Sum					-0.61	+0.52	+215.6
	Sn_{Li}_{octa}	Ru-O _A	1.85	1.66	0.28	0.42	-0.19	+0.14	+50.9
		Ru-O _B	1.9	1.67	0.19	0.37	-0.23	+0.18	+91.0
		Ru-O _C	1.83	1.66	0.29	0.43	-0.17	+0.14	+49.2
		Ru-O _D	1.85	1.7	0.28	0.38	-0.15	+0.10	+36.6
		Sum					-0.74	+0.56	+227.7
	Sn_{Li}_{TM layer}	Ru-O _A	1.83	1.66	0.29	0.41	-0.17	+0.12	+42.0
		Ru-O _B	1.83	1.66	0.29	0.43	-0.17	+0.15	+51.8
		Ru-O _C	1.9	1.67	0.19	0.37	-0.24	+0.18	+92.7
		Ru-O _D	1.9	1.68	0.19	0.38	-0.22	+0.19	+96.3
		Sum					-0.80	+0.63	+282.8
$\text{Li}_{0.5}\text{Ir}_{0.5}\text{Sn}_{0.5}\text{O}_3$	Sn_{Li}_{tetra}	Ir-O _A	1.94	1.72	0.24	0.42	-0.22	+0.18	+77.0
		Ir-O _B	1.94	1.76	0.24	0.34	-0.18	+0.10	+43.5
		Ir-O _C	1.94	1.71	0.24	0.4	-0.22	+0.16	+64.6
		Sum					-0.62	+0.44	+185.1
	Sn_{Li}_{octa}	Ir-O _A	1.94	1.74	0.24	0.38	-0.20	+0.14	+60.5
		Ir-O _B	1.94	1.79	0.24	0.3	-0.16	+0.06	+26.5
		Ir-O _C	1.94	1.73	0.24	0.39	-0.21	+0.15	+62.1
		Ir-O _D	1.94	1.8	0.24	0.3	-0.14	+0.07	+27.8
		Sum					-0.70	+0.42	+177.0
	Sn_{Li}_{TM layer}	Ir-O _A	1.94	1.76	0.24	0.38	-0.18	+0.13	+55.8
		Ir-O _B	1.94	1.74	0.24	0.36	-0.20	+0.12	+50.5
		Ir-O _C	1.94	1.81	0.24	0.28	-0.13	+0.05	+19.2
		Ir-O _D	1.94	1.77	0.24	0.33	-0.17	+0.09	+36.7
		Sum					-0.68	+0.39	+162.2

Table 2.18. Bader charge changes involved with Sn migration in $\text{Li}_{0.5}\text{Ru}_{0.5}\text{Sn}_{0.5}\text{O}_3$ and $\text{Li}_{0.5}\text{Ir}_{0.5}\text{Sn}_{0.5}\text{O}_3$. Positive value means the loss of electron.

Dangling TM-O bonds			Li _{0.5} Ru _{0.5} Sn _{0.5} O ₃			Li _{0.5} Ir _{0.5} Sn _{0.5} O ₃		
			Sn _{Li, tetra}	Sn _{Li, octa}	Sn _{Li, TM layer}	Sn _{Li, tetra}	Sn _{Li, octa}	Sn _{Li, TM layer}
Dangling TM-O bonds	Ru/Ir- O _A	Ru/Ir	+0.11	+0.36	+0.15	+0.26	+0.32	+0.19
		O _A	+0.37	+0.39	+0.35	+0.54	+0.61	+0.38
	Ru/Ir- O _B	Ru/Ir	+0.09	+0.09	+0.10	+0.28	+0.11	+0.22
		O _B	+0.46	+0.40	+0.34	+0.51	+0.50	+0.43
	Ru/Ir- O _C	Ru/Ir	+0.16	+0.38	+0.35	+0.28	+0.37	+0.16
		O _C	+0.37	+0.39	+0.53	+0.53	+0.57	+0.36
	Ru/Ir- O _D	O _D	.	+0.28	+0.48	.	+0.52	+0.48
	Sum(Dangling M)		+0.36	+0.83	+0.60	+0.82	+0.80	+0.57
	Sum(Dangling O)		+1.19	+1.46	+1.71	+1.57	+2.21	+1.65
	The other Ru/Ir ions in the cell			+0.71	+0.41	+0.46	-0.21	-0.46
The other O ions in the cell			-2.21	-2.70	-2.77	-2.13	-2.54	-2.06
All Sn ions in the cell			-0.06	0.00	0.00	-0.06	0.00	0.00

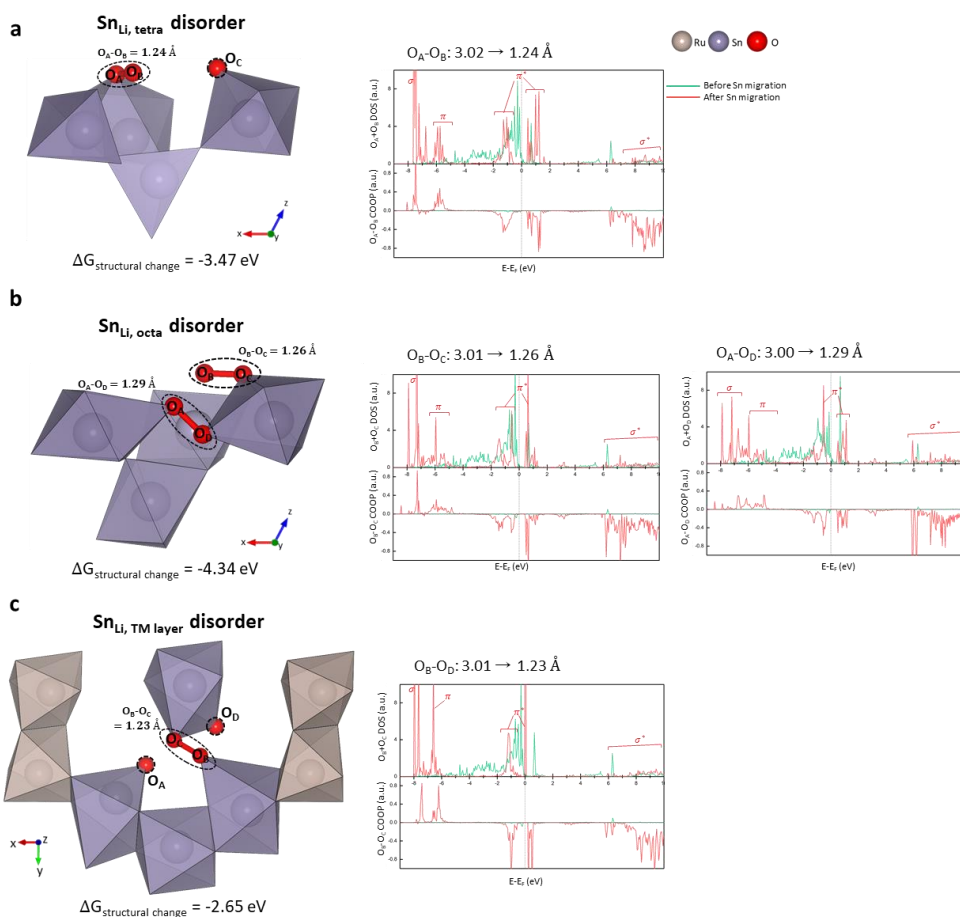


Figure 2.36. We exchanged one Ru and one Sn in the most stable Ru/Sn ordering of $\text{Li}_2\text{Ru}_{0.5}\text{Sn}_{0.5}\text{O}_3$ (figure 2.13a), so that a Sn ion is surrounded by three Sn ions. This arrangement is only 9.05 meV per atom unstable than the most stable arrangement. For $\text{Li}_{0.5}\text{Ru}_{0.5}\text{Sn}_{0.5}\text{O}_3$ with this modulated Ru/Sn arrangement, the effects of Sn migration were calculated and presented in **a-c**. **a-c**, Bonding rearrangements and electronic reshuffling involved with $\text{Sn}_{\text{Li, tetra}}$ (**a**), $\text{Sn}_{\text{Li, octa}}$ (**b**), and $\text{Sn}_{\text{Li, TM layer}}$ (**c**) disordering. For each case, the Li-vacancy ordering was optimized to be most stable, and Li ions are omitted for clarity.

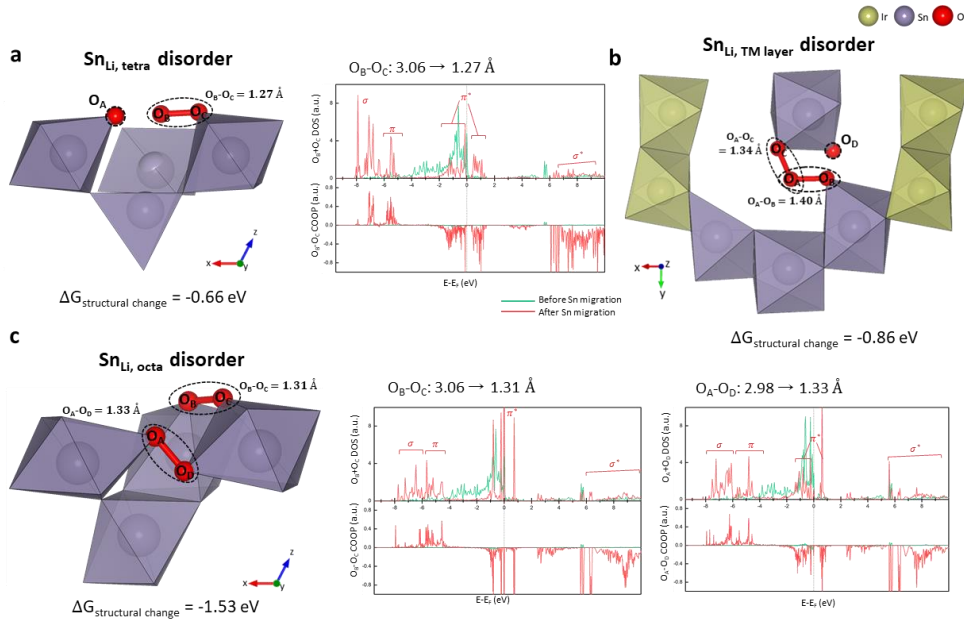


Figure 2.37. We exchanged one Ir and one Sn in the most stable Ir/Sn ordering of $\text{Li}_2\text{Ir}_{0.5}\text{Sn}_{0.5}\text{O}_3$ (figure 2.13b), so that a Sn ion is surrounded by three Sn ions. This arrangement is only 4.53 meV per atom unstable than the most stable arrangement. For $\text{Li}_{0.5}\text{Ir}_{0.5}\text{Sn}_{0.5}\text{O}_3$ with this modulated Ir/Sn arrangement, the effects of Sn migration were calculated and presented in **a-c**. **a-c**, Bonding rearrangements and electronic reshuffling involved with $\text{Sn}_{\text{Li, tetra}}$ (**a**), $\text{Sn}_{\text{Li, octa}}$ (**b**), and $\text{Sn}_{\text{Li, TM layer}}$ (**c**) disordering. For each case, the Li-vacancy ordering was optimized to be most stable, and Li ions are omitted for clarity.

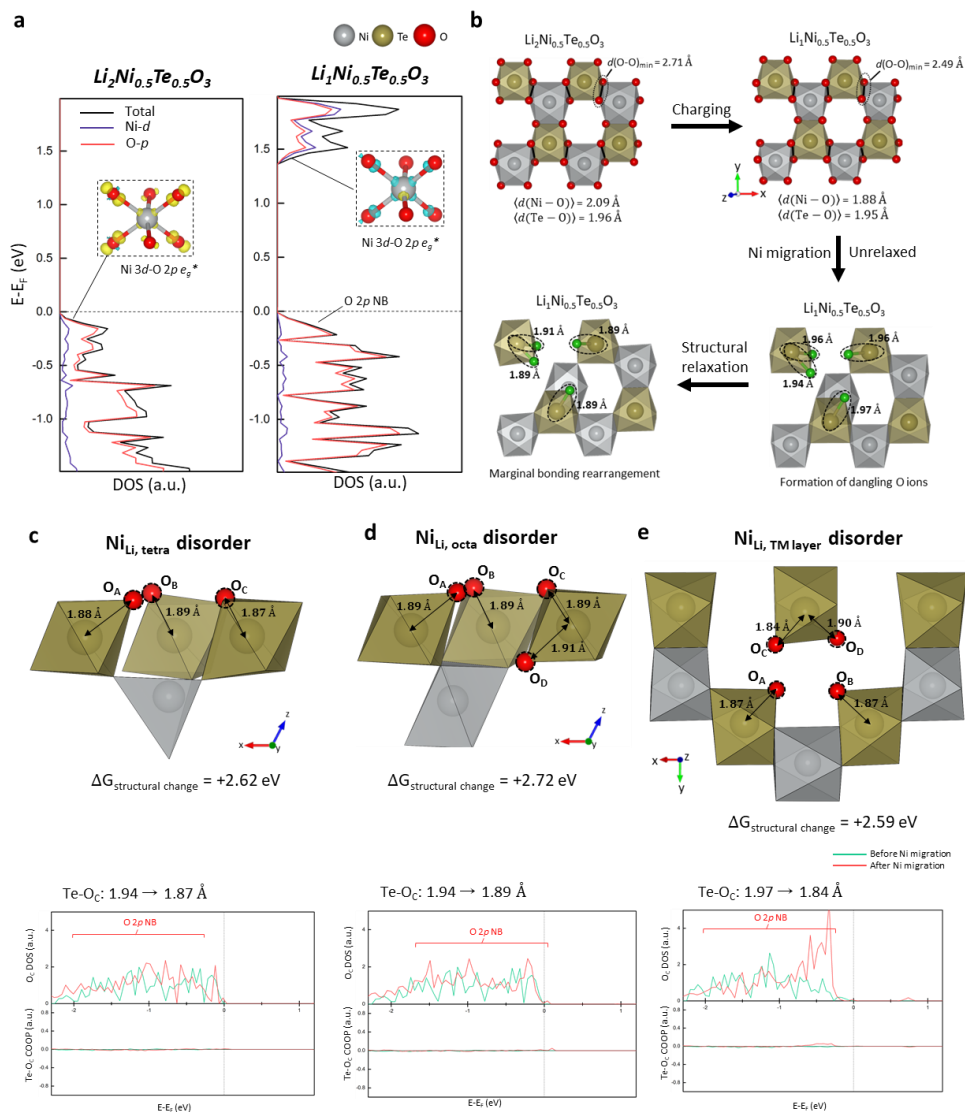


Figure 2.38. **a**, DOS of $\text{Li}_2\text{Ni}_{0.5}\text{Te}_{0.5}\text{O}_3$ and $\text{Li}_1\text{Ni}_{0.5}\text{Te}_{0.5}\text{O}_3$ without any structural disorder. Their in-plane Ni/Te ordering is represented in figure 2.13c. (Inset) The positive and negative Fukui functions that visualize the charge density of electronic states just above and below the Fermi level, respectively. Yellow and blue corresponds to negative and positive changes, respectively. DOS and the Fukui

functions indicate in common that the delithiation from $\text{Li}_2\text{Ni}_{0.5}\text{Te}_{0.5}\text{O}_3$ to $\text{Li}_1\text{Ni}_{0.5}\text{Te}_{0.5}\text{O}_3$ is entirely charge compensated by the depopulation of Ni $3d$ -O $2p$ e_g^* states, corresponding to $\text{Ni}^{2+/4+}$ redox. **b**, Bonding rearrangements involved with charging and $\text{Ni}_{\text{Li, octa}}$ formation in $\text{Li}_{2-x}\text{Ni}_{0.5}\text{Te}_{0.5}\text{O}_3$. Dangling oxygen ions formed with cation migration are colored green. **c-e**, Bonding arrangements and corresponding electronic structures calculated for $\text{Li}_1\text{Ni}_{0.5}\text{Te}_{0.5}\text{O}_3$ with $\text{Ni}_{\text{Li, tetra}}$ (**c**), $\text{Ni}_{\text{Li, octa}}$ (**d**), and $\text{Ni}_{\text{Li, TM layer}}$ (**e**). For each case, the Li-vacancy ordering was optimized to be most stable. Note that the formation energies of these cation disorders are very positive, and thus the amount of cation disorder in $\text{Li}_1\text{Ni}_{0.5}\text{Te}_{0.5}\text{O}_3$ will be negligible in practice. In **b-e**, Li ions are omitted for clarity.

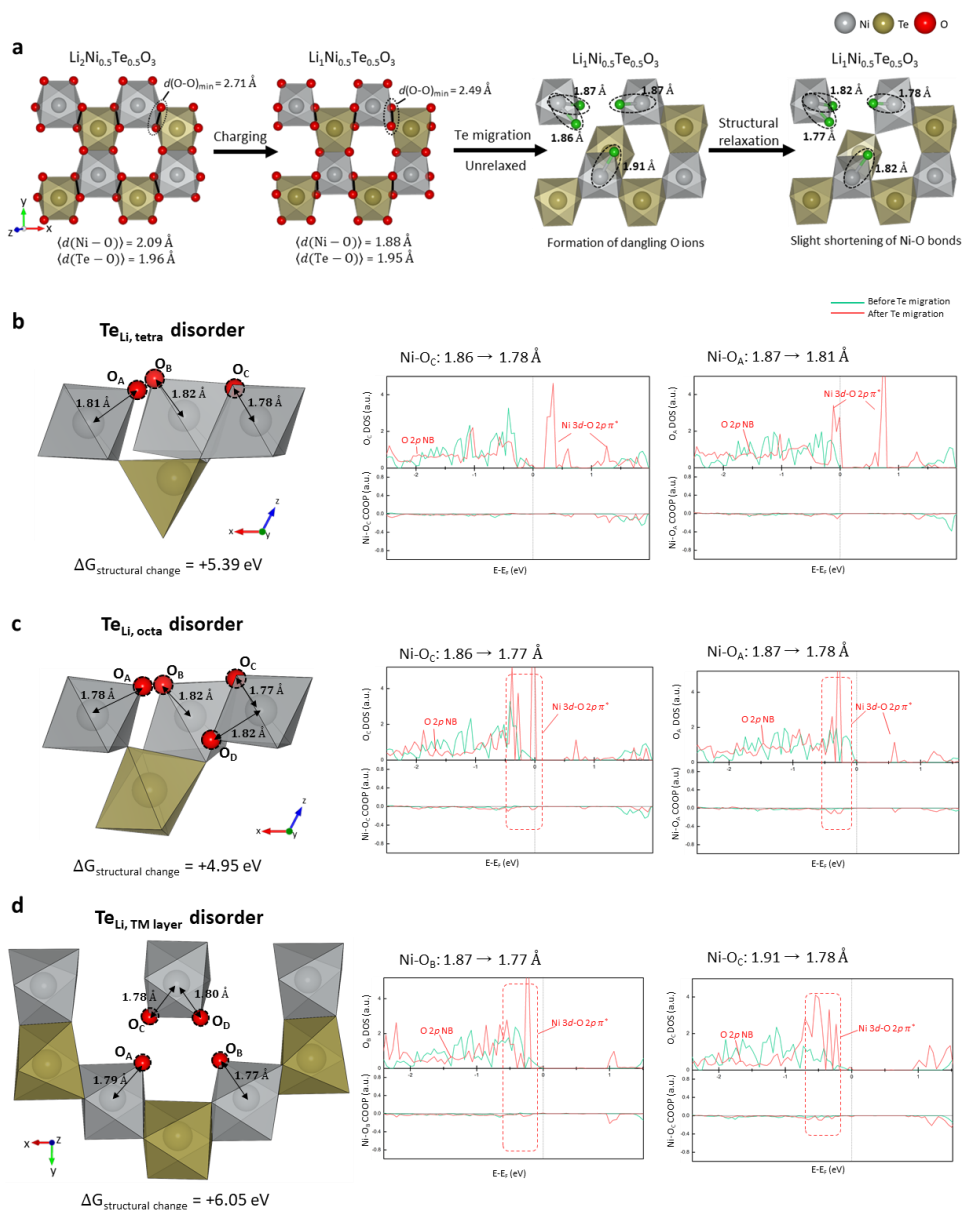


Figure 2.39. **a**, Bonding rearrangements involved with charging and Te_{Li} formation in $\text{Li}_{2-x}\text{Ni}_{0.5}\text{Te}_{0.5}\text{O}_3$. Dangling oxygen ions formed with cation migration are colored green. **b-d**, Bonding arrangements and corresponding electronic structures calculated for $\text{Li}_1\text{Ni}_{0.5}\text{Te}_{0.5}\text{O}_3$ with $\text{Te}_{\text{Li, tetra}}$ (**b**), $\text{Te}_{\text{Li, octa}}$ (**c**), and $\text{Te}_{\text{Li, TM layer}}$

(**d**). For each case, the Li-vacancy ordering was optimized to be most stable. Note that the formation energies of these cation disorders are very positive, and thus the amount of cation disorder in $\text{Li}_1\text{Ni}_{0.5}\text{Te}_{0.5}\text{O}_3$ will be negligible in practice. In **a-d**, Li ions are omitted for clarity.

Table 2.19. Bond length changes and bond order changes of dangling oxygen ions accompanying cation migration in $\text{Li}_1\text{Ni}_{0.5}\text{Te}_{0.5}\text{O}_3$. ICOOP(eF) is the integration of COOP up to the Fermi level, which has been known to be proportional to the bond order^{14,26}.

Disorder type	Dangling bond	Bond length (Å)		ICOOP (eF) (a.u.)		Δ Bond length (Å)	Δ ICOOP (eF) (a.u.)
		$M_{\text{original site}}$	$M_{\text{migrated site}}$	$M_{\text{original site}}$	$M_{\text{migrated site}}$		
Ni_{Li} , tetra	Te-O _A	1.96	1.88	0.14	0.19	-0.08	+0.05
	Te-O _B	1.97	1.89	0.14	0.19	-0.08	+0.05
	Te-O _C	1.94	1.87	0.14	0.19	-0.07	+0.05
Ni_{Li} , octa	Te-O _A	1.96	1.89	0.14	0.18	-0.07	+0.03
	Te-O _B	1.97	1.89	0.14	0.18	-0.07	+0.04
	Te-O _C	1.94	1.89	0.14	0.17	-0.05	+0.03
	Te-O _D	1.96	1.91	0.14	0.17	-0.05	+0.02
Ni_{Li} , TM layer	Te-O _A	1.94	1.87	0.14	0.19	-0.07	+0.05
	Te-O _B	1.94	1.87	0.14	0.19	-0.07	+0.05
	Te-O _C	1.97	1.84	0.14	0.22	-0.12	+0.08
	Te-O _D	1.97	1.90	0.14	0.17	-0.07	+0.03
Te_{Li} , tetra	Ni-O _A	1.87	1.81	0.18	0.21	-0.06	+0.02
	Ni-O _B	1.91	1.82	0.16	0.17	-0.09	+0.01
	Ni-O _C	1.86	1.78	0.18	0.2	-0.09	+0.02
Te_{Li} , octa	Ni-O _A	1.87	1.78	0.18	0.19	-0.09	+0.01
	Ni-O _B	1.91	1.82	0.16	0.17	-0.09	+0.01
	Ni-O _C	1.86	1.77	0.18	0.19	-0.09	+0.004
	Ni-O _D	1.87	1.82	0.18	0.14	-0.04	-0.04
Te_{Li} , TM layer	Ni-O _A	1.87	1.79	0.18	0.19	-0.08	+0.01
	Ni-O _B	1.87	1.77	0.18	0.19	-0.09	+0.01
	Ni-O _C	1.91	1.78	0.16	0.17	-0.13	+0.02
	Ni-O _D	1.91	1.8	0.16	0.15	-0.11	-0.005

Table 2.20. Bader charge changes involved with cationic disordering in $\text{Li}_1\text{Ni}_{0.5}\text{Te}_{0.5}\text{O}_3$. Positive value means the loss of electron.

Dangling bonds		Ni migration			Dangling bonds		Te migration		
		$\text{Ni}_{\text{Li, tetra}}$	$\text{Ni}_{\text{Li, octa}}$	$\text{Ni}_{\text{Li, TM layer}}$			$\text{Te}_{\text{Li, tetra}}$	$\text{Te}_{\text{Li, octa}}$	$\text{Te}_{\text{Li, TM layer}}$
Te- O_A	Te	0.00	0.00	0.00	Ni- O_A	Ni	-0.11	-0.07	-0.11
	O_A	-0.22	-0.10	-0.11		O_A	+0.97	+0.76	+0.73
Te- O_B	Te	0.00	0.00	0.00	Ni- O_B	Ni	-0.10	-0.07	-0.06
	O_B	-0.27	-0.20	-0.13		O_B	+0.71	+0.77	+0.79
Te- O_C	Te	0.00	0.00	0.00	Ni- O_C	Ni	-0.02	-0.02	-0.05
	O_C	-0.18	-0.02	-0.24		O_C	+0.97	+0.74	+0.75
Te- O_D	O_D	.	-0.22	-0.27	Ni- O_D	O_D	.	+0.56	+0.46
Sum(Dangling O)		-0.67	-0.54	-0.75	Sum(Dangling O)		+2.65	+2.83	+2.73
The other O ions in the cell		+1.06	+1.04	+1.14	The other O ions in the cell		-2.17	-2.13	-2.24
All Ni ions in the cell		-0.40	-0.50	-0.39	All Ni ions in the cell		-0.25	-0.28	-0.27
All Te ions in the cell		0.00	0.00	0.00	All Te ions in the cell		0.00	-0.27	0.00

2.4 Concluding remarks

We have established a trilateral picture linking structural disorder, covalent bonding, and oxygen redox chemistry in lithium-rich layered transition metal oxide electrodes. Our findings demonstrate that structural disordering and concomitant bonding rearrangements occur in the direction of stabilizing oxygen redox. It was elucidated that the extent of O-O and TM-O π hybridization is primarily governed by the occupancy of O 2*p* NB states and metal-oxygen covalency. Our results support the important perspective that although the initial oxygen redox capacity is rooted in the presence of oxygen non-bonding states, the hybridized TM-O and O-O states will be the major sources of charge compensation after structural reorganization¹⁴. In this light, the present understandings of some redox mechanisms need to be revisited.

Despite the stabilization effects, bonding rearrangements inevitably compromise the redox symmetry by significantly altering the electronic structure. The restoration of bonding arrangements is inhibited by the hysteretic nature of structural disorder and the severe structural deformation due to oxygen dimerization. Therefore, future research should be dedicated to identifying the alternative mechanisms capable of stabilizing oxygen redox not involving structural disorders. Our theoretical insight here is expected to expedite the development of electrodes based on oxygen redox, and broadly enrich the fundamental understandings in related fields of oxygen redox reactions such as water splitting and solid oxide fuel cell as well.

2.5 References

1. Cano, Z. P. *et al.* Batteries and fuel cells for emerging electric vehicle markets. *Nature Energy* **3**, 279-289 (2018).
2. Seo, D.-H. *et al.* The structural and chemical origin of the oxygen redox activity in layered and cation-disordered Li-excess cathode materials. *Nature Chemistry* **8**, 692-697 (2016).
3. Li, M. *et al.* Cationic and anionic redox in lithium-ion based batteries. *Chemical Society Reviews* **49**, 1688-1705 (2020).
4. Konishi, H. *et al.* Origin of hysteresis between charge and discharge processes in lithium-rich layer-structured cathode material for lithium-ion battery. *Journal of Power Sources* **298**, 144-149 (2015).
5. Assat, G. *et al.* Fundamental interplay between anionic/cationic redox governing the kinetics and thermodynamics of lithium-rich cathodes. *Nature Communications* **8**, 2219 (2017).
6. Assat, G., Glazier, S. L., Delacourt, C. & Tarascon, J.-M. Probing the thermal effects of voltage hysteresis in anionic redox-based lithium-rich cathodes using isothermal calorimetry. *Nature Energy* **4**, 647-656 (2019).
7. Assat, G., Iadecola, A., Delacourt, C., Dedryvère, R. & Tarascon, J.-M. Decoupling Cationic–Anionic Redox Processes in a Model Li-Rich Cathode via Operando X-ray Absorption Spectroscopy. *Chemistry of Materials* **29**, 9714-9724 (2017).

8. Gent, W. E., Abate, I. I., Yang, W., Nazar, L. F. & Chueh, W. C. Design Rules for High-Valent Redox in Intercalation Electrodes. *Joule* **4**, 1369-1397 (2020).
9. Eum, D. *et al.* Voltage decay and redox asymmetry mitigation by reversible cation migration in lithium-rich layered oxide electrodes. *Nature Materials* **19**, 419-427 (2020).
10. House, R. A. *et al.* Superstructure control of first-cycle voltage hysteresis in oxygen-redox cathodes. *Nature* **577**, 502-508 (2020).
11. House, R. A. *et al.* First-cycle voltage hysteresis in Li-rich 3d cathodes associated with molecular O₂ trapped in the bulk. *Nature Energy* **5**, 777-785 (2020).
12. Kleiner, K. *et al.* Origin of High Capacity and Poor Cycling Stability of Li-Rich Layered Oxides: A Long-Duration in Situ Synchrotron Powder Diffraction Study. *Chemistry of Materials* **30**, 3656-3667 (2018).
13. Nakamura, T. *et al.* Oxygen defect engineering for the Li-rich cathode material Li_{1.2}Ni_{0.13}Co_{0.13}Mn_{0.54}O_{2-δ}. *Journal of Materials Chemistry A* **9**, 3657-3667 (2021).
14. Hong, J. *et al.* Metal–oxygen decoordination stabilizes anion redox in Li-rich oxides. *Nature Materials* **18**, 256-265 (2019).
15. Talaie, E., Kim, S. Y., Chen, N. & Nazar, L. F. Structural Evolution and Redox Processes Involved in the Electrochemical Cycling of P2–Na_{0.67}[Mn_{0.66}Fe_{0.20}Cu_{0.14}]O₂. *Chemistry of Materials* **29**, 6684-6697 (2017).

16. Gent, W. E. *et al.* Coupling between oxygen redox and cation migration explains unusual electrochemistry in lithium-rich layered oxides. *Nature Communications* **8**, 2091 (2017).
17. Luo, K. *et al.* Charge-compensation in 3d-transition-metal-oxide intercalation cathodes through the generation of localized electron holes on oxygen. *Nature Chemistry* **8**, 684-691 (2016).
18. Yan, P. *et al.* Injection of oxygen vacancies in the bulk lattice of layered cathodes. *Nature Nanotechnology* **14**, 602-608 (2019).
19. Li, Q. *et al.* Dynamic imaging of crystalline defects in lithium-manganese oxide electrodes during electrochemical activation to high voltage. *Nature Communications* **10**, 1692 (2019).
20. Ku, K. *et al.* Suppression of Voltage Decay through Manganese Deactivation and Nickel Redox Buffering in High-Energy Layered Lithium-Rich Electrodes. *Advanced Energy Materials* **8**, 1800606 (2018).
21. Hu, E. *et al.* Evolution of redox couples in Li- and Mn-rich cathode materials and mitigation of voltage fade by reducing oxygen release. *Nature Energy* **3**, 690-698 (2018).
22. Langmuir, I. THE ARRANGEMENT OF ELECTRONS IN ATOMS AND MOLECULES. *Journal of the American Chemical Society* **41**, 868-934 (1919).
23. Ben Yahia, M., Vergnet, J., Saubanère, M. & Doublet, M.-L. Unified picture of anionic redox in Li/Na-ion batteries. *Nature Materials* **18**, 496-502 (2019).

24. Vergnet, J., Saubanère, M., Doublet, M.-L. & Tarascon, J.-M. The Structural Stability of P2-Layered Na-Based Electrodes during Anionic Redox. *Joule* **4**, 420-434 (2020).
25. Sudayama, T. *et al.* Multiorbital bond formation for stable oxygen-redox reaction in battery electrodes. *Energy & Environmental Science* **13**, 1492-1500 (2020).
26. Xie, Y., Saubanère, M. & Doublet, M. L. Requirements for reversible extra-capacity in Li-rich layered oxides for Li-ion batteries. *Energy & Environmental Science* **10**, 266-274 (2017).
27. Chen, Z., Li, J. & Zeng, X. C. Unraveling Oxygen Evolution in Li-Rich Oxides: A Unified Modeling of the Intermediate Peroxo/Superoxo-like Dimers. *Journal of the American Chemical Society* **141**, 10751-10759 (2019).
28. Blöchl, P. E. Projector augmented-wave method. *Physical Review B* **50**, 17953-17979 (1994).
29. Kresse, G. & Furthmüller, J. Efficiency of ab-initio total energy calculations for metals and semiconductors using a plane-wave basis set. *Computational Materials Science* **6**, 15-50 (1996).
30. Perdew, J. P., Burke, K. & Ernzerhof, M. Generalized Gradient Approximation Made Simple. *Physical Review Letters* **77**, 3865-3868 (1996).
31. Heyd, J., Scuseria, G. E. & Ernzerhof, M. Hybrid functionals based on a

- screened Coulomb potential. *The Journal of Chemical Physics* **118**, 8207-8215 (2003).
32. Kresse, G. & Furthmüller, J. Efficient iterative schemes for ab initio total-energy calculations using a plane-wave basis set. *Physical Review B* **54**, 11169-11186 (1996).
33. Dronskowski, R. & Bloechl, P. E. Crystal orbital Hamilton populations (COHP): energy-resolved visualization of chemical bonding in solids based on density-functional calculations. *The Journal of Physical Chemistry* **97**, 8617-8624 (1993).
34. Deringer, V. L., Tchougréeff, A. L. & Dronskowski, R. Crystal Orbital Hamilton Population (COHP) Analysis As Projected from Plane-Wave Basis Sets. *The Journal of Physical Chemistry A* **115**, 5461-5466 (2011).
35. Toukmaji, A. Y. & Board, J. A. Ewald summation techniques in perspective: a survey. *Computer Physics Communications* **95**, 73-92 (1996).
36. Wang, L., Maxisch, T. & Ceder, G. Oxidation energies of transition metal oxides within the GGA+U framework. *Physical Review B* **73**, 195107 (2006).
37. Chase, M. W. *et al.* JANAF Thermochemical Tables, 1982 Supplement. *Journal of Physical and Chemical Reference Data* **11**, 695-940 (1982).
38. Nosé, S. A unified formulation of the constant temperature molecular dynamics methods. *The Journal of Chemical Physics* **81**, 511-519 (1984).
39. Hoover, W. G. Canonical dynamics: Equilibrium phase-space distributions. *Physical Review A* **31**, 1695-1697 (1985).

40. Nakayama, K., Ishikawa, R., Kobayashi, S., Shibata, N. & Ikuhara, Y. Dislocation and oxygen-release driven delithiation in Li_2MnO_3 . *Nature Communications* **11**, 4452 (2020).
41. Du, K. *et al.* Exploring reversible oxidation of oxygen in a manganese oxide. *Energy & Environmental Science* **9**, 2575-2577 (2016).
42. Song, B. *et al.* A novel P3-type $\text{Na}_{2/3}\text{Mg}_{1/3}\text{Mn}_{2/3}\text{O}_2$ as high capacity sodium-ion cathode using reversible oxygen redox. *Journal of Materials Chemistry A* **7**, 1491-1498 (2019).
43. Cramer, C. J., Tolman, W. B., Theopold, K. H. & Rheingold, A. L. Variable character of O—O and M—O bonding in side-on (η^2) 1:1 metal complexes of O_2 . *Proceedings of the National Academy of Sciences* **100**, 3635 (2003).
44. Grimaud, A. *et al.* Chemical Activity of the Peroxide/Oxide Redox Couple: Case Study of $\text{Ba}_5\text{Ru}_2\text{O}_{11}$ in Aqueous and Organic Solvents. *Chemistry of Materials* **30**, 3882-3893 (2018).
45. Morrison, S. R. *The chemical physics of surfaces*. (Springer Science & Business Media, 2013).
46. Abrahams, S. C. & Kalnajs, J. The crystal structure of [alpha]-potassium superoxide. *Acta Crystallographica* **8**, 503-506 (1955).
47. Pandey, B., Ansari, A., Vyas, N. & Rajaraman, G. Structures, bonding and reactivity of iron and manganese high-valent metal-oxo complexes: A computational investigation. *Journal of Chemical Sciences* **127**, 343-352 (2015).

48. Hughbanks, T. & Hoffmann, R. Chains of trans-edge-sharing molybdenum octahedra: metal-metal bonding in extended systems. *Journal of the American Chemical Society* **105**, 3528-3537 (1983).
49. Strobel, P. & Lambert-Andron, B. Crystallographic and magnetic structure of Li_2MnO_3 . *Journal of Solid State Chemistry* **75**, 90-98 (1988).
50. Kitchaev, D. A., Vinkeviciute, J. & Van der Ven, A. Delocalized Metal–Oxygen π -Redox Is the Origin of Anomalous Nonhysteretic Capacity in Li-Ion and Na-Ion Cathode Materials. *Journal of the American Chemical Society* **143**, 1908-1916 (2021).
51. Yu, Y. *et al.* Revealing Electronic Signatures of Lattice Oxygen Redox in Lithium Ruthenates and Implications for High-Energy Li-Ion Battery Material Designs. *Chemistry of Materials* **31**, 7864-7876 (2019).
52. Li, B. *et al.* Understanding the Stability for Li-Rich Layered Oxide Li_2RuO_3 Cathode. *Advanced Functional Materials* **26**, 1330-1337 (2016).
53. Trnka, T. M. & Parkin, G. A survey of terminal chalcogenido complexes of the transition metals: trends in their distribution and the variation of their M=E bond lengths. *Polyhedron* **16**, 1031-1045 (1997).
54. Ning, F. *et al.* Inhibition of oxygen dimerization by local symmetry tuning in Li-rich layered oxides for improved stability. *Nature Communications* **11**, 4973 (2020).
55. McCalla, E. *et al.* Visualization of O-O peroxo-like dimers in high-capacity layered oxides for Li-ion batteries. *Science* **350**, 1516 (2015).

56. Taylor, Z. N. *et al.* Stabilization of O–O Bonds by d^0 Cations in $\text{Li}_{4+x}\text{Ni}_{1-x}\text{WO}_6$ ($0 \leq x \leq 0.25$) Rock Salt Oxides as the Origin of Large Voltage Hysteresis. *Journal of the American Chemical Society* **141**, 7333-7346 (2019).
57. Luo, N. *et al.* Anionic Oxygen Redox in the High-Lithium Material Li_8SnO_6 . *Chemistry of Materials* **33**, 834-844 (2021).
58. Kim, I., Do, J., Kim, H. & Jung, Y. Charge-transfer descriptor for the cycle performance of $\beta\text{-Li}_2\text{MO}_3$ cathodes: role of oxygen dimers. *Journal of Materials Chemistry A* **8**, 2663-2671 (2020).
59. Yamada, I. *et al.* Systematic Study of Descriptors for Oxygen Evolution Reaction Catalysis in Perovskite Oxides. *The Journal of Physical Chemistry C* **122**, 27885-27892 (2018).
60. Sathiya, M. *et al.* Reversible anionic redox chemistry in high-capacity layered-oxide electrodes. *Nature Materials* **12**, 827-835 (2013).
61. Lyu, Y. *et al.* Correlations between Transition-Metal Chemistry, Local Structure, and Global Structure in $\text{Li}_2\text{Ru}_{0.5}\text{Mn}_{0.5}\text{O}_3$ Investigated in a Wide Voltage Window. *Chemistry of Materials* **29**, 9053-9065 (2017).
62. Sathiya, M. *et al.* $\text{Li}_4\text{NiTeO}_6$ as a positive electrode for Li-ion batteries. *Chemical Communications* **49**, 11376-11378 (2013).
63. Ku, K. *et al.* A new lithium diffusion model in layered oxides based on asymmetric but reversible transition metal migration. *Energy & Environmental Science* **13**, 1269-1278 (2020).

64. Lin, C., Mitra, C. & Demkov, A. A. Orbital ordering under reduced symmetry in transition metal perovskites: Oxygen vacancy in SrTiO₃. *Physical Review B* **86**, 161102 (2012).
65. Vinckevičiūtė, J., Radin, M. D., Faenza, N. V., Amatucci, G. G. & Van der Ven, A. Fundamental insights about interlayer cation migration in Li-ion electrodes at high states of charge. *Journal of Materials Chemistry A* **7**, 11996-12007 (2019).
66. Tan, X., Liu, R., Xie, C. & Shen, Q. Modified structural characteristics and enhanced electrochemical properties of oxygen-deficient Li₂MnO_{3-δ} obtained from pristine Li₂MnO₃. *Journal of Power Sources* **374**, 134-141 (2018).
67. Tsuchimoto, A. *et al.* Nonpolarizing oxygen-redox capacity without O-O dimerization in Na₂Mn₃O₇. *Nature Communications* **12**, 631 (2021).
68. Abate, I. I. *et al.* Coulombically-stabilized oxygen hole polarons enable fully reversible oxygen redox. *arXiv preprint arXiv:2010.13107* (2020).
69. Okubo, M. & Yamada, A. Molecular Orbital Principles of Oxygen-Redox Battery Electrodes. *ACS Applied Materials & Interfaces* **9**, 36463-36472 (2017).
70. Assat, G. & Tarascon, J.-M. Fundamental understanding and practical challenges of anionic redox activity in Li-ion batteries. *Nature Energy* **3**, 373-386 (2018).
71. Zaanen, J., Sawatzky, G. A. & Allen, J. W. Band gaps and electronic

- structure of transition-metal compounds. *Physical Review Letters* **55**, 418-421 (1985).
72. Song, J.-H. *et al.* Anionic Redox Activity Regulated by Transition Metal in Lithium-Rich Layered Oxides. *Advanced Energy Materials* **10**, 2001207 (2020).
 73. Holland, P. L. Metal–dioxygen and metal–dinitrogen complexes: where are the electrons? *Dalton Transactions* **39**, 5415-5425 (2010).
 74. Chen, H. & Islam, M. S. Lithium Extraction Mechanism in Li-Rich Li_2MnO_3 Involving Oxygen Hole Formation and Dimerization. *Chemistry of Materials* **28**, 6656-6663 (2016).
 75. Lee, E. & Persson, K. A. Structural and Chemical Evolution of the Layered Li-Excess Li_xMnO_3 as a Function of Li Content from First-Principles Calculations. *Advanced Energy Materials* **4**, 1400498 (2014).
 76. Wang, R. *et al.* Atomic Structure of Li_2MnO_3 after Partial Delithiation and Re-Lithiation. *Advanced Energy Materials* **3**, 1358-1367 (2013).
 77. Croy, J. R. *et al.* First-Cycle Evolution of Local Structure in Electrochemically Activated Li_2MnO_3 . *Chemistry of Materials* **26**, 7091-7098 (2014).
 78. Rong, X. *et al.* Structure-Induced Reversible Anionic Redox Activity in Na Layered Oxide Cathode. *Joule* **2**, 125-140 (2018).
 79. Wu, J. *et al.* Dissociate lattice oxygen redox reactions from capacity and voltage drops of battery electrodes. *Science Advances* **6**, eaaw3871 (2020).

80. de la Llave, E. *et al.* Improving Energy Density and Structural Stability of Manganese Oxide Cathodes for Na-Ion Batteries by Structural Lithium Substitution. *Chemistry of Materials* **28**, 9064-9076 (2016).
81. Kang, S. M. *et al.* Structural and Thermodynamic Understandings in Mn-Based Sodium Layered Oxides during Anionic Redox. *Advanced Science* **7**, 2001263 (2020).
82. Dai, K. *et al.* High Reversibility of Lattice Oxygen Redox Quantified by Direct Bulk Probes of Both Anionic and Cationic Redox Reactions. *Joule* **3**, 518-541 (2019).
83. Yabuuchi, N. *et al.* A new electrode material for rechargeable sodium batteries: P2-type $\text{Na}_{2/3}[\text{Mg}_{0.28}\text{Mn}_{0.72}]\text{O}_2$ with anomalously high reversible capacity. *Journal of Materials Chemistry A* **2**, 16851-16855 (2014).
84. Maitra, U. *et al.* Oxygen redox chemistry without excess alkali-metal ions in $\text{Na}_{2/3}[\text{Mg}_{0.28}\text{Mn}_{0.72}]\text{O}_2$. *Nature Chemistry* **10**, 288-295 (2018).
85. House, R. A. *et al.* What Triggers Oxygen Loss in Oxygen Redox Cathode Materials? *Chemistry of Materials* **31**, 3293-3300 (2019).
86. Rong, X., Gao, F., Lu, Y., Yang, K. & Hu, Y. P2-type $\text{Na}_{0.6}[\text{Mg}(\text{II})_{0.3}\text{Mn}(\text{IV})_{0.7}]\text{O}_2$ as a new model material for anionic redox reaction. *Chinese Chemical Letters* **29**, 1791-1794 (2018).
87. Reed, J. & Ceder, G. Role of Electronic Structure in the Susceptibility of Metastable Transition-Metal Oxide Structures to Transformation. *Chemical Reviews* **104**, 4513-4534 (2004).

88. Sathiya, M. *et al.* Origin of voltage decay in high-capacity layered oxide electrodes. *Nature Materials* **14**, 230-238 (2015).
89. Bao, J., Wu, D., Tang, Q., Ma, Z. & Zhou, Z. First-principles investigations on delithiation of $\text{Li}_4\text{NiTeO}_6$. *Physical Chemistry Chemical Physics* **16**, 16145-16149 (2014).

Chapter 3. Voltage decay and redox asymmetry mitigation by reversible cation migration in lithium-rich layered oxide electrodes

(The content of this chapter has been published in *Nature Materials*. [Eum, D., Kim, B. *et al.*, *Nature Materials* **2020**, 19, 419-427.]-Reproduced by permission of Nature Publishing Group)

3.1 Introduction

With the advent of electrified transportation, there is a pressing demand for improvements of rechargeable lithium-ion batteries¹. In particular, the energy-density ceiling placed on the cathode materials has been a primary factor precluding the full-scale deployment of green energy technologies². Among cathode materials foreseen to transcend such limitations, lithium-rich layered oxides hold the greatest promise because of their high reversible capacity (exceeding 250 mAh g⁻¹) and high-voltage anionic redox chemistry^{3,4}. Nonetheless, the voltage decay, or gradual decrease in the average discharge voltage during cycling, and the resulting inevitable energy decay remain some of the most pernicious problems jeopardizing their real-world application, while some technical hurdles such as lower crystallographic/tap densities than current lithium-stoichiometric layered oxides (lithium nickel-cobalt-aluminum oxides and lithium nickel-manganese-cobalt oxides) still need to be

addressed⁴⁻⁶. Moreover, the voltage decay is pronounced in 3d metal-based layered lithium-rich oxides of practical interest, such as $\text{Li}[\text{Li}_x\text{Ni}_y\text{Mn}_{(1-x-y)}]\text{O}_2$ (denoted as LLNMOs) and $\text{Li}[\text{Li}_x\text{Ni}_y\text{Mn}_z\text{Co}_{1-x-y-z}]\text{O}_2$ (denoted as LLNMCOs)^{4,7,8}. With this backdrop, formidable research efforts have been focused on unraveling the origin of the voltage decay and suppressing it based on established understandings.

A clear consensus has been reached that the voltage decay is primarily rooted in progressive structural transformation of lithium-rich layered oxides^{6,7,9-11}. Cation migration from the transition metal (TM) layer to the Li layer to form $\text{TM}_{\text{Li}}\text{-V}_{\text{TM}}$ anti-site defect pairs during the charging of lithium-rich layered 3d metal oxides has been identified experimentally and confirmed using various analytical tools^{9,11,12}. The limited reversibility of intra-cycle TM migration results in the cumulative formation of a spinel-like disordered phase¹²⁻¹⁴, and this growth of the low-voltage spinel-like phase has commonly been associated with voltage decay¹⁴⁻¹⁶. More specifically, a comprehensive investigation of the $\text{Li}_2\text{Ru}_{1-x}\text{M}_x\text{O}_3$ ($\text{M} = \text{Mn, Ti, Sn}$) system⁶ and LLNMCOs^{11,17} demonstrated that upon extended cycling, more TM ions were trapped in the Li layer with exacerbated voltage fade. Of paramount importance in understanding the fundamentals of the voltage decay is that its essential determinant is not the TM migration itself but the resulting confinement of TM ions in the Li layer. At the low Li stoichiometries of most lithium-rich layered oxides, TM migration to the Li layer is thermodynamically favorable and is thus an unavoidable phenomenon during the charge process¹⁸⁻²⁰. Therefore, although various effective

approaches, including surface coating¹², cation doping²¹, additives to electrolyte²², and composition tuning^{7,23}, have been used to mitigate the TM migration, its ultimate prevention during long-term cycling has not yet been achieved.

Considering both the underlying origin of the voltage decay and the inevitability of TM migration, a substantive key lies in improving the intra-cycle reversibility of TM migration. In lithium layered oxides, what limits the reversible return of TM ions is thought to be the intralayer movements of TM ions within the Li layer, which is generally initiated by the TM migration from the initial tetrahedral site to neighboring octahedral sites in Li layer. For example, in conventional O3-type layered oxides, TM ions once migrated to the intermediary tetrahedral site of the Li layer can readily and permanently move to adjacent octahedral Li sites because of the thermodynamic preference for octahedral sites, as indicated by the yellow arrow in figure 3.1a²⁴. Therefore, the quest for reversible TM migration necessitates the implementation of thermodynamic or kinetic roadblocks that prevent intralayer movements of TM ions. In terms of thermodynamic approaches, recent reports on sodium layered oxides have suggested that the use of distinct oxygen lattices with the P3-^{25,26} or P2-²⁷ structure can prevent the TM occupation of guest-ion sites benefiting from the size mismatch between the TM ion and the large prismatic site. In a similar vein, a qualitative hypothesis has been proposed in studies on lithium layered oxides that by employing an O2-type layered structure with ABCBA oxygen stacking²⁸ (see figure 3.1b), some Li sites can be thermodynamically destabilized

against TM migration^{29,30}. The local environments of Li sites in the O2 and O3 structures substantially differ: LiO₆ octahedra share faces with TMO₆ octahedra in the former, whereas they share only edges with TMO₆ octahedra in the latter. Thus, in the O2 structure, TM migration from the intermediate sites to adjacent Li sites is expected to be unfavorable because of the large electrostatic repulsion between face-shared cations. This blockade of face-shared sites can facilitate the return of TM ions during the discharge process by streamlining the return path, as illustrated in figure 3.1b. However, despite these implications, no direct approach has been reported to observe or achieve reversible TM migration by utilizing an alternative oxygen lattice for lithium-rich layered oxides.

In this work, we first demonstrate that reversible intra-cycle TM migration can be achieved by modifying the oxygen lattice of lithium-rich layered oxides. To achieve this aim, we apply the O2 structure to cobalt-free LLNMOs with archetypal TM composition to obtain the O2-phase Li_x(Li_{0.2}Ni_{0.2}Mn_{0.6})O₂ ($x \approx 0.83$), whose preliminary electrochemical activity was very recently reported³¹. We demonstrate that O2-LLNMOs inherently allow reversible intra-cycle TM migration, thus delivering outstanding voltage retention over extended cycling and far outperforming their O3-phase counterparts and other lithium-rich layered 3d metal oxides. Structural characterization using scanning transmission electron microscopy (STEM), X-ray Diffraction (XRD), Raman spectroscopy, and high-resolution TEM (HR-TEM) analyses reveal that the suppressed voltage decay arises from the

retention of the pristine layered structure with highly reversible TM migration over extended cycling. In addition, with the aid of first-principles calculations, it is shown that high energy penalties associated with the TM occupation of Li sites of O2-LLNMOs prevent movements of TM ions in Li layer, facilitating the return of TM ions to the original sites. We further confirm that the improved reversibility of TM migration also benefits mitigating the asymmetry of the anionic redox, which has been suspected to stem from the presence of TM ions in the Li layer during discharging and afflict the cells by inducing voltage hysteresis^{10,32,33}. Our findings indicate that tailoring the migration path of TM ions provides a viable strategy to address the issues of voltage decay and hysteresis, which may help rejuvenate the research field of lithium-rich layered oxides.

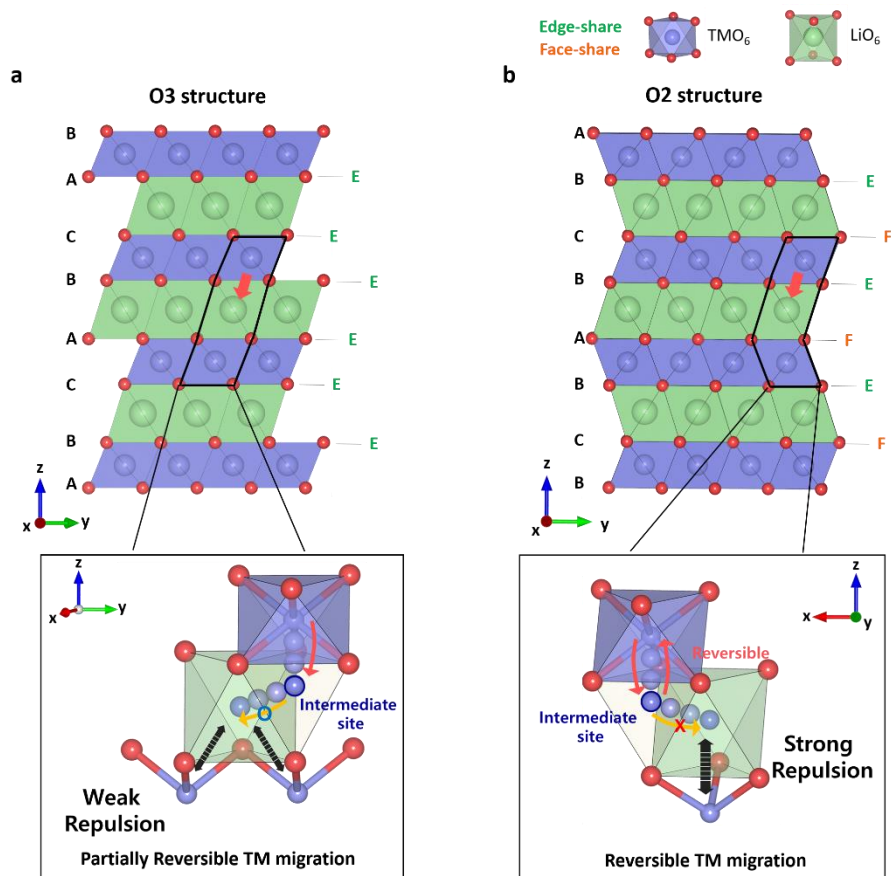


Figure 3.1. Comparison of crystal structures and cation migration paths.

Schematic illustrations of crystal structures of **a**, O3-type and **b**, O2-type lithium layered oxides. The figures below show the TM migration paths on a magnified scale. Although TM ions in the O3 structure can readily occupy Li sites that share only edges with neighboring cations, the TM ions in the O2 structure are subject to strong repulsion when they occupy Li sites face-sharing with neighboring cations.

3.2 Experimental and computational details

3.2.1 Synthesis

To synthesize $\text{P2-Na}_{5/6}(\text{Li}_{0.2}\text{Ni}_{0.2}\text{Mn}_{0.6})\text{O}_2$, stoichiometric amounts of $\text{LiCH}_3\text{COO}\cdot 2\text{H}_2\text{O}$ (99%, Sigma-Aldrich), $\text{NaCH}_3\text{COO}\cdot 3\text{H}_2\text{O}$ (99%, Sigma-Aldrich), $\text{Ni}(\text{CH}_3\text{COO})_2\cdot 4\text{H}_2\text{O}$ (98%, Sigma-Aldrich), and $\text{Mn}(\text{CH}_3\text{COO})_2\cdot 4\text{H}_2\text{O}$ (99%, Sigma-Aldrich) were dissolved in distilled water containing appropriate amounts of resorcinol (99%, Sigma-Aldrich) and formaldehyde. To mediate the volatility of lithium and sodium at high temperature, 5% excess of lithium and sodium sources were compensated by Li_2CO_3 (99.99%, Sigma-Aldrich) and Na_2CO_3 (99%, Sigma-Aldrich). The mixture was heated with continuous stirring at 70 °C for 2 h and then at 90 °C overnight without stirring. Finally, the P2 phase was obtained by additional heat treatment at 500 °C for 5 h and 900 °C for 10 h with intermediate grinding. In the following ion-exchange step, the resultant P2-phase powders were added to 10 times excess amount of 5 M LiBr (99%, Sigma-Aldrich) solution in hexanol and then heated at 120 °C for 24 h to obtain O2-phase material. After ion exchange, the product was rinsed with ethanol and distilled water several times. The entire ion-exchange process was repeated once more to complete the substitution of sodium with lithium.

3.2.2 Electrochemistry

The electrodes were fabricated using the following steps. A slurry of 80 wt% active materials, 10 wt% carbon black (Super P), and 10 wt% polyvinylidene fluoride

dissolved in *N*-methyl-2-pyrrolidone (NMP; 99.5%, Sigma-Aldrich) was cast onto aluminum foil. The resultant mixture was dried in a 70 °C vacuum oven overnight to allow the NMP to evaporate. Coin cells (CR2032, Hohsen) were assembled using the electrodes, a lithium counter electrode, a separator (GF/F filter, Whatman), and a 1 M solution of LiPF₆ in a mixture of ethyl carbonate and dimethyl carbonate (EC/DMC, 1:1 v/v) in an Ar-filled glove box. The galvanostatic charge/discharge process was performed in the voltage range of 2.0–4.8 V at room temperature using a potentiogalvanostat (WBCS 3000, WonA Tech).

3.2.3 XRD

as-prepared samples were characterized using XRD (D8 ADVANCE, Bruker, Bremen, Germany) with Cu-K α radiation ($\lambda=1.54178$ Å) at a scanning speed of 0.167° min⁻¹ in the 2θ range of 10°–70°. High-resolution powder diffraction (HRPD) was performed at beamline 9B at the Pohang Light Sources (PLS) in the Pohang Accelerator Laboratory (PAL), Republic of Korea. The data were collected over the 2θ range of 10°–133° with a step size of 0.01°, step time of 4 s, and wavelength of $\lambda=1.5226$ Å. Rietveld refinement of the XRD patterns was performed using the FullProf program.

3.2.4 Raman spectroscopy

Raman spectra of the pristine and 40-cycled electrodes were recorded using a Raman spectrometer (LabRAM HV Evolution, HORIBA, Japan) with an Ar laser as the excitation light source ($\lambda=532$ nm). The scattered light of the Raman signal was

collected in a backscattering geometry using a 50× microscope objective lens. The data were measured using an acquisition time of 20 s and 10 accumulations. The spectra were deconvoluted using the XPS Peak program.

3.2.5 XANES

XANES spectra of the harvested electrodes were obtained at beamline 7D at the PLS using a double-crystal monochromator containing two sets of Si(111) crystals. All the measurements were performed at room temperature, and the Ni and Mn K-edge spectra were collected in total electron yield mode. To accurately calibrate the energy scale and any drift of the monochromator position, metal foils were placed in a third chamber as a reference. All of the spectra were normalized and compared using the Athena program.

3.2.6 STXM

STXM analysis was performed at beamline 10A at the PLS to obtain the O K-edge and Ni and Mn L₃-edge spectra. Primary particles were drop-cast onto carbon-coated Cu TEM grids for the measurements. By keeping the focal position at the same particle, the two-dimensional transmitted photon intensity was recorded in pixel form at a fixed energy. To obtain image stacks, the same measurements were repeated over different X-ray energy ranges. The image stacks were acquired in 0.2 eV steps with a 2 ms dwell time and were aligned using the aXis 2000 software package.

3.2.7 SEM

Field-emission scanning electron microscopy (FE-SEM; SU-70, Hitachi, Japan)

analysis was used to examine the surface morphological changes during the ion-exchange process. To compensate for the low conductivity of both materials, the active materials were coated with Pt nanoparticles three times.

3.2.8 HR-TEM

The electrodes harvested in the pristine state and after 40 cycles were sonicated into particles in ethanol and transferred onto carbon-coated Cu grids to obtain HR-TEM images and SAED patterns using field-emission transmission electron microscopy (FE-TEM; JEOL, JEM-2100F, Japan).

3.2.9 Cs-STEM

Cross-sectional TEM specimens of the as-prepared and cycled electrode slurry films were prepared using focused ion beam (FIB) milling (FEI, Helios 650). The prepared specimens were used for high-angle annular dark-field imaging under 80 keV using aberration-corrected STEM (Cs-STEM; JEOL, JEM-ARM200F, Japan) with a point-to-point resolution of 0.08 nm.

3.2.10 First-principles calculations

The first-principles calculations in this work were conducted based on spin-polarized DFT calculations, as implemented in the Vienna *ab initio* simulation package (VASP)³⁴. All the DFT energies were estimated within the GGA + *U* parameterization using the Perdew–Burke–Ernzerhof (PBE) functional³⁵. Effective Hubbard-*U* parameters of 3.9 and 6.0 were applied to the 3d electrons of Mn and Ni atoms, respectively, in accordance with the values reported in previous works^{36,37}. A

plane-wave basis set was utilized with an energy cutoff of 520 eV and a $3 \times 3 \times 2$ gamma-point-centered k -point mesh. Unless otherwise stated, the lattice parameters and atomic positions were fully relaxed until the interatomic forces were smaller than 0.02 eV Å⁻¹. Detailed information regarding the model construction and TM migration analysis is provided in Chapter 3.3.6.

3.2.11 mRIXS

mRIXS experiments were performed in the iRIXS endstation at BL8.0.1 of the Advanced Light Source at Lawrence Berkeley National Laboratory³⁸. The emission energy resolution is about 0.25 eV through a VLS-spectrograph. The excitation energy resolution is about 0.3 eV. Data were collected with 0.2 eV steps upon excitation energies across the whole Oxygen K absorption edge.

3.3 Result and discussion

3.3.1 Electrochemistry of O2-LLNMOs

O2-LLNMOs were synthesized by applying ion-exchange method to as-synthesized P2-phase sodium layered oxides. Details on the crystal structure and chemical compositions, $\text{Li}_x(\text{Li}_{0.2}\text{Ni}_{0.2}\text{Mn}_{0.6})\text{O}_2$ ($x \approx 0.83$), are provided in Chapter 3.3.4. Figure 3.2a presents the first and second charge–discharge curves of O2-LLNMOs cycled in the voltage range of 2.0–4.8 V at 5 mA g^{-1} . A capacity of 235 mA g^{-1} was delivered for the first charge process of the O2-LLNMOs. Unlike the first cycle of the O3- $\text{Li}(\text{Li}_{0.2}\text{Ni}_{0.2}\text{Mn}_{0.6})\text{O}_2$, which was synthesized for a more precise comparison, the O2-LLNMOs delivered a markedly reduced irreversible capacity of 13.5 mAh g^{-1} , in comparisons with the first irreversible capacity of 74.3 mAh g^{-1} for O3-type counterparts (figure 3.3), implying highly reversible first-cycle redox behavior. Scanning transmission X-ray microscopy (STXM) analysis, which enables bulk-sensitive characterization of the redox centers^{39,40}, identified that the oxidation states of Ni and Mn in pristine O2- $\text{Li}_x(\text{Li}_{0.2}\text{Ni}_{0.2}\text{Mn}_{0.6})\text{O}_2$ were close to +2 and +4, respectively (figure 3.4)^{41,42}. Upon initial charging, cationic $\text{Ni}^{2+}/\text{Ni}^{4+}$ redox occurs in the low-voltage region, whereas the oxidation of the oxygen non-bonding states accounts for the charge compensation of the high-voltage plateau region. Further in-depth characterization of the redox mechanism and meticulous comparison of the O2 and O3 phases will be elaborated later.

For the initial two cycles (figure 3.2a), it is notable that the voltage profile of the second discharge was almost identical to that of the first discharge except for a small decrease in the capacity. To further clarify the long-term voltage retention of the O2-LLNMOs, cycling for additional 40 cycles was performed. Figure 3.2b presents the discharge profile of the O2-LLNMOs for the first and every 10 cycles until 40 cycles. Negligible voltage decay was observed in the discharge of the O2-LLNMOs during the 40 cycles. The average discharge voltages were well preserved and close to 3.5 V (see inset in figure 3.2b): 3.53, 3.53, and 3.48 V for the 1st, 20th, and 40th discharge process, respectively. This outstanding voltage retention and the high redox voltage of O2-LLNMOs are in stark contrast with that of the O3 phase, which revealed severe voltage fades in the same electrochemical cycling (figure 3.5), in accordance with many previous reports^{7,12,14,43}. Comparison of the dQ/dV^{-1} profiles tells clear suppression of the voltage decay in the O2-LLNMOs compared with that in the O3-LLNMOs (figure 3.2c). In the low-voltage region, a drastic down-shift of voltage was observed for the O3-LLNMOs upon cycling, and the major electrochemical activity was observed near 3.0 V (*vs.* Li/Li⁺) even after 10 cycles. In contrast, this change was absent and the redox peaks remained constant in the O2-LLNMOs, with the primary redox activity maintained between 3.5 and 4.0 V (*vs.* Li/Li⁺). The cycle stability of the O2-LLNMOs in figure 3.2d was comparable to that of the O3-LLNMOs, indicating that the retention of the practical energy density of the O2-LLNMOs ($\approx 82.5\%$, 599.6 Wh kg⁻¹ after 40 cycles) was superior to that of the O3-LLNMOs ($\approx 71.8\%$, 550 Wh kg⁻¹ after 40 cycles) because of the suppressed

voltage decay.

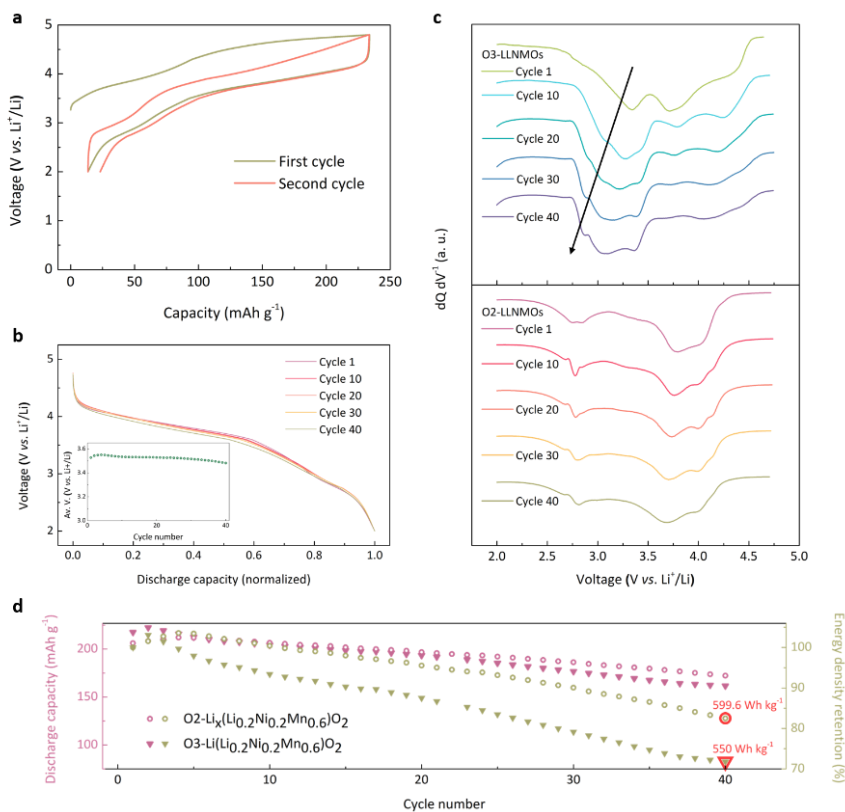


Figure 3.2. Suppression of voltage decay in O2-LLNMOs. **a**, First and second charge–discharge curves of O2-LLNMOs cycled in the voltage range of 2.0–4.8 V at a current density of 5 mA g⁻¹. **b**, Normalized discharge curves of O2-LLNMOs for 40 cycles. The data were collected every 10 cycles. The inset shows the change in the average voltage over 40 cycles. **c**, Comparison of voltage decay in dQ dV⁻¹ curves of O2- and O3-LLNMOs. The arrow in the profile of O3-LLNMOs highlights the drastic shift toward low voltage with cycling. **d**, Comparison of discharge capacity and energy density retention in O2- and O3-LLNMOs.

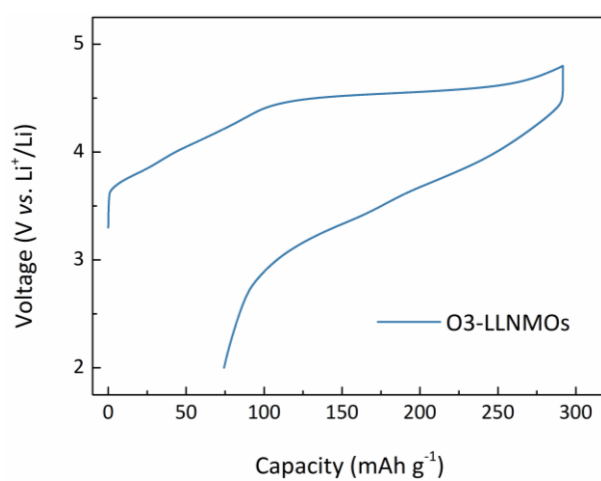


Figure 3.3. First cycle electrochemical profile of O3-LLNMOs measured at a current density of 5 mA g⁻¹ between 4.8 and 2.0 V.

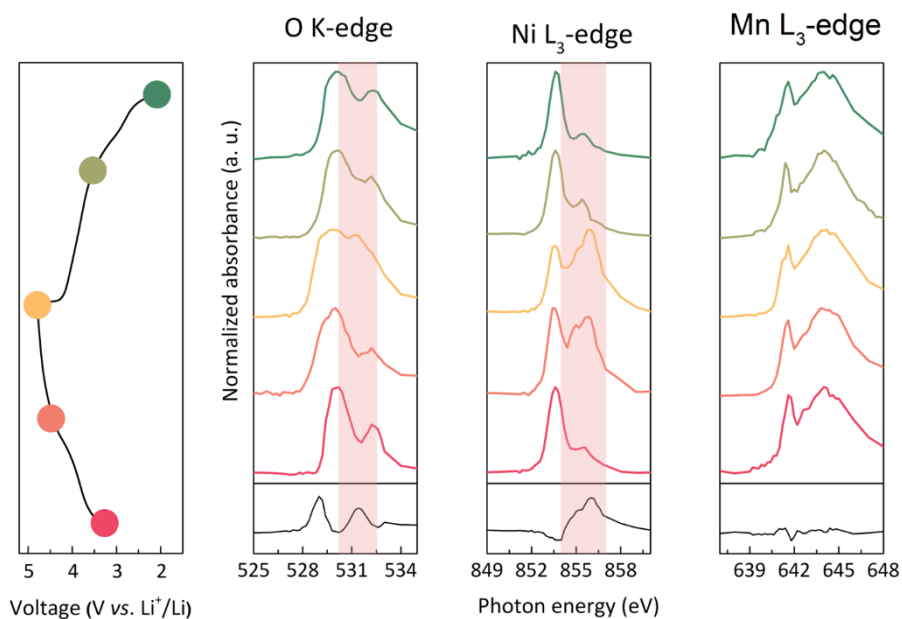


Figure 3.4. STXM spectra of the O K-edge and Ni, Mn L_3 -edges for different five points in the electrochemical curve of O₂-LLNMOs. The signal profiles at the bottom of each plot indicate the differences between absorbance of 4.8 V charged and pristine samples. The shaded regions represent evolution of 531.0 and 856 eV peaks in O K-edge and Ni L_3 -edge, respectively.

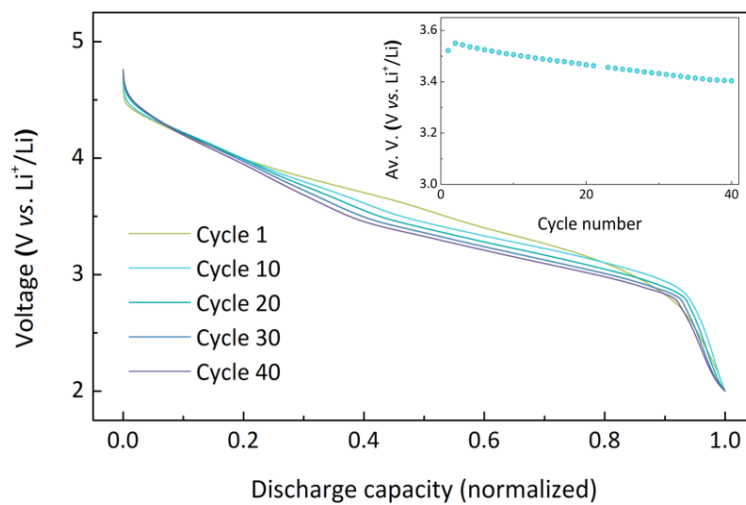


Figure 3.5. Normalized discharge capacity curves of O3-LLNMOs for 40 cycles. The data are collected for every 10 cycles. The inset shows the average voltage during 40 cycles.

3.3.2 Reversible cation migration in O2-LLNMOs

To understand the origin of the remarkable voltage retention of the O2-LLNMOs from the perspective of structural transitions, we carefully probed the configuration of the TM ions using spherical-aberration-corrected scanning transmission electron microscopy (Cs-STEM). Figure 3.6a and b present high-angle annular dark-field (HAADF) images of samples in charged and discharged states, respectively. HAADF images were obtained using Z-contrast imaging, and thus, the predominant signals in the images belong to heavy transition metals^{27,44}. In the HAADF-STEM image of the pristine O2-LLNMOs (figure 3.7), alternating TM layers and Li layers are clearly visible with no signal of TM ions detected in the Li layer, confirming the absence of $\text{TM}_{\text{Li}}\text{-V}_{\text{TM}}$ anti-site defects in the pristine state. In addition, the dumbbell-like spots in TM layers indicate the $\text{Li}^+\text{Mn}^{4+}_6$ or $(\text{Li}^+_x\text{Ni}^{2+}_{1-x})\text{Mn}^{4+}_6$ honeycomb ordering in the pristine O2-LLNMOs, which is a typical signature of lithium-rich layered materials (Chapter 3.3.5)^{7,45}. In contrast, the HAADF image for the charged samples (~ 4.8 V vs. Li/Li^+) provided in figure 3.6a reveals the noticeable presence of TM ions in the Li layer. The signal profile along the vertical direction in the box in figure 3.6a shows the evolution of new peaks at the center of two adjacent TM layers, as denoted by the arrows. These peaks suggest that a substantial amount of TM ions occupy vacant Li sites during the charge process. Selected area electron diffraction (SAED) patterns along the $[1\bar{1}0]$ axis also confirm the same TM behavior over a much broader region ($150\times$ magnified), with new diffraction spots as highlighted in the yellow

boxes in figure 3.6c. To assign these spots, we simulated SAED patterns assuming the disordered O2 structure in which 25% of TM ions occupy octahedral sites or tetrahedral sites in the Li layer (figure 3.8). The consistency between the experimental and simulated patterns indicates that massive TM migration occurred during the charge process, which is consistent with the TM migration behavior observed for the charge process of O3-LLNMOs^{11,33}. Surprisingly, in the STEM image of the fully discharged O2-LLNMOs, no signal of TM ions in the Li layer was detected (figure 3.6b). Contrast to the charged state, the peaks between the TM layers completely disappeared in the HAADF signal profile, indicating the complete return of TM ions to the TM layer upon discharge. The SAED pattern of the discharged samples no longer contained characteristic spots of TM_{Li} defects (the yellow boxes in figure 3.6c), as observed in figure 3.6d. The STEM analyses unequivocally confirm that interlayer TM migration is highly reversible during the successive charge and discharge of O2-LLNMOs. This phenomenon has not been observed in other lithium-rich layered oxides that contain a considerable amount of 3d TMs such as Mn and Ni^{11,33}.

We performed first-principles calculations to elucidate the energetics of the TM migrations that enable this reversible behavior in O2-LLNMOs. Figure 3.6e presents schematic illustrations of the interlayer migration paths of TM ions in the O2 and O3 structures, respectively (see Chapter 3.3.6 for details). In the case of O3 structure, TM ions can migrate to the nearest neighboring tetrahedral site in the Li layer and subsequently to the octahedral Li site during the charge process. On the other hand,

in the O2 structure, TM ions can either migrate to the neighboring tetrahedral intermediate site (path A) or octahedral intermediate site (path B), followed by subsequent migration to the final octahedral (path A) and tetrahedral sites (path B), respectively. For these potential migration paths for O3 and O2 structures, we comparatively calculated the relative site energies of the intermediate and final sites considering all the possible TM configurations. Figure 3.6f presents the energy landscapes of selected cases in which migration to the intermediate site was the most thermodynamically feasible (see Tables 3.4–3.6 for the energetics of other cases). When TM ions move in the O3 structure, the lowest relative site energy of the intermediate site is estimated to be -0.19 eV, and that of the adjacent Li octahedral site (“Edge_{octa}”) is -0.06 eV. It indicates that once TM ion moves to the intermediate site, further migration to the adjacent octahedral Li site is quite feasible. It would inevitably complicate the return of the TM ions to the initial site. TM ions may be led astray by further interactions with Li ions or other TM ions in the Li layer, making the return of TM ions to the original TM site nearly impossible. However, for TM ions in the O2 phase, the relative site energy at the final Li site is substantially higher (0.52 and 0.91 eV for path A (“Face_{octa}”) and path B (“Face_{tetra}”), respectively) destabilizing TM occupancy, whereas the TM in intermediate sites may remain stable in the de-lithiated states. These results suggest that TM migrations to the Li layer occur in the charged states, as observed in figure 3.6a, but that further intra-layer migration in the Li layer is significantly inhibited in the O2 structure. The intra-layer migration along paths A and B in the O2 structure requires a thermodynamic penalty

of approximately 0.91 and 1.19 eV, respectively. And, while these values are obtained for the cases in which a moving TM ion share a face with Mn in the TM layer, the site energies are all positive at other face-sharing sites in the O2 structure, regardless of the type of cation that faces the moving TM ion (see Chapter 3.3.6). This result is reasonable considering that the final Li sites in the O2 phase share a face with cations in the TM layer, as shown in figure 3.1b. Because TM ions in O2-LLNMOs are predicted to remain in the original or intermediate sites during charging, they can readily return to the original sites upon re-lithiation, as demonstrated in figure 3.6b. Note that in certain circumstances where the empty Li sites in the TM layer provide electrostatically favorable sites for TM ion, the one-step intra-layer TM migration can be occasionally allowed. Nonetheless, such one-step migrations were not expected to significantly reduce the overall reversibility due to the rarity of such circumstances and the difficulties of subsequent TM migrations (Chapter 3.3.6).

To further verify the reversible cation migration in O2-LLNMOs over extended cycling, powder XRD analysis of the pristine and 10-, 20-, and 40-cycled electrodes was conducted (figure 3.9a and Table 3.1). The XRD pattern of the pristine state contains well-defined honeycomb superstructure peaks at $2\theta = 20.8^\circ$, 24.2° , 29.1° , and 33.3° , which correspond to $(1/3\ 1/3\ 0)$, $(1/3\ 1/3\ 1)$, $(1/3\ 1/3\ 2)$, and $(1/3\ 1/3\ 3)$ planes, respectively³⁰. Each superstructure peak is well preserved even after 40 cycles, which indicates that the honeycomb orderings in the discharged samples were not destroyed by any permanent TM migrations, further supporting the reversibility of TM migration upon extended cycling. This behavior contrasts with that of the O3

phase, which typically loses in-plane cation ordering in the TM layers as the amount of TM/Li disordering increases with prolonged cycling^{6,11,33}.

Raman spectroscopy analysis was also conducted to determine the changes in the bonding character during cycling. Figure 3.9b presents Raman spectra of the pristine and cycled O2-LLNMOs in the 300–700 cm^{-1} range whose peaks are attributed to the various vibration modes of TM–O bonding in lithium layered oxides^{13,41}. The first two peaks at 595 and 473 cm^{-1} are signatures of symmetric stretching (A_{1g}) and symmetrical deformation (E_g) of TM–O, respectively, in the layered structure, whereas the peak at 420 cm^{-1} arises from the LiMn_6 honeycomb ordering, which is exclusively observed in lithium-rich layered oxides. Notably, all of these Raman peaks were observed for both samples and were preserved even after 40 cycles. This finding clearly contrasts with the case for O3-LLNMOs. Previous studies have shown that the Raman peak at 595 cm^{-1} completely shifted to 572 cm^{-1} only after 5 cycles because of the substantial layered-to-spinel phase transformation of O3-LLNMOs^{13,41}. According to these previous reports, the peak at 627 cm^{-1} can be attributed to the symmetrical stretching of TM–O in the spinel domain, and the peak at 572 cm^{-1} results from the shift of the peak at 595 cm^{-1} in a new TM coordinating environment¹³. Although we also detected peaks at 627 and 572 cm^{-1} after 40 cycles, their intensities were much smaller than those in previous reports on O3-LLNMOs^{7,13}. In principle, the spinel phase formation in the O2 phase is inaccessible via room-temperature electrochemical cycling because the oxygen lattices are essentially incompatible, and phase transition requires major breakage of the strong metal–

oxygen bonds^{29,46}. Therefore, the evolution of these new peaks is likely to originate from the O3 phase impurity present in the sample during the pre-ion-exchange step.

HR-TEM analysis also supports the long-term structure preservation of O2-LLNMOs. As observed in figure 3.12 and figure 3.9c, the characteristic hexagonal $P6_3mc$ spot patterns were consistently observed both for the pristine and 40-cycled O2-LLNMOs. There were no signatures of any secondary phases, including a spinel-like phase or the traces of TM/Li disordering, in the patterns of the 40-cycled electrodes. More specifically, compared with the simulated pattern of the disordered O2 structure (figure 3.13), characteristic spots such as $\bar{1}\bar{1}0$, $0\bar{1}\bar{3}$, and $10\bar{3}$ pertaining to the disordered phase did not appear in the SAED pattern or its signal profile (figure 3.9c). This result differs from that for O3-LLNMOs, in which the spots of the spinel-like and disordered phase evolved only after 5 cycles⁷. The comparisons of structural evolution in the O2 and O3 phases using complementary XRD, Raman, and HR-TEM analyses clearly demonstrate that the global and local structures of the O2-LLNMOs are well maintained over extended cycling, benefiting from the preeminent reversibility of TM migration unlike conventional LLNMOs, which lose the structural integrity in a few cycles.

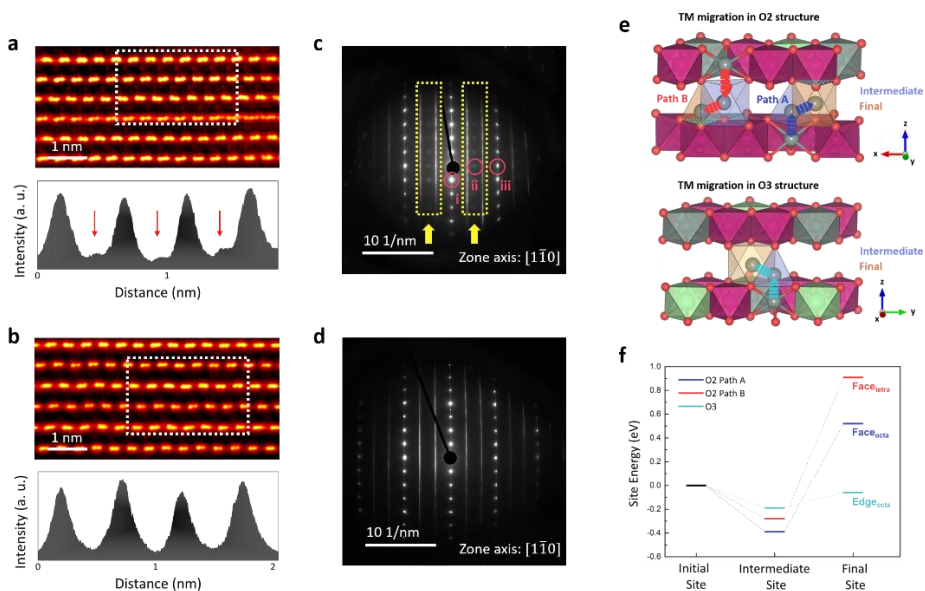


Figure 3.6. Highly reversible cation migration in O2-LLNMOs. HAADF-STEM images along the $[1\bar{1}0]$ zone axis for **a**, 4.8-V charged and **b**, 2.0-V discharged O2-LLNMOs. The graphs below are the HAADF signal profiles of the regions enclosed by the dotted lines in the STEM images. The arrows in the signal profile of the charged sample indicate the evolution of TM_{Li} defects. SAED patterns of **c**, 4.8-V charged and **d**, 2.0-V discharged O2-LLNMOs along the $[1\bar{1}0]$ direction. The extra spots in the areas enclosed by the yellow dotted boxes in **c** represent significant cation migration into the Li layers. In **c**, spots marked with red circles correspond to (i) $00\bar{2}$ (ordered structure and cation-disordered structure), (ii) $\bar{1}\bar{1}0$ (cation-disordered structure), and (iii) the overlap of $\bar{1}\bar{1}0$ (ordered structure) and $\bar{2}\bar{2}0$ (cation-disordered structure), respectively. Other spots are indexed in figure 3.8. **e**, TM migration paths from initial to intermediate and final Li sites. **f**, Relative site

energies of intermediate and final sites calculated along the migration path of TM ions. (The case where final sites share a face with Mn is presented here. See Chapter 3.3.6 for details.)

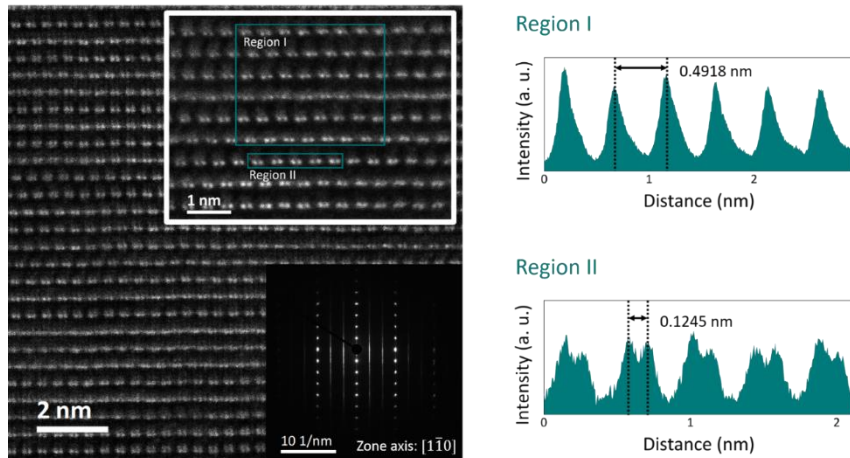


Figure 3.7. The $[1\bar{1}0]$ HAADF-STEM image of pristine O2-LLNMOs with 15M \times magnification. The 30M \times magnified image and corresponding SAED patterns are shown in the insets. The streak lines in the diffraction patterns indicate the existence of stacking faults (O4- or O6-stackings) in the pristine O2-LLNMOs^{47,48}. The HAADF signal profiles measured for Region I (vertical), II (horizontal) in the inset are represented at the right.

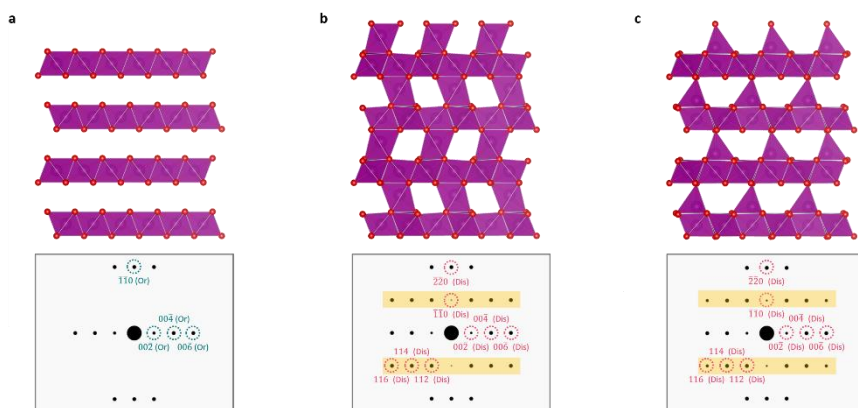


Figure 3.8. Simulated SAED patterns along the $[1\bar{1}0]$ zone axis for **a**, ordered (Or) and **b**, **c**, disordered (Dis) O2-LLNMOs. In disordered structures, 25 % of TM ions occupy **b**, octahedral sites and **c**, tetrahedral sites in the Li layer, respectively. The yellow shaded areas in the pattern of disordered phase indicate newly emerged spots compared with the pattern of ordered phase.

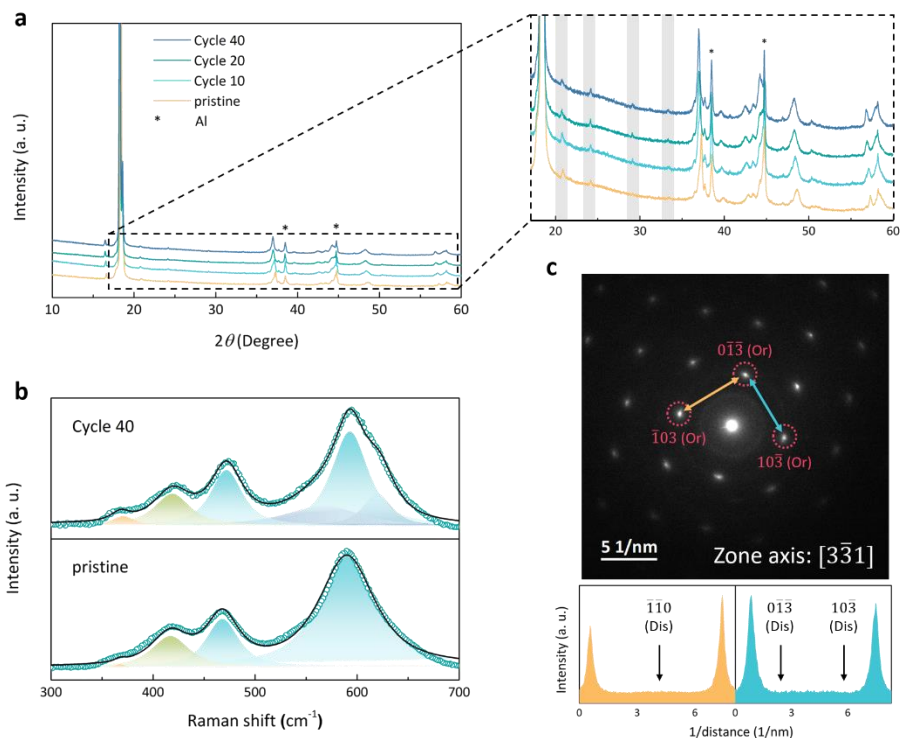


Figure 3.9. Mitigation of structural evolution in O2-LLNMOs for 40 cycles. a, *Ex situ* XRD patterns of pristine and 10-, 20-, and 40-cycled O2-LLNMOs. The magnified view clearly shows honeycomb superstructure peaks are preserved even after cycles (grey shaded). **b,** Comparison of Raman spectra for pristine and 40-cycled samples. The newly emerging blue peaks at 627 and 572 cm^{-1} after 40 cycles correspond to the layered-to-spinel transitions. **c,** SAED pattern of O2-LLNMOs along the $[\bar{3}\bar{3}1]$ zone axis after 40 cycles (top, Or: ordered). SAED signal profiles for yellow and blue lines in SAED pattern (bottom, Dis: disordered). The arrows indicate the expected positions of additional spots of disordered O2-LLNMOs.

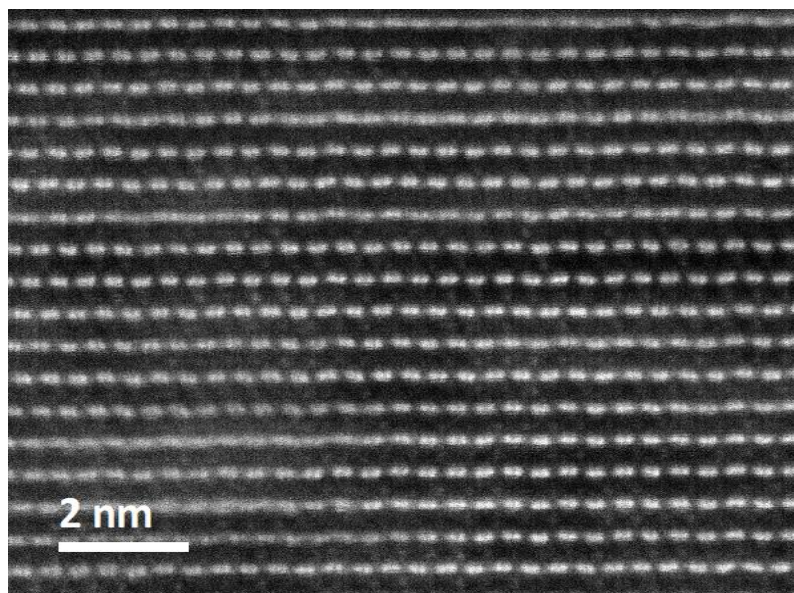


Figure 3.10. The $[1\bar{1}0]$ HAADF-STEM image of 4.8 V charged O₂-LLNMOs with 15M \times magnification. This image clearly shows a substantial amount of TM ions migrated to the Li layer.

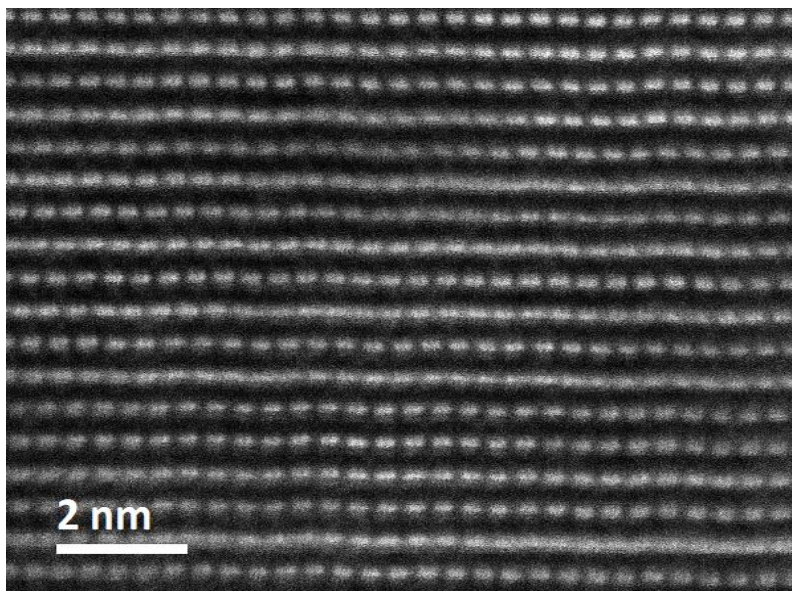


Figure 3.11. The $[1\bar{1}0]$ HAADF-STEM image of O2-LLNMOs after one cycle (2.0 V discharged) with 15M \times magnification. This image shows no signal of TM ions in the Li layer confirming the excellent reversibility of TM migration.

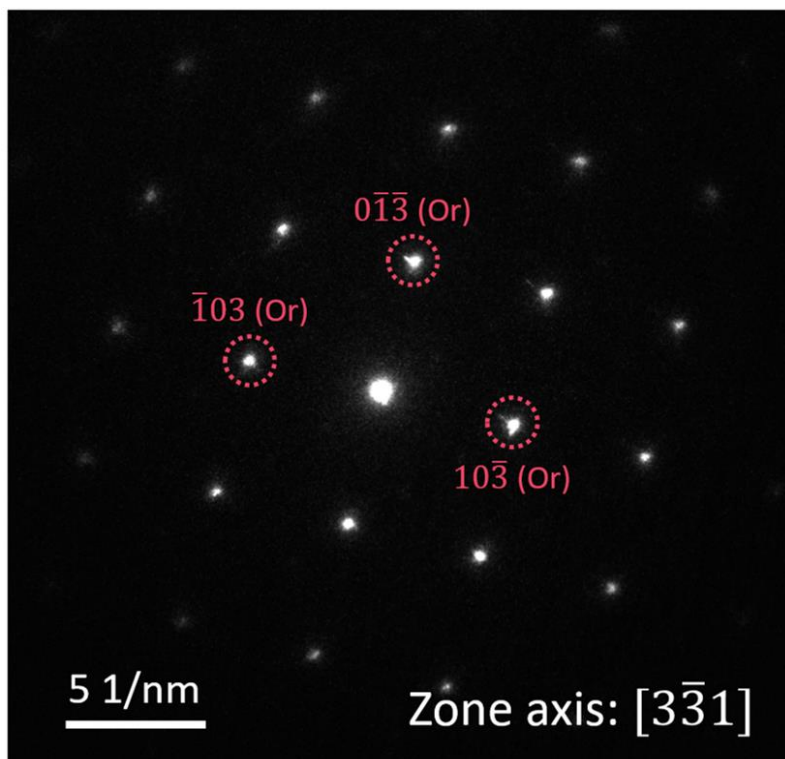


Figure 3.12. SAED patterns of pristine O2-LLNMOs along the $[3\bar{1}\bar{1}]$ zone axis (Or: ordered).

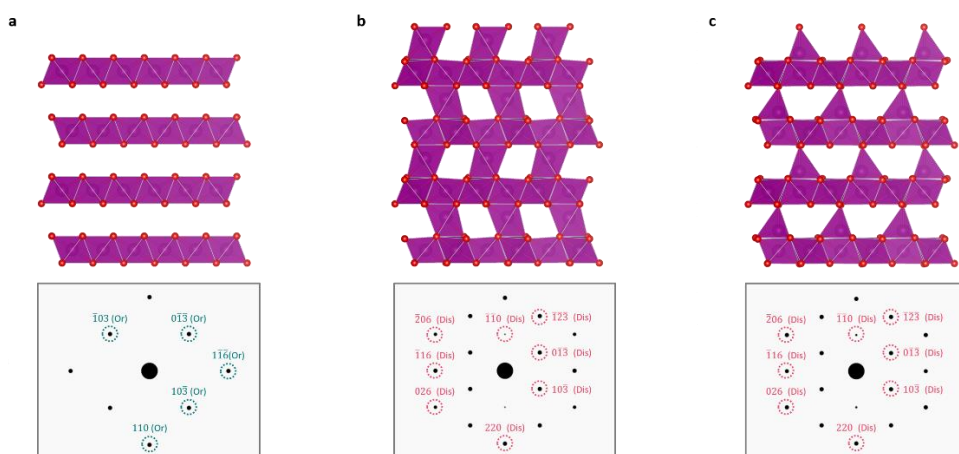


Figure 3.13. Simulated SAED patterns along the $[3\bar{3}1]$ zone axis for **a**, ordered (Or) and **b, c**, disordered (Dis) O2-LLNMOs. Same models with figure 3.8 are used for the simulation.

Table 3.1. Lattice parameters of pristine and 10-, 20-, and 40-cycled O2-LLNMOs obtained from *ex-situ* XRD results.

Cycle	a (Å)	b (Å)	c (Å)
Pristine	2.8624 (2)	2.8624 (2)	9.6332 (1)
10	2.8628 (2)	2.8628 (2)	9.6706 (4)
20	2.8640 (2)	2.8640 (2)	9.7137 (2)
40	2.8628 (2)	2.8628 (2)	9.7083 (5)

3.3.3 High-potential O redox behavior preserved in O2-LLNMOs

Notably, recent studies on lithium-rich layered oxides have demonstrated the intrinsic coupling between the anionic redox and cation migration^{33,39}. According to mechanistic investigation of LLNMCOs, TM migration to the Li layer decreases the redox potential of oxygen by >1 V, thereby leading to asymmetry of the anionic redox between charge and discharge³³. This asymmetrical behavior of the anionic redox has been alleged to play a detrimental role in triggering voltage hysteresis, which exacerbates the voltage retention along with voltage decay phenomenon^{10,32,49,50}. However, considering the reversibility of TM migration in O2-LLNMOs, a distinct anionic chemistry in contrast to the conventional mechanism is expected for O2-LLNMOs. To corroborate this hypothesis, we closely examined the evolution of redox couples during the charge and discharge of O2-LLNMOs. Figure 3.14a shows the change in the O K-edge and Ni, Mn L₃-edge absorbance spectra determined from STXM analysis during the first cycle of O2-LLNMOs. The six points in figure 3.14a correspond to the (1) pristine, (2) 4.5-V charged, (3) 4.8-V charged, (4) 3.8-V discharged, (5) 3.4-V discharged, and (6) 2.0-V discharged states, and the differences in the absorbance between two designated points are shown below. The results indicate that the charge process is compensated by the redox of Ni²⁺/Ni⁴⁺ at relatively low voltage (3.3–4.5 V) and subsequently by O²⁻/Oⁿ⁻ (n < 2) redox at high voltage (4.5–4.8 V), as previously discussed. When charging from 3.3 to 4.5 V ('1' → '2'), a peak appears at 856 eV in the Ni L₃-edge spectra with the

simultaneous emergence of a low-energy peak around 529 eV in the O K-edge spectra, signifying the depopulation of the hybridized $\text{Ni}_{3d}\text{-O}_{2p}$ antibonding state^{33,51}. From 4.5 to 4.8 V ('2' \rightarrow '3'), the peak at 531.0 eV evolves in the O K-edge spectra, which is indicative of oxygen redox states at high potentials³³. This oxygen redox is further evidenced by mapping of resonant inelastic X-ray scattering (mRIXS) analysis (figure 3.14b). We note that O K-edge mRIXS has recently been demonstrated as a tool-of-choice for detecting the lattice oxygen redox states in both Li- and Na-ion battery electrodes^{33,39,52,53}. In particular, the emergence of a distinct feature at 531.0 eV excitation energy and 523.7 eV emission energy (red circles in figure 3.14b) indicates the presence of oxidized lattice oxygens in battery electrodes. The results show that such oxidized oxygen feature is absent in mRIXS until '2', but becomes distinct in '3', demonstrating oxygen oxidation at high potentials ('2' \rightarrow '3'). No characteristic peaks are observed in the Mn L_3 -edge STXM spectra throughout the entire charging regime, confirming the redox-inactive properties of Mn^{4+} . Ni and Mn K-edge X-ray absorption near edge spectroscopy (XANES) analyses (figure 3.15) also revealed a consistent redox mechanism during the charging process. Overall, the charging of O2-LLNMOs accompanies the sequence of redox couples, which is the same as that for their O3-type counterparts^{41,42}. This accordance is reasonable considering that the tendency of TM migration during the charging is similar in both compounds.

In the subsequent discharge process, we found that the anionic ($\text{O}^{2-}/\text{O}^{n-}$ ($n < 2$)) redox occurs quite reversibly at the high voltage region for O2-LLNMOs. As can be

seen from mRIXS images in figure 3.14b, during the initial discharge, the oxidized oxygen feature dropped its intensity significantly from ‘3’ to ‘4’, and completely disappeared at ‘5’ state. This indicates that majority of the oxygen reduction takes place at high potentials (‘3’ \rightarrow ‘4’) and is completed by ‘5’. The oxygen redox activity is thus completely absent at low potentials (‘5’ \rightarrow ‘6’). Consistently, in STXM spectrum for the equivalent discharge region (‘3’ \rightarrow ‘5’), the O K-edge peak at 531.0 eV disappears, clearly indicating the reduction of O_{2p} states at high-voltage region. Moreover, the signature of TM_{3d}-O_{2p} reduction was presented with the disappearance of the peak at 856 eV at the Ni L₃-edge as well as that at 529 eV at the O K-edge, indicating the simultaneous cationic (Ni⁴⁺ to Ni²⁺) reduction. This observation is in contrast to the typical anionic redox behavior observed in the O3-LLNMOs, which was recently demonstrated with the major anionic redox activities at low potential region after the cation redox reaction³³. And, this asymmetric anionic redox reaction for the charge (high potential charging) and the discharge (low potential discharging) was accounted for the voltage hysteresis of LLNMOs. In the O2-LLNMOs, on the other hand, the oxygen redox activity was solely observed at the high-voltage region without the signature in the low-voltage region (‘5’ \rightarrow ‘6’), which is mainly compensated by partial manganese reduction (Chapter 3.3.7). For O3-type LLNMCOs (Li_{1.17}Ni_{0.21}Co_{0.08}Mn_{0.54}O₂), Gent *et al.* demonstrated that the lowered discharge potential of anionic redox originates from the significant coordination loss of oxygen in the TM layer, whose originally coordinated TM ions move to the Li layer³³. Such coordination loss of oxygen inevitably shifts the O_{2p}

states to the higher level in the electronic structure, and thus decreases the voltage of oxygen redox. However, according to our STEM and theoretical observations, TM ions in the Li layer readily return to the TM layer upon re-lithiation of charged O2-LLNMOs, which would rapidly restore the coordination environment of oxygen. This behavior is dissimilar to that for O3-type compounds, wherein a substantial amount of TM ions remains in the Li layer. This finding implies that the anomalously symmetrical redox properties of O2-LLNMOs must result from the facile return of migrated TM ions upon discharge. Mitigation of the asymmetry of the anionic redox may be beneficial to the long-term cyclability as it decreases the voltage hysteresis, although there have been few attempts aimed at improvement of the redox symmetry.

In order to further support the O redox at high potential discharge, several electrochemical tests were additionally performed. Figure 3.14b presents two model $dQ\ dV^{-1}$ experiments, in which the anionic redox is separated from TM–O redox by cycling two cells; (i) below 4.35 V without triggering of the O redox (black dotted line) and (ii) with O redox triggered (colored solid line). Excluding the cation redox activity (yellow region), the additional electrochemical activity achieved after the O redox triggered (blue region) is solely exhibited at the high potentials without any additional activities in the yellow region. The invariance of the cation redox region even after the O redox triggered is in line with the STXM data, supporting the anionic reduction at high redox potentials. In figure 3.14c, we also investigated the change in the discharge profiles of O2-LLNMOs as a function of the current density, considering that that anionic redox exhibits much more sluggish kinetics than cation

redox, thus the variations of the anionic and cationic redox regimes are readily distinguishable^{32,45}. Upon increasing the current density, the discharge capacity of the high-voltage region (above 3.4 V) steadily and drastically decreases from 136 mAh g⁻¹ at 5 mA g⁻¹ to 74 mAh g⁻¹ at 200 mA g⁻¹ (see figure 3.14d). However, the capacity of the redox region below 3.4 V is well maintained with only minor changes of less than 6 mAh g⁻¹ until the current density reaches 100 mA g⁻¹. The observation that the capacity fade at high rates mainly arises in the high-voltage region supports the sluggish anionic redox occurring in the high voltage range on discharge. Notably, it contrasts with that of O3-LLNMOs in which the substantial capacity drops are observed in both regions (above 3.4 V and below 3.4 V), which is attributed to anionic redox activity spread into the low-voltage region (figure 3.16).

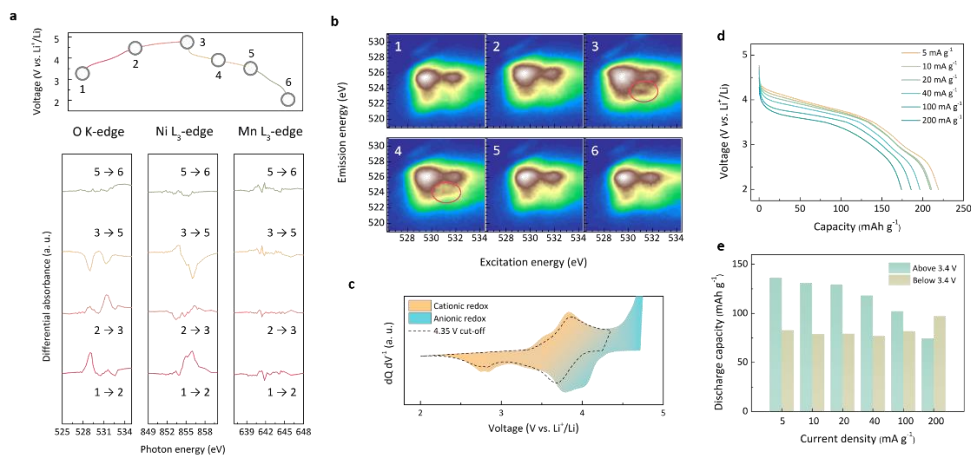


Figure 3.14. Anomalous anionic redox behavior in O2-LLNMOs. **a**, STXM differential absorbance spectra of O K-edge and Ni, Mn L₃-edges for the first charge and discharge cycle. Each spectrum shows the difference between two designated points in the electrochemical curve. **b**, O K-edge mRIXS of O2-LLNMOs for the first cycle obtained at each point of **a**. Distinct oxygen redox features are indicated by red circles. **c**, dQ dV⁻¹ curve of O2-LLNMOs measured at a current density of 5 mA g⁻¹. **d**, Electrochemical curves of O2-LLNMOs for current densities ranging from 5 to 200 mA g⁻¹. **e**, Variation of discharge capacity as a function of current density estimated for the two classified voltage ranges, 2.0–3.4 V and 3.4–4.8 V.

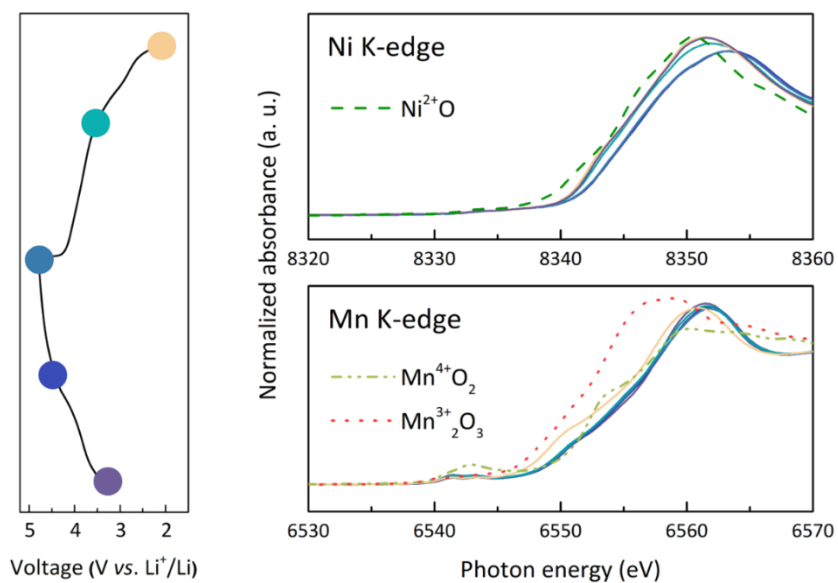


Figure 3.15. Ni and Mn K-edge XANES spectra measured for five points in the electrochemical curve of O2-LLNMOs.

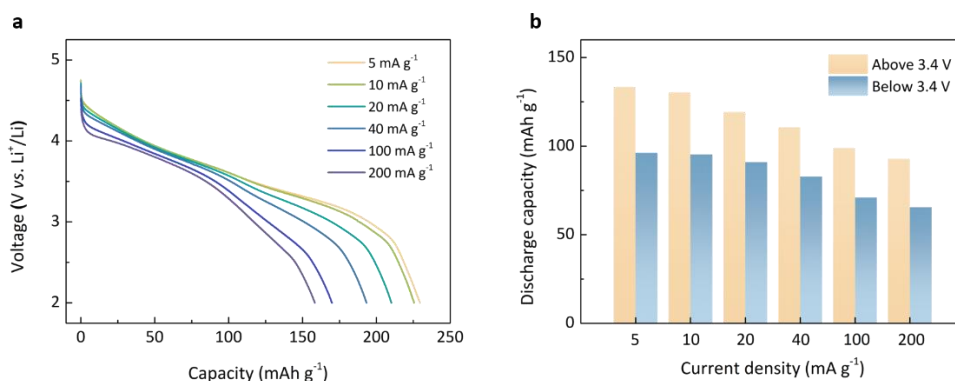


Figure 3.16. a, Electrochemical curves of O3-LLNMOs for current densities ranging from 5 to 200 mA g⁻¹. **b,** Variation of discharge capacity of O3-LLNMOs as a function of current density estimated for the two classified voltage ranges, 2.0–3.4 V and 3.4–4.8 V.

3.3.4 Synthesis of O2-LLNMOs

To synthesize the metastable O2 phase, the soft chemical ion-exchange method was applied^{30,31}. In this process, P2-type sodium layered oxides with the same transition metal composition as that of the targeted O2 phase, i.e., $\text{Na}_{5/6}(\text{Li}_{0.2}\text{Ni}_{0.2}\text{Mn}_{0.6})\text{O}_2$, were synthesized in advance with a small amount of O3 phases (less than 10 wt%) using a controlled sol–gel method^{54,55} (see figure 3.17). Na^+/Li^+ ion exchange was then conducted on the as-prepared P2-type $\text{Na}_{5/6}(\text{Li}_{0.2}\text{Ni}_{0.2}\text{Mn}_{0.6})\text{O}_2$ with LiBr in hexanol solution at low temperature^{56,57} to produce O2-phase LLNMOs. The crystal structure of the ion-exchanged LLNMOs was confirmed to correspond to the O2 phase (space group $P6_3mc$) using X-ray powder diffraction (see figure 3.18a). The in-plane honeycomb Li/TM superstructure in the TM layers was identified using the high-resolution powder diffraction (HRPD) data presented in Figure 3.18a;^{58,59} this result indicates that the in-plane atomic ordering of the as-prepared P2-phase compound was well maintained after the ion-exchange process. In addition, inductively coupled plasma-atomic emission spectroscopy (ICP-AES) analysis verified that the composition of the obtained powder was $\text{Li}_x(\text{Li}_{0.2}\text{Ni}_{0.2}\text{Mn}_{0.6})\text{O}_2$ ($x \approx 5/6$), which is very similar to the archetypal composition of LLNMOs (see Table 3.3). SEM analysis confirmed the homogeneous size and morphology of the particles, and HR-TEM measurements confirmed the well-defined layered structure of the ion-exchanged particles (figure 3.18b–e). These observations collectively demonstrate that the ion-exchange process did not lead to deterioration of the crystallinity of the

particles and that $\text{Li}_x(\text{Li}_{0.2}\text{Ni}_{0.2}\text{Mn}_{0.6})\text{O}_2$ with O2-type oxygen stacking was successfully synthesized.

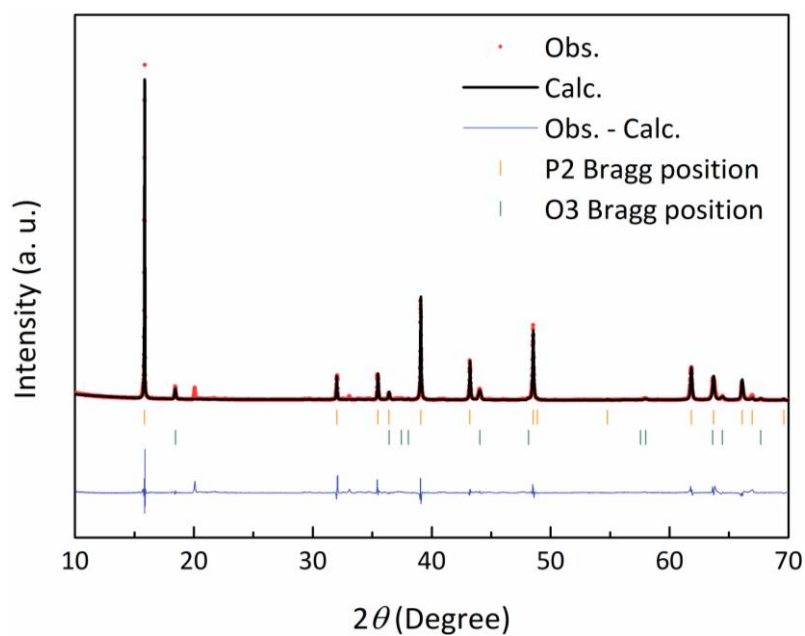


Figure 3.17. HRPD pattern of $\text{P2-Na}_{5/6}(\text{Li}_{0.2}\text{Ni}_{0.2}\text{Mn}_{0.6})\text{O}_2$ material refined with $P6_3/mmc$ and $R\bar{3}m$ space groups.

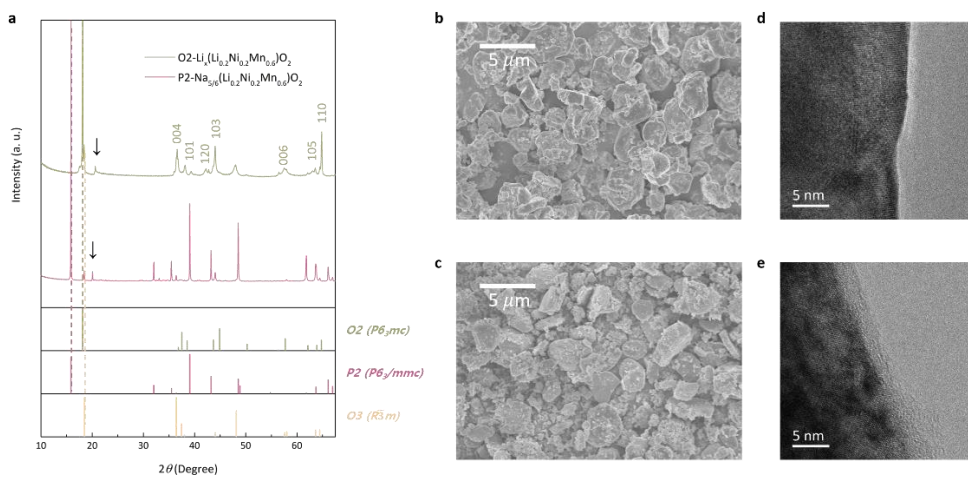


Figure 3.18. a, HRPD data for $\text{P2-Na}_{5/6}(\text{Li}_{0.2}\text{Ni}_{0.2}\text{Mn}_{0.6})\text{O}_2$ and $\text{O2-Li}_x(\text{Li}_{0.2}\text{Ni}_{0.2}\text{Mn}_{0.6})\text{O}_2$ with reference peaks. The arrows at $20 - 25^\circ$ indicate superstructure peaks which are attributed to Li/TM honeycomb ordering in the TM layers^{3,58,59}. SEM and HR-TEM images for P2- (b, d) and O2-phases (c, e), respectively.

Table 3.2. Rietveld refinements of P2-Na_{5/6}(Li_{0.2}Ni_{0.2}Mn_{0.6})O₂ materials. ($R_p = 12.5\%$)

Phase	Atom	x	Y	z	Occupancy
P2 <i>P6₃/mmc</i> (90.76 wt%)	Na1	0.3333	0.6667	0.75	0.792 (1)
	Li1	0	0	0	0.2 (7)
	O1	0.3333	0.6667	0.4097 (5)	1.086 (5)
	Ni1	0	0	0	0.2
	Mn1	0	0	0	0.6
	a (Å)		b (Å)		c (Å)
	2.8852 (1)		2.8852 (1)		11.0410 (2)
	Atom	x	y	z	Occupancy
	Li1	0	0	0	1.068 (8)
	Li2	0.3333	0.6667	0.1667	0.2
O3 <i>R$\bar{3}m$</i> (9.24 wt%)	O1	0	0	0.2439 (13)	1.032 (8)
	Ni1	0.3333	0.6667	0.1667	0.2 (2)
	Mn1	0.3333	0.6667	0.1667	0.576 (2)
	a (Å)		b (Å)		c (Å)
	2.8556 (1)		2.8556 (1)		14.2285 (11)

Table 3.3. ICP-AES results for P2-Na_{5/6}(Li_{0.2}Ni_{0.2}Mn_{0.6})O₂ and O2-Li_x(Li_{0.2}Ni_{0.2}Mn_{0.6})O₂ materials.

Phase	Na (ppm)	Li (ppm)	Ni (ppm)	Mn (ppm)	Mn/Ni (mol ratio)	Li/Ni (mol ratio)	(Na+Li)/ Ni (mol ratio)
P2	201251. 83	14813.47	117655.5 7	334550.78	3.04	1.06	5.43
O2	578.05	90427.64	146205.5 0	414059.21	3.03	5.23	5.24

3.3.5 Structural characterization of O2-LLNMOs

The dumbbell-like spots in Region II in figure 3.7 indicate the perfect $\text{Li}^+\text{Mn}^{4+}_6$ or $(\text{Li}^+_x\text{Ni}^{2+}_{1-x})\text{Mn}^{4+}_6$ honeycomb ordering in the pristine O2-LLNMOs, which is a typical signature of lithium-rich layered materials^{58,59}. The inter-layer spacing of 0.4918 nm along the *c*-axis and TM–TM dumbbell interval of 0.1245 nm are close to the values obtained in our first-principles calculations (0.4921 and 0.1455 nm, respectively). We note that a portion of the pristine structure contains domains of stacking faults similar to those observed for many other compounds that have undergone the ion-exchange process^{46,60}. Nevertheless, the predominant structure of the pristine O2-LLNMOs consists of O2 stacking, which can be seen from the well-defined O2 peaks in the HRPD data (figure 3.18a).

3.3.6 Theoretical investigation of cation migration pathways

For the computational models of LLNMOs, we employed $2 \times 3 \times 2$ supercells containing 12 formula units of the LiMO_2 ($M = \text{Li}, \text{Ni}, \text{and Mn}$) primitive cell (space group: $P6_3mc$ and $C2/m$ for O2 and O3 phases, respectively). For both phases, supercells consist of two TM layers and two Li layers (six cations per each layer). And composition of supercells is $\text{Li}_{14}\text{Ni}_3\text{Mn}_7\text{O}_{24}$, equivalently $\text{Li}[\text{Li}_{0.17}\text{Mn}_{0.58}\text{Ni}_{0.25}]\text{O}_2$, to be close to the composition of our experimental materials. To designate cation arrangements at the pristine state, the 50 lowest electrostatic energy configurations were selected for each phase using the Ewald summation method^{61,62}. Then, GGA+U calculations were performed for selected configurations to identify the most stable structures. Figure 3.19a represents in-plane cation arrangements in the most stable structures, which are same for O2- and O3-LLNMOs. In the one TM layer (TM layer -1), an excess Li ion is surrounded by 6 Mn ions, whereas in the other (TM layer-2), an excess Li ion is surrounded by 5 Mn ions and 1 Ni ion. Cation arrangement in our computational models are exactly same with that of the O3-phase model in previous work⁶³, and most consistent with arrangements from experimental observations on O3-LLNMOs^{64,65}.

In the process of calculating site energies, we considered the path along which TM ions move to the neighboring site in the Li layer through the face shared by the two sites rather than through the edge because the energy penalty of the narrow edge path is too high²⁴. To exclude the effects of Li configurations, we used simplified models

with one Li layer empty. TM migration is local phenomena sensitive to the local atomic environment²¹. Thus, along the migration path of each TM ion, we estimated the site energies considering all the case where the local environments of intermediate sites and final lithium sites are different, as shown in Tables 3.4-3.6. First coordination sphere was considered to assign the local environment of each site. We would like to note that established supercells of O2- and O3-LLNMOs have the same in-plane cation orderings; thus, the oxygen stacking is the only factor causing the differences in the calculation of both structures.

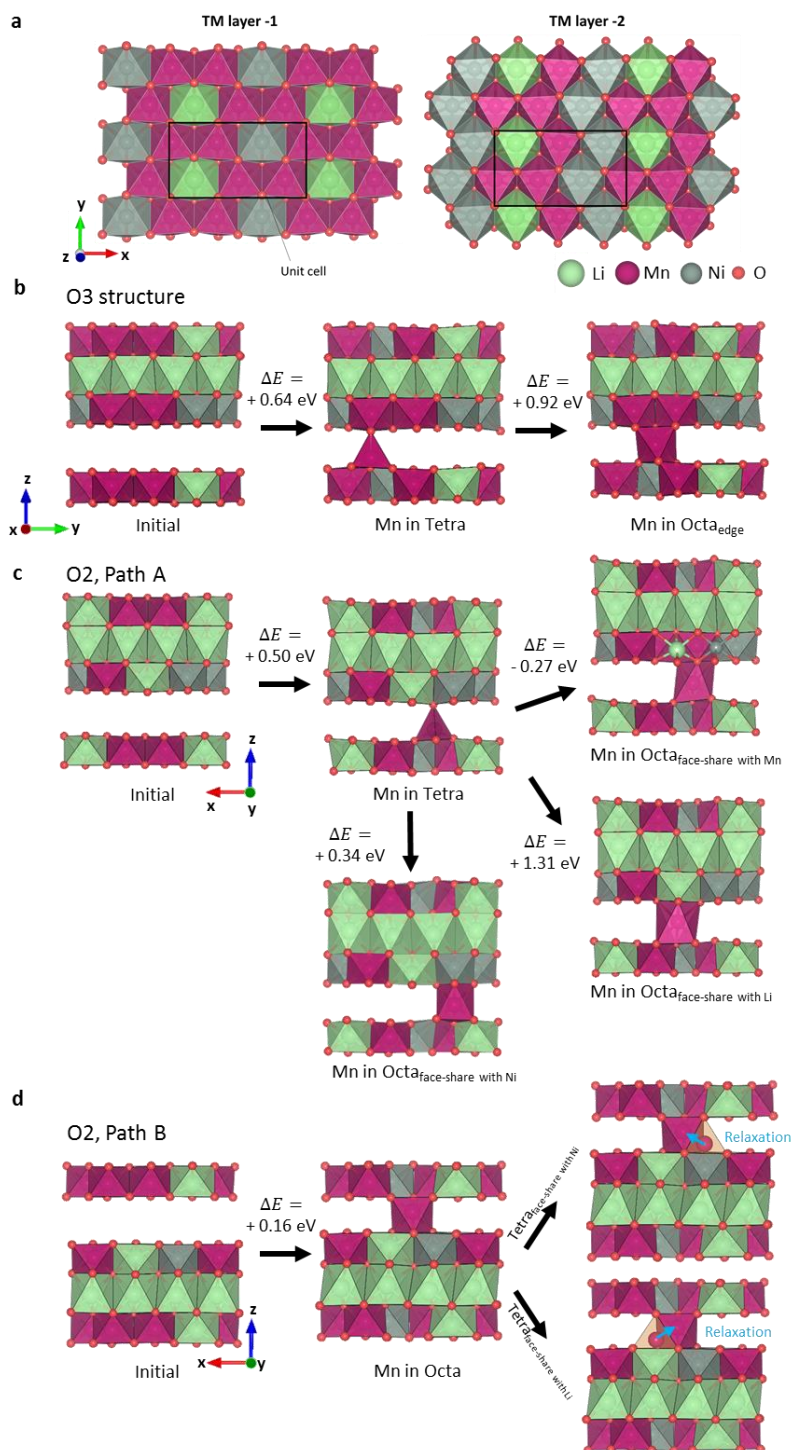
Figure 3.19b-g present the stepwise TM migration pathways in O2- and O3-LLNMOs for the representative TM ions for which initial migrations to the Li layer are the most thermodynamically feasible. Overall, the initial TM migrations were predicted to be much more likely to occur for Ni ions than for Mn ions due to the lower oxidation states of Ni ions. In all considered paths, Mn migrations to the intermediate sites always involve thermodynamic energy penalties (figure 3.19b-d). In contrast, ‘initial’ Ni migrations to the intermediate sites were verified to include thermodynamically spontaneous cases in O3 structure (figure 3.19e), and in both path A (figure 3.19f) and B (figure 3.19g) of the O2 structure. This is consistent with previous observations that Ni is the most liable to migrate to the Li layer in $\text{Li}_{1+x}\text{Ni}_y\text{Co}_z\text{Mn}_{1-x-y-z}\text{O}_2$ layered cathodes ($x \geq 0$, y and $z > 0$)⁶⁶⁻⁶⁸, and suggests that the movement of Ni ions is particularly important when considering the TM migrations between layers. When Ni ion moves from the intermediate tetrahedral site of O3 structure, the migration to the neighboring octahedral site requires only

0.13 eV of energy penalty, while the return to the original site necessitates a higher energy penalty (0.19 eV). It indicates that, in a moving situation, Ni ion at the intermediate site prefers to move within the Li layer rather than return to its original site. On the other hand, when Ni ion moves from the intermediate tetrahedral (path A) or octahedral (path B) site of the O2 structure to neighboring sites in Li layer, it requires a significant energy penalty regardless of face-sharing with either TM or Li ions in the TM layer. Figure 3.19f and g show that migrations to Li-facing sites entail less energy penalty than migrations to Mn-facing sites. However, even considering the most thermodynamically plausible pathways, Ni migrations to the face-sharing sites require a thermodynamic penalty of at least 0.66 eV. These results suggest that during charging, the intra-layer movements of Ni ions are thermodynamically prohibited, and Ni ions would be confined at the intermediate sites.

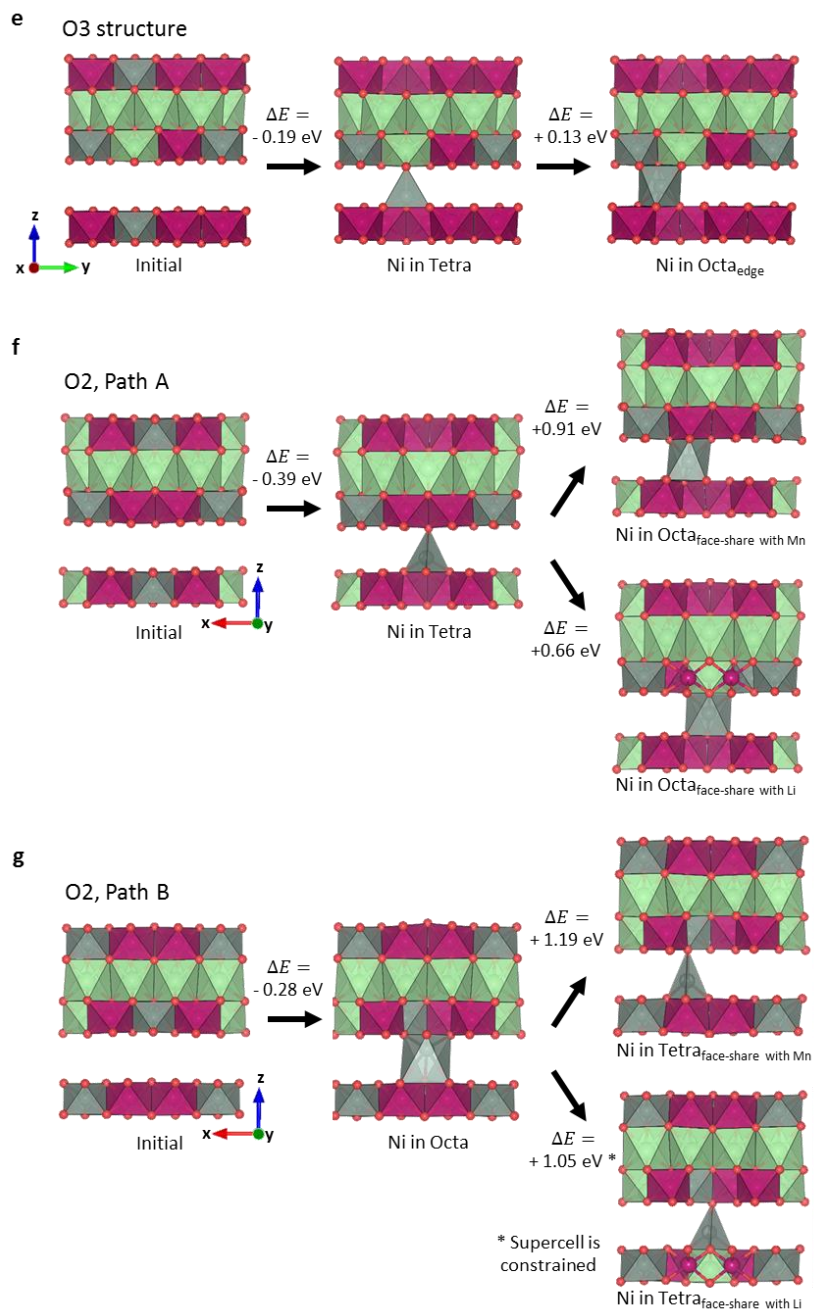
It is worth noting that in lithium-rich layered oxides, Li ions in the TM layer can also be extracted during charging. Figure 3.19h and i represent the TM migration pathways calculated for O2-LLNMOs model where Li ions in the TM layers are additionally extracted. The initial Mn migrations to the Li layer are expected to be unlikely in this situation as well (figure 3.19h). Notable among Ni migration pathways is that Ni migration from intermediate tetrahedral site to the octahedral site, which shares face with Li vacancy, was predicted to be thermodynamically feasible (path A, 'ii' \rightarrow 'iii' in figure 3.19i). It signifies that at certain circumstances where TM ion at the intermediate site is in contiguity with the Li site of the TM layer, and

Li vacancies are sufficiently secured in both TM and Li layers, the intra-layer TM migration can be allowed in the O2 structure. Nonetheless, it should be noted that a further subsequent TM migration in the Li layer, following the face-sharing with vacancy, is expected to be highly improbable because other sites in the Li layer maintain their face-sharing with cations. In order for this further off-course of TM to occur, the same conditions of Li vacancy in TM layer need to be continuously applied to the TM migration in the following step, which means there should be the region of segregated lithium ions in the TM layer. And, it is unlikely to occur in conventional LLNMOs. The relaxation of structures placing Ni ion at the neighboring sites of the vacancy-facing site caused Ni ion to move back to the vacancy-facing site, suggesting prohibitively substantial instabilities of such neighboring sites ('iv' in figure 3.19i). More importantly, when the vacant sites of the TM layer are re-lithiated during discharging, the site that shared the face with the vacancy becomes unstable again. In that case, TM ion would prefer to return to the intermediate site because adjacent TM layer site of the intermediate site is empty. Indeed, the return of Ni ion to the intermediate site was calculated to be energetically favorable by 0.30 eV, while its other migrations in the Li layer require energy penalties of at least 0.72 eV ('v' in figure 3.19i). Therefore, although the one-step intra-layer TM migration can be occasionally allowed due to the Li vacancy in the TM layer, it would not lead to the astray of TM ions benefiting from the difficulties of the multi-step TM migrations in the Li layer.

While we consider only the positions of TM ions assuming that a configuration and composition of Li ions do not change during TM migration, TM migration in real situation would involve the rearrangement of Li ions. Our calculation provides comparison of the TM migration spontaneity in terms of site energies only, and further work is required to identify more precise mechanism of TM migration including various Li contents, Li configurations around moving TM ions, different in-plane cation arrangements, and kinetic contributions.



When relaxed at the face-sharing tetrahedral sites, Mn ion returns to the intermediate octahedral site



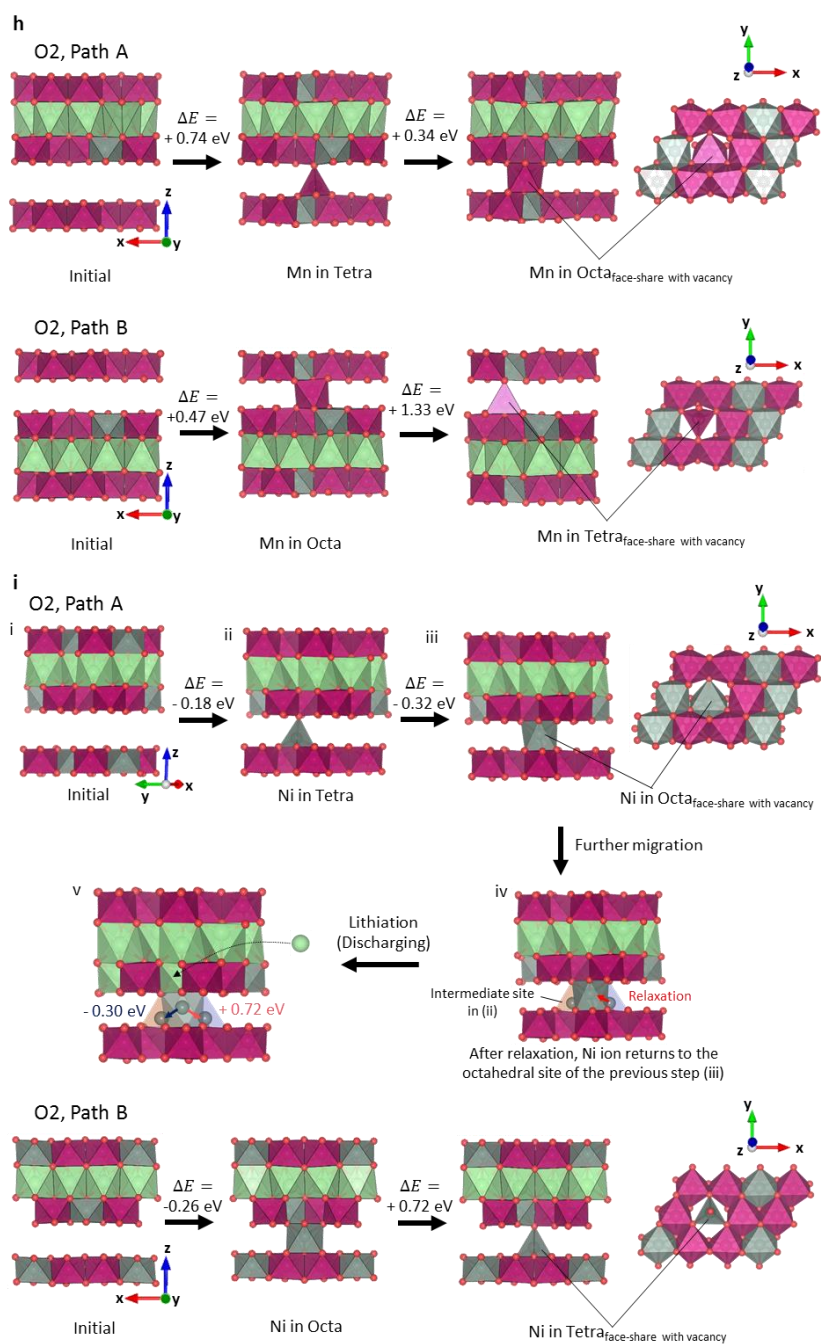


Figure 3.19. TM migration pathways in lithium-rich layered oxides with O2-

and O3- staking. a, The in-plane cation arrangements in the most stable structures of LLNMOs, which are same for both O2- and O3-LLNMOs. **b-d,** Migration of Mn ion **b**, in O3-LLNMOs, and along **c**, the path A and **d**, the path B in O2-LLNMOs. **e-g,** Migration of Ni ion **e**, in O3-LLNMOs, and along **f**, the path A and **g**, the path B in O2-LLNMOs. **h** and **i** present the TM migration behavior in O2-LLNMOs where the Li sites in the TM layer are vacant ($\text{Li}_{0.5}[\text{Li}_0\text{Mn}_{0.58}\text{Ni}_{0.25}]\text{O}_2$ composition), for the h, Mn and i, Ni, respectively. Migrations pathways are described for the representative Ni and Mn ions whose initial migrations to the Li layer are the most thermodynamically favorable.

Table 3.4. Relative Site energies calculated along the migration path of TM ions in O3-LLNMOs (O: original site, I: intermediate tetrahedral site, F: final lithium site).

TM	Site	Local environment	Relative Site E (eV)
Mn 1	O	Edge-share with (1 Li, 2 Ni, 3 Mn)	0
	I	.	0.85
	F	Edge-share with (1 Li, 1 Ni, 3 Mn)	0.60
Mn 2	O	Edge-share with (1 Li, 2 Ni, 3 Mn)	0
	I	.	0.64
	F	Edge-share with (1 Li, 1 Ni, 3 Mn)	1.56
	F	Edge-share with (1 Li, 2 Ni, 2 Mn)	1.66
Mn 3	O	Edge-share with (2 Li, 1 Ni, 3 Mn)	0
	I	.	1.00
	F	Edge-share with (1 Li, 2 Ni, 2 Mn)	0.76
Mn 4	O	Edge-share with (2 Li, 1 Ni, 3 Mn)	0
	I	.	1.05
	F	Edge-share with (1 Li, 1 Ni, 3 Mn)	1.05
Ni 1	O	Edge-share with (0 Li, 0 Ni, 6 Mn)	
	I	.	-0.19
	F	Edge-share with (1 Li, 1 Ni, 3 Mn)	-0.06
	F	Edge-share with (1 Li, 0 Ni, 4 Mn)	0.42
Ni 2	O	Edge-share with (1 Li, 2 Ni, 3 Mn)	0
	I	.	0.10
	F	Edge-share with (1 Li, 1 Ni, 3 Mn)	0.28
	F	Edge-share with (1 Li, 0 Ni, 4 Mn)	0.43
Ni 3	O	Edge-share with (0 Li, 2 Ni, 4 Mn)	.
	I	.	0.61
	F	Edge-share with (1 Li, 1 Ni, 3 Mn)	0.56

Table 3.5. Relative Site energies calculated along the migration path A in O 2-LLNMOs (see figure 3.6e for the path A, O: original site, I: intermediate tetrahedral site, F: final octahedral lithium site).

TM	Site	Local environment	Relative Site E (eV)
Mn 1	O	Edge-share with (1 Li, 2 Ni, 3 Mn)	0
	I	.	0.72
	F	Face-share with Mn	0.30
	F	Face-share with Li	1.59
Mn 2	O	Edge-share with (1 Li, 2 Ni, 3 Mn)	0
	I	.	0.50
	F	Face-share with Mn	0.23
	F	Face-share with Ni	0.84
	F	Face-share with Li	1.81
Mn 3	O	Edge-share with (2 Li, 1 Ni, 3 Mn)	0
	I	.	0.71
	F	Face-share with Mn	1.43
	F	Face-share with Ni	1.71
Mn 4	O	Edge-share with (2 Li, 1 Ni, 3 Mn)	0
	I	.	0.71
	F	Face-share with Mn	0.83
	F	Face-share with Ni	1.05
Ni 1	O	Edge-share with (0 Li, 0 Ni, 6 Mn)	0
	I	.	-0.39
	F	Face-share with Li	0.27
	F	Face-share with Mn	0.52
Ni 2	O	Edge-share with (1 Li, 2 Ni, 3 Mn)	0
	I	.	0.40
	F	Face-share with Mn	0.53
	F	Face-share with Li	1.02
Ni 3	O	Edge-share with (0 Li, 2 Ni, 4 Mn)	0
	I	.	-0.21
	F	Face-share with Li	0.38
	F	Face-share with Mn	0.62

Table 3.6. Relative Site energies calculated along the migration path B in O2-LLNMOs (see figure 3.6e for the path B). When the input structures contain a TM ion in the lithium site, there are cases where the TM ion moves back to the intermediate site after relaxation. These cases imply the instability of lithium sites and are indicated as ‘Back to I’. For two configurations where the stacking order is partially changed after unconstrained relaxation, the results of constrained relaxations were presented by fixing cell parameters equal to those of the reference supercell (marked with an asterisk).

TM	Site	Local environment	Relative Site E (eV)
Mn 1	O	Edge-share with (1 Li, 2 Ni, 3 Mn)	0
	I	.	0.18
	F	Face-share with Mn	Back to I
	F	Face-share with Li	Back to I
Mn 2	O	Edge-share with (1 Li, 2 Ni, 3 Mn)	0
	I	.	0.16
	F	Face-sharing with Ni	Back to I
	F	Face-sharing with Li	Back to I
Mn 3	O	Edge-share with (2 Li, 1 Ni, 3 Mn)	0
	I	.	0.49
	F	Face-share with Ni	Back to I
	F	Face-share with Mn	Back to I
Mn 4	O	Edge-share with (2 Li, 1 Ni, 3 Mn)	0
	I	.	0.46
	F	Face-share with Ni	Back to I
	F	Face-share with Mn	Back to I
Ni 1	O	Edge-share with (0 Li, 0 Ni, 6 Mn)	0
	I	.	-0.04
	F	Face-share with Mn	Back to I
	F	Face-share with Li*	0.58
Ni 2	O	Edge-share with (1 Li, 2 Ni, 3 Mn)	0
	I	.	0.22
	F	Face-share with Mn	1.11
	F	Face-share with Li	1.29
Ni 3	O	Edge-share with (0 Li, 2 Ni, 4 Mn)	0
	I	.	-0.28
	F	Face-share with Mn	Back to I
	F	Face-share with Mn	0.91
	F	Face-share with Li*	0.77

3.3.7 Partial manganese reduction during discharge

When O2-LLNMOs are discharged from 3.4 V to 2.0 V ('4' \rightarrow '5' in figure 3.14a), the O K-edge and Ni L₃-edge spectra no longer exhibit an appreciable differential peak, and a slight shoulder appears in the Mn L₃-edge spectra at 640–642 eV. The emergence of these peaks implies that the partial reduction of Mn⁴⁺ to Mn³⁺ accounts for the redox capacity below 3.4 V. XANES analysis further clarifies this partial manganese reduction (figure 3.15). The edge position in the XANES spectra of the pristine samples indicates that the initial oxidation state of Mn was +4 and that this edge position was maintained until the cell was fully charged and then discharged to 3.4 V. Upon further discharge to 2.0 V, the value shifted toward a lower energy close to that of the Mn(III)₂O₃ reference, whereas the Ni K-edge spectra did not shift in this low-voltage range. In the electrochemical tests (figure 3.14d), the small increase of the discharge capacity at 200 mA g⁻¹ most likely results from the fast manganese redox substituting for some portion of the unfulfilled anionic redox activity below 3.4 V. Partial manganese reduction at the low voltage of discharge is a common phenomenon that has been previously observed in O3-Li_{1.2}Ni_{0.2}Mn_{0.6}O₂ as well as other lithium-rich layered 3d metal oxides^{7,55}.

3.4 Concluding remarks

In summary, we proposed a new strategy to improve the reversibility of TM migration by employing an O2-type structural framework wherein the cation migration path is effectively modified because of the unique site preferences. The intra-cycle reversible behavior of TM ions was visualized through STEM measurements, and complementary XRD, Raman spectroscopy, and HR-TEM analyses confirmed the preservation of the pristine structure over long-term cycling. Owing to this excellent reversibility, O2-LLNMOs exhibit remarkable reduction in voltage fade and redox asymmetry compared with their O3-phase counterparts. Theoretical calculations consistently presented that the intra-layer TM migration is thermodynamically prevented because of the large repulsion between face-sharing cations in O2-LLNMOs, facilitating the reverse migration.

This work provides robust guidance that will help steer strategies to resolve the issues of voltage decay and hysteresis in a range of lithium-rich layered oxides. In a broader context, tailoring site preference to drive reversible cation migration is also applicable to other fields where irreversible cation migration is critical to performance degradation of materials, such as conventional layered cathodes^{69,70}, electrocatalysis⁷¹, and photovoltaics⁷². Important directions for further study include exploring rich chemical spaces within the O2 structural framework through the careful control of cation and anion compositions. For example, recent studies have revealed for O3-LLNMOs and O3-LLNMCOs that migration tendencies of TM ions

can be dependent on their metal compositions^{7,23}. Therefore, the combination of O2 structural framework and optimized lithium-rich chemistry will offer further unexplored opportunities in securing better structural reversibility and energy retention. Another remaining task for lithium-rich layered oxides is narrowing the gap between academic solutions and industrial needs with the improvement of engineering and synthetic process. Notably, alternative synthetic routes to produce O2 phase are needed to circumvent the cost and lithium loss issues associated with the ion-exchange method that was employed in this study.

3.5 References

1. Larcher, D. & Tarascon, J. M. Towards greener and more sustainable batteries for electrical energy storage. *Nature Chemistry* **7**, 19 (2014).
2. Li, W., Song, B. & Manthiram, A. High-voltage positive electrode materials for lithium-ion batteries. *Chemical Society Reviews* **46**, 3006-3059 (2017).
3. Hong, J., Gwon, H., Jung, S.-K., Ku, K. & Kang, K. Review—Lithium-Excess Layered Cathodes for Lithium Rechargeable Batteries. *Journal of The Electrochemical Society* **162**, A2447-A2467 (2015).
4. Assat, G. & Tarascon, J.-M. Fundamental understanding and practical challenges of anionic redox activity in Li-ion batteries. *Nature Energy* **3**, 373-386 (2018).
5. Bettge, M. *et al.* Voltage Fade of Layered Oxides: Its Measurement and Impact on Energy Density. *Journal of The Electrochemical Society* **160**, A2046-A2055 (2013).
6. Sathiya, M. *et al.* Origin of voltage decay in high-capacity layered oxide electrodes. *Nature Materials* **14**, 230-238 (2015).
7. Ku, K. *et al.* Suppression of Voltage Decay through Manganese Deactivation and Nickel Redox Buffering in High-Energy Layered Lithium-Rich Electrodes. *Advanced Energy Materials* **8**, 1800606 (2018).
8. Zheng, J. *et al.* Li- and Mn-Rich Cathode Materials: Challenges to Commercialization. *Advanced Energy Materials* **7**, 1601284 (2017).

9. Mohanty, D. *et al.* Unraveling the Voltage-Fade Mechanism in High-Energy-Density Lithium-Ion Batteries: Origin of the Tetrahedral Cations for Spinel Conversion. *Chemistry of Materials* **26**, 6272-6280 (2014).
10. Gallagher, K. G. *et al.* Correlating hysteresis and voltage fade in lithium- and manganese-rich layered transition-metal oxide electrodes. *Electrochemistry Communications* **33**, 96-98 (2013).
11. Kleiner, K. *et al.* Origin of High Capacity and Poor Cycling Stability of Li-Rich Layered Oxides: A Long-Duration in Situ Synchrotron Powder Diffraction Study. *Chemistry of Materials* **30**, 3656-3667 (2018).
12. Gu, M. *et al.* Formation of the Spinel Phase in the Layered Composite Cathode Used in Li-Ion Batteries. *ACS Nano* **7**, 760-767 (2013).
13. Hong, J. *et al.* Structural evolution of layered $\text{Li}_{1.2}\text{Ni}_{0.2}\text{Mn}_{0.6}\text{O}_2$ upon electrochemical cycling in a Li rechargeable battery. *Journal of Materials Chemistry* **20**, 10179-10186 (2010).
14. Zheng, J. *et al.* Structural and Chemical Evolution of Li- and Mn-Rich Layered Cathode Material. *Chemistry of Materials* **27**, 1381-1390 (2015).
15. Mohanty, D. *et al.* Correlating cation ordering and voltage fade in a lithium–manganese-rich lithium-ion battery cathode oxide: a joint magnetic susceptibility and TEM study. *Physical Chemistry Chemical Physics* **15**, 19496-19509 (2013).
16. Wu, Y. *et al.* Probing the initiation of voltage decay in Li-rich layered

- cathode materials at the atomic scale. *Journal of Materials Chemistry A* **3**, 5385-5391 (2015).
17. Rinaldo, S. G. *et al.* Physical Theory of Voltage Fade in Lithium- and Manganese-Rich Transition Metal Oxides. *Journal of The Electrochemical Society* **162**, A897-A904 (2015).
 18. Lee, E. & Persson, K. A. Structural and Chemical Evolution of the Layered Li-Excess Li_xMnO_3 as a Function of Li Content from First-Principles Calculations. *Advanced Energy Materials* **4**, 1400498 (2014).
 19. Kim, S. *et al.* Material design of high-capacity Li-rich layered-oxide electrodes: Li_2MnO_3 and beyond. *Energy & Environmental Science* **10**, 2201-2211 (2017).
 20. Lim, J.-M. *et al.* The origins and mechanism of phase transformation in bulk Li_2MnO_3 : first-principles calculations and experimental studies. *Journal of Materials Chemistry A* **3**, 7066-7076 (2015).
 21. Li, Q. *et al.* K^+ -Doped $\text{Li}_{1.2}\text{Mn}_{0.54}\text{Co}_{0.13}\text{Ni}_{0.13}\text{O}_2$: A Novel Cathode Material with an Enhanced Cycling Stability for Lithium-Ion Batteries. *ACS Applied Materials & Interfaces* **6**, 10330-10341 (2014).
 22. Nayak, P. K., Grinblat, J., Levi, M. & Aurbach, D. Understanding the Effect of Lithium Bis(oxalato) Borate (LiBOB) on the Structural and Electrochemical Aging of Li and Mn Rich High Capacity $\text{Li}_{1.2}\text{Ni}_{0.16}\text{Mn}_{0.56}\text{Co}_{0.08}\text{O}_2$ Cathodes. *Journal of The Electrochemical Society*

- 162**, A596-A602 (2015).
23. Shi, J.-L. *et al.* Mitigating Voltage Decay of Li-Rich Cathode Material via Increasing Ni Content for Lithium-Ion Batteries. *ACS Applied Materials & Interfaces* **8**, 20138-20146 (2016).
 24. Reed, J. & Ceder, G. Role of Electronic Structure in the Susceptibility of Metastable Transition-Metal Oxide Structures to Transformation. *Chemical Reviews* **104**, 4513-4534 (2004).
 25. Du, K. *et al.* Exploring reversible oxidation of oxygen in a manganese oxide. *Energy & Environmental Science* **9**, 2575-2577 (2016).
 26. Rong, X. *et al.* Structure-Induced Reversible Anionic Redox Activity in Na Layered Oxide Cathode. *Joule* **2**, 125-140 (2018).
 27. Maitra, U. *et al.* Oxygen redox chemistry without excess alkali-metal ions in $\text{Na}_{2/3}[\text{Mg}_{0.28}\text{Mn}_{0.72}]\text{O}_2$. *Nature Chemistry* **10**, 288-295 (2018).
 28. Delmas, C., Braconnier, J.-J., Fouassier, C. & Hagenmuller, P. Electrochemical intercalation of sodium in Na_xCoO_2 bronzes. *Solid State Ionics* **3-4**, 165-169 (1981).
 29. Paulsen, J. M., Thomas, C. L. & Dahn, J. R. Layered Li-Mn-Oxide with the O2 Structure: A Cathode Material for Li-Ion Cells Which Does Not Convert to Spinel. *Journal of The Electrochemical Society* **146**, 3560-3565 (1999).
 30. Yabuuchi, N. *et al.* New O2/P2-type Li-Excess Layered Manganese Oxides as Promising Multi-Functional Electrode Materials for Rechargeable Li/Na

- Batteries. *Advanced Energy Materials* **4**, 1301453 (2014).
31. de Boisse, B. M., Jang, J., Okubo, M. & Yamada, A. Cobalt-Free O₂-Type Lithium-Rich Layered Oxides. *Journal of The Electrochemical Society* **165**, A3630-A3633 (2018).
 32. Assat, G. *et al.* Fundamental interplay between anionic/cationic redox governing the kinetics and thermodynamics of lithium-rich cathodes. *Nature Communications* **8**, 2219 (2017).
 33. Gent, W. E. *et al.* Coupling between oxygen redox and cation migration explains unusual electrochemistry in lithium-rich layered oxides. *Nature Communications* **8**, 2091 (2017).
 34. Kresse, G. & Furthmüller, J. Efficient iterative schemes for ab initio total-energy calculations using a plane-wave basis set. *Physical Review B* **54**, 11169-11186 (1996).
 35. Dudarev, S. L., Botton, G. A., Savrasov, S. Y., Humphreys, C. J. & Sutton, A. P. Electron-energy-loss spectra and the structural stability of nickel oxide: An LSDA+U study. *Physical Review B* **57**, 1505-1509 (1998).
 36. Seo, D.-H. *et al.* The structural and chemical origin of the oxygen redox activity in layered and cation-disordered Li-excess cathode materials. *Nature Chemistry* **8**, 692-697 (2016).
 37. Jain, A. *et al.* A high-throughput infrastructure for density functional theory calculations. *Computational Materials Science* **50**, 2295-2310 (2011).

38. Qiao, R. *et al.* High-efficiency in situ resonant inelastic x-ray scattering (iRIXS) endstation at the Advanced Light Source. *Review of Scientific Instruments* **88**, 033106 (2017).
39. Hong, J. *et al.* Metal–oxygen decoordination stabilizes anion redox in Li-rich oxides. *Nature Materials* **18**, 256-265 (2019).
40. Lim, J. *et al.* Origin and hysteresis of lithium compositional spatiodynamics within battery primary particles. *Science* **353**, 566 (2016).
41. Li, X. *et al.* Direct Visualization of the Reversible O^{2-}/O^- Redox Process in Li-Rich Cathode Materials. *Advanced Materials* **30**, 1705197 (2018).
42. Luo, K. *et al.* Anion Redox Chemistry in the Cobalt Free 3d Transition Metal Oxide Intercalation Electrode $Li[Li_{0.2}Ni_{0.2}Mn_{0.6}]O_2$. *Journal of the American Chemical Society* **138**, 11211-11218 (2016).
43. Gao, S. *et al.* The Role of Various Components of Transition Metal Layer on the Properties of Li-Rich Cathode $Li_{1.2}[M_{0.4}Mn_{0.4}]O_2$ (M = Ni, Co, $Ni_{1/2}Mn_{1/2}$ and Fe). *Journal of The Electrochemical Society* **164**, A3824-A3831 (2017).
44. Myeong, S. *et al.* Understanding voltage decay in lithium-excess layered cathode materials through oxygen-centred structural arrangement. *Nature Communications* **9**, 3285 (2018).
45. Assat, G., Iadecola, A., Delacourt, C., Dedryvère, R. & Tarascon, J.-M. Decoupling Cationic–Anionic Redox Processes in a Model Li-Rich Cathode via Operando X-ray Absorption Spectroscopy. *Chemistry of Materials* **29**,

- 9714-9724 (2017).
46. Paulsen, J. M., Thomas, C. L. & Dahn, J. R. O₂ Structure Li_{2/3}[Ni_{1/3}Mn_{2/3}]O₂: A New Layered Cathode Material for Rechargeable Lithium Batteries. I. Electrochemical Properties. *Journal of The Electrochemical Society* **147**, 861-868 (2000).
 47. Dupraz, M., Beutier, G., Rodney, D., Mordehai, D. & Verdier, M. Signature of dislocations and stacking faults of face-centred cubic nanocrystals in coherent X-ray diffraction patterns: a numerical study This article will form part of a virtual special issue of the journal, presenting some highlights of the 12th Biennial Conference on High-Resolution X-ray Diffraction and Imaging (XTOP2014). *Journal of Applied Crystallography* **48**, 621-644 (2015).
 48. Jarvis, K. A., Deng, Z., Allard, L. F., Manthiram, A. & Ferreira, P. J. Atomic Structure of a Lithium-Rich Layered Oxide Material for Lithium-Ion Batteries: Evidence of a Solid Solution. *Chemistry of Materials* **23**, 3614-3621 (2011).
 49. Konishi, H. *et al.* Potential hysteresis between charge and discharge reactions in Li_{1.2}Ni_{0.13}Mn_{0.54}Co_{0.13}O₂ for lithium ion batteries. *Solid State Ionics* **300**, 120-127 (2017).
 50. Konishi, H. *et al.* Origin of hysteresis between charge and discharge processes in lithium-rich layer-structured cathode material for lithium-ion

- battery. *Journal of Power Sources* **298**, 144-149 (2015).
51. Hu, E. *et al.* Evolution of redox couples in Li- and Mn-rich cathode materials and mitigation of voltage fade by reducing oxygen release. *Nature Energy* **3**, 690-698 (2018).
 52. Yang, W. & Devereaux, T. P. Anionic and cationic redox and interfaces in batteries: Advances from soft X-ray absorption spectroscopy to resonant inelastic scattering. *Journal of Power Sources* **389**, 188-197 (2018).
 53. Dai, K. *et al.* High Reversibility of Lattice Oxygen Redox Quantified by Direct Bulk Probes of Both Anionic and Cationic Redox Reactions. *Joule* **3**, 518-541 (2019).
 54. Shaju, K. M. & Bruce, P. G. Macroporous $\text{Li}(\text{Ni}_{1/3}\text{Co}_{1/3}\text{Mn}_{1/3})\text{O}_2$: A High-Power and High-Energy Cathode for Rechargeable Lithium Batteries. *Advanced Materials* **18**, 2330-2334 (2006).
 55. Luo, K. *et al.* Charge-compensation in 3d-transition-metal-oxide intercalation cathodes through the generation of localized electron holes on oxygen. *Nature Chemistry* **8**, 684-691 (2016).
 56. Park, Y.-U. *et al.* In Situ Tracking Kinetic Pathways of Li^+/Na^+ Substitution during Ion-Exchange Synthesis of $\text{Li}_x\text{Na}_{1.5-x}\text{VOPO}_4\text{F}_{0.5}$. *Journal of the American Chemical Society* **139**, 12504-12516 (2017).
 57. Armstrong, A. R. & Bruce, P. G. Synthesis of layered LiMnO_2 as an electrode for rechargeable lithium batteries. *Nature* **381**, 499-500 (1996).

58. Mortemard de Boisse, B. *et al.* Intermediate honeycomb ordering to trigger oxygen redox chemistry in layered battery electrode. *Nature Communications* **7**, 11397 (2016).
59. Thackeray, M. M. *et al.* Li_2MnO_3 -stabilized LiMO_2 (M = Mn, Ni, Co) electrodes for lithium-ion batteries. *Journal of Materials Chemistry* **17**, 3112-3125 (2007).
60. Lu, Z., Donaberger, R. A. & Dahn, J. R. Superlattice Ordering of Mn, Ni, and Co in Layered Alkali Transition Metal Oxides with P2, P3, and O3 Structures. *Chemistry of Materials* **12**, 3583-3590 (2000).
61. Toukmaji, A. Y. & Board, J. A. Ewald summation techniques in perspective: a survey. *Computer Physics Communications* **95**, 73-92 (1996).
62. Ong, S. P. *et al.* Python Materials Genomics (pymatgen): A robust, open-source python library for materials analysis. *Computational Materials Science* **68**, 314-319 (2013).
63. Xu, B., Fell, C. R., Chi, M. & Meng, Y. S. Identifying surface structural changes in layered Li-excess nickel manganese oxides in high voltage lithium ion batteries: A joint experimental and theoretical study. *Energy & Environmental Science* **4**, 2223-2233 (2011).
64. Bréger, J. *et al.* High-resolution X-ray diffraction, DIFFaX, NMR and first principles study of disorder in the Li_2MnO_3 - $\text{Li}[\text{Ni}_{1/2}\text{Mn}_{1/2}]\text{O}_2$ solid solution. *Journal of Solid State Chemistry* **178**, 2575-2585 (2005).

65. Meng, Y. S. *et al.* Cation Ordering in Layered O₃ Li[Ni_xLi_{1/3-2x/3}Mn_{2/3-x/3}]O₂ ($0 \leq x \leq 1/2$) Compounds. *Chemistry of Materials* **17**, 2386-2394 (2005).
66. Yan, P. *et al.* Atomic-Resolution Visualization of Distinctive Chemical Mixing Behavior of Ni, Co, and Mn with Li in Layered Lithium Transition-Metal Oxide Cathode Materials. *Chemistry of Materials* **27**, 5393-5401 (2015).
67. Yan, P., Zheng, J., Zhang, J.-G. & Wang, C. Atomic Resolution Structural and Chemical Imaging Revealing the Sequential Migration of Ni, Co, and Mn upon the Battery Cycling of Layered Cathode. *Nano Letters* **17**, 3946-3951 (2017).
68. Yan, P. *et al.* Injection of oxygen vacancies in the bulk lattice of layered cathodes. *Nature Nanotechnology* **14**, 602-608 (2019).
69. Manthiram, A., Knight, J. C., Myung, S.-T., Oh, S.-M. & Sun, Y.-K. Nickel-Rich and Lithium-Rich Layered Oxide Cathodes: Progress and Perspectives. *Advanced Energy Materials* **6**, 1501010 (2016).
70. Schipper, F. *et al.* Stabilizing nickel-rich layered cathode materials by a high-charge cation doping strategy: zirconium-doped LiNi_{0.6}Co_{0.2}Mn_{0.2}O₂. *Journal of Materials Chemistry A* **4**, 16073-16084 (2016).
71. Grimaud, A. *et al.* Activation of surface oxygen sites on an iridium-based model catalyst for the oxygen evolution reaction. *Nature Energy* **2**, 16189 (2016).

72. Domanski, K. *et al.* Migration of cations induces reversible performance losses over day/night cycling in perovskite solar cells. *Energy & Environmental Science* **10**, 604-613 (2017).

Chapter 4. Summary

In this thesis, the working mechanism of lithium-rich layered oxide electrodes and the engineering strategy of cathode materials are comprehensively investigated. The contents include (i) the unified theoretical picture concerning the relations between structural disorders, bond arrangements, and oxygen redox chemistry in oxygen-redox-active electrodes, and (ii) the strategy to resolve the voltage decay and hysteresis problems of lithium-rich layered oxide electrodes.

In the first part, I have established a theoretical picture linking structural disorder, covalent bonding, and oxygen redox chemistry in lithium/sodium-ion electrodes. It is demonstrated that the formation of structural disorders and concomitant bonding rearrangements contribute to the stabilization of oxygen. I elucidate that the extent of oxygen hybridization is determined by the utilization of oxygen states and the covalency of metal-oxygen bond. Moreover, it is discussed that bonding rearrangements in the structure inevitably induce redox asymmetry by irreversibly reorganizing the oxygen electronic structure. The restoration of the original bonding nature is found to be limited by the hysteretic nature of structural disorder and the astray of oxygen dimer in the structure. It is my belief that my theory will expedite the development of electrode materials based on high-valent redox, and will enrich other fields exploiting oxygen redox reactions.

In the second part, I proposed a design strategy to improve the reversibility of cation

migration by employing O2 type structural framework wherein the cation migration path is effectively modified owing to unique site preferences. STEM measurements visualized the intra-cycle reversible behavior of metal ions, and complementary experiments based on XRD, Raman, and HR-TEM analyses verified the preservation of pristine structure over long-term cycles. As a consequence of the excellent reversibility, O2-LLNMOs exhibits the significant reduction in voltage fade and hysteresis compared to O3-phase counterparts. First-principles calculations prove that the intra-layer cation migration is energetically prevented due to a large repulsion between face-sharing cations in O2-LLNMOs, which accounts for the improvement in structural reversibility. This work presents a robust guidance to resolve the long-standing problems of lithium-rich layered oxide electrodes, and I believe that these engineering strategies will help rejuvenate related fields that suffer from structural degradation problems.

Abstract in Korean

초록

에너지 수요가 급증하고 환경 문제에 대한 인식이 제고되면서, 전기자동차 및 에너지저장시스템의 시장이 급속도로 성장하고 있다. 이와 발맞추어, 에너지 저장장치의 성능향상에 대한 수요 역시 급증하고 있다. 다양한 에너지 저장장치 중, 리튬이온 이차전지는 높은 에너지 밀도, 우수한 출력 특성 및 수명 특성으로 인하여 지난 수십 년간 이동식 전자장치와 전기자동차의 표준 에너지 장치로 활용되어 왔다. 하지만 차세대 에너지 기술로의 완전한 전환을 위해서는, 현 배터리 시스템에서 에너지 밀도의 비약적인 향상이 요구된다. 이러한 배경에서 다양한 차세대 전극을 개발하려는 시도가 이어지고 있다. 특히 리튬과잉 양극 소재 (lithium-rich layered oxides)는 에너지 밀도가 기존의 양극재보다 현저하게 높아 차세대 양극 소재로써 많은 관심을 받고 있다. 하지만 리튬과잉 양극 소재는 에너지 보존 성능 측면에서 명확한 한계가 있어, 에너지 보존 및 수명 특성을 향상시키는 것이 시급한 상황이다. 본 학위논문에서는 리튬과잉 양극재의 전압 강하 현상에 대한 이론적인 연구를 제시한다. 나아가 충·방전 동안 전극의 전기화학적 가역성을 향상시킬 수 있는 디자인 전략을 소개한다.

제 2장에서는 리튬과잉 양극소재에서 산화환원 메커니즘과 구조적 결함의 상관관계에 대한 통합적인 이론을 제시한다. 리튬 및 소듐 과잉 양극 소재의 산소 산화 환원은 전기화학적 비가역성과 전압 강하를 야기한다는 문제가 제기되어 왔다. 비가역적인 산소 환원과 구조적 결함의 현상적 상관관계에 대한 실험적 관찰에도 불구하고, 그 상관관계는 아직 이론적으로 설명되지 않았다. 본 연구는 구조적 결함, 결함 배열, 산소 산화환원 메커니즘 간의 다차원적 상관성을 종합적으로 연구한다. 본 연구는 넓은 범위의 리튬 과잉 양극 소재를 대상으로 하며, 양이온성 구조 결함과 음이온성 구조 결함을 모두 포함한다. 양이온성 구조 결함의 경우, 강한 산소-산소, 금속-산소 혼성을 강화시켜 산소를 안정시키며, 그 혼성의 정도는 산소의 전하량과 금속-산소 공유결합성에 의해 결정되는 것을 증명한다. 또한 구조결함으로 인한 산소 혼성이 구조적 가역성에 미치는 영향을 제시하며, 특히 구조내 생성되는 산소 이량체가 심각한 구조적 비가역성을 야기한다는 것을 제안한다. 본 연구는 오랜 기간 보고되어온 구조적 결함과 산소 산화환원 사이의 현상적 상관관계를 설명하며, 산소 산화 환원의 가역성을 향상시킬 수 있는 이론적 토대를 제시할 것으로 기대된다.

제 3장에서는 반복된 충방전 동안 리튬과잉 양극 소재의 구조적 가역성을 향상시킬 수 있는 전략을 제시한다. 이러한 전략은 소재의

전압강하 현상이 주로 전이금속의 비가역적인 이동에서 기인한다는 기존의 이해에 기초한다. 앞서 전이금속의 이동 자체를 줄이려는 시도가 많았지만, 이동의 열역학적 안정성 때문에 장사이클 동안의 구조 보존은 불가능 하였다. 본 연구는 구조 변화 자체를 억제하는 것이 아닌, 구조의 가역성을 높임으로써 리튬 과잉소재의 전압강하 현상을 해결한다. 니켈·망간 기반 리튬과잉 산화물의 산소 격자를 O3 형태에서 O2형태로 조절하고, 이를 통해 구조적 가역성을 상당히 향상시키면서 전압 강하 현상을 억제할 수 있음을 제시한다. X선 회절 분석, 주사투과 전자 현미경, 라만 분광법을 통해 충전 중 리튬 층으로 이동한 전이 금속이, 방전 시 원래의 자리로 가역적으로 돌아가는 것을 관찰한다. 나아가 제일 원리 계산을 통해 O2 산소 격자내 전이금속 자리와 리튬 자리가 서로 면을 공유하고, 이로 인한 반발력이 구조의 가역성에 크게 기여한다는 것을 증명한다. 본 연구는 재료의 구조를 리튬과잉 양극 소재의 전압 강하 및 전압 히스테리시스 현상을 해결하며, 구조적 가역성이 중요한 다양한 분야에 널리 적용될 수 있을 것으로 기대된다.

주요어 : 에너지 저장장치, 배터리, 제일원리 계산, 양극, 리튬과잉 층상형 산화물, 산소 산화환원

학번 : 2016-20773